UNIVERSITY OF LONDON

IMPERIAL COLLEGE OF SCIENCE AND TECHNOLOGY

DEPARTMENT OF ELECTRICAL ENGINEERING

MICROMACHINE SIMULATION OF STEAM POWER PLANT

BY

RAFAEL HERNANDEZ MILLAN, ELEC. ENG.

Thesis submitted for the degree of
Doctor of Philosophy in the
Faculty of Engineering

LONDON, MARCH, 1973

ABSTRACT

Owing to the continued growth in turbogenerator size, the dynamics of the steam power plant in a power station have assumed importance. Two mathematical models of a steam power plant were developed to analyse the dynamic characteristics of the relevant part of the power system, one of these models is suitable for digital calculations and the other for analogue computer studies. In contrast with most transient stability studies that have appeared in the literature, the models in this thesis consider the turbine and boiler characteristics in detail.

The main object of this thesis is the simulation of the transient phenomena in a steam power station after a fault has taken place. For this purpose, a turbine dynamic characteristic simulator for a micromachine set was developed that was linked to the boiler simulator.

A comparison is presented between results of tests carried out in the Goldington and Northfleet power stations, micromachine simulations and digital calculations. In particular, load rejection and pole-slipping transients in these two power stations are discussed in detail. For both transients, a comprehensive explanation of the control aspects of the phenomena is attempted, and two ways of dealing with short duration faults in the transmission system are suggested.

Since the advent of the thyristor, controlled rectifiers have been extensively used, such rectifiers being in many instances part of a closed-loop system. A controlled rectifier operating under constant current control was employed to drive the micromachine set. In an attempt to analyse the dynamics of the micromachine drive system, two new discrete rectifier models were developed, a rigorous one capable of simulating large perturbation transients and a linearised one suitable for small perturbations. Using these models, an optimum design for the micromachine drive was achieved.

ACKNOWLEDGEMENTS

I wish to express my gratitude to Dr. L. L. Freris, M. Sc. (Eng.), Ph. D., D.I.C., C. Eng., M. I. E. E., under whose supervision the work described in this thesis was carried out, for helpful guidance and useful discussions.

I am grateful to the Electrical Engineering Department, Imperial College of Science and Technology for the facilities generously provided to pursue this work.

I greatly appreciate financial support from the Universidad Central de Venezuela.

I also wish to thank all my colleagues for their help, in particular J. P. Sucena-Paiva with whom many ideas in the field of rectifier dynamics were exchanged, M. Bolton for helpful discussions about the idiosyncracies of governors and M. Hardy who gave me many original ideas on turbine dynamics. General assistance in the laboratory from Mr. H. Hardie and Mr. P. Austin is gratefully acknowledged.

Finally, I would like to thank my brother Carlos, for his most loyal support.

to my parents

List of symbols

δ	load angle
V_f	field voltage
$V_{kd,kq}$	damper windings voltage
$V_{d,q}$	direct and quadrature armature voltage
V_b	bus bar voltage
V_t	machine terminal voltage
$V_{m1,m2}$	magnetic amplifiers input voltage
V_{exc}	exciter input voltage
V_{exs}, V_{ms}	exciter and amplifier stabiliser output
ψ_f	field flux linkages
$\psi_{d,q}$	direct and quadrature armature flux linkage
$\psi_{kd,kq}$	direct and quadrature damper winding flux linkages
ψ_{fo}	field current induced flux linkage in armature windings
ω_o	nominal supply angular frequency
$T_{HP,IP,LP}$	time lags associated with HP, IP, LP cylinders
$x_{md,q}$	mutual direct and quadrature axis reactances
$x_{fl,al,kdl,kql}$	field, armature, direct damper winding and quadrature damper winding leakage reactances
$x'_{d,q}$	direct and quadrature transient reactances
$x''_{d,q}$	direct and quadrature subtransient reactances
x_{ext}	equivalent reactance from machine terminals to infinite bus bar

$r_{f,a}$	field and armature resistance
$r_{rd,kq}$	direct and quadrature damper winding resistance
T_{do}	field open circuit time constant
$f_1 * f_2$	$\int_0^t f_1(\tau)\ f_2\ (t-\tau)\ d\tau$
$T'_{d,q}$	direct and quadrature transient time constants
$T''_{d,q}$	direct and quadrature subtransient time constants
p	Carson differential operator
$i_{d,q}$	direct and quadrature armature current
$i_{kd,kq}$	direct and quadrature damper winding currents
i_f	field current
$G_{m1,m2,vs,ex,ms,exs,eq}$	gains associated with excitation system
$T_{m1,m2,ex,ms,exs,eq}$	time constant associated with excitation system
W	steam flow
$W_{B,TV,IV}$	boiler, throttle and interceptor valve steam flows
$W_{HP,IP,LP}$	HP, IP, LP cylinder steam flow
T	temperature
P_{Loss}	fixed loss coefficient
$P_{HP,\ IP,\ LP}$	HP, IP, LP cylinder power output
R^I	Universal gas constant
γ	ratio of specific heat (c_p/c_v)
η_p	polytropic efficiency

$T^*_{1,2,3}$	time constants of hydraulic relays
$T_{a,b}$	equivalent time constants of hydraulic relay
$K_{p,d}$	gains associated with pressure controllers
$T_{i,de}$	time constant associated with pressure controllers
$\hat{\eta}_{nbi}$	variation of cylinder efficiency with speed
A	orifice area
g	gravitational acceleration
F	firing rate
C_f	control signal transmitted to fuel and air supply systems
S_v	virtual steam production
S_x	boiler steam production output
P_b	boiler pressure
P_t	pressure before throtle valve
$P_{HP,IP,LP}$	pressure at HP, IP, LP cylinder bowls
$T_{F,v,B}$	time constants associated with boiler modelling
$G_{1,2}$	gains associated with governor system
H, J	turbogenerator inertia constant
$\frac{\partial f}{\partial x}$	partial derivative of f with respect to x
$Q_{IN,OUT}$	energy entering and leaving the boiler
T_e	synchronous machine electrical torque
T_t	turbine torque

T_{si}	turbine simulator torque
δ_i	quality factors $(i = 0,1,2,...6)$
$p^j_{i,o}$	inlet and outlet pressures at turbine cylinder j
$T^j_{i,o}$	inlet and outlet temperatures at turbine cylinder j
p_t	turbine power output
n	turbine or micromachine rotor velocity
p_{si}	turbine simulator power output
T'_{si}	overall equivalent time constant of turbine simulator
q	rectifier number of controlled phases
$v_c(t)$	rectifier control voltage
$v_d(t)$	rectifier output voltage
$v_j(t)$	rectifier phase voltage
$v^j_r(t)$	ramp reference signal of the j^{th} pulsing unit
$v'_1(t)$	rectifier output voltage $(u=0)$
$v'_2(t)$	rectifier voltage drop owing to commutation
V	peak phase voltage
V_{dc}	d.c. component of the rectifier output voltage under no load and $\alpha = 0$
E_o	d.c. back voltage of load
$i_d\ (t)$	rectifier output current
$i_j\ (t)$	rectifier phase current
$i_{d1,2}\ (t)$	components of rectifier output current
$i_c\ (t)$	rectifier commutation current

I_d	d.c. component of $i_d(t)$
I_{ref}	direct current reference value
K	control amplifier gain
T_1	control amplifier time constant
T_1'	time constant of load plus rectifier circuit when only one valve conducts
T_2	time constant of load plus rectifier circuit (average conditions)
T_2'	time constant of load rectifier circuit under commutation
ω	angular frequency
ω_s	sampling angular frequency
ω_c	frequency at which self oscillations start
Z_{1e}, R_{1e}, X_{1e}	impedance, resistance and reactance of commutation circuit
Z_{ch}, R_{ch}, X_{ch}	impedance, resistance and reactance of the choke
Z_a, R_a, X_a	impedance, resistance and reactance of d.c machine armature
T_S	sampling or firing period
T_u	commutation time
t	time
$h(t)$	error signal in the rectifier current control system
$G(s)$	transfer function of control amplifier
$\delta(t)$	impulse function
$r(t)$	current ripple
m	a numeric such that at all times $o \leq m \leq 1$

F^*	gain correction factor
K_{crit}	critical gain of control amplifier for instability
R	load resistance plus average internal resistance of rectifier
L	load inductance plus average internal inductance of rectifier
α	firing angle
u	commutation angle
s	Laplace operator
z	$\exp(T_s s)$, z-transform operator
Δ	difference operator
$d(t-T)$	function expressing a pure delay of T seconds on the function it multiplies
$\mathcal{L}\,f$	Laplace transform of function f
$\mathcal{Z}\,f$	z-transform of function f
Superscript ^{o}	denotes steady-state values
Superscript *	denotes sampled variable
$K_{1,9}, S_{1,6}, A, A', B, B', C, C', D, D'$	auxiliary constants defined as they appear

other constants defined as they appear

INITIALS

HP, IP, LP	high, intermediate and low pressure
AVR	automatic voltage regulator
d.c	direct current
a.c.	alternating current

INDEX

CHAPTER 1

INTRODUCTION

1.1 General

Over the past decade considerable research has been undertaken on the analysis of high order dynamic systems. First, a mathematical model of the system is usually postulated after which the quality of the model can be assessed by simulation of true life situations. Predictions can then be effected with a degree of confidence determined by the closeness of the simulation results to the real situation and finally, a synthesis can be made if optimization of the dynamic process is sought.

This work is concerned with the simulation of power systems. As economic optimization of power system operation and design is attractive due to the considerable cost saving that may result, there is a real need for accurate simulation of power system dynamic behaviour. The solutions of the problems arising in power system simulation studies are important not only in the power field but also in other branches of theoretical and applied science that deal with high order controlled systems.

The main purpose of this thesis is the simulation of post-fault phenomena that can jeopardize the system reliability. In particular, the behaviour of a single steam power plant connected to a large system is studied using a micromachine.

1.2 Historical review of micromachine studies

As early as 1923 Schurig[1] constructed a per-unit scale model of a power system using small synchronous machines. Schurig in his pionering work did not model synchronous machine parameters, turbine characteristics or AVR action as his work was concerned with the transmission system overvoltages and overcurrents arising from system faults.

Late in the 30s and during the 40s extensive work was carried out in the U.S.S.R.[2] In 1950, Robert[3,4] published in France the laws of similarity for the modelling of large synchronous machines by means of micromachines and restricted his investigations to the turbogenerator transient behaviour after a fault. He also devised a systems approach to the multimachine problem and developed what has been known as 'microreseaux', in which scale models of large synchronous generators are interconnected by model transmission lines.

In 1957, the dynamic behaviour of several alternative extensions of the U.S.S.R. grid was assessed using micromachines[5]. This work provided the specifications for the new hydro power stations supplying consumer centres through very long transmission lines[5].

In the 50s, apart from France and the U.S.S.R., there were only a few other countries possessing micromachine instalations. Of particular importance was the work carried out at Imperial College[6]. Work has also been in progress in Australia[7].

The beginning of the 60s saw the digital computer becoming an increasingly powerful tool for the analysis of power system dynamic behaviour. Power system simulation studies were given a boost but interest in micromachines somewhat decayed as it was considered that the digital computer would be a more economic and flexible tool for simulation studies.

During the 60s, micromachines were used at Imperial College to corroborate digital computer calculations with experimantal results [8,9,10,11,12], in particular, Park's equations were solved and the merits of the d-q transformation were evaluated.

A CIGRE exercise was carried out in 1962 to evaluate transient stability methods of analysis. The report of the exercise was published in 1964[13] and was based on the results of the High Marnham tests[14]. The microreseaux simulation of Electricite de France in the CIGRE exercise compared favourably with digital and analogue computer results and network analyser simulations.

In 1970, a second CIGRE exercise was carried out[15] and the results of the Northfleet tests[16] were taken now as a basis for comparison. On this occasion, the micromachine simulation compared less favourably with test results than in the previous exercise. This was a direct consequence of poor parameter similarity and a realization that in certain aspects of direct simulation of power system dynamics, micromachines were being superseded by the more versatile digital computer.

During the last few years, several developing countries have shown interest in micromachines and some have actually bought microreseaux instalations. This may stimulate further research and it is hoped that micromachines will continue to play an important role in power system dynamic studies.

1.3 Present research on micromachines

Since the advent of the digital computer the aims of micromachine studies have changed. In the same way, recent advances in the electronic field have rendered obsolete many micromachine components. Moreover, rapid progress in technology made possible the introduction of more powerful controllers in power stations. As a result, research in micromachines is proceeding simultaneously in three main directions:

1) development of the micromachine system,

2) simulation studies, and

3) experimental support for innovations in power system control.

1.3.1 Development of the micromachine system

Micromachine designs are under continuous review, in particular, efforts are directed toward a reduction of the high per-unit resistances which adversely affect simulation results [12,17,18]. It is interesting to point out that the reduction of the microalternator resistances is an economic problem as larger micromachines do not suffer from this deficiency, but, the microreseaux cost is severely increased if ratings are augmented.

Research is also orientated towards implementing improved instrumentation. It is of particular importance to monitor the load angle, rotor speed, acceleration and torque. References 10, 19, 20, 21, 22 describe monitoring schemes arising from micromachine research which may find, in the future, direct application in a real power station.

A considerable part of this thesis is dedicated to the simulation of turbine characteristics for micromachine studies. The simulation of these characteristics was first implemented by Robert[3,4] in 1950, the resulting scheme being dynamically slow and accurate only for small perturbations.

Turbine simulation on micromachines can be pursued in two directions, namely a speed control system for the d.c. machine drive and development of the simulation of turbine characteristics.

In the search for a speed control system, Evans et al[23] in Australia have recently developed for this purpose a power amplifier based upon pulse width modulation techniques with about 1 ms sampling time. The author [24] and Hammons[25] have developed three-phase fully controlled rectifiers, with sampling time of 3.3 miliseconds. Recent work in rectifier dynamics, described in chapter 4, has permitted the design of a rectifier speed control system with a negligible overall transient response compared to the turbine transient characteristics.

In this thesis a scheme is developed capable of taking into account with reasonable accuracy large perturbations and therefore capable of simulating turbine characteristics under any operating conditions. Special care is taken to represent both the torque and the torque-speed--slope at any operating point.

The high per-unit loss of the micromachine set is discussed in chapter 3 where it is concluded that the microalternator losses are excessively high and thus core loss compensation is necessary. However, I^2r losses in the armature circuit of the microalternator are more difficult to estimate and no compensation was attempted.

Recently, other turbine simulators for micromachine studies[26,27] have been suggested, but in the author's opinion, these simulators do not compare favourably either in transient response or in steady-state accuracy with the representation developed here. In particular, special analogue circuitry was developed to account for the singular behaviour of the hydraulic amplifier transfer function (section 2.8).

1.3.2 Simulation studies

In this work, the simulation studies of other investigators in the field are extended so that a more comprehensive dynamic model of a steam turbine could be considered. The simulation of the interceptor valve behaviour is shown to be of particular importance in the event of load rejection and pole-slipping conditions. A boiler model is also developed enabling power system disturbances of up to several minutes to be studied with reasonable validity.

In addition, full load rejections have been successfully simulated on a micromachine set for the first time and pole-slipping conditions were also simulated resulting in a comprehensive explanation of the phenomena involved.

All simulations described in this thesis are concerned with the Goldington[28] and Northfleet[16] tests. Several reports of simulation studies carried out by other investigators[15,28,29,30,31] are available for comparison purposes.

1.3.3 Experimental support for innovations in power system control

Micromachines are capable of providing experimental validation of new control schemes. An example of this type of research is at present being carried out at Imperial College, in which a direct digital control is being implemented on a turbogenerator in order to test various optimum control strategies[32].

1.4 Power system dynamic simulation

Developments in the power simulation field during the last few years have produced an increased accuracy[33,34,35]. The introduction of the boiler in this simulation has permitted the analysis of the dynamic behaviour of power systems over longer periods[33,34,36]. The trend in the search for a general purpose complete power system simulator influenced the work of this thesis and as a result the author introduced a boiler into the micromachine simulation.

Little detailed consideration has been given in the past to the turbine behaviour but in this work, the turbine and its controllers are considered in some depth.

The various components of the simulated power system are now introduced in greater detail.

1.4.1 The transmission system and load

The transmission system does not in theory offer difficulties, but for system studies a great deal of research is necessary to simplify transmission networks systematically and to extract the fundamental characteristics. A single power station connected to an infinite bus bar by an impedance is used throughout this study.

The behaviour of the load under disturbed voltage and frequency conditions has lately received attention in the literature[37,38,39]. If the simplifying assumption of an infinite bus bar is lifted and load characteristics are simulated, frequency and voltage variations will take place and, with due regard to boiler characteristics, a complete power system simulation can be obtained. The coordination of all control systems, from boiler pressure controllers, turbine governors, and voltage regulators to strategies for load shedding and line switching can then be embodied in a single study.

1.4.2 The synchronous machine and automatic voltage regulator

The basic theory of synchronous machine modelling has been well established in the literature by Tesla[40], Blondel[41], Park[42], and Adkins[43]. This theory is based on a first harmonic Fourier approximation of space-time waves, but nevertheless the theory has been used with some success to predict phenomena like the backswing (section 5.5.3) which takes place over very short time intervals. Furthermore, nonlinearities like saturation have been taken into account in this approach with a fair degree of accuracy resulting in closer approximations to synchronous machine dynamics. In this context, a micromachine is a particularly useful model because the full harmonic content of the space-time wave is considered and it can be argued that saturation is better represented in a micromachine than in most digital computer simulations.

The author has developed in this thesis (section 2.4) a simplified mathematical model of a synchronous machine directly from Park's equations [29,44] as written by White and Woodson[45].

A Cauer expansion technique[46] was used to reduce the order of automatic voltage regulator transfer functions for system studies. This technique offers two main advantages of simplicity and accuracy over Bode diagram approximationsdescribed in reference 47 and used by most investigators.

1.4.3 The turbine and governor system

The torque speed characteristics of a turbine require special attention and an analysis of the basic mechanism of power transfer that takes place in a turbine blade is pertinent. From this analysis, briefly described in section 2.7, and well known to blade designers[48], it is shown that constant power lines in the torque-speed plane are good approximations to turbine steady-state characteristics. The foundations of the analysis of blade power transfer mechanisms are well established from the experimental results on blade simulators by Waren-Keenan[49], Dollin[50] and the Steam Nozzles Research Committee[51]. Oakden[52] has assessed favourably the validity of blade simulator investigations with reference to the application of one dimensional analysis to a three dimensional process. However, this one dimensional method of analysis breaks down when long blades are studied. This may be the case when last blade rows of LP turbine cylinders are considered as has been pointed out by Kearton[53]. Experimental corroboration of turbine steady-state characteristics have been obtained for ship[54] and train[55] steam drives.

In this study a dynamic model of a turbine cylinder is rigorously developed from the early works of Stodola[56] and Kearton,[57] where from the model of a cylinder, the dynamic equations describing the behaviour of a non-reheat turbine are readily derived[58]. In reference 28 a similar set of equations for modelling a non-reheat turbine is employed and good correlation with experimental results is obtained in the event of a full load rejection (section 5.2).

The steady-state evaluation of turbine characteristics (section 2.7) is in agreement with the extensive experimental research carried out by General Electric[59,60,61,62].

Using the Stodola[56] and Kearton[57] equations, a circuit formulation of the steam path of a reheat turbine is made in section 2.7 [63]. This formulation is similar to the approach suggested by Jolley[64] and results in a non-linear model. The circuit formulation can be used as a basis for comparison of the classical linear approach to reheat turbine dynamic characteristics[34,64,65,66]. It can be shown that this classical approach in which the turbine characteristics are assumed to be linear is not a linear incremental approximation of the more rigorous non-linear circuit model and hence the classical model produces errors of roughly 10 to 20% in both small and large perturbation studies. Similar conclusions have been drawn by Jolley[64] and Hughes[67] who have also pointed out that if the turbine characteristics are assumed to be linear the HP cylinder is poorly represented.

The governor behaviour under large disturbances is of special importance. It is shown that a slow opening rate of the hydraulic relays as compared with the closing rate improves stability margins. Particular importance is also given to governor multiple time lag characteristics[64] and relay constraints.

1.4.4 Boiler dynamics

Early boilers had a very large stored energy capacity and for all practical purposes, boiler dynamics were decoupled from turbine and generator controllers. During the last two decades with the accumulation of knowledge on the heat transfer process, boiler dimensions were relatively reduced with a resulting reduction in the relative energy storage[68]. This trend culminated in the "once through" boiler having a very low energy storage[69]. As power stations grew in size, the per-unit boiler stored energy decreased and it is therefore not correct to assume in such cases non-interaction between the boiler, the turbine and generator controllers. Laubli and Fenton[70] have shown that instability of these controllers is likely to occur if adequate allowances are not made to avoid it.

The boiler model developed here is a modified version of Profos[69] original approach and the experimental work reported recently by Astrom[71] supports the modelling approach employed in this thesis.

Of all boiler dynamic models published in the literature only the works by IBM[33], Young[34], Profos[69], Laubli-Fenton[70] and Astrom[71] are relevant for large power system studies. Other boiler dynamic models [72,73,74,75,76,77] involve detailed analysis of heat transfer dynamics and are not directly relevant to the problem under discussion.

1.5 Rectifier dynamics

The controlled rectifier is one of the fastest power amplifiers available. Since the advent of the thyristor, such amplifiers have found a large number of applications. In this work, a three phase fully controlled rectifier was used for speed control on the d.c. machine drive motor of the micromachine set. The torque speed characteristic specifications for the d.c. motor demand that the rectifier forms part of a closed-loop current-control system. Experimentally, it was found that instability occured when the gain of the current-control loop was made too large. In order to analyse the instability phenomena as well as to attain a specified transient performance, dynamic modelling of the rectifier was necessary.

In chapter 4, first a rigorous mathematical model of the rectifier system employed is developed based on the "central process" idea[78] and this model describes the dynamic behaviour of the rectifier under any operating conditions. Good correlation was obtained between experimental results and digital computer calculations using this model. These calculations, however, are time consuming and a small perturbation model was required, and thus a critical analysis of existing rectifier small perturbation models was undertaken.

As early as 1951, Busemann[79] studied the hunting of convertors operating under current-control, and modelled the rectifier using impulsive analysis. Busemann's method can determine whether a particular operating point is stable without any indication of the stability margin. This method neglects resistances, overlap angles and pulsing circuitry characteristics.

Reider[80] in 1957 modelled the rectifier using the principle of "equivalent areas", later used by Andeen[81,82] to model pulse-width modulated systems. In chapter 4 it is shown that this principle, as applied by Reider, is restricted to extremely simple system configurations. Reider, however, was first to use sampled data systems theory and thus was capable of giving an indication of the degree of stability of the system using Nyquist plots.

Bjäresten[83] modelled the rectifier in 1963 using impulsive analysis and was first to take into account the pulsing circuitry. Bjäresten neglected resistances and overlap angles and analysed the system under short circuit conditions only.

Fallside et al[84,85] also used impulsive analysis, but employing Fourier transform rather than z-transform techniques they obtained an infinite series expansion for the critical gain. This infinite series expansion for the critical gain can be shown to be equivalent to Bjäresten's earlier work[86]. Taking only the first term of the Fourier transform of the infinitesimally small rectifier voltage output at the critical stability point, Fallside derived a so-called describing function approximation to the convertor transfer function. This approach has the main disadvantage that the frequency of self-oscillations has to be postulated. Like Fallside, Persson[87] used a first harmonic approximation, although this author was more concerned with the representation of the a.c. system impedance attached to the rectifier mains supply.

Lately other authors[88,89,90] have modelled the rectifier using a sample and hold circuit based upon a shape similarity idea. In chapter 4 it is shown that this idea has severe limitations when applied to rectifier systems.

In this thesis a comprehensive analysis of the rectifier under small perturbations is presented which results in an exact linear incremental model[91]. The analysis permits the inclusion of overlap angle effects and a thorough representation of the pulsing circuitry.

An alternative, equally rigorous, procedure due to Flower and Hazel[92] is the linearisation of the rectifier difference equations. Flower and Hazel, however, considered only a very simple system structure.

CHAPTER 2

STEAM POWER PLANT SIMULATION

2.1 General

In this chapter the simulation principles for a general purpose steam power plant model will be discussed. The model should be capable of simulating two steam power plant major disturbances, namely a short circuit near the synchronous machine terminals and a full load rejection. The emphasis of the simulation is placed on governor action and therefore governor, turbine and synchronous generator modelling are considered in detail. As the boiler stored energy plays an important part in long term power system dynamics, a boiler model suitable for power system studies is introduced.

Two models were developed, one suitable for digital computer applications and another for analogue computer studies which were used in conjunction with a micromachine set to simulate the synchronous machine behaviour. The size of the digital model was kept within 20 first order differential equations so that computation could be carried out economically. A systems approach towards the problem was maintained throughout the study.

2.2 Physical description of a steam power plant

The physical processes involved in the generation of electricity in a steam power plant are described diagramatically in Fig. 2.1. The plant consists of a boiler in which chemical energy from a fuel is transformed into heat, this heat raises steam the energy of which is transformed into mechanical energy in a turbine. In turn this energy is transformed into electrical energy in a generator from where it is transmitted to the consumer. The modelling of such a process will now be described.

2.3 The micromachine system

The micromachine system consists of a small synchronous machine and a two phase tachogenerator both driven by a d.c. motor. This small synchronous machine is designed to give a range of parameters that correspond, on a per-unit basis, with those of large alternators. The micro-alternator is connected through a network to a fixed supply of a much bigger capacity than that of the set and which can be treated as an infinite bus. A selection of flywheels may be fixed to the shaft of the set for adjustment of the inertia constant of the system.

On scaling down a large machine, a desired simulation is achieved in most respects with the exception of the

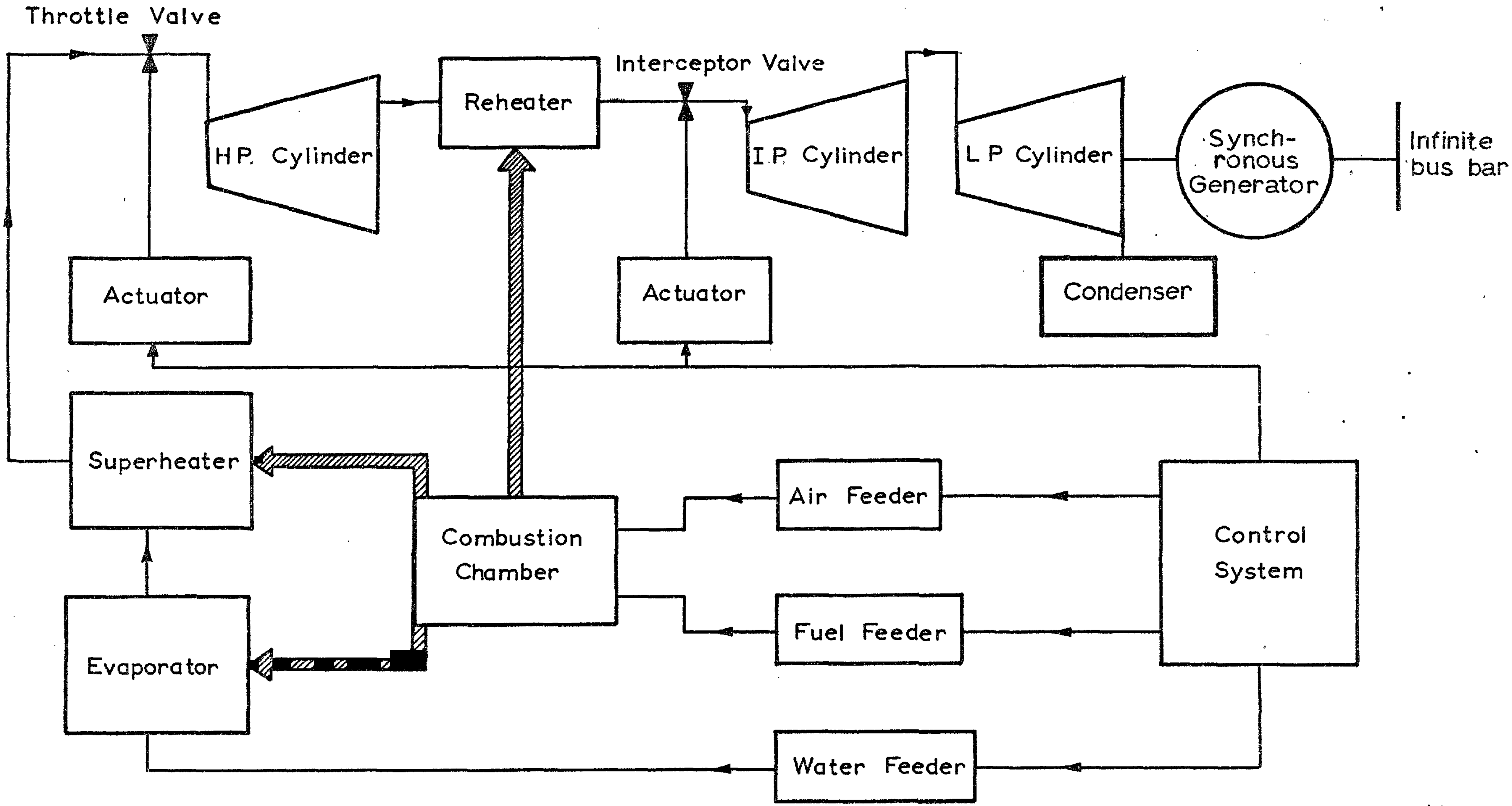

Fig.2.1. General Block Diagram of a Power Plant where Steam Extractions are not shown.

open circuit time constant of the field winding of the micro machine which owing to physical limitations is much smaller than that of a large alternator. The time constant regulator is a device designed to reduce the effective field resistance and therefore alter the open circuit time constant to the order of those required for the simulation of a large machine. A time constant regulator developed at Imperial College and used in earlier experiments is shown in Fig. 2.2.[9] The transient and frequency response of this device were measured and the results are presented in Fig. 2.2. The transfer function of this time constant regulator can be identified now as a second order system with a break frequency of 25 Hz. The break frequencies of the Goldington and Northfleet exciters are in comparison two orders of magnitude smaller, therefore, the transient behaviour of the time constant regulator can be neglected without introducing any serious error.

The high armature resistance and the small subtransient time constant of the micromachine per-unit parameters show a certain amount of disagreement with the corresponding parameters of the synchronous generators being simulated. These discrepancies were accepted as it was practically impossible to avoid some differences (Table 2.1, pp 88).

The turbine torque-speed characteristics were simulated by armature control of the d.c. machine. The system adopted is described in chapter 3.

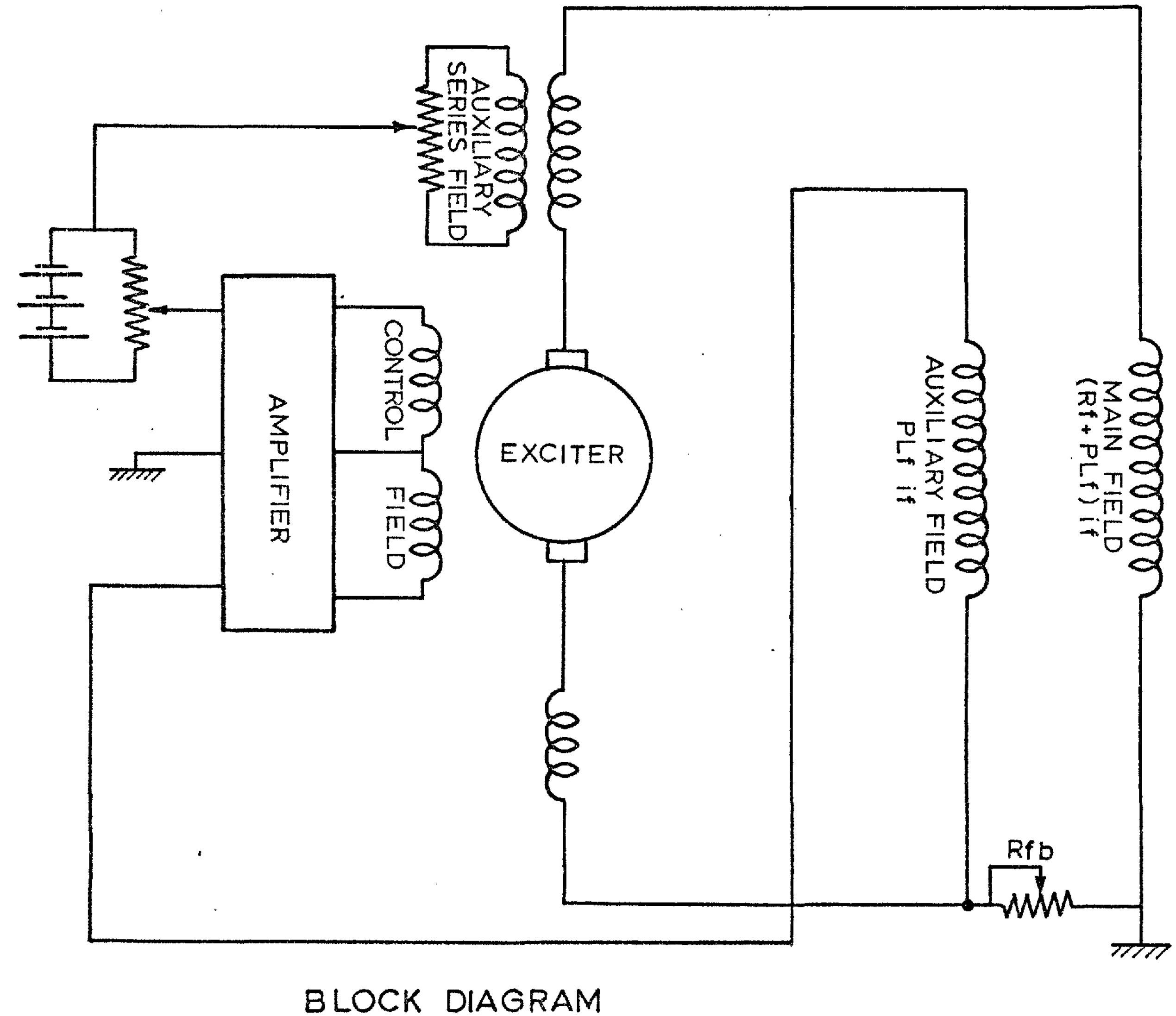

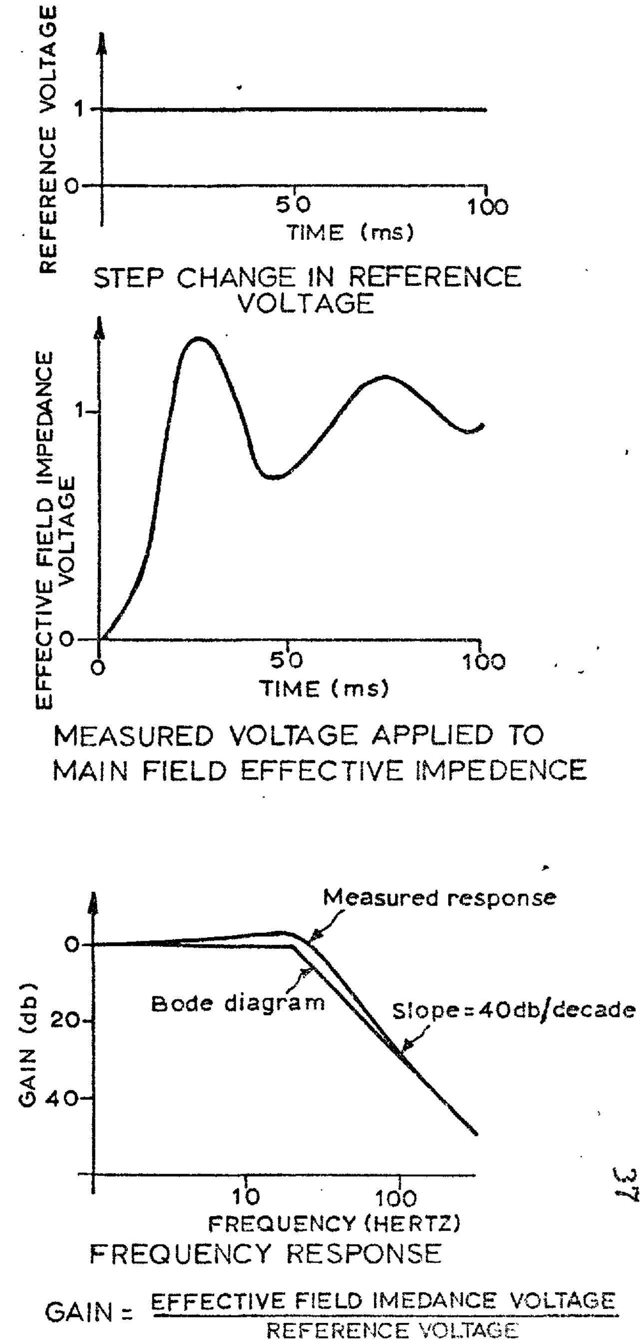

Fig. 2.2. Time constant regulator

Three states of the micromachine system were measured: the micromachine terminal voltage, the shaft speed and the load angle.

The micromachine terminal voltage was monitored by means of a step down voltage transformer, rectifier and smoothing circuitry as shown in Fig. 2.3.

The shaft speed was obtained by rectifying the two phase tachogenerator output voltage and passing it through smoothing and scaling circuitry as shown in Fig. 2.4.

The micromachine load angle was measured with reference to the infinite bus bar. The shaft driven tachogenerator generates a sinusoidal voltage whose phase with respect to the infinite bus voltage changes in accordance with the rotor position[10], thus the rotor angle detection problem can be transformed into a phase detection problem between the infinite bus bar voltage and the tachogenerator output voltage. The sensor that was designed and tested by another research student [10] has an operating range of 180 degrees, however as pole-slipping with load angle variations of 360 degrees were expected the original design was modified. In the new design the load angle is measured as shown diagramatically in Fig. 2.5. Additional filtering is introduced to reject the 50 Hz component present in the output of the load angle detector owing to this modification. The final design of the filter is shown in Fig. 2.6.

709 OPA OPERATIONAL AMPLIFIER
T 3 SINGLE PHASE TRANSFORMERS
R 10K
C .5μF

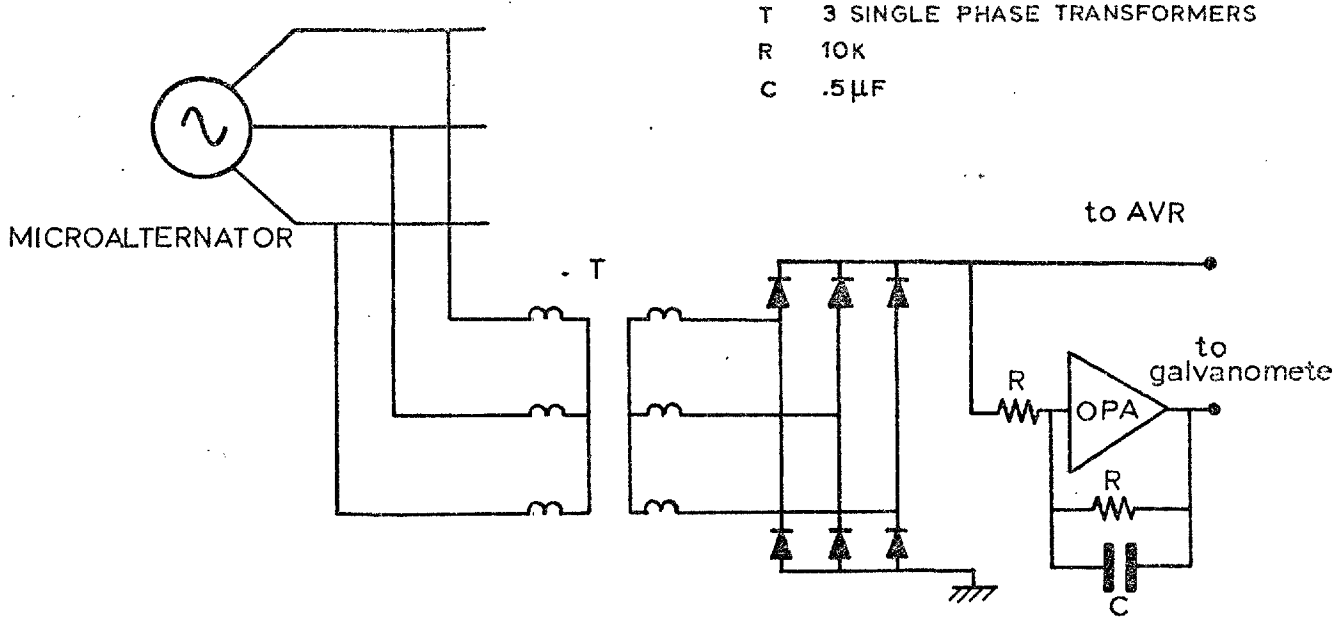

Fig. 2.3. Microalternator voltage sensing device

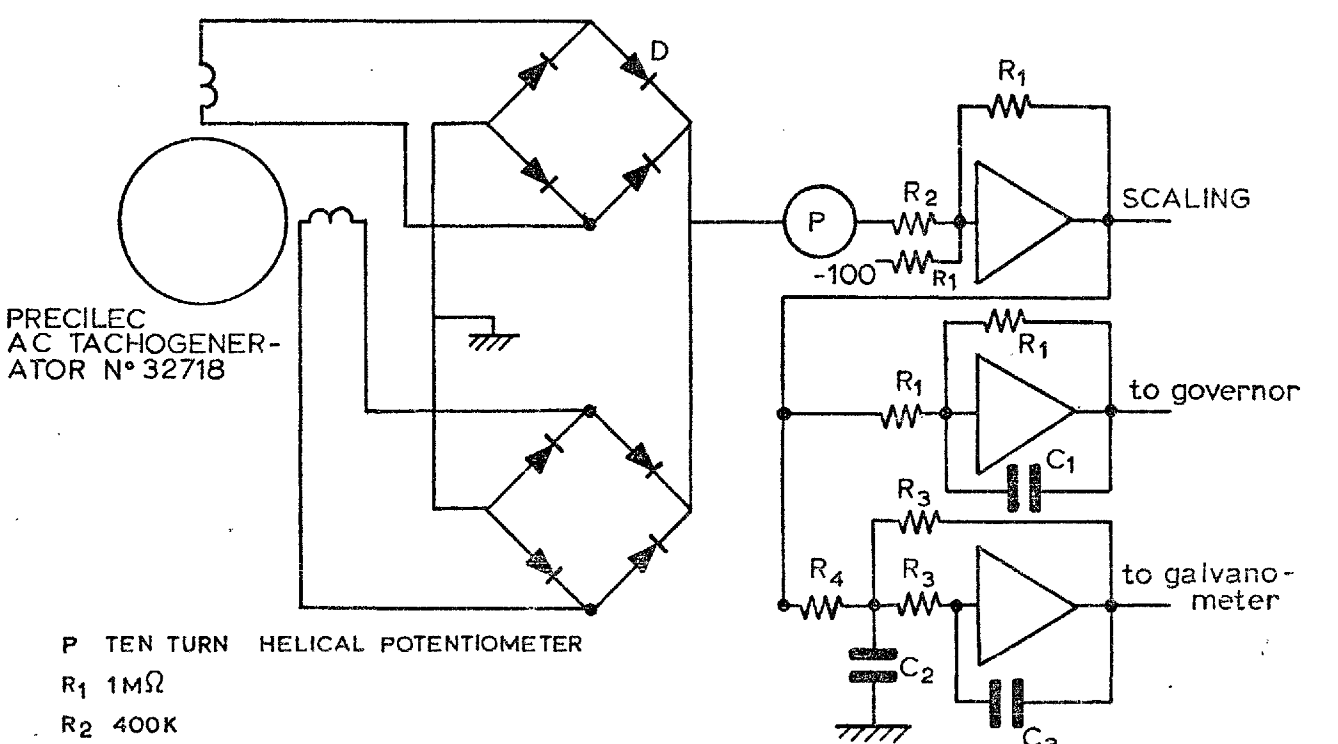

P TEN TURN HELICAL POTENTIOMETER
R_1 1MΩ
R_2 400K
C_1 0.015μF C_2 = 1 μF C_3 = 2.2 μF
R_3 10 K
R_4 100 K
D 0A81

Fig. 2.4. Microalternator speed sensing device

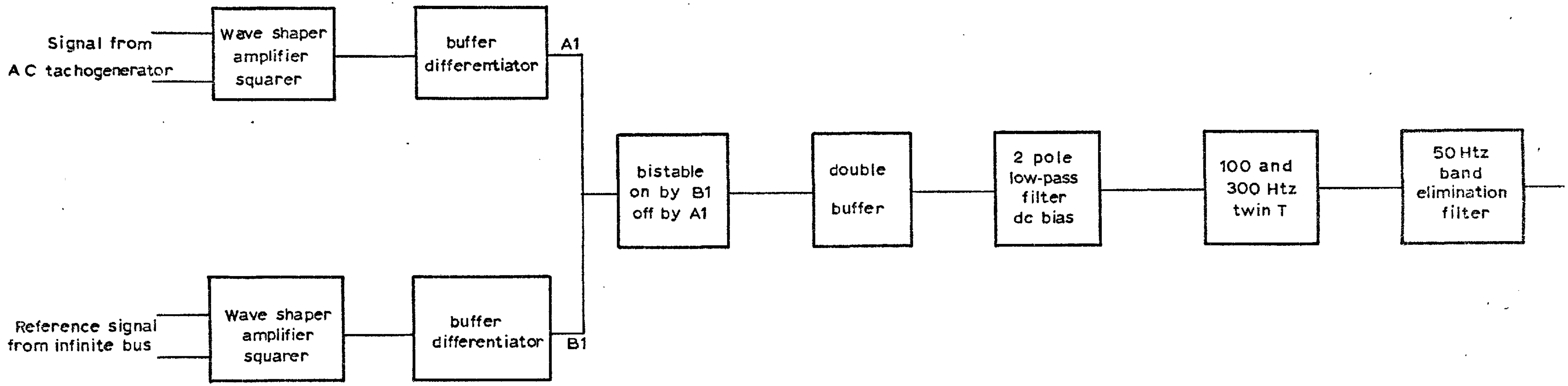

Fig. 2.5. Block diagram of microalternator load angle sensing device

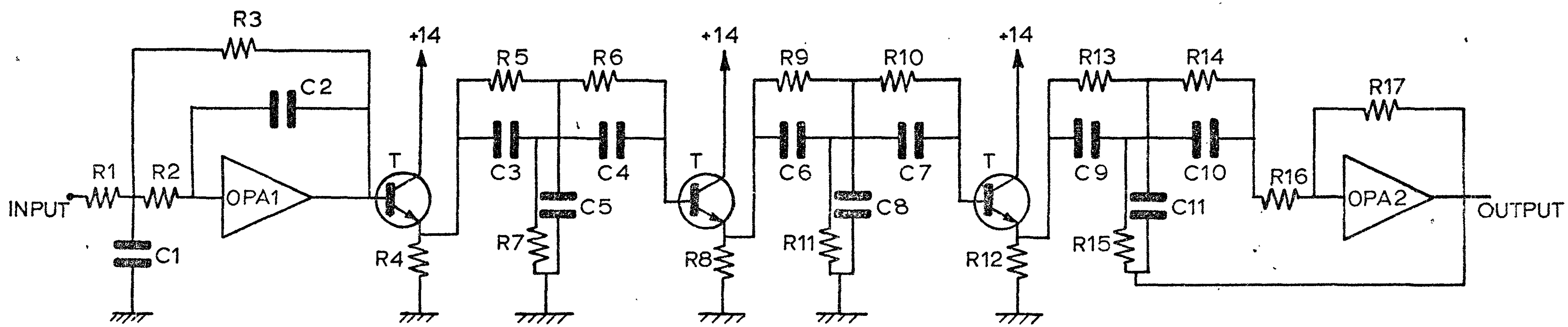

R1	47KΩ	R11	2.35KΩ	C4	0.39µF
R2	5.6KΩ	R12	5.6 KΩ	C5	0.78µF
R3	18KΩ	R13	6.4KΩ	C6	0.113µF
R4	5.6KΩ	R14	3.2KΩ	C7	0.113µF
R5	4.7KΩ	R15	3.2KΩ	C8	0.22µF
R6	4.7KΩ	R16	240KΩ	C9	0.6µF
R7	2.35KΩ	R17	50KΩ	C10	0.6µF
R8	5.6KΩ	C1	0.22µF	C11	1.4µF
R9	4.7KΩ	C2	0.22µF	OPA1	SL701B
R10	4.7KΩ	C3	0.39µF	OPA2	709 OPA
				T1	ME4103

Fig 2.6. Circuit diagram of load angle detector filters

(overall characteristics : cut frequency 20 Hertz; band elimination at 50, 100 and 150 Htz)

A block diagram of the micromachine system for the simulation of a steam power station is presented in fig.2.7 in which an analogue computer was used for the simulation of the governor, turbine and boiler.

In order to check the validity of the micromachine simulation against test results, a mathematical model of a synchronous machine suitable for digital computer calculations was next developed.

2.4 Mathematical modelling of synchronous machines

According to the "generalized machine theory"[43] the equations describing mathematically the dynamic behaviour of a synchronous machine after applying a modified form of Park transformation[42,93] to the original phase variables are given in reference 45 and reproduced here. The same sign convention and per-unit system are adopted.

Voltage equations

$$\begin{aligned}
V_f &= r_f\, i_f + p\, \psi_f \\
V_{kd} &= 0 = r_{kd}\, i_{kd} + p\, \psi_{kd} \\
V_{kq} &= 0 = r_{kq}\, i_{kq} + p\, \psi_{kq} \qquad (2.1) \\
V_d &= -r_a\, i_d + p\, \psi_d - \omega\, \psi_q \\
V_q &= -r_a\, i_q + p\, \psi_q + \omega\, \psi_d
\end{aligned}$$

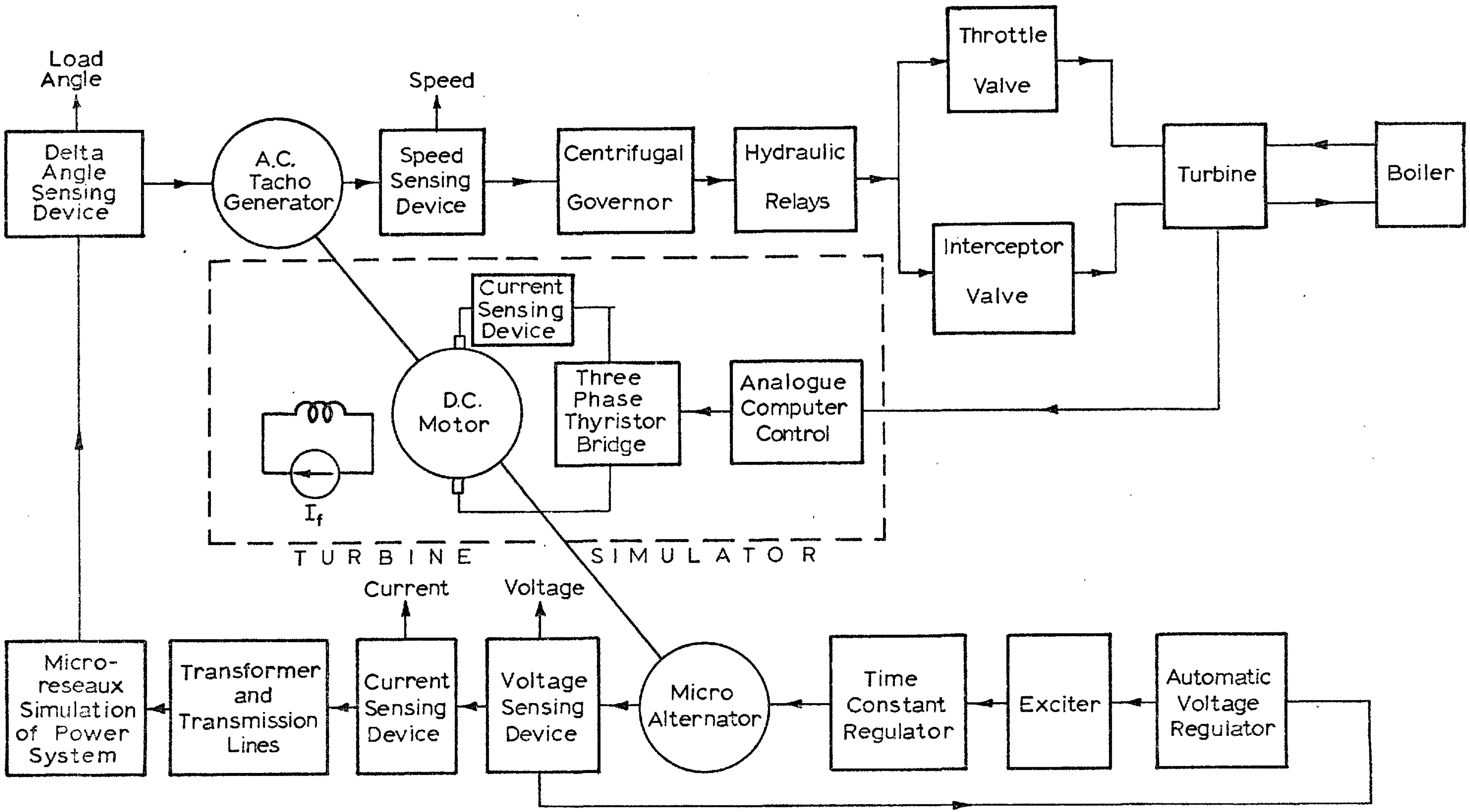

Fig. 2.7 Block diagram of a micromachine system for power station simulation

Mechanical equation:

$$T_{tur} = J\,p\,\frac{\omega}{n} + n\,(\psi_d\, i_q - \psi_q\, i_d)$$

Flux linkages equations:

$$\omega_o \psi_f = (x_{md} + x_{fl})\, i_f - x_{md}\, i_d + x_{md}\, i_{kd}$$

$$\omega_o \psi_d = x_{md}\, i_f - (x_{md} + x_{al}) i_d + x_{md}\, i_{kd} \qquad (2.1)$$

$$\omega_o \psi_q = -(x_{mq} + x_{al}) i_q + x_{mq}\, i_{kq}$$

$$\omega_o \psi_{kd} = x_{md}\, i_f - x_{md}\, i_d + (x_{md} + x_{kde}) i_{kd}$$

$$\omega_o \psi_{kq} = -x_{mq}\, i_q + (x_{mq} + x_{kql}) i_{kq}$$

In order to save computer time and to keep the order of the simulation within reasonable limits it was considered necessary to reduce the order of the mathematical model representing the synchronous machine. This was achieved by reducing the number of energy storage elements considered. The most important output quantities of a synchronous machine from a system point of view are the rotor angle, the rotor speed, the armature current and the terminal voltage; all energy storage elements which do not have a significant effect upon the variations of these output quantities may be neglected without seriously affecting the accuracy of the simulation[44].

Damper windings are responsible for large damping torques and their effect should be taken into account. A convenient way adopted by many investigators, of considering this effect, is to introduce a variable velocity damping coefficient thereby reducing the number of energy storage elements by two. Crary[94] gives the following formula for this damping coefficient:

$$T_d = V_b^2 \left[T''_d \left(\frac{1}{x''_d} - \frac{1}{x'_d} \right) \sin^2\delta + T''_q \left(\frac{1}{x''_q} - \frac{1}{x'_q} \right) \cos^2\delta \right] \quad (2.2)$$

Energy storage elements associated with the stator coils can be eliminated by neglecting $p\ \psi_d$ and $p\ \psi_q$ terms in the voltage equations. The effect of eliminating these two terms has been assessed in the literature and shown to be equivalent to neglecting 50 Hz transients[29,31,95]. These transients influence the output quantities of the alternator significantly only during very short time intervals and are therefore neglected here.

Synchronous machine equations are obtained neglecting saturation[42] . Some investigators have introduced the effects of saturation by changing synchronous machine coefficients according to flux levels. These methods have been succesfull in obtaining closer approximations to machine dynamics. Saturation is neglected here because saving on computer time was desirable and its inclusion would not have changed qualitatively the solution of the problem although it would have increased its accuracy. On the basis of no saturation, a simplified set of equations describing synchronous machine dynamics with constant coefficients is obtained as follows:

Voltage equations

$$V_f = r_f\, i_f + p\, \psi_f$$

$$V_d = -r_a\, i_d - \omega\, \psi_q$$

$$V_q = -r_a\, i_q + \omega\, \psi_d$$

Mechanical equations

$$T_{tur} = J\, p\, \frac{\omega}{n} + n\, (\psi_d\, i_q - \psi_q\, i_d) + T_d\, p\delta \qquad (2.3)$$

Flux linkages equations

$$\omega_o\, \psi_f = (x_{md} + x_{f1}) i_f - x_{md}\, i_d$$

$$\omega_o\, \psi_d = x_{md}\, i_f - (x_{md} + x_{a1})\, i_d$$

$$\omega_o\, \psi_q = -(x_{mq} + x_{a1})\, i_q$$

Having neglected all but three of the synchronous machine energy storage elements it is vital to choose judiciously the state variables. If the field current were chosen as a state variable numerical difficulties would be introduced because the corresponding state equations would be a function of the derivative of the machine terminal voltage. As during faults the machine terminal voltage changes step-wise, its derivative becomes infinite[44]. In order to avoid this difficulty ψ_f was selected as a state variable.

Equations 2.3 are now rewritten in state space form as a set of three first order differential equations with constant coefficients and δ, $p\delta$ and ψ_f as state variables (appendix 1).

$$p[\delta] = [p\delta]$$

$$p[p\delta] = \frac{25}{H}\Big[T_{tur} - T_d\ p\delta - S_1 \sin^2\delta - S_2 \cos^2\delta - S_3[\omega_o \psi_f]^2 - S_4 \sin\delta\cos\delta - S_5 \sin\delta\,[\omega_o\psi_f] - S_6\cos\delta\,[\omega_o\psi_f]\Big]$$

$$p[\omega_o\psi_f] = \omega_o v_f - B[\omega_o \psi_{fd}] + C\sin\delta + D\cos\delta \tag{2.4}$$

2.5 Representation of excitation systems and automatic voltage regulators

The excitation systems and voltage regulators considered here correspond to those in action during two tests carried out on the British grid. Relevant descriptions are given in references 16 and 28 that deals with the tests of Goldington and Northfleet power stations.

A block diagram of the Goldington automatic voltage regulator and exciter is shown in Fig. 2.8. The equations describing the dynamic behaviour of this system are reproduced here from reference 28

$$
\begin{aligned}
V_{m1} &= -G_{vs} (V_t - V_r) \\
V_{m2} &= \frac{G_{m1}}{1+T_{m1}p} (V_{m1} + V_{exs} + V_{ms}) + K_{m1} \qquad V_{m2_{max}} \geq V_{m2} \geq V_{m2_{min}} \\
V_{exc} &= \frac{G_{m2}}{1+T_{m2}p} V_{m2} + K_{m2} \qquad V_{exc_{max}} \geq V_{exc} \geq V_{exc_{min}} \\
V_f &= \frac{G_{ex}}{1+T_{ex}p} V_{exc} \\
V_{ms} &= G_{ms} \frac{T_{ms}p}{1+T_{ms}p} V_{exc} \\
V_{exs} &= G_{exs} \frac{T_{exs}p}{1+T_{exs}p} V_f
\end{aligned}
\qquad (2.5)
$$

No reference is made to the rectifiers since it is assumed their characteristics are linear and the ripple in the voltage output of the rectifier does not affect significantly the system response. Equations 2.5 include several constraints imposed upon the voltage output of the magnetic amplifiers and the exciter; in the analysis that

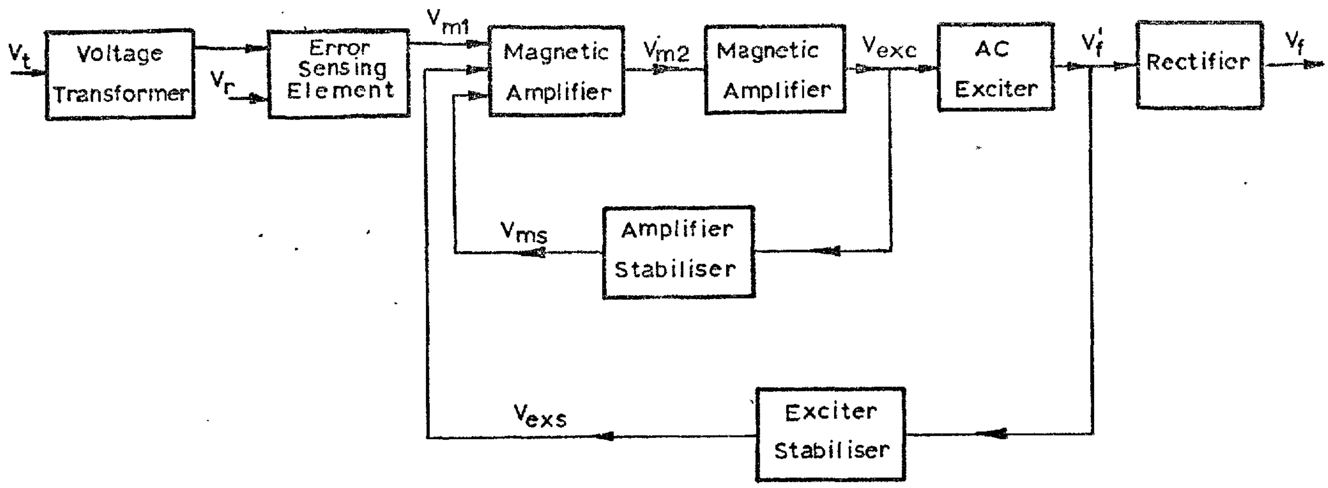

Fig. 2.8. Block diagram of Goldington voltage regulator

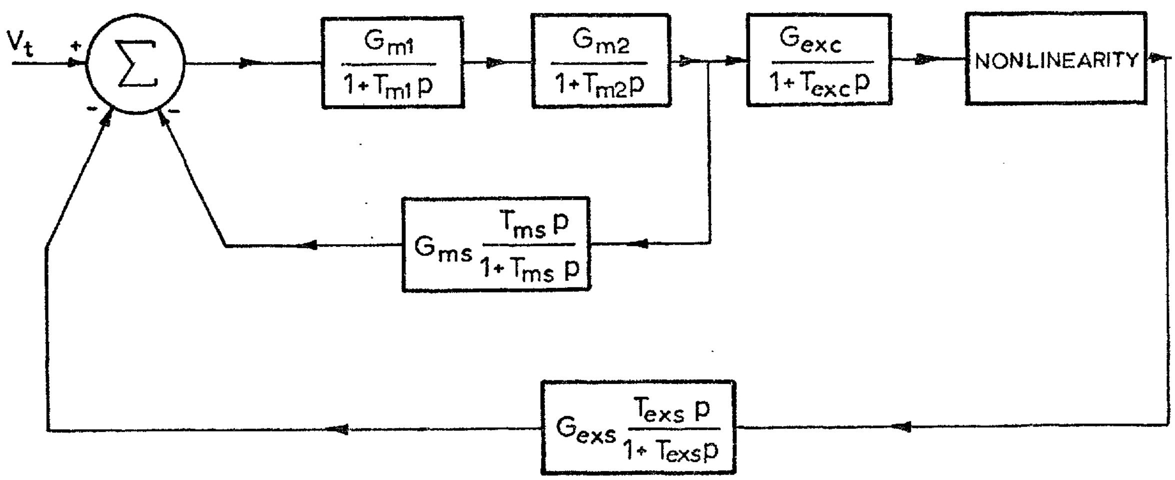

Fig. 2.9. Block diagram of Goldington voltage regulator after having lumped all nonlinearities into a single block.

follows, in order to reduce the complexity of the voltage regulator and exciter representations, these constraints are lumped together into one single nonlinear block which represents excitation ceiling voltages. The excitation system can thus be represented as shown in Fig. 2.9.

The set of transfer functions defining the behaviour of the magnetic amplifiers, amplifier stabilisers and a.c. exciter can be lumped into one single transfer function $H(p)$ as shown diagramatically in Fig. 2.10; $H(p)$ can be obtained analytically from Fig. 2.9 as

$$H(p) = \frac{G_{m1}G_{m2}G_{ex}(1+T_{ms}p)}{(1+T_{exc}p)((1+T_{m1}p)(1+T_{m2}p)(1+T_{ms}p)+G_{m1}G_{m2}G_{ms}T_{ms}p)} \tag{2.6}$$

Equation 2.6 can be decomposed into the following form[46],

$$H(p) = \cfrac{G_{eq}}{1 + \cfrac{T_1 p}{1 + \cfrac{T_2 p}{1 + \cfrac{T_3 p}{1 + \cdots\cdots}}}} \tag{2.7}$$

Where T_i are known as "partial coefficients", and the form of this expansion is due to Cauer[46]. Based on this

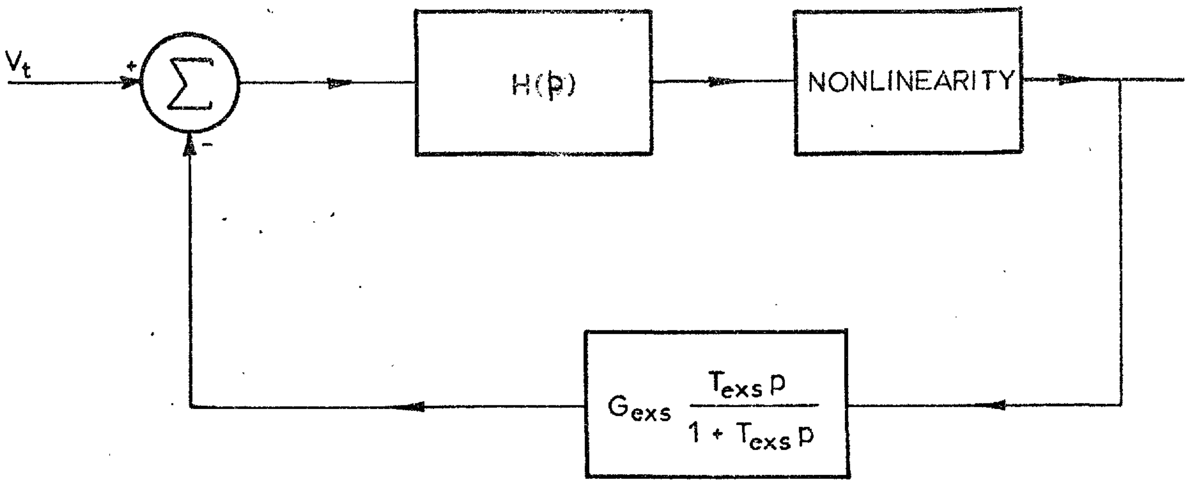

Fig. 2.10. Structure of Goldington voltage regulator after having lumped all nonlinearities into a single block and obtained a transfer function H(S) for all magnetic amplifiers and stabilisers.

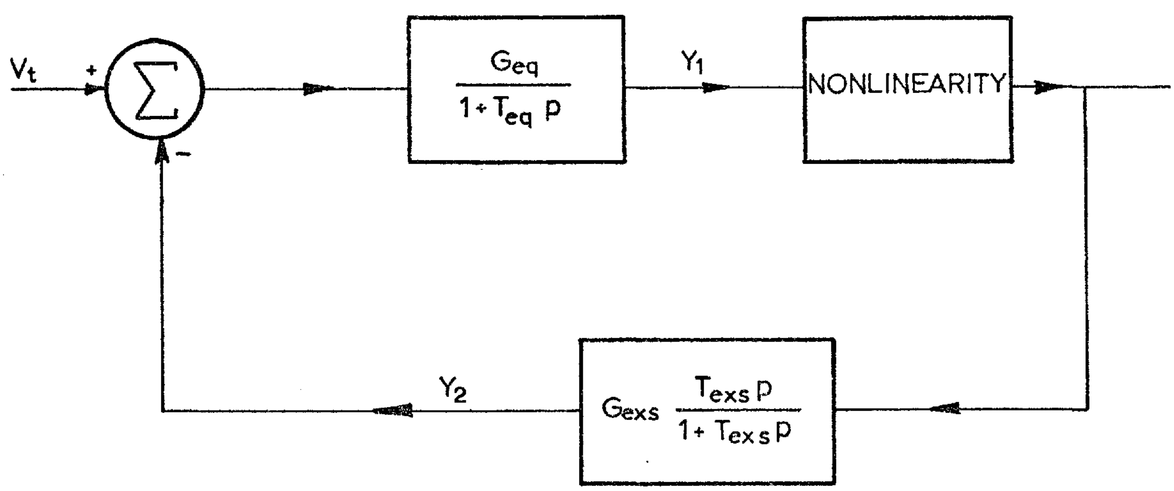

Fig. 2.11. Structure of Goldington voltage regulator after having reduced the order of the system.

Cauer expansion, reduced models can be built discarding a certain number of high order partial coefficients. In general, an approximation is said to be of order n if all T_i for $i>n$ are made equal to zero. In chapter 5 will be shown that a first order Cauer approximation for $H(p)$ is sufficient for the accuracy required, i.e.

$$H(p) = \frac{G_{eq}}{1+T_{eq}p} \tag{2.8}$$

where

$$G_{eq} = G_{m1}G_{m2}G_{exc}$$

$$T_{eq} = T_{m1} + T_{m2} + T_{ms}G_{m1}G_{m2}G_{ms} + T_{exc}$$

The final structure of the excitation system is presented in Fig. 2.11 where Y_1 and Y_2 were selected as state variables. For reducing the order of the system this approach is simpler and gives better or equally good results compared to curve fitting methods by trial and error in Bode planes as described in reference 47 and used by most investigators.

The voltage regulator and exciter of the Northfleet test generator is similar to Goldington's but it has three rather than two stages of magnetic amplification and a d.c. exciter instead of an a.c. exciter. From the numerical values of the nominal-exciter-response given in reference 16, an equivalent time constant for the exciter response can be obtained[96], thus the Northfleet exciter was represented as a simple time lag and a limiter representing exciter ceiling voltages.

2.6 Network simulation

Single line diagrams of the system chosen for study are given in Figs. 2.12 and 2.13.

The Goldington unit transformer and transmission line are represented by impedances in series with the machine terminals. The resistances associated with these impedances are lumped with the machine armature resistance and the reactances are lumped with the machine leakage reactance for calculation purposes. In the micromachine system two external reactances were used to connect the micromachine terminals to the microreseaux infinite bus bar.

The Northfleet system depicted in Fig. 2.13 is more complicated. Here, there is a mixture of cables, overhead lines and other components. For calculation purposes and micromachine simulation the same general procedure as described for Goldington was used for Northfleet.

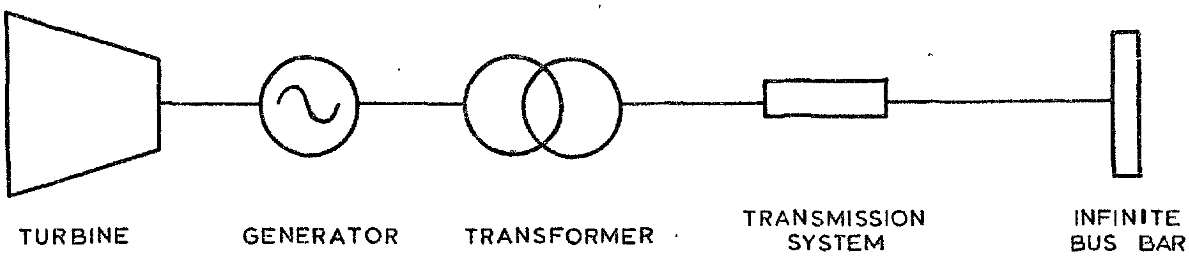

Fig. 2.12. Goldington test system

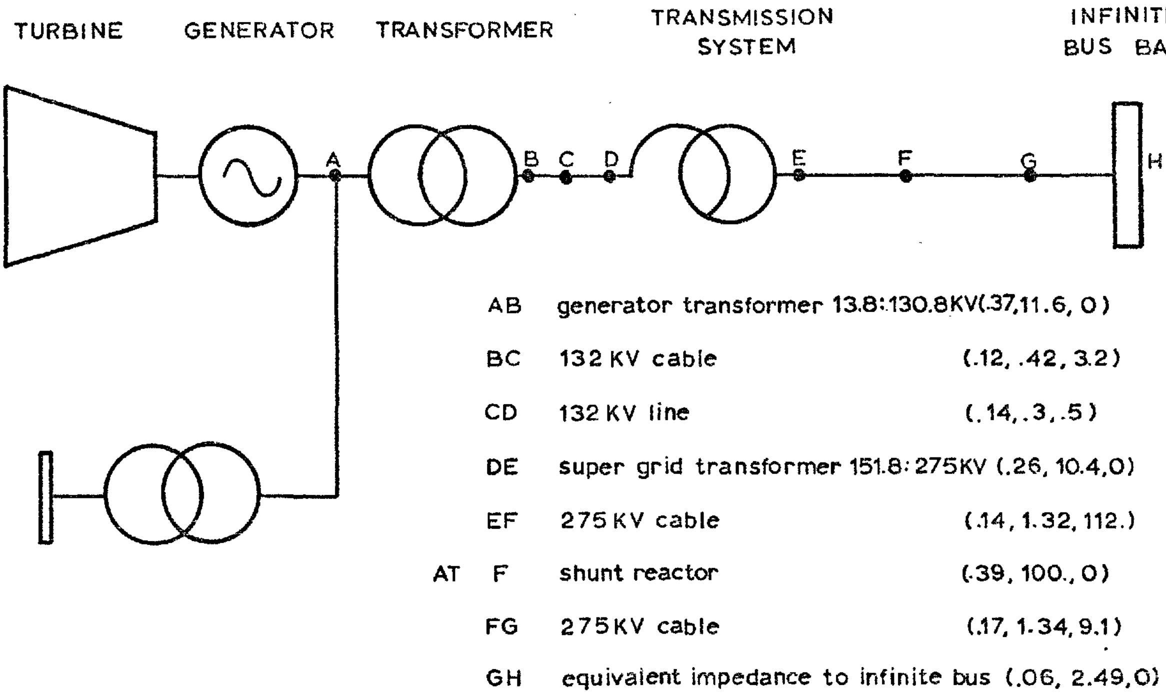

Fig. 2.13. Northfleet test system

2.7 Simulation of modern steam turbines

The turbine external characteristics as seen by the boiler, governor and generator must be modelled mathematically in order to simulate a power plant. The simulation of these external characteristics requires adequate modelling of the turbine steam flow, the turbine torque applied to the shaft of the generator as a function of the shaft speed, the steam quality at the turbine's inlet and outlet and the throttle and interceptor valve positions[33]. Internal turbine characteristics are of secondary importance; however, in order to model the turbine external characteristics the internal turbine behaviour should be considered in at least an approximate manner.

Most modern steam turbines consist of high, intermediate and low pressure cylinders with several steam extractions along the steam path. A survey of several turbine designs made by the author showed that on average, steam extractions are negligible in the high pressure cylinder, of the order of 5% of the main steam flow in the intermediate pressure cylinder and about 15% in the low pressure cylinder. Thus, steam extractions form a small enough part of the steam main flow, to enable dynamic effects of these extractions to be neglected in this study. The block diagram of a steam turbine is now shown diagramtically in Fig. 2.14, where steam extractions from the main flow are not shown.

The mathematical approach taken here to model a

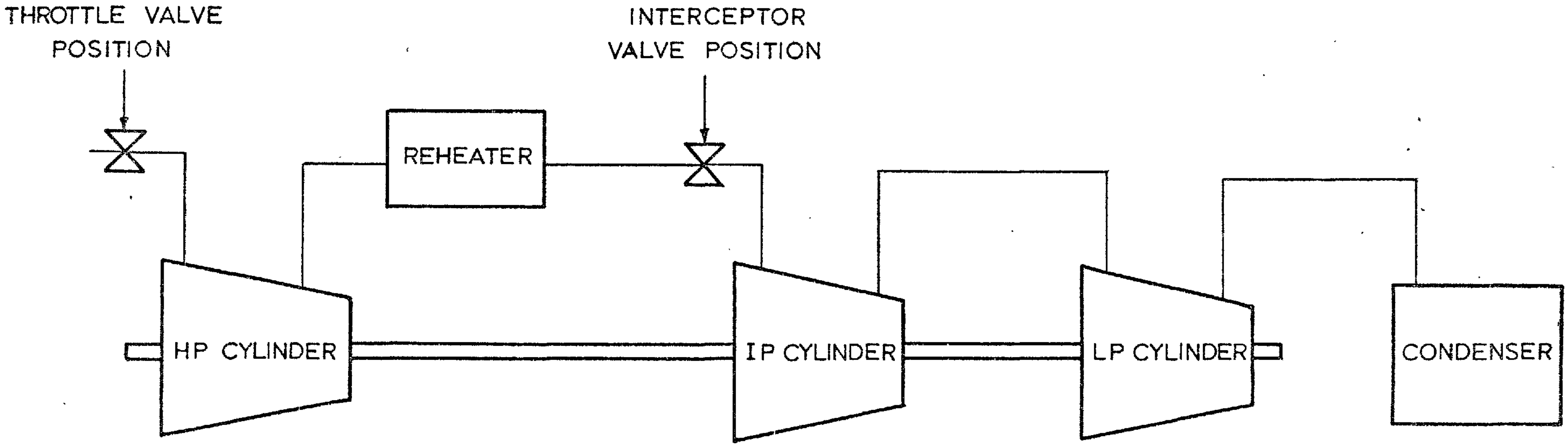

Fig. 2.14. General block diagram of a reheat turbine where steam extractions are not shown.

reheat turbine steam circuit is shown in the form of a flow chart in Fig. 2.15. Each cylinder is assumed to act instantaneously and time lags introduced by entrained steam are lumped before each cylinder.

In this work temperature variations throughout the plant will be neglected but the effects of neglecting these variables are difficult to assess. From the turbine point of view, the power output of a cylinder depends upon the square root of the steam inlet absolute temperature and variations in efficiency with variations in temperature are negligible; therefore, temperature variations have only a minor influence on cylinder dynamic performance. Moreover, the temperature is strongly dependent on the space variables and thus the success of a method that assumes constant temperature drop across a cylinder is limited.

Turbine characteristics will now be analysed under two sets of different operating conditions; first the steam quality at the turbine's inlet and outlet are assumed invariant but the speed of the rotating shaft is allowed to vary; and second the speed is assumed constant but the steam quality is allowed to vary. The first analysis will give the torque-speed characteristics of the turbine and the second will define the turbine performance.

Assuming that the steam state at the turbine's inlet and outlet remains constant, turbine torque speed characteristics can be obtained by analysing the principles under

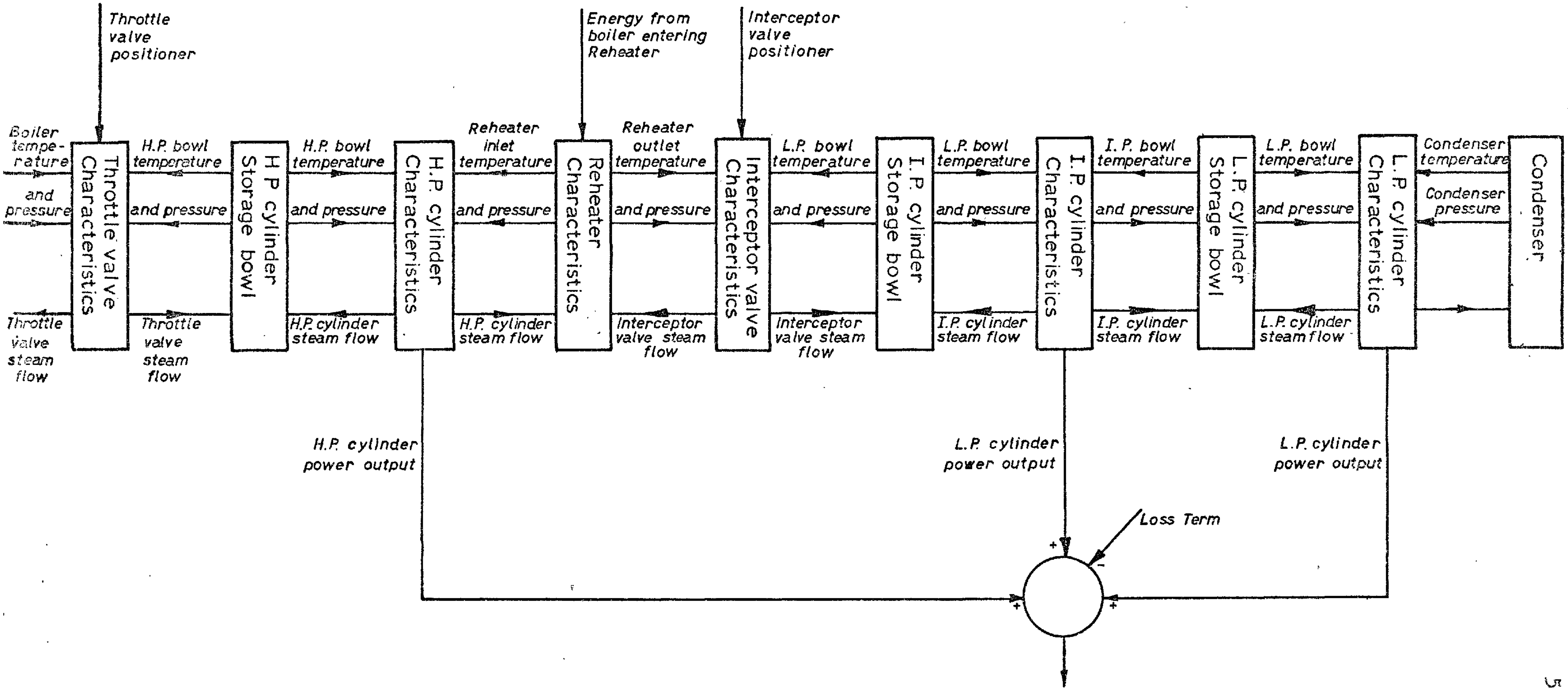

Fig. 2.15. Block diagram showing the general mathematical formulation of the dynamics of a reheat turbine

which energy is transfered from the steam to the rotor, namely, the impulse principle and the reaction principle. Modern large steam turbines used in power systems have blades of the reaction type[97]. The variation in stage efficiency with speed ratio is obtained in appendix 2 for a 50% reaction blade by means of velocity diagrams and the results are shown graphically in Fig. 2.16[48,56,57]. Since turbine blades are designed to work in the plateau part of this curve, it is concluded that the turbine efficiency is insensitive to relatively large variations in the shaft speed; thus turbine power output can be assumed to be independent of the shaft speed for power system studies where only relatively small speed variations occur.

In modern reheat turbines the degree of reaction is small at the blade root increasing progressively toward the blade tip[97]; this effect of having different degrees of reaction along the blade introduces a severe complication into turbine analysis[53,57,98]. The blade has to be subdivided into several small sections and the resulting torque-speed characteristics obtained as the vectorial addition of all velocity diagrams. This requires that the turbine should be considered as a three dimensional gas dynamic system, a problem which is outside the scope of the present work. These effects, however, are only important for blades with a mean radius which can not be considered representative of the blade radius. Turbine blades where this effect is rather marked are those at the exhaust end of the cylinder(and constitute less than 10% of the total blading).

In this work, a symmetrical 50% reaction blade will be assumed to be representative of all turbine blades.

The turbine performance will now be evaluated under the assumption that the shaft speed remains constant. Kearton[57] has shown that if in a turbine the following assumptions are valid,

(1) there are no leakages or extractions,

(2) the system is in equilibrium,

(3) the variations in load speed ratio with load variations are negligible (Kearton[99] has shown that this assumption is justified for all turbine stages but the last few),

(4) steam flow is subsonic,

(5) steam expansion processes are essentially polytropic,

(6) the deviation from the blade root and tip velocity is not marked, and

(7) an overall efficiency coefficient gives a good approximation of the efficiency of all stages;

then the turbine flow is given by

$$W = k'\sqrt{\left[\frac{P_{in}}{V_{in}} - \frac{P_{out}}{V_{out}}\right]} \qquad (2.9)$$

where:

W steam turbine flow

$P_{in,out}$ inlet and outlet turbine pressure

$V_{in,out}$ inlet and outlet turbine specific volume

k' a constant

In a condensing turbine (low pressure cylinder of a reheat turbine) the ratio P_{out}/V_{out} is very small compared with P_{in}/V_{in} and may be ignored, then to a good approximation

$$W = k'\sqrt{\frac{P_{in}}{V_{in}}} \qquad (2.10)$$

Superheated steam may be assumed to behave as a perfect gas (PV = RT), therefore equation 2.10 becomes

$$W = k'' \frac{P_{in}}{\sqrt{T_{in}}} \qquad (2.11)$$

As temperature variations are neglected the turbine flow becomes proportional only to the turbine inlet pressure.

The validity of equation 2.10 can be assessed more rigorously if the distribution of pressures along the cylinder is considered. In appendix 3 it is shown that the subsonic steam flow through a nozzle is given by

$$W_i = k_1\, C_q\, A\sqrt{\left\{2\, \frac{\gamma}{\gamma-1}\, \frac{P_{i-1}}{V_{i-1}} \left[\left(\frac{P_i}{P_{i-1}}\right)^{\frac{\gamma}{2}} - \left(\frac{P_i}{P_{i-1}}\right)^{\frac{\gamma+1}{\gamma}}\right]\right\}} \qquad (2.12)$$

where

P_i stage i outlet pressure

P_{i-1} stage i inlet pressure

γ is the ratio of specific heats c_p/c_v

When the turbine inlet pressure changes, the inlet pressures to all stages change proportionally, therefore the pressure ratio P_i/P_{i-1} remains unchanged for all stages except the last and the term $((P_i/P_{i-1})^{\frac{\gamma}{2}} - (P_i/P_{i-1})^{\frac{\gamma+1}{\gamma}})$ does not vary; thus equation 2.12 is equivalent to equation 2.10 for all stages except the last. The inlet pressure for the last stage changes proportionally with the turbine inlet pressure and as the condenser pressure remains essentially unchanged the pressure ratio for the last stage changes. Nevertheless, economic design dictates that the last stage flow must be just critical and if this were the case relatively large changes in the pressure ratio could occur without a significant change in the steam flow as can be seen graphically in Fig. 2.17. Cotton and Schofield[100] have in fact shown that the deviation from linearity of the flow with pressure is less than 5% for the first stage owing to the large amount of work done in this row of blades which cause the inlet temperature for the second stage to become smaller; this departure from linearity diminishes for successive stages.

For a noncondensing cylinder, i.e. the high pressure and intermediate pressure cylinders of a reheat turbine, equation 2.9 must be used fully.

As a polytropic process is considered, equation

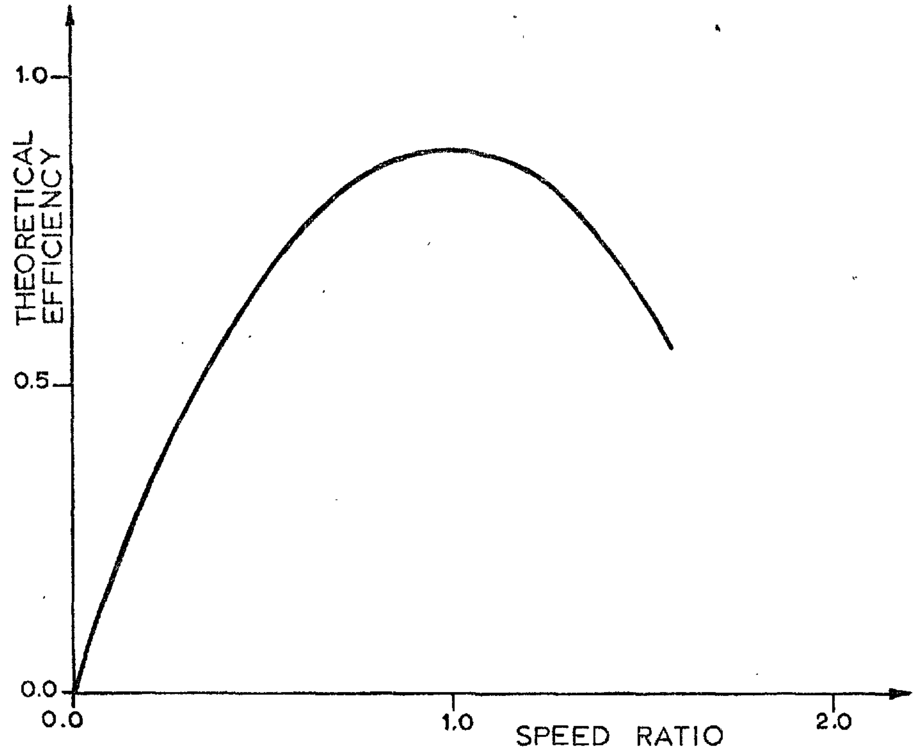

Fig. 2.16. Combined nozzle and blading efficiencies of a reaction stage as a function of the velocity ratio

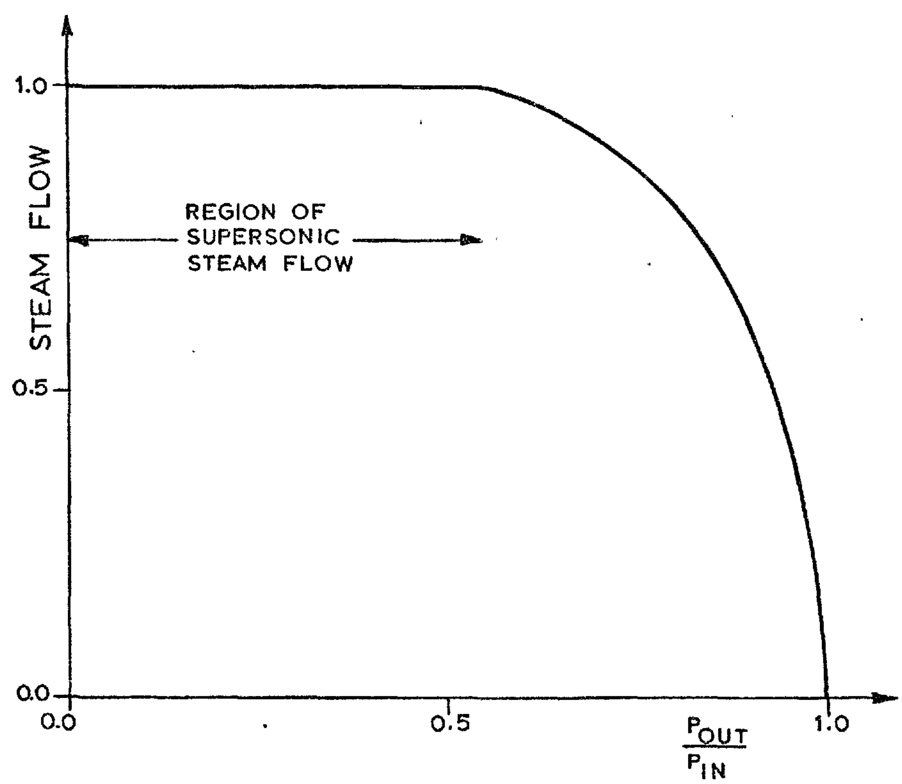

Fig. 2.17. Steam flow through a nozzle as a function of the pressure ratio, for constant pressure at the nozzle inlet

2.9 becomes

$$W = k' \frac{P_{in}}{\sqrt{\{P_{in} V_{in}\}}} \sqrt{\left[1 - \left(\frac{P_{out}}{P_{in}}\right)^{2-\eta_p \frac{\gamma-1}{\gamma}}\right]} \qquad (2.13)$$

where

η_p is the polytropic efficiency.

Superheat steam may again be assumed to behave as a perfect gas, and therefore equation 2.13 becomes

$$W = \frac{k'}{\sqrt{\{R\ T_{in}\}}} P_{in} \sqrt{\left[1 - \left(\frac{P_{out}}{P_{in}}\right)^{2-\eta_p \frac{\gamma-1}{\gamma}}\right]} \qquad (2.14)$$

If temperature variations were neglected then

$$W = k'' P_{in} \sqrt{\left[1 - \left(\frac{P_{out}}{P_{in}}\right)^{2-\eta_p \frac{\gamma-1}{\gamma}}\right]} \qquad (2.15)$$

Equation 2.15 is very close to Stodola's experimental ellipses law[56] given by

$$W = k'' P_{in} \sqrt{\left[1 - \left(\frac{P_{out}}{P_{in}}\right)^{2}\right]} \qquad (2.16)$$

Stodola's law has two advantages over equation 2.15; first, it is simpler to implement numerically and second it has strong experimental support; hence Stodola's law is used in this study.

As a polytropic process is being considered the drop ΔH in enthalpy for a turbine cylinder can be obtained as shown in appendix 2

$$\Delta H = K'T \left[1 - \left(\frac{P_{out}}{P_{in}} \right)^{\eta_p \frac{\gamma - 1}{\gamma}} \right] \tag{2.17}$$

If temperature variations are neglected equation 2.17 can be written as

$$\Delta H = K'' \left[1 - \left(\frac{P_{out}}{P_{in}} \right)^{\eta_p \frac{\gamma - 1}{\gamma}} \right] \tag{2.18}$$

The power output of a turbine cylinder is obtained as the product of the steam flow, the enthalpy drop and the representative stage efficiency as a function of the shaft velocity

$$P_{o_i} = W_i \, \Delta H_i \, \eta_{nbi} \tag{2.19}$$

In the general case of a multicylinder turbine

$$P_{out} = \sum_{\substack{\text{all turbine} \\ \text{cylinders}}} \left[W_i \; H_i \; \eta_{nbi} \right] \tag{2.20}$$

As both the steam flow and the enthalpy drop are functions of the steam quality at the turbine inlet and outlet, and variations in efficiency according to speed are neglected in this study, the product $W_i \, \Delta H_i \, \eta_{nbi}$ can be considered to be a function of F_i, the inlet and outlet steam states

$$P_{out} = \sum_{\substack{\text{all turbine} \\ \text{cylinders}}} F_i(P^i_{in},\ P^i_{outlet};\ T^i_{in},\ T^i_{outlet}) \tag{2.21}$$

Turbine losses are an important factor under certain conditions. For example, during transients when turbine valves may be fully closed turbogenerator losses have a great influence in the variations of the shaft speed; as a consequence, the modelling of loss terms should be accurate. Part of the turbine losses have been already taken into account by the efficiency coefficients. However, rotational and other fixed losses not yet considered will be modelled, for computational purposes, by a fixed loss coefficient (P_{loss}), following the example of other investigators[64,66,101]. This is justified, by the fact that steam turbines in power systems experience only small speed variations.

The entrained steam in different bowls introduces time lags in the steam circuit of a turbine and this effect may be modelled as shown in appendix 4.

All the elements of the steam circuit of a reheat turbine (Fig.2.14) have been considered and modelled mathematically. A block diagram showing how the integration of the relevant differential equations was carried out is presented in Fig. 2.18. Pressures were chosen as state variables.

As shown in Fig. 2.19, the system is partially linearised so that the turbine equations are now amenable to analogue computation [34,65].

2.8 Governor simulation

The governor of a modern reheat steam turbine consists of a speed sensing device, several stages of amplification, the valve positioners in the form of hydraulic relays and the throttle and interceptor valves.

The speed sensing device can be realized as an a.c. tachogenerator or a flyweight governor; the speed of response of such a system is faster than that of the hydraulic relay by at least an order of magnitude in the case of the governor or even more in the case of the tachogenerator, hence the dynamic effects of the speed sensing device can be neglected without serious error.

The speed sensing device is thus represented by its steady-state characteristics

$$X = G_1 \; p\delta - Y_0 \qquad X_{min} \leq X \leq X_{max} \tag{2.22}$$

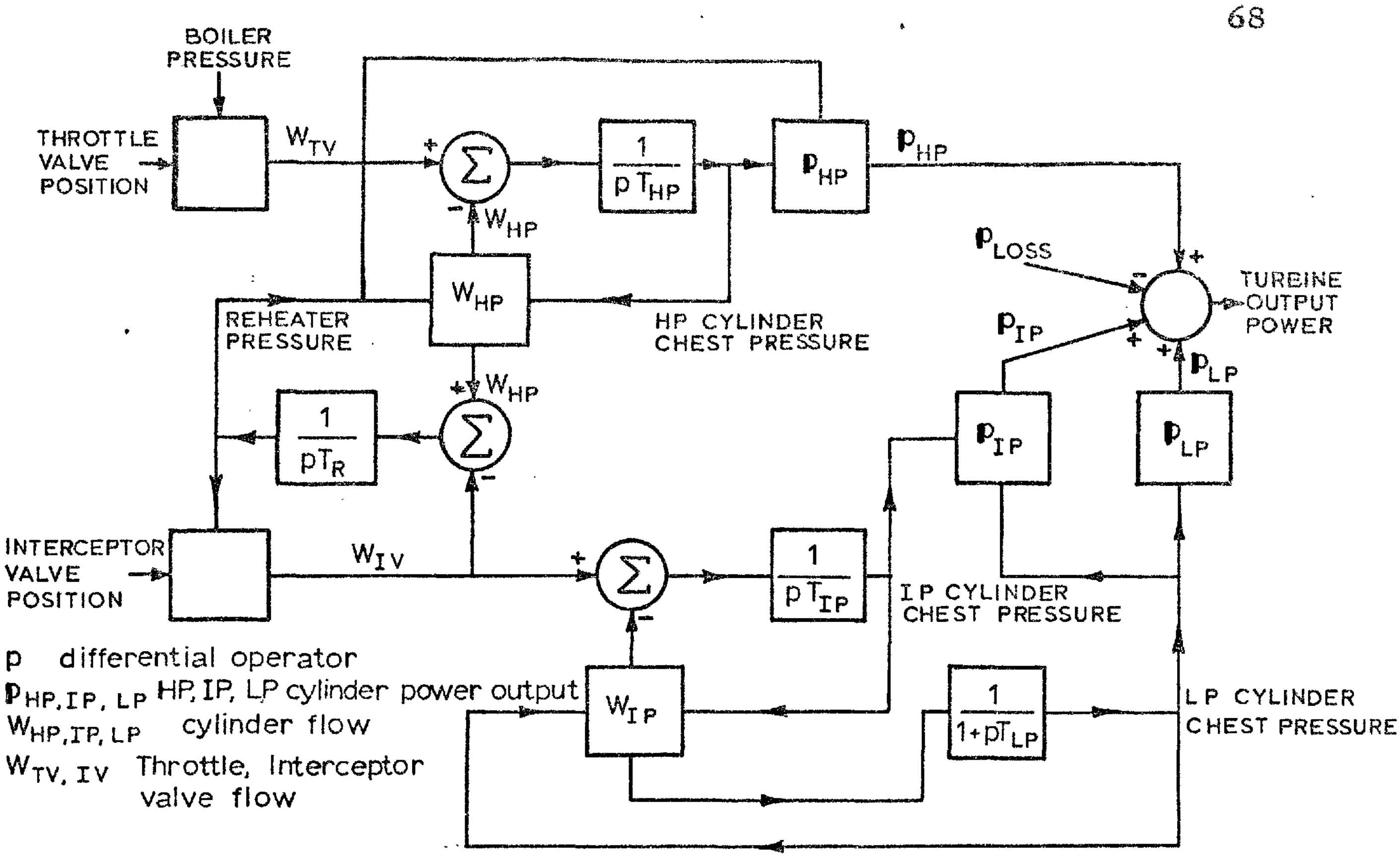

Fig. 2.18. Block diagram of steam turbine for detailed dynamic studies

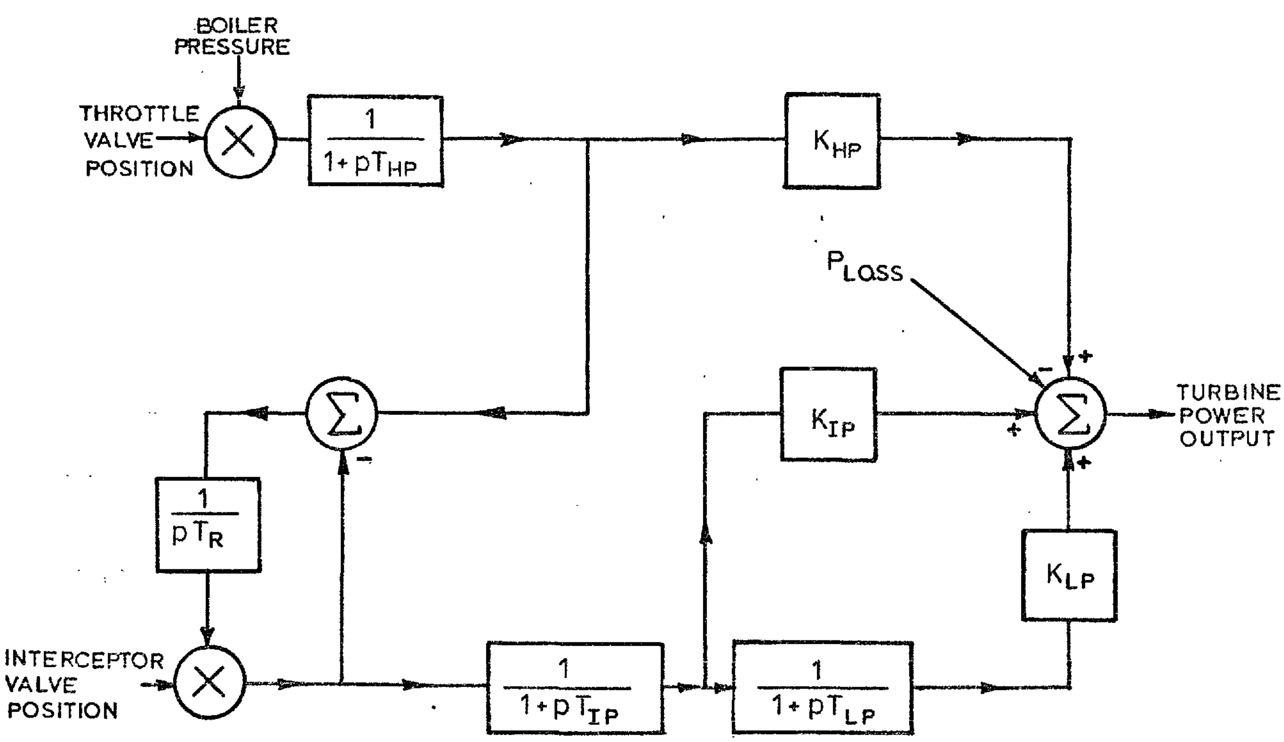

Fig. 2.19. Block diagram of steam turbine for analogue computer studies

The hydraulic relay has no competitor as a force amplifier for steam valve actuation and its dynamics are considered next. No other form of mechanical or electrical amplifier can be produce the very high power demanded by modern steam turbine valves together with the high ratio of torque to inertia for the quick action required.

A typical hydraulic relay is shown in Fig. 2.20. The analysis of this mechanism is presented in appendix 5, where it is shown that to a good approximation this system can be modelled as follows [33,102,103].

$$Y = \frac{X}{1 + pT^*} \qquad Y_{min} \leq Y \leq Y_{max} \qquad (2.23)$$

Many turbine relays are single acting, with oil in only one side of the main piston and a spring acting on the other. As a result, the pressures on the piston are not equal on opening and on closing hence piston velocity will be different at the same point of travel for the two operations. It is regarded as good practice to arrange the relays so that they respond faster in the closing as compared to the opening action.

This effect is simulated using a different time constant for each relay, in the closing and opening action. This nonlinearity is of prime importance in the dynamic response of the system and has a significant effect on the stability as will be shown in chapter 5.

The opening rate of the relay is limited by placing orifices in the oil inlet of the relay to avoid any depression of the pump delivery pressure causing malfunction of the low pressure protection system. This is simulated by imposing a limit on the rate of movement of the piston.

These last two sources of asymmetry introduce two very nonlinear characteristics in the dynamics of the system. The special analogue circuit shown in Fig. 2.21 was designed to take into account both asymmetries. The effect of imposing a limit on the rate of opening of the relay was not represented because the magnitude of this factor was not known.

An important characteristic of governor relays is that they operate in cascade, therefore the governor response is characterized by multiple time lags giving the impression of the existence of a pure delay[64]. This can be explained mathematically by the following expression the validity of which can be easily proved:

$$e^{-Ts} = \lim_{n \to \infty} \frac{1}{(1 + \frac{T}{n} s)^n} \tag{2.24}$$

where

T is a constant

An approximation of order n can now be obtained for a pure delay as

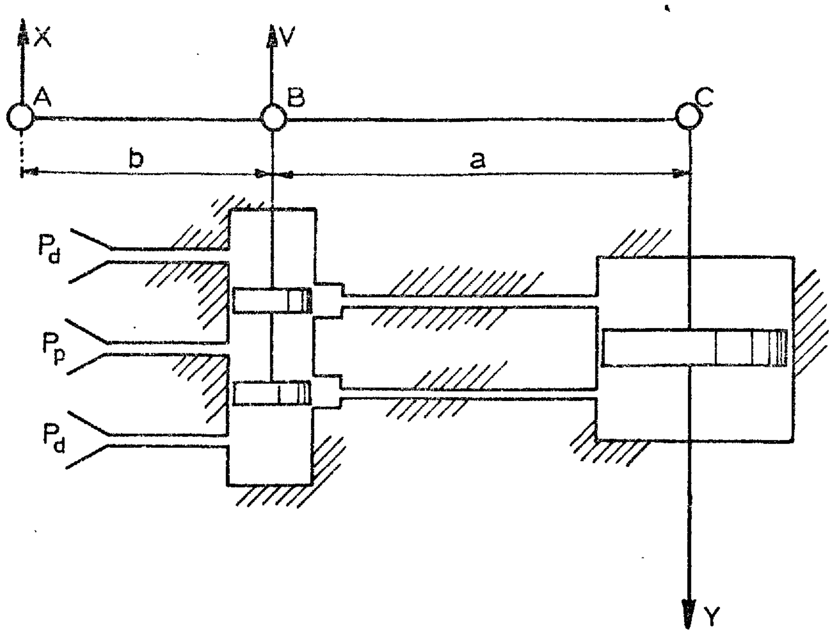

Fig. 2.20. Schematic diagram of a hydraulic relay

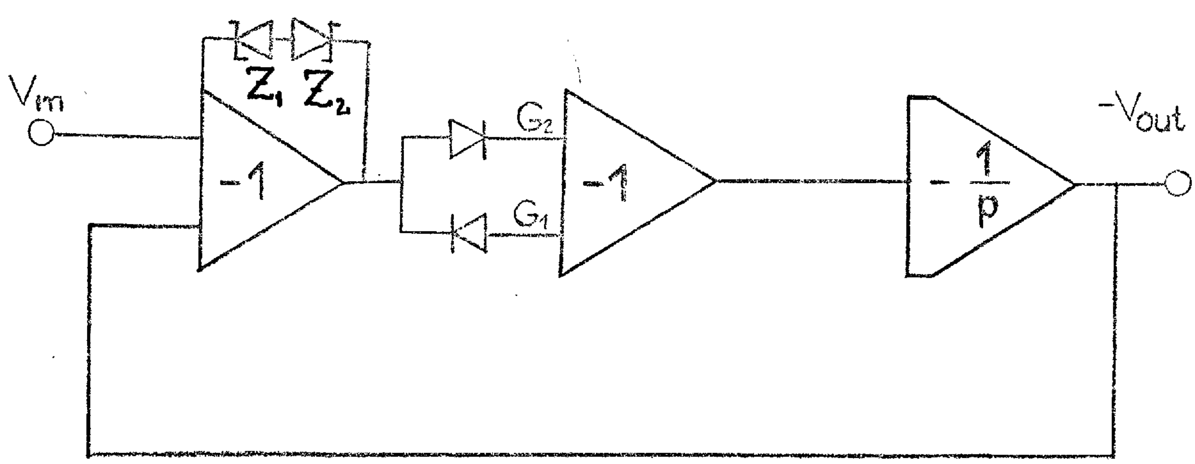

Transfer function:

$$\frac{V_{OUT}}{V_{IN}} = \frac{-1}{1 + pT}$$

$$T_{opening} = \frac{1}{G_1}$$

$$T_{closing} = \frac{1}{G_2}$$

Maximum opening rate V_1/G_1

Maximum closing rate V_2/G_2

Z_i Zenner Diode (Zenner Voltage V_i)

Fig. 2.21. Analogue simulation of a hydraulic relay

$$e^{-Ts} \cong \frac{1}{(1 + \frac{T}{n} s)^n} \qquad (2.25)$$

Thus, in order to simulate accuratelly the effect of multiple time lags it is necessary to model as many relays as practicable. The Goldington governor has two relays both of which were simulated. The Northfleet governor, however, has six relays and bearing in mind that each relay simulation requires three operational amplifiers, modelling of all relays became prohibitively expensive. In order to save analogue components each set of three relays was represented by two equivalent time constants, the numerical values of which were obtained by the following optimum second order approximation:

$$\frac{1}{(1+sT_1^*)(1+sT_2^*)(1+sT_3^*)} \cong \frac{1}{(1+sT_a)(1+sT_b)} \qquad (2.26)$$

where

$T^*_{1,2,3}$ time constants of hydraulic relays

$T_{a,b}$ time constants of equivalent relays

The relationship between a valve position and the steam flow through the valve chest will be determined next. This relationship is obtained assuming a steam valve is an orifice of variable area. The flow of a gas through an orifice was obtained in appendix 3 as

$$W = A\, C_d\, P_d\, f'(T_u, \frac{P_d}{P_u}) \qquad (2.27)$$

where

W	flow through valve chest
A	orifice area
C_d	discharge coefficient
P_d	upstream pressure
P_u	downstream pressure
T_u	stagnation temperature

$$f'(T_u, \frac{P_d}{P_u}) = \begin{cases} \sqrt{\left[\frac{2\gamma}{\gamma-1}\; g\; \frac{1}{RT_u}\; \left(\left(\frac{P_u}{P_d}\right)^{\gamma/2} - \left(\frac{P_u}{P_d}\right)^{\frac{\gamma+1}{\gamma}}\right)\right]} & \frac{P_u}{P_d} \geq \text{critical pressure ratio} \\ \sqrt{\left[\left(\frac{2}{\gamma+1}\right)^{\frac{\gamma+1}{\gamma-1}}\; g\; \frac{\gamma}{RT_u}\right]} & \frac{P_u}{P_d} \leq \text{critical pressure ratio} \end{cases}$$

Equation 2.27 is used in the elaborate digital model for modelling the steam flow through a valve. In the analogue solution the following simpler form is used:

$$W = K_o\, P_d\, A \qquad (2.28)$$

This equation is again nonlinear but much easier to implement in an analogue computer. The use of this equation is justified for supersonic valve flows which normally occur for less than maximum rating.

2.9 Boiler simulation

The most important dynamic aspects of a boiler from a complete power station simulation study are those external characteristics that affect the turbine behaviour. These characteristics can be obtained through modelling of (a) the pressure variations before the throttle valve for changes in the operating conditions and (b) the flow of energy through the reheater. When the temperature variations are neglected, the flow of energy through the reheater becomes unimportant. The approach taken here to model a boiler is that of energy balance[69,71]. Ideal feedwater mechanisms are assumed.

First the dynamic behaviour of the firing system will be considered. Following Profos's approach[69], the term dynamic behaviour of the firing system is here used to denote the variation of the fire intensity F on the control variable C_f, where C_f is the loading signal transmitted to the fuel and air supply systems. In this work a transfer function of the following form has been used to describe firing system dynamics

$$F = \frac{1}{(1 + pT_F)} C_f \tag{2.29}$$

This transfer function naturally depends upon the type of firing system used.

The dynamic behaviour of the steam generator is considered next. The starting point in the modelling of a steam generator is to consider the boiler as a reservoir of energy. The evolution of the system in time can then be described mathematically as a "fill-in" process, as can be seen diagramatically in Fig. 2.22. Thus

$$\frac{1}{p}\left(Q_{in} - Q_{out}\right) = J \qquad (2.30)$$

where

Q_{in}	flow of energy entering the boiler from the firing system
Q_{out}	flow of energy leaving the boiler
J	energy content of the boiler

The flow of energy entering the boiler can be assumed to be proportional to the firing rate, the flow of energy leaving the boiler being a function of the steam flow leaving the boiler and the state of this steam. Profos[69] has shown that good correlation is obtained when the energy flow leaving the boiler is assumed to be proportional to the virtual steam production S_v. Therefore, equation 2.30 becomes

$$\frac{1}{p}\left(F - S_v\right) = J \qquad (2.31)$$

Profos[69] has also shown that good correlation is obtained if J is assumed to be a function of only the virtual steam production (Fig.2.23). Profos assumption is also jus-

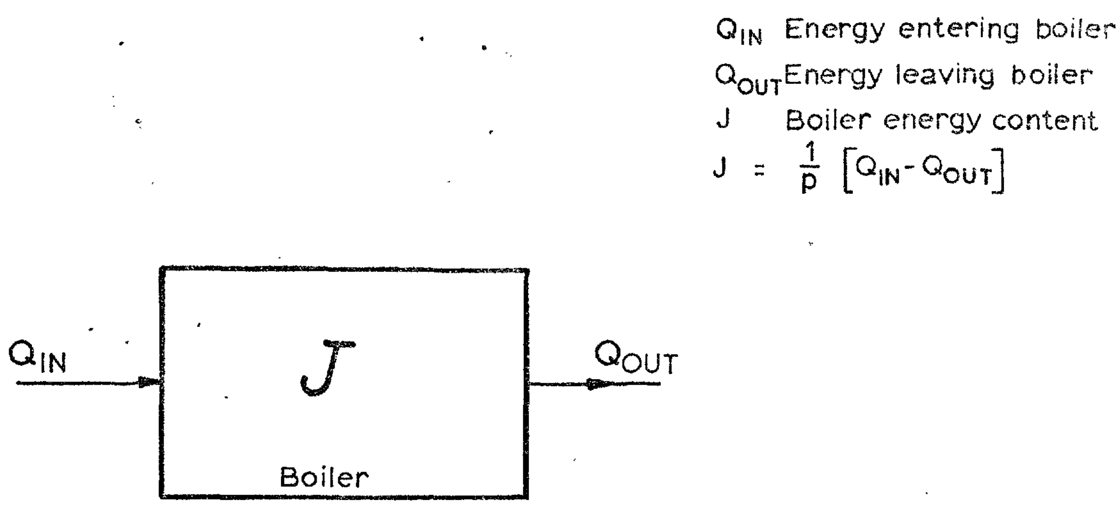

Fig. 2.22. Schematic picture of a boiler as an energy reservoir

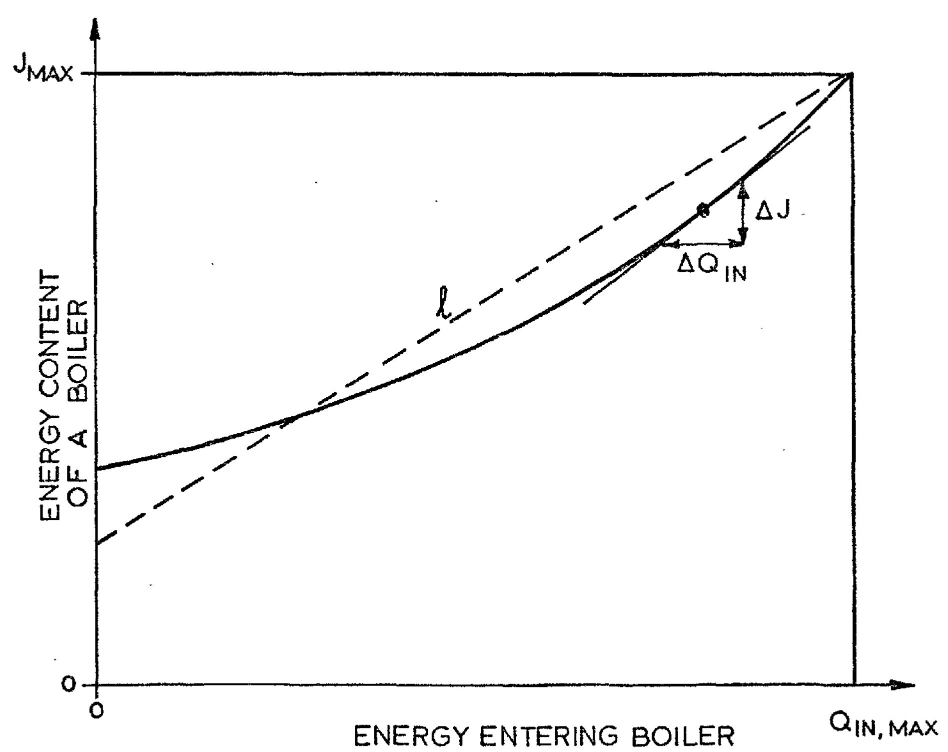

Fig. 2.23. Energy content of a boiler as a function of the steam production

tified by Astrom[71] who showed that "if the distribution of energy stored in the steam and the iron masses do not change during transients, then any state representing the boiler can define its energy content".

$$\frac{1}{p}\,(F - S_v) = J(S_v) \tag{2.32}$$

and for small perturbations around an operating point

$$\frac{1}{T_v p}\,(F - S_v) = S_v \tag{2.33}$$

where

$$T_v = \frac{\partial J(S_v)}{\partial S_v}$$

Figure 2.23 also illustrates, that equation 2.33 can be employed for large perturbations as well, however, T_v should be defined now as the slope of an optimum linear fitting to J(Sv) as depicted in Fig. 2.23 by the line 1.

As shown in Appendix 5, pressure variations in the boiler can be modelled as a fill-in process in the working medium. Therefore

$$\frac{1}{T_B p}\,(S_v - S_x) = P_b \tag{2.34}$$

The steam flow in the boiler pipes is in a turbulent state and therefore, the steam flow is proportional to the square root of the pressure difference[31] as

$$S_x = \sqrt{\{P_b - P_t\}} \qquad (2.35)$$

where

P_t pressure before the throttle valve

There remains another delay caused by the entrained steam in the piping connecting the boiler with the turbine main throttle valve which can be modelled as shown in appendix 5.

The pressure control system of the boiler is assumed to have a proportional plus derivative plus integral structure and to be acted upon according to the firing rate, thus

$$C_f = K_p \,(P_{bo} - P_t)\left(1 + \frac{1}{pT_i} + K_d \frac{pT_{de}}{1+pT_{de}}\right) \qquad (2.36)$$

where

P_{bo} pressure setting and other terms as defined in the list of symbols

Fig. 2.24 shows the block diagram of the nonlinear boiler mathematical model developed above. In fig. 2.25

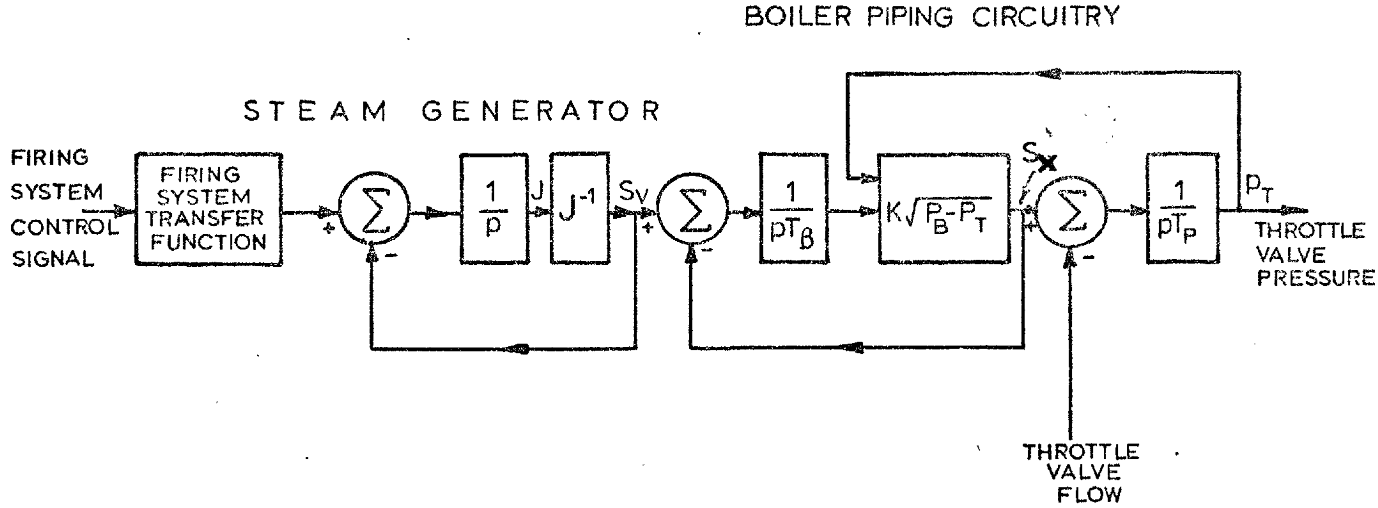

Fig. 2.24. Block diagram of a boiler for detailed simulation

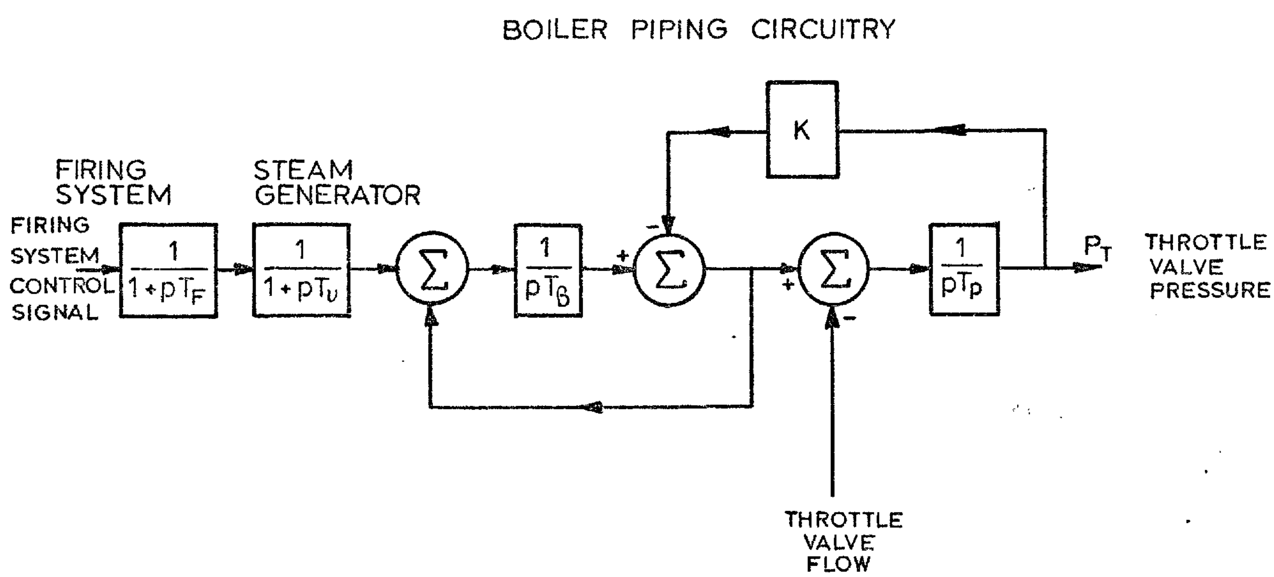

Fig. 2.25. Block diagram of a linearised dynamic model of a boiler for analogue studies

a linearised approximation to boiler dynamics is presented suitable for analogue simulation.

2.10 General system representation of a reheat turbogenerator, governor and boiler for digital computer studies

In this section the system equations of a steam power plant as developed in the previous paragraphs of this chapter are summarised in state space form

$$
\begin{aligned}
\dot{y}(1) &= Ka\ \dot{y}(6) - y(1)\ T_{de} \\
\dot{y}(2) &= K_{pi}\ (T_{pi}\ y(6) + \dot{y}(6) + y(1)) && y_{i\ min} \leq y(2) \leq y_{i\ max} \\
\dot{y}(3) &= (y(2) - y(3))/T_F && 0 \leq y(3) \leq y_{3\ max} \\
\dot{y}(4) &= (y(3) - y(4))/T_v \\
\dot{y}(5) &= (y(4) - W_B)/T_B \\
\dot{y}(6) &= (W_B - W_{TB})/T_P \\
\dot{y}(7) &= (W_{TB} - W_{HP})/T_{HP} \\
\dot{y}(8) &= (W_{HP} - W_{IV})/T_R \\
\dot{y}(9) &= (W_{IV} - W_{IP})/T_{IP} && (2.37) \\
\dot{y}(10) &= (W_{IP} - W_{LP})/T_{LP} \\
\dot{y}(11) &= (y(12) - y(11))/T_{TV2} \\
\dot{y}(12) &= (G_1 y_1 - y(12))/T_{TV1} && y_{TV\ min} \leq y(12) \leq y_{TV\ max} \\
\dot{y}(13) &= (y(14) - y(13))/T_{IV2} \\
\dot{y}(14) &= (G_2\ y_2 - y(14))/T_{IV1} && y_{IV\ min} \leq y(14) \leq y_{IV\ max} \\
\dot{y}(15) &= (P_{tur} - P_{ELEC})/(H(1 + D\ Y(15)) \\
\dot{y}(16) &= y(15) \\
\dot{y}(17) &= \omega_o\ y(18) - A\ y(17) + B\sin(y(16)) + C\cos(y(16)) \\
\dot{y}(18) &= G_{eq}(V_t - V_{ref} - y(19) - y(18))/T_{eq} \\
& && V_{f\ min} \leq y(18) \leq V_{f\ max}
\end{aligned}
$$

$$\dot{y}(19) = (G_{exs}\ T_{exs}\ \dot{y}(18) - y(19))/T_{exs} \tag{2.37}$$

where

$y(1)$	derivative signal of the pressure controller
$y(2)$	proportional plus integral signal of the pressure controller
$y(3)$	firing rate
$y(4)$	virtual steam production
$y(5)$	boiler pressure
$y(6)$	pressure before throttle valve
$y(7)$	HP cylinder chest pressure
$y(8)$	reheater pressure
$y(9)$	IP cylinder chest pressure
$y(10)$	LP cylinder chest pressure
$y(11)$	first throttle valve relay position
$y(12)$	second throttle valve relay position
$y(13)$	first interceptor valve relay position
$y(14)$	second interceptor valve relay position
$y(15)$	shaft speed
$y(16)$	load angle
$y(17)$	field flux linkages
$y(18)$	exciter voltage
$y(19)$	derivative signal of exciter stabiliser
$y_1 =$	$G_1\ y(15) - y_o \qquad y_{1\ min} \le y_1 \le y_{1\ max}$
$y_2 =$	$G_2\ g(y(15)) - y_o' \qquad y_{2\ min} \le y_2 \le y_{2\ max}$
	$g(y)$ dead band characteristics
$W_B =$	$K_1 \sqrt{\{y(5) - y(6)\}}$

W_{TV} = $K_2 \ y(12) \ f'\left(\frac{y(6)}{y(7)}\right)$

W_{IV} = $K_3 \ y(14) \ f'\left(\frac{y(8)}{y(9)}\right)$

W_{HP} = $K_4\sqrt{\{y(7)^2 - y(8)^2\}}$

W_{IP} = $K_5\sqrt{\{y(9)^2 - y(10)^2\}}$

W_{LP} = $K_6 \ y(10)$

P_{elec} = $T_d(y(16))y(15) + S_1 \sin^2(y(16)) + S_2 \cos^2(y(16)) + S_3 \ y(17)^2 + S_4 \sin(y(16)) \cos(y(16)) + S_5 \sin(y(16)) \ y(17) + S_6 \cos(y(16)) \ y(17)$

P_{tur} $P_{HP} + P_{IP} + P_{LP} - P_{Loss}$

P_{HP} = $K_7 \ W_{HP} \left(1 - \left[\frac{y(8)}{y(7)}\right]^{\eta_p \frac{\gamma-1}{\gamma}}\right)$

P_{IP} = $K_8 \ W_{IP} \left(1 - \frac{y(10)}{y(9)}^{\eta_p \frac{\gamma-1}{\gamma}}\right)$

P_{LP} = $K_9 \ W_{LP}$

V_t = machine terminal voltage

$T_{TV1,TV2,IV1,IV2}$ subject to constraints and limiting action as described in section 2.8

$K_{1,2,\ldots 9}$ constants

The above 19 differential equations were integrated using a standard Runge-Kutta-Gill subroutine [104] in a CDC 6600 digital computer. A special subroutine was used to determine boiler and turbine initial constants; the data required for determining these constants being available from the results of an acceptance test carried out on a turbine[105]. The data from the Laubli-Fenton paper[70] was assumed to be representative of a modern boiler and was used in this study. The initial condition problem of this set of differential equation does not require the solution of a set of nonlinear equations but can be obtained through an exact algebraic noniterative algorithm from readily available data.

2.11 General system representation of a reheat turbogenerator governor and boiler for analogue computer studies

In section 2.10 the system equations representing a steam power plant supplying power to an infinite bus bar were summarised; almost all these equations were nonlinear. In this section approximations to equations 2.37 are presented in order to make these equations amenable for analogue computation.

Two analogue simulations will be described; firstly, a pure analogue model of a steam power plant is presented in fig. 2.26 where the synchronous generator is modelled only by its inertia constant. This model is similar to the one described in section 2.10; the differences are only that the power output and steam flows of the turbine cylinders are linearised to save analogue computer components and a cruder representation of the synchronous generator is used. The details of this analogue simulation are shown diagramatically in Fig. 2.27.

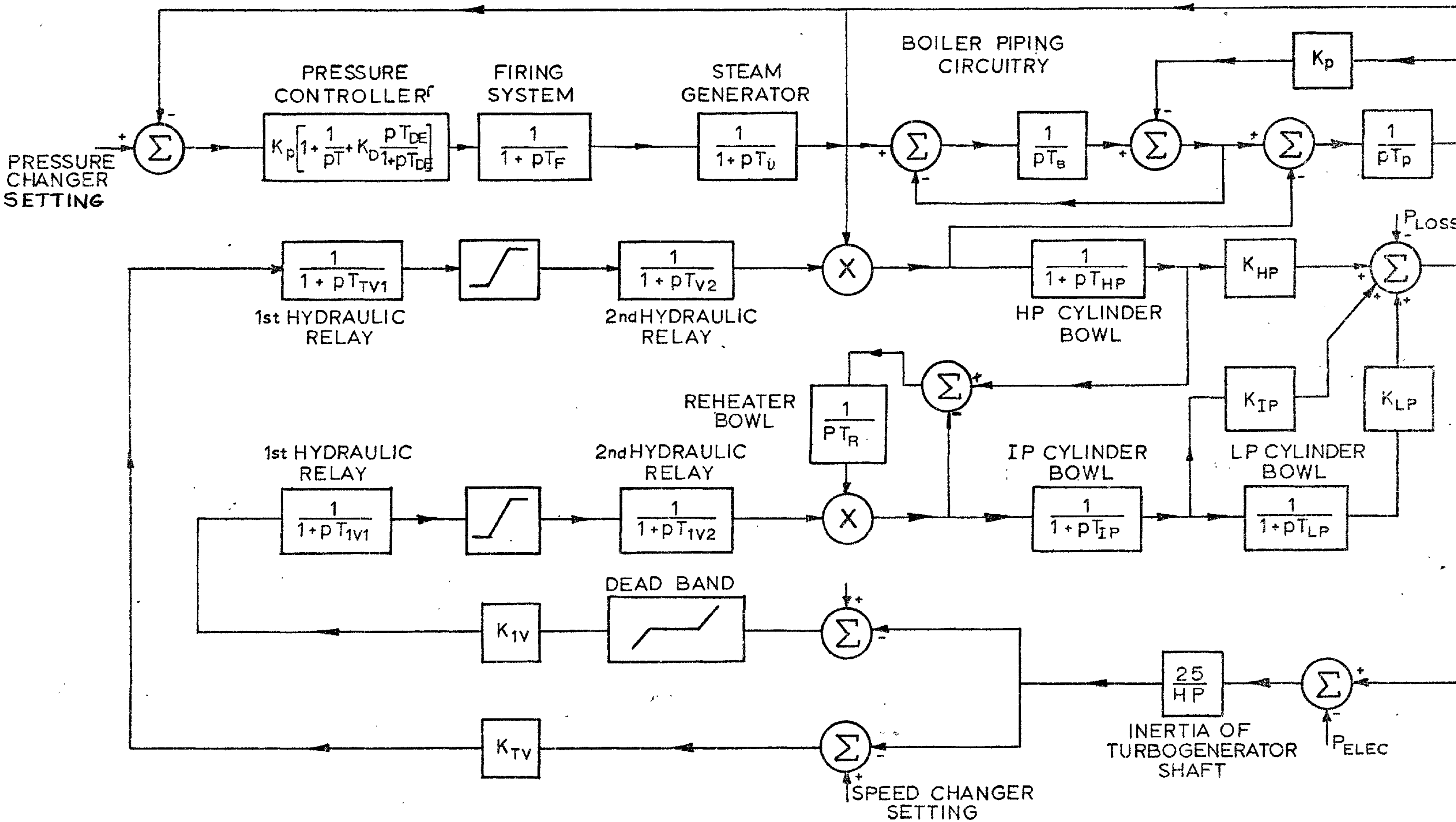

Fig. 2.26. Block diagram representation of a steam power plant for analogue computer studies

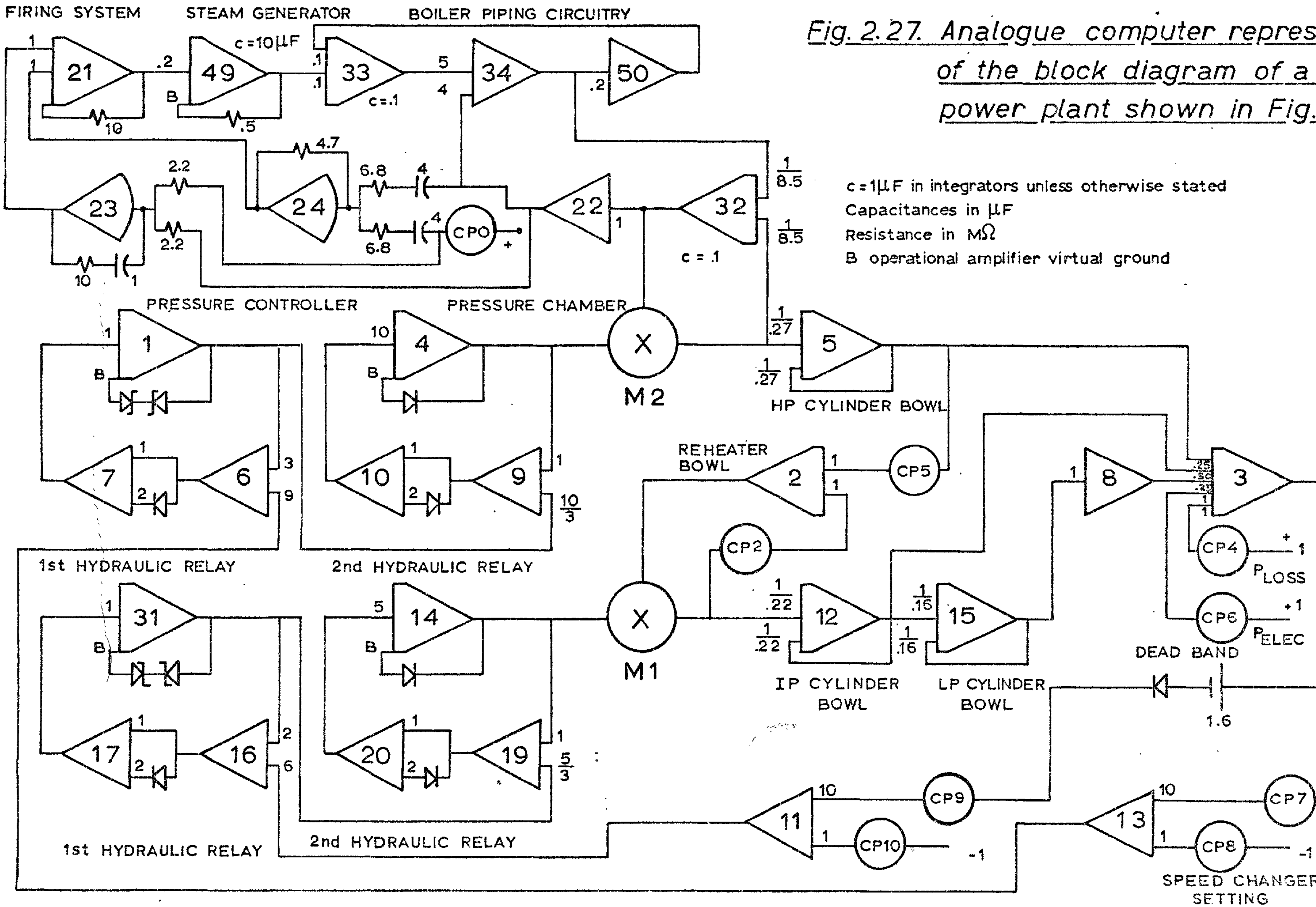

Fig. 2.27. Analogue computer representation of the block diagram of a steam power plant shown in Fig. 2.26.

Secondly, the synchronous machine representation in the analogue computer simulation of a steam power plant, shown in Fig. 2.26, was greatly improved upon using a micromachine set as described in section 2.3. The quality of this synchronous machine approximation can be appreciated in table 2.1, where the per-unit parameters of the micromachine set are compared with Northfleet constants; and in Fig. 2.28 where a comparison of the micromachine with Northfleet open circuit characteristics is presented.

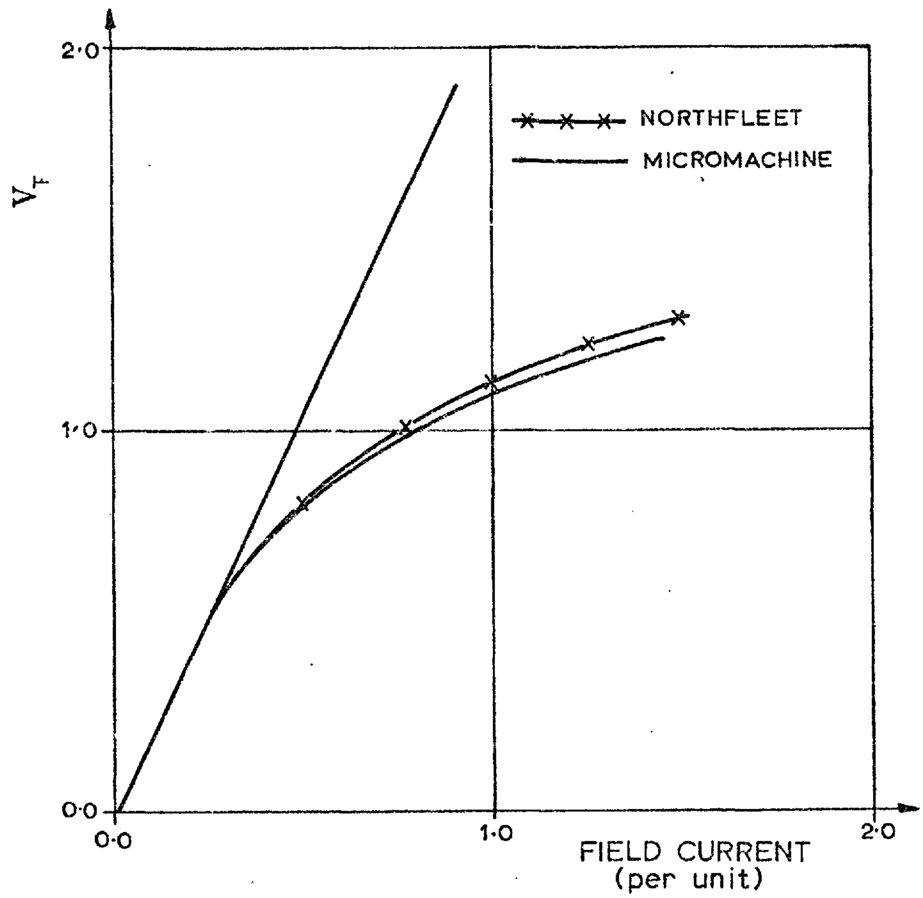

Fig. 2.28 Open circuit characteristic of Northfleet synchronous generator compared with micromachine

TABLE 2.1

Per-unit parameters of Northfleet turbogenerator and micromachine (micromachine stator No. 334818, rotor No. 334827)

Particulars	Northfleet	Micromachine
Base voltage	13.8 KV	.25 KV
Power factor	.8	.8
Base current	6.28 KA	5.77 A
Base stator impedance	1.27	25
Base armature power	150 MVA	2.5 KVA
Synchronous reactance X_d (50%)	1.85	1.84
X_q (50%)	1.76	1.67
Armature leakage reactance	.175	.131
Transient reactance	.270	.216
Subtransient reactance	.190	.15
Field open circuit time constant	6.6 s	6.6 s
Transient time constant	.97 s	.63 s
Subtransient time constant	.046 s	.008 s
Armature reistance	.0014	.0127
Inertia constant	3.36 s	3.22 s
Equivalent impedance to infinite bus	.499	.48
Speed	3000 rpm	1500 rpm

Saturation characteristics (see Fig. 2.28)

CHAPTER 3

SIMULATION OF STEAM TURBINE CHARACTERISTICS

3.1 General

The mathematical model of prime mover dynamics consists of differential equations which may be simulated on an analogue or digital computer as was shown in chapter 2. If these equations were to be integrated by a computer at a rate which is faster than or equal to real time, a micromachine set could be linked to such a computer in order that the correct torque and torque-speed-slope is enforced at all times (Fig. 3.1). This chapter describes the micromachine turbine simulation and the principles dictating the link between the micromachine and the computer.

3.2 Principles of turbine simulation on micromachines

In chapter 2 it was shown that for power system studies and to a good approximation the output power of a turbine cylinder in steady state is a function of the steam state at the cylinder's inlet and outlet. Thus, the power output of a multicylinder turbine can be expressed by

$$P_t = \sum_{\substack{\text{all turbine}\\ \text{cylinders}}} F\,(P_i^j,\ T_i^j;\ P_o^j,\ T_o^j) \qquad (3.1)$$

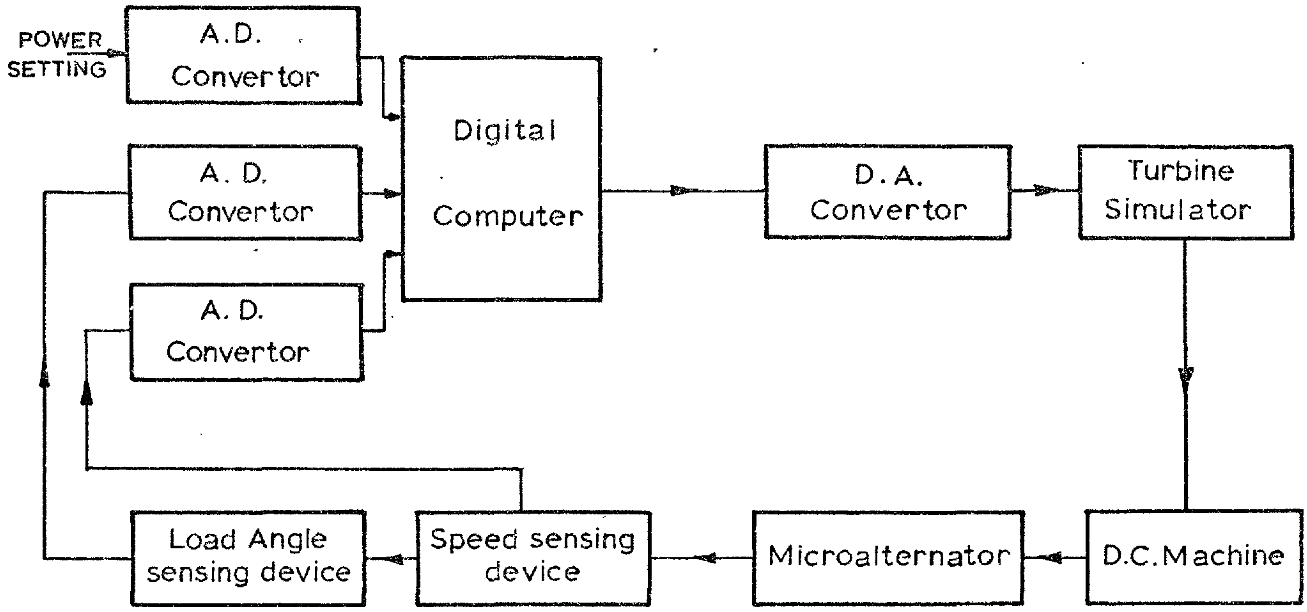

Fig. 3.1a. Digital Computer simulating turbine dynamics on a micromachine set. (A.D. analogue to digital convertor)

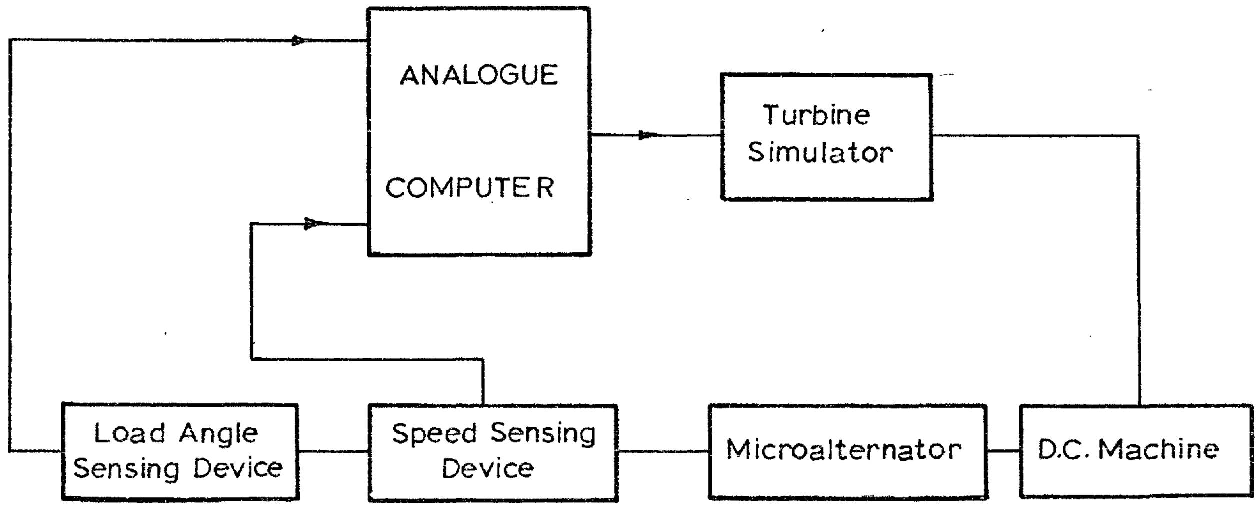

Fig. 3.1b. Analogue computer simulating turbine dynamics on a micromachine set.

As

$$T_t = \frac{P_t}{n} \qquad (3.2)$$

it follows that

$$\frac{\partial T_t}{\partial n} < 0 \qquad (3.3)$$

$$\frac{\partial^2 T_t}{\partial n^2} > 0$$

The Taylor expansion is used here to analyse different approximations to the turbine characteristics. An incremental linear approximation to the turbine characteristics around an operating point (p_t^o , n^o) must satisfy the following three conditions:

$$T_t\ (p^o,\ n^o) = T_{si}(p^o, n^o) \qquad (3.4)$$

$$\left[\frac{\partial T_t}{\partial n}\right]_{p^o,\ n^o} = \left[\frac{\partial T_{si}}{\partial n}\right]_{p^o,\ n^o} \qquad (3.5)$$

$$\left[\frac{\partial T_t}{\partial p_t}\right]_{p_t^o,\ n^o} = \left[\frac{\partial T_{si}}{\partial p_{si}}\right]_{p_{si}^o,\ n^o} \qquad (3.6)$$

Such an approximation is adequate for dynamic studies involving small perturbations around an operating point, but if the behaviour of the system to large perturbations were required, then

$$T_t(p_t, n) = T_{si}(p_{si}, n) \tag{3.7}$$

should be satisfied throughout the operating range. If equation 3.7 were satisfied then the simulation would be exact. As will be shown later, it is an almost impossible task to design a prime mover for a micromachine set capable of satisfying this requirement, therefore, only approximations to equation 3.7 will be considered.

Extending the analysis to second derivatives, the quality factors δ_i $(i = 1,6)$ give a measure of the goodness of a given approximation:

$$\begin{aligned}
\delta_1 &= T_t(p_t, n) - T_{si}(p_{si}, n) \\
\delta_2 &= \frac{\partial T_t}{\partial n} - \frac{\partial T_{si}}{\partial n} \\
\delta_3 &= \frac{\partial T_t}{\partial p_t} - \frac{\partial T_{si}}{\partial p_{si}} \\
\delta_4 &= \frac{\partial^2 T_t}{\partial n^2} - \frac{\partial^2 T_{si}}{\partial n^2} \\
\delta_5 &= \frac{\partial^2 T_t}{\partial p_t \partial n} - \frac{\partial^2 T_{si}}{\partial p_{si} \partial n} \\
\delta_6 &= \frac{\partial^2 T_t}{\partial p_t^2} - \frac{\partial^2 T_{si}}{\partial p_{si}^2}
\end{aligned} \tag{3.8}$$

The factors δ_i (i = 1, 6) can be embodied in δ_o as

$$\delta_o = \int_A \left[\delta_1^2 + a\,(\delta_2^2 + \delta_3^2) + b(\delta_4^2 + \delta_5^2 + \delta_6^2)\right] dpdn \qquad (3.9)$$

where, a and b are weighting parameters and A is the working area.

From equations 3.4, 3.5, 3.6 and 3.8 it is clear that a linear incremental approximation requires that $\delta_i = 0$ (i = 1, 2 and 3) at the operating point.

The object of the following sections is to synthesize a scheme capable of minimizing δ_o.

3.3 Early work on turbine simulation on micromachines

An early turbine simulator consisted of a direct voltage source driving a d.c. motor through an external resistance with excitation current held constant as shown in Fig. 3.2; such a system can be described mathematically by

$$V_{si} = (R' + R_a)\, i_d + X_{md}\, n\, i_f \qquad (3.10)$$

As the torque produced by a d.c. machine is given by

$$T_{si} = \frac{X_{md}\, i_f}{2\pi}\, i_d \qquad (3.11)$$

then substituting equation 3.10 into 3.11, the torque speed characteristic of the system shown in Fig. 3.2 is obtained as

$$T_{si} = A - B\,n \tag{3.12}$$

where

$$A = \frac{X_{md}\, i_f\, V_{si}}{2\pi(R'+R_a)}$$

$$B = \frac{X_{md}\, i_f}{2\pi(R'+R_a)}$$

A linear incremental approximation to turbine characteristics may be synthesized at the oprating point (p^o, n^o) if governor action is ignored. At the operation point the quality factors $\delta_i = 0$ $(i = 1,\ 2)$ thus

$$T_t(p^o,\ n^o) = \frac{p^o}{n^o} = A - B\,n^o$$

$$\frac{\partial T_t}{\partial n^o} = -\frac{p_t^o}{n^{o2}} = -B \tag{3.13}$$

and these two equations can be satisfied by properly selecting V_{si} and R' as

$$V_{si} = 2\,X_{md}\,n^o\,i_f$$

$$R' = \frac{X_{md}^2 \, i_f \, n^o}{2\pi p_t^o} - R_a$$

As governor action is neglected $\delta_3 = 0$. The necessary and sufficient conditions for a linear incremental approximation to turbine characteristics are satisfied because $\delta_i = 0$ ($i = 1$, 2 and 3). The quality of this approximations can be observed graphically in Fig. 3.4.

The following conclusions can now be drawn:

1 this scheme is inefficient as the voltage drop across the resistor R' demands an excessive voltage and power capability from the source V_{si},

2 no governor action or pressure variations are allowed for, thus only transients under these simplifying conditions could be studied, and

3 the model is only valid for small perturbations.

The performance of this system can be improved greatly if the resistor R' were introduced artificially by means of a controllable voltage source the magnitude of which is made dependent on the d.c. machine armature current through a feedback loop [2,3,4,5,25,24].

The controllable voltage source required by the turbine simulator may be realized by means of a three phase fully controllable rectifier as shown in Fig. 3.3.

The steady-state performance of a three-phase rectifier is developed in chapter 4. Neglecting harmonic effects the rectifier shown in Fig. 3.3 may be represented in steady state by a d.c. voltage $V_{dc} \cos \alpha$ and an internal resistance R_c, where

$$V_{dc} = \frac{3\sqrt{3}\ V}{\pi}$$

$$R_c = \frac{3X_s}{\pi}$$

The firing angle may be determined by inspection of Fig. 3.3

$$\alpha = \alpha^o + K^o\ i_d \qquad (3.15)$$

also

$$V_{dc} \cos \alpha = (R_c + R_a)\ i_d + X_{md}\ n\ i_f \qquad (3.16)$$

Substituting equations 3.15 and 3.16 into 3.11 and rearranging, the torque speed characteristic of the system shown in Fig. 3.3 is obtained as

$$n = A' \cos (\alpha^o + B'\ T_{si}) - C'\ T_{si} \qquad (3.17)$$

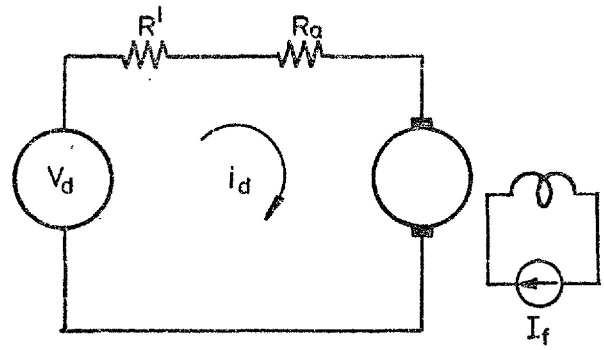

Fig. 3.2. Early turbine simulator (Linear incremental model)

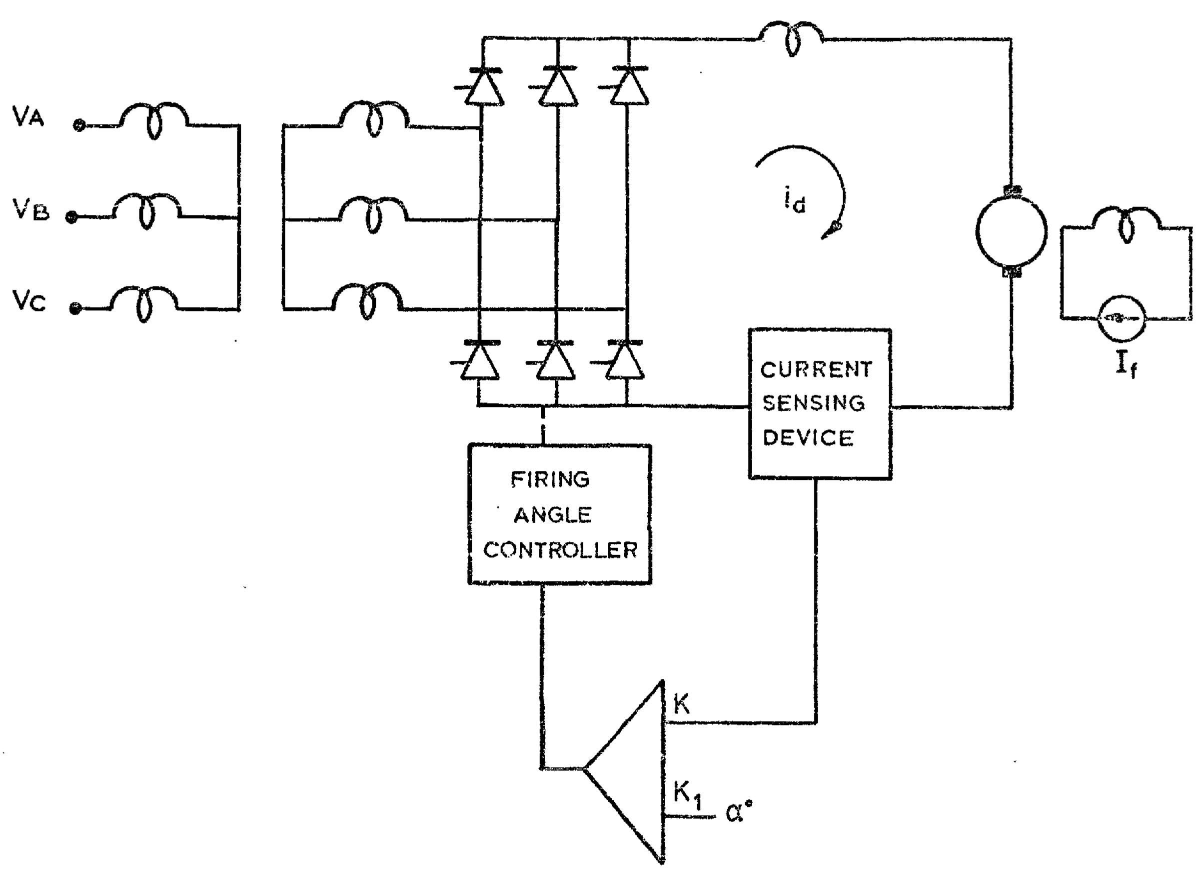

Fig. 3.3. Turbine simulator (linear incremental model)

where

$$A' = \frac{3\sqrt{3}\ V}{\pi\ X_{md}\ i_f}$$

$$B' = \frac{2\pi\ K^o}{X_{md}\ i_f}$$

$$C' = \frac{2(R_c + R_a)\pi}{X_{md}^2\ i_f^2}$$

As previously, a linear incremental approximation to turbine characteristics around an operating point (p_{si}^o, n^o) can now be synthesized if governor action is omitted. At the operating point, the quality factors $\delta_i = 0 (i = 1, 2)$, and therefore

$$\begin{aligned} n^o &= A' \cos\left(\alpha^o + B' \frac{p_{si}^o}{n^o}\right) - C' \frac{p_{si}^o}{n^o} - \\ -\frac{{n^o}^2}{p_{si}^o} &= -A'\ B' \sin\left(\alpha^o + B' \frac{p_{si}^o}{n^o}\right) - C' \end{aligned} \tag{3.18}$$

These two equations can be satisfied by properly selecting α^o and K^o as follows:

$$\begin{aligned} \alpha^o &= \cos^{-1} D - \left(p_{si}^o + C' \frac{p_{si}^o}{n^o}\right) D'^2 \\ K^o &= \frac{X_{md}\ i_f\ D'}{2} (n^o + C') \end{aligned} \tag{3.19}$$

where

$$D = \frac{1}{A'} \left(n^o + C' \, p^o_{si} \right)$$

$$D' = \sqrt{\left[A'^2 - n^o + C' \, \frac{p^o_{si}}{n^o} \right]}$$

Thus a linear incremental approximation to the turbine characteristics has been obtained. The quality of this approximation can be observed graphically in Fig. 3.4. At the point of the approximation the concavities of the two curves are,however, different. In the model under consideration

$$\frac{\partial^2 T_{si}}{\partial n^2} < 0$$

whereas, according to equation 3.3, for the real turbine

$$\frac{\partial^2 T_t}{\partial n^2} > 0$$

As a result δ_6 increases the further the deviation from the operating point.

Some authors[2,3,4,5,25] have introduced governor action by making α^o dependent on the power level as given by the simulation of turbine dynamics. This procedure is inaccurate since according to equation 3.5 for a given increment of speed around a new operating point, corresponding increments in torque would be different in the turbine simulator

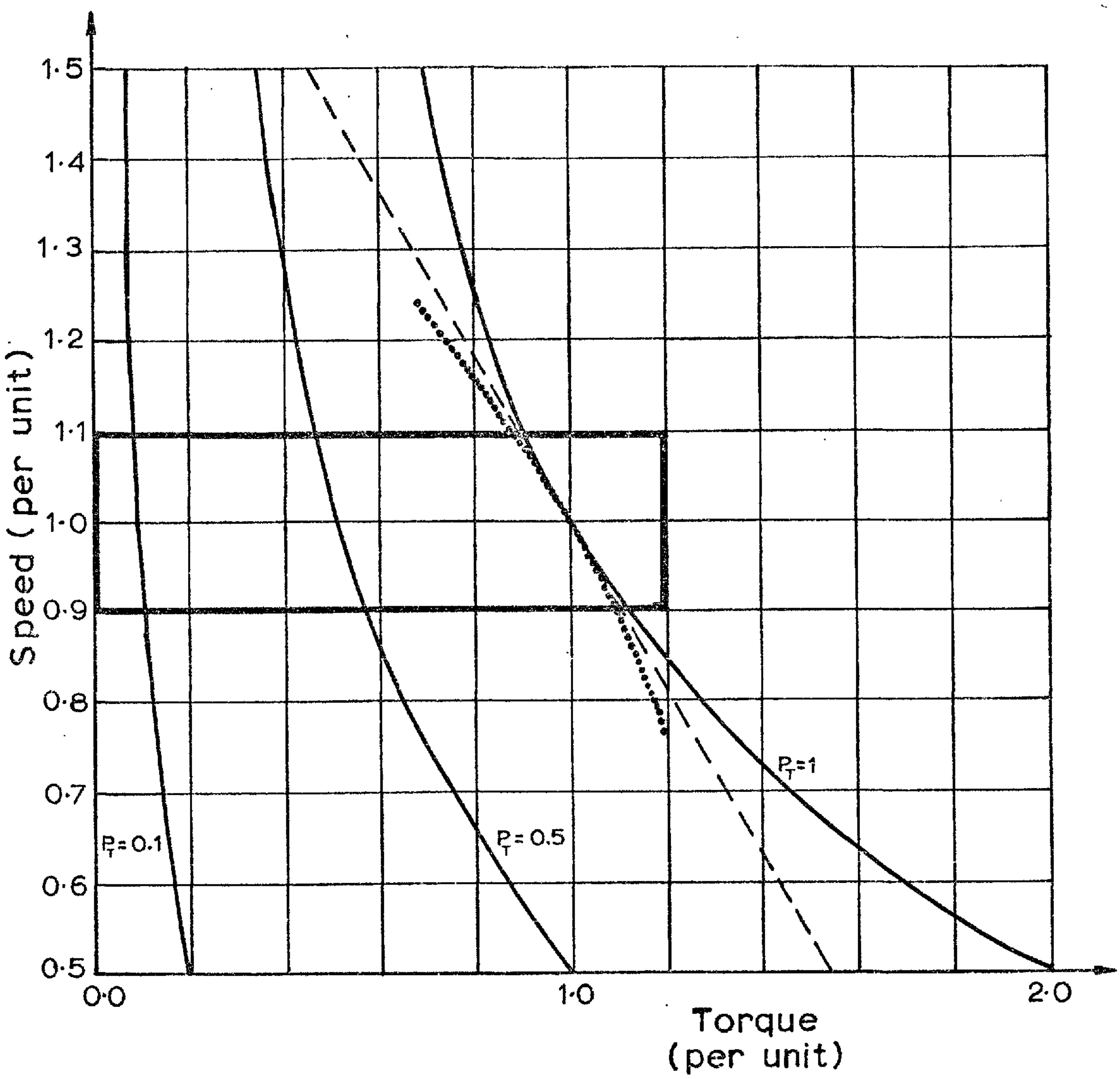

Fig. 3.4. Torque-speed characteristic of a turbine

Real turbine torque speed characteristic ————

Early turbine simulator torque speed characteristic — — —

Linear incremental turbine simulator torque speed characteristic realized by means of a controlled rectifier ••••••••

if compared to the real turbine. Furthermore, the relationship between α^o and the power level applied to the shaft of the microalternator is nonlinear, thus further compensation is required. Such an approximation would be accurate only for small perturbations about a fixed operating point.

3.4 Improved turbine simulation on micromachines

Previous turbine simulators were not capable of simulating turbine characteristics accurately for large perturbations because the torque and the torque-speed-slope imposed by the d.c. machine on to the shaft of the microalternator, were not equal to those supplied by the real turbine to the shaft of the real generator. To achieve this compatibility, α^o and K^o should change with the operating point in order to fulfil the torque and the torque-speed-slope equalities throughout the operating region. Turbine simulation on a micromachine can, however, be extended throughout the region of interest by storing functions $\alpha(p_{si}, n)$ and $K(p_{si}, n)$ as shown in Fig. 3.5, thus satisfying the strong condition of approximation given by equation 3.8 and therefore $\delta_i = 0$ $(i = 0, 1, ...6)$. As this approach is very expensive to implement simpler schemes were considered.

A first simplification would be to consider the turbine simulator as a controllable constant power supply source. The controlled rectifier can be used as a constant power source through a feedback loop incorporating a power

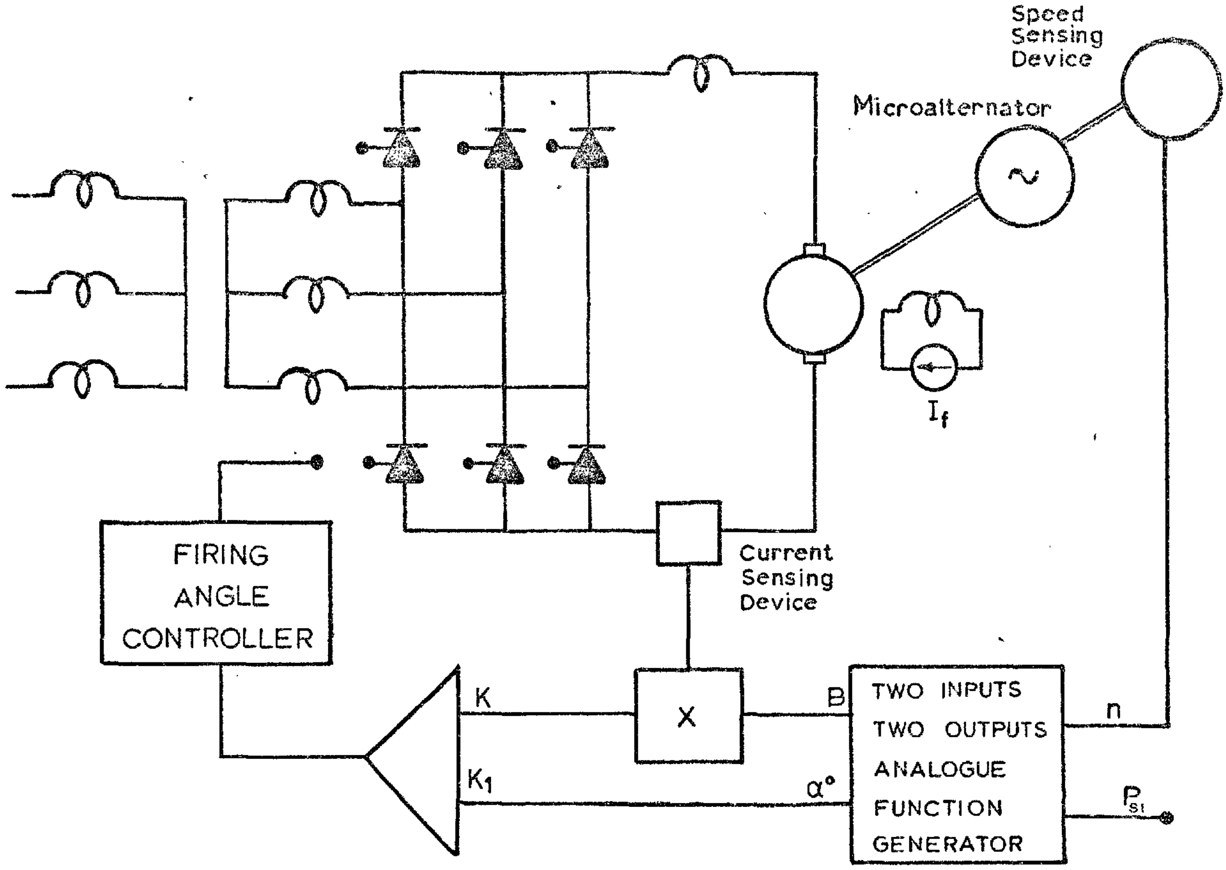

Fig. 3.5. Optimum turbine simulator

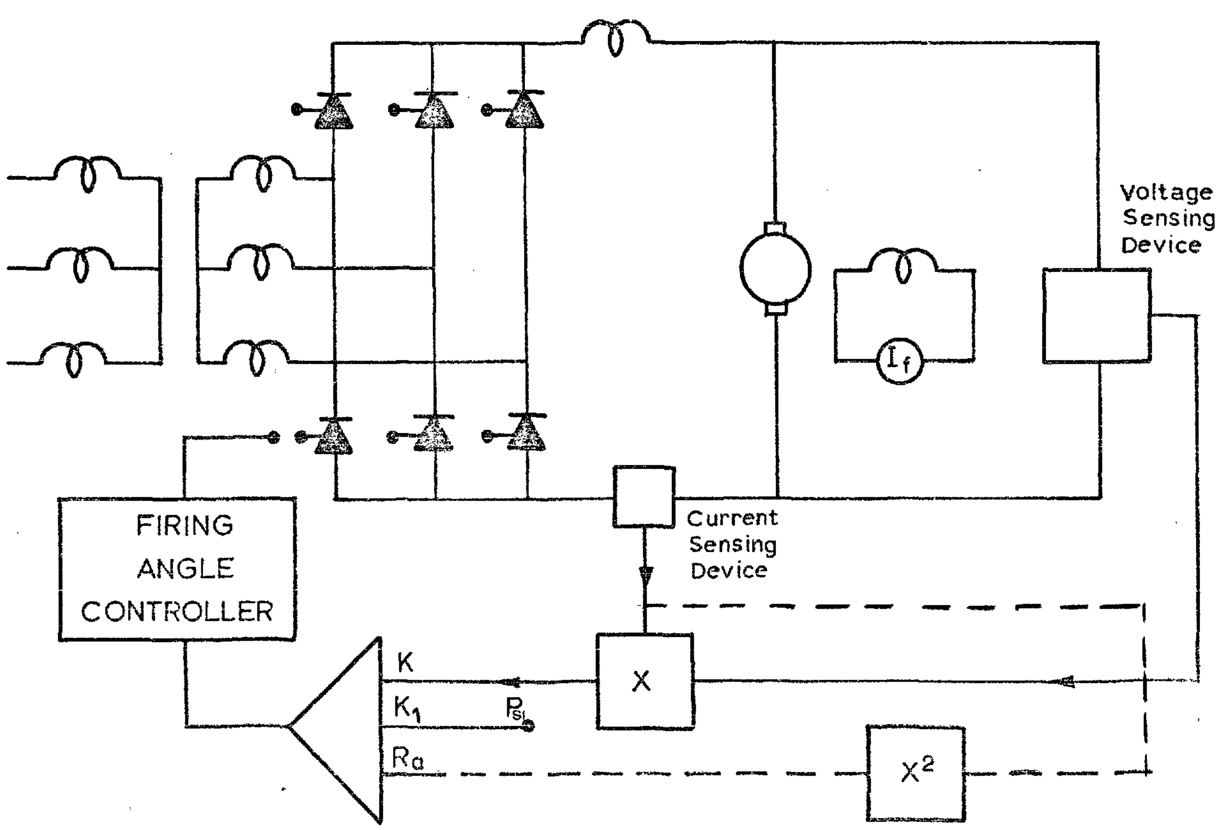

Fig. 3.6. Turbine simulator. (First approximation)

sensor as shown in Fig. 3.6. Here, the losses in the armature resistance of the d.c. machine need compensation and therefore an additional loop supplying a signal equal to this loss term has been added. A steady-state error arises from this implementation since the gain K_1 can not be made infinite because otherwise steady-state errors would be inherent to this type of regulator.

A second possibility would be to omit the speed feedback loop shown in Fig. 3.5 as due to governor action speed variations should be small. The function generator shown in Fig. 3.5 is now simplified to two single input single output function generators as shown in Fig. 3.7. These two function generators are calibrated in such a way that for each power level p_{si} an incremental linear approximation to turbine characteristics is obtained at nominal speed. The quality of this approximation may be appreciated graphically in Fig. 3.8, where both the real turbine and the simulated turbine characteristics are shown. Theoretical calculations showed that the maximum error between the real turbine and the simulated turbine would be less than 1% if speed variations of ±10% around nominal speed are considered.

The evaluation of function generators F_1 and F_2 (Fig. 3.7), using equations 3.19, showed that to a good approximation F_1 could be represented by a first order hyperbola ($F_1(p_{si}) = A/p_{si}$, where A is a constant) and F_2 by a straight line as in Fig. 3.9. The nonlinear elements in Fig. 3.7 can be replaced, to a good approximation, by only one

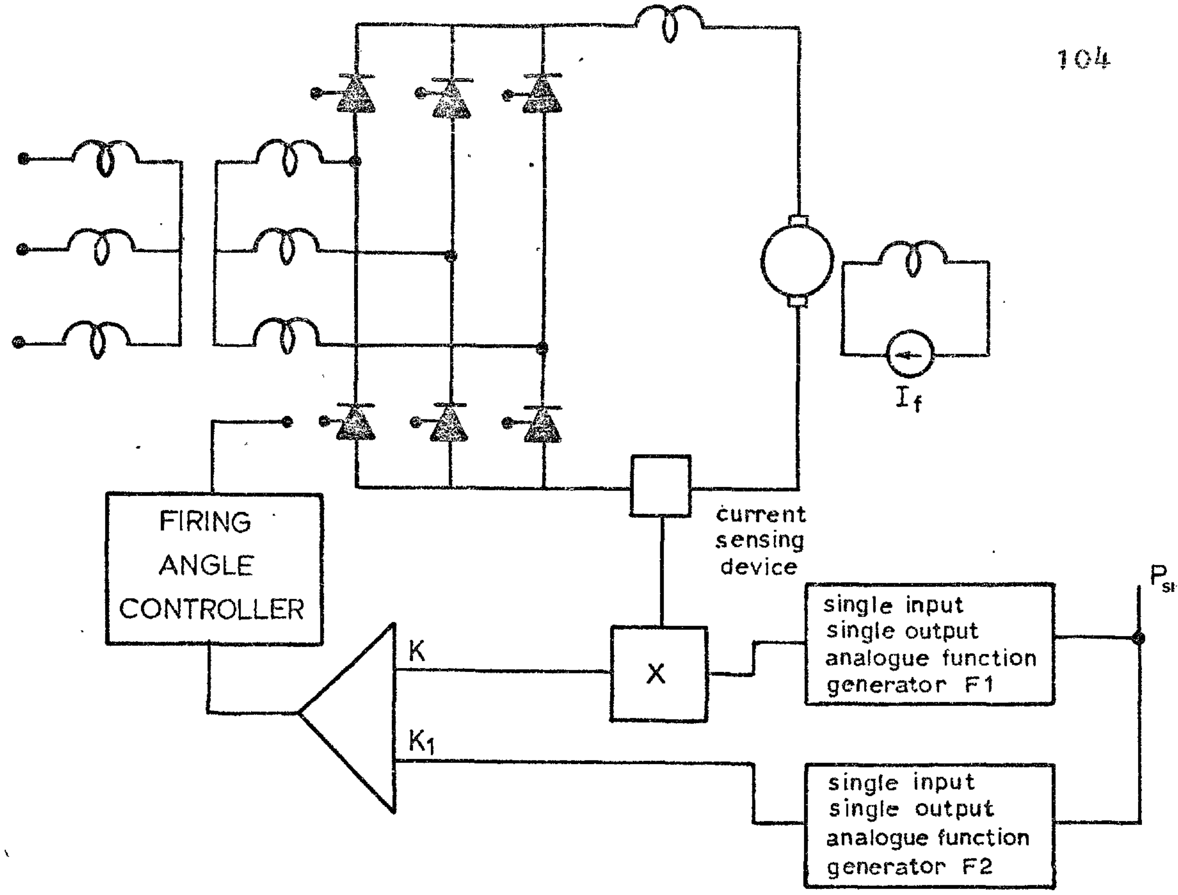

Fig. 3.7. Turbine simulator (Second approximation

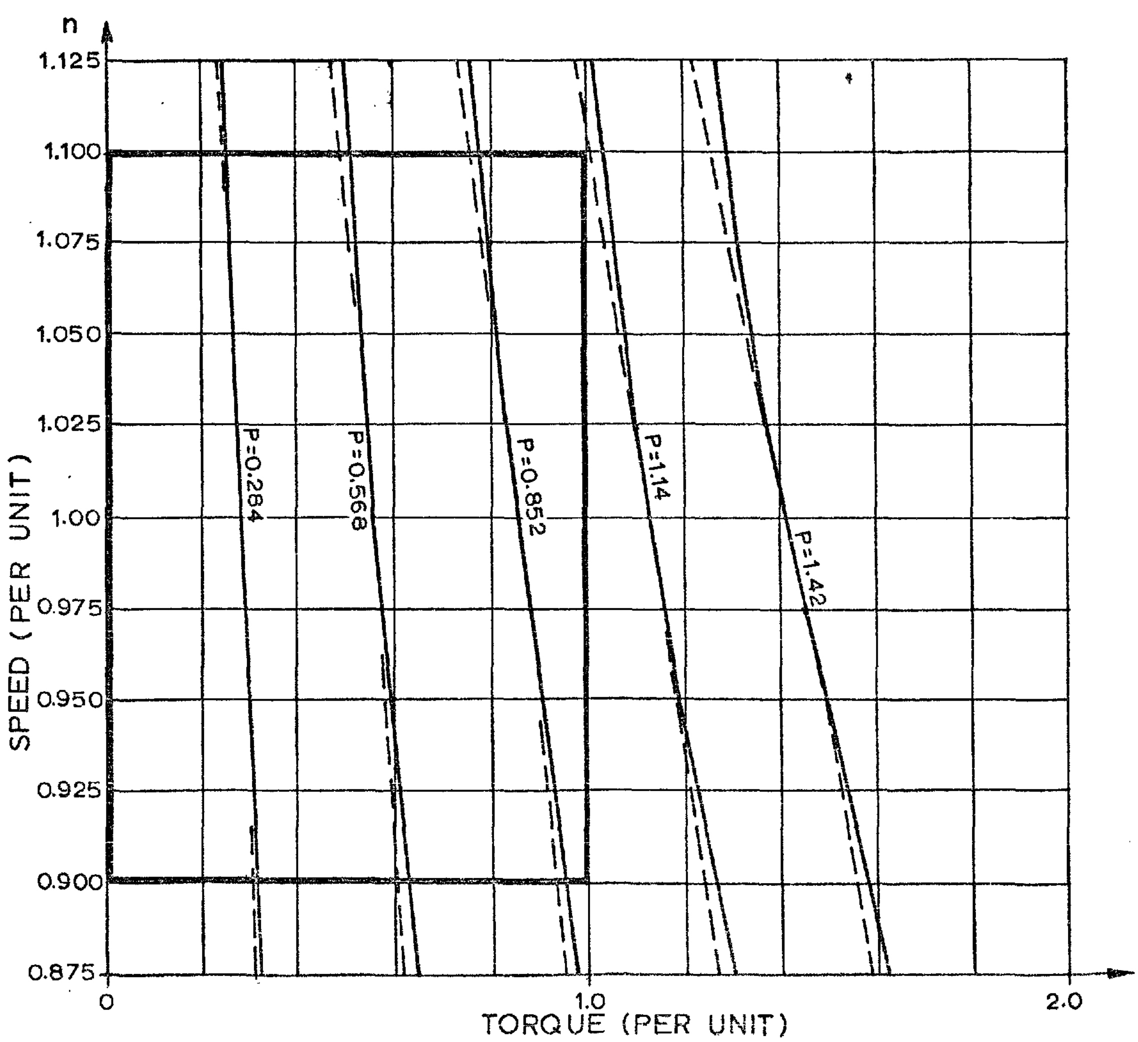

Fig. 3.8. Torque speed characteristics of the turbine simulator Second approximation

—— Torque speed characteristic of steam turbine

– – Torque speed characteristic of turbine simulator

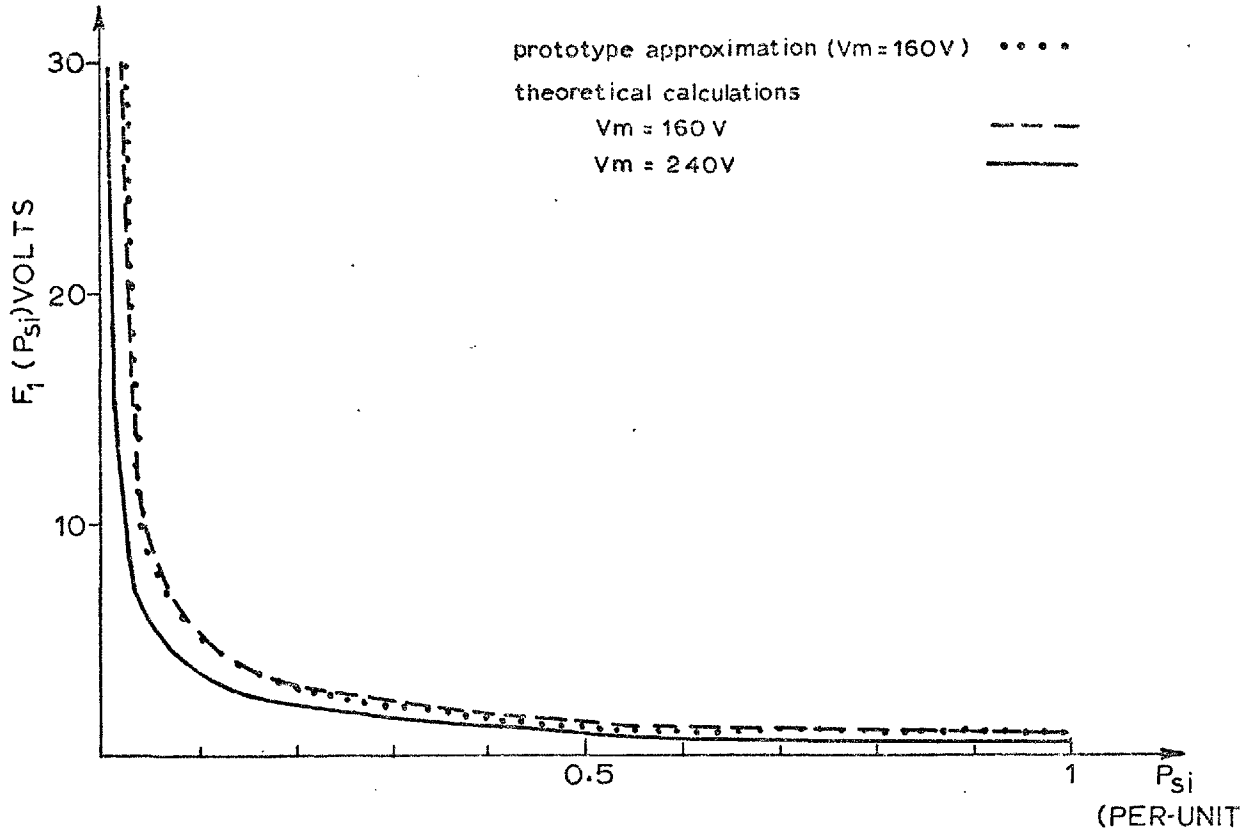

Fig. 3.9a. Calculations of function generator F_1 for two different rectifier mains voltage and prototype approximation (Vm = a.c. phase to phase, r.m.s. rectifier mains supply voltage)

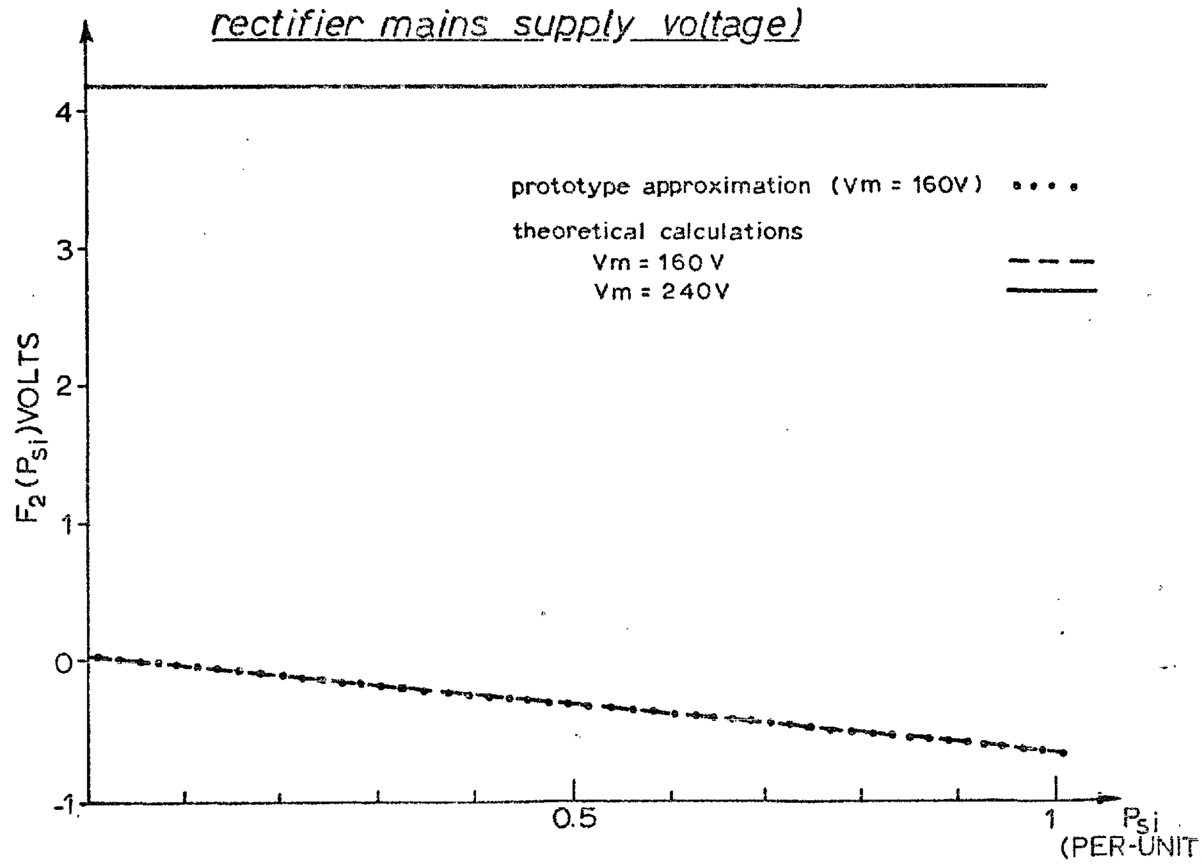

Fig. 3.9 b. Calculations of function generator F_2 (P) for two different rectifier mains voltage and prototype approximation

nonlinear element as shown in Fig. 3.10. The model of Fig. 3.10 combines accuracy with simplicity. Details of this simulator design are given in appendix 6.

3.5 Loss compensation

The losses in the micromachine set can be subdivided as follows:

1 losses in the armature and field winding resistances of the d.c. machine,

2 losses in the armature and field winding resistances of the microgenerator,

3 losses in the magnetic circuit of the d.c. machine,

4 losses in the magnetic circuit of the microgenerator, and

5 rotational losses.

The turbine simulator takes into account losses in the d.c. machine windings; furthermore, losses in the microgenerator windings may be assessed quantitatively although they will be higher than in the real generator. However, modelling of the losses in the magnetic circuits of the micromachine set is outside the scope of this work. Compensation of all

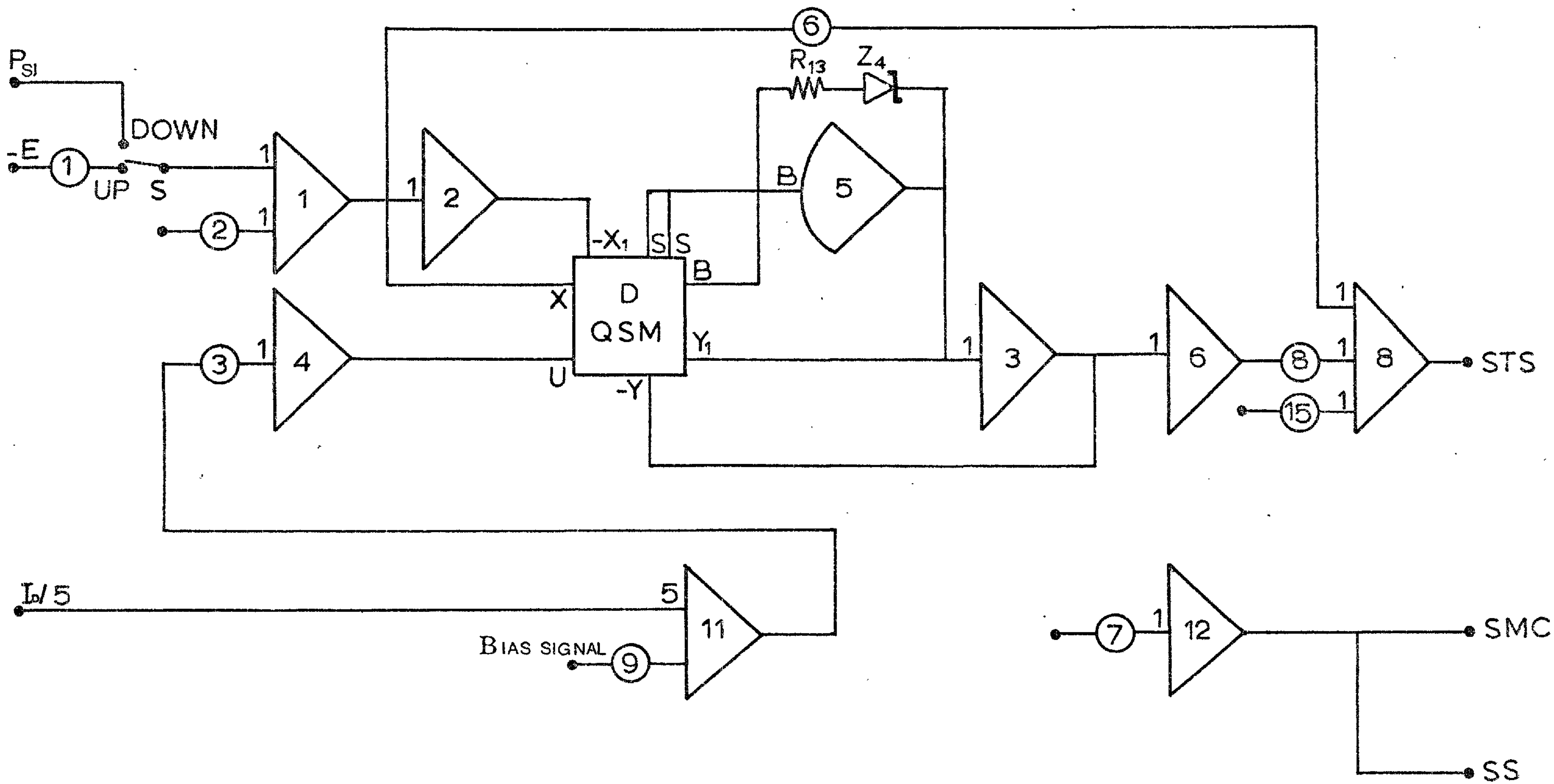

Fig. 3.10. Prototype turbine simulator. Analogue realization of function generators F_1 and F_2

S Switch on position 1 indicates manual power control through potentionmeter P1

S Switch on position 2 indicates automatic power control from turbine valves

Table 3.1 Amplifier and potentiometer table (with reference to analogue set up shown on Fig. 3.10)

POTENTIOMETER TABLE

P	Function	VALUE
1	power output of the turbine simulator when manually controlled	P_{si}
2	Steady-state power compensation	0 normally
3	scaling factor K_o	.5
6	Steady-state power compensation	to be tuned
7	Manual control of the firing angle of the rectifier	
8	As determined by equation 3.19, $K^o/(K_o.10)$	
9	Loss compensation and drift correction (small setting)	to be tuned
15	Setting valve for 1 per unit power output	to be tuned

AMPLIFIER TABLE

A	Function	
1	Power output of the simulator (Buffer)	P_{si}
2	Power output of the simulator (INVERTOR)	$-P_{si}$
3	$10\frac{I_d}{P_{si}}$ (output of nonlinear element)	$10\frac{I_d}{P_{si}}$
4	$K_o I_d$ inverted stage	$.5I_\alpha$
5	$-10\frac{I_d}{P_{si}}$ (inverted output of nonlinear)	$-10\frac{I_d}{P_{si}}$
6	$-10\frac{I_d}{P_{si}}$ (Buffer stage)	"
8	Control voltage of pulsing circuitry	v_c
11	Last amplification stage of the current sensing device	I_d
12	Firing angle (when on manual or starter control)	α

open circuit losses of the micromachine set, neverthless, was implemented successfully and thus it was possible for valid load rejection simulations to be carried out.

The microgenerator electrical torque, from Park's equations, is given by

$$T_e = n(\psi_d\, i_q - \psi_q\, i_d) \tag{3.20}$$

If open circuit operation of the microgenerator is considered

$$T_e = i_d = i_q = 0 \tag{3.21}$$

Variations in the open circuit voltage of the microgenerator armature owing to variations in the microgenerator field current do not in theory produce variations in the electric torque and although, under these conditions current may circulate in the damper windings , this power is drawn from the exciter. In practice, however, losses in the magnetic circuit of the microgenerator vary substantially with the armature voltage, the necessary power being extracted from the prime mover. These effects are not shown in Park's equations because of the symplifying assumptions involved in their derivation. Under open circuit conditions oscillations of the shaft of a real generator are governed by

$$T_{tur} - T_{elec} - T_{loss} = J\,\frac{d^2\delta}{dt^2} \tag{3.22}$$

The turbine simulator obeys a similar differential equation, but the loss term is much larger and therefore compensation is necessary. This compensation is achieved by introducing a bias signal in the current sensing device (Fig. 3.10), a procedure which is valid as automatic voltage regulator action keeps the machine terminal voltage roughly constant and as it is shown later in chapter 5, load rejection tests using this mode of compensation give very acceptable results.

3.6 The turbine simulator in transient state

The turbine simulator does not act instantaneously, therefore, under transient conditions there would be a time lag between the power level as determined from the simulation of turbine dynamics and the required torque being applied to the shaft of the microalternator. Compensation of this time lag may be required.

From Fig. 3.7 it can be seen that the turbine simulator current feedback loop gain is given by $K\,F_1(p_{si})$ and from Fig. 3.9 it can be observed that

$$\lim_{p_{si}\to 0} K\,F_1(p_{si}) = \infty \qquad (3.23)$$

This gain cannot be implemented physically because of scaling constraints in the analogue circuitry and due to the fact that the simulator becomes unstable when the gain of the current feedback loop is made too large.

As it can be seen, there were conflicting demands of steady-state accuracy, scaling of analogue circuitry, and transient response and stability. No methods were available in the literature suitable for analysing the dynamic behaviour of control systems involving controlled rectifiers, as the one shown in Fig. 3.5, when a fast transient response was specified. As a result, small perturbation and large perturbation models were developed for the system under consideration as shown in chapter 4 after which the dynamics of the system were better understood.

In chapter 4 it is shown theoretically that with no time delay in the current feedback loop the system being studied is stable regardless of the gain. It turned out, however, that the saturation of chopper amplifiers placed directly in the current feedback loop of the turbine simulator is detrimental to stability margins; this is so because their transient response becomes worse when they are driven into saturation. The relatively large ripple in the output current of rectifiers and the high gain involved in the current feedback loop resulted in a greatly amplified ripple content in the current error signal which tended to saturate these amplifiers.

In the analogue set-up shown in Fig. 3.10, amplifier No. 5 goes first into saturation during the peak of the current harmonics. The Zener diode shown was employed to remove these peaks and to limit the gain of the current feedback circuitry without affecting significantly the steady--state behaviour of the system. The effect of the Zener diode on the gain of the current feedback loop can be seen graphically in Fig. 3.11. The turbine simulator developed, because of amplifier saturation effects, becomes unstable for large gains of the current feedback loop, when the Zener diode is removed from the circuitry.

As the output current of the rectifier is not smooth, it is difficult to assess qualitatively a mathematical structure for its transient response. In chapter 4 it is shown that the rectifier output current evolves exponentially for small step disturbances if the effects of overlap angles and current ripple are neglected. For the purpose of estimating quantitatively the transient behaviour of the simulator, the rectifier may be modelled in this manner, as in Fig. 3.12a. An equivalent time constant for the simulator can be obtained as follows

$$T'_{si} = \frac{L_L}{V_{dc} \sin\alpha^o K^o + R'} \tag{3.24}$$

The simulator equivalent time constant depends on the operating point as K^o and α^o depend on that point. Theoretically and experimentally it was found that this

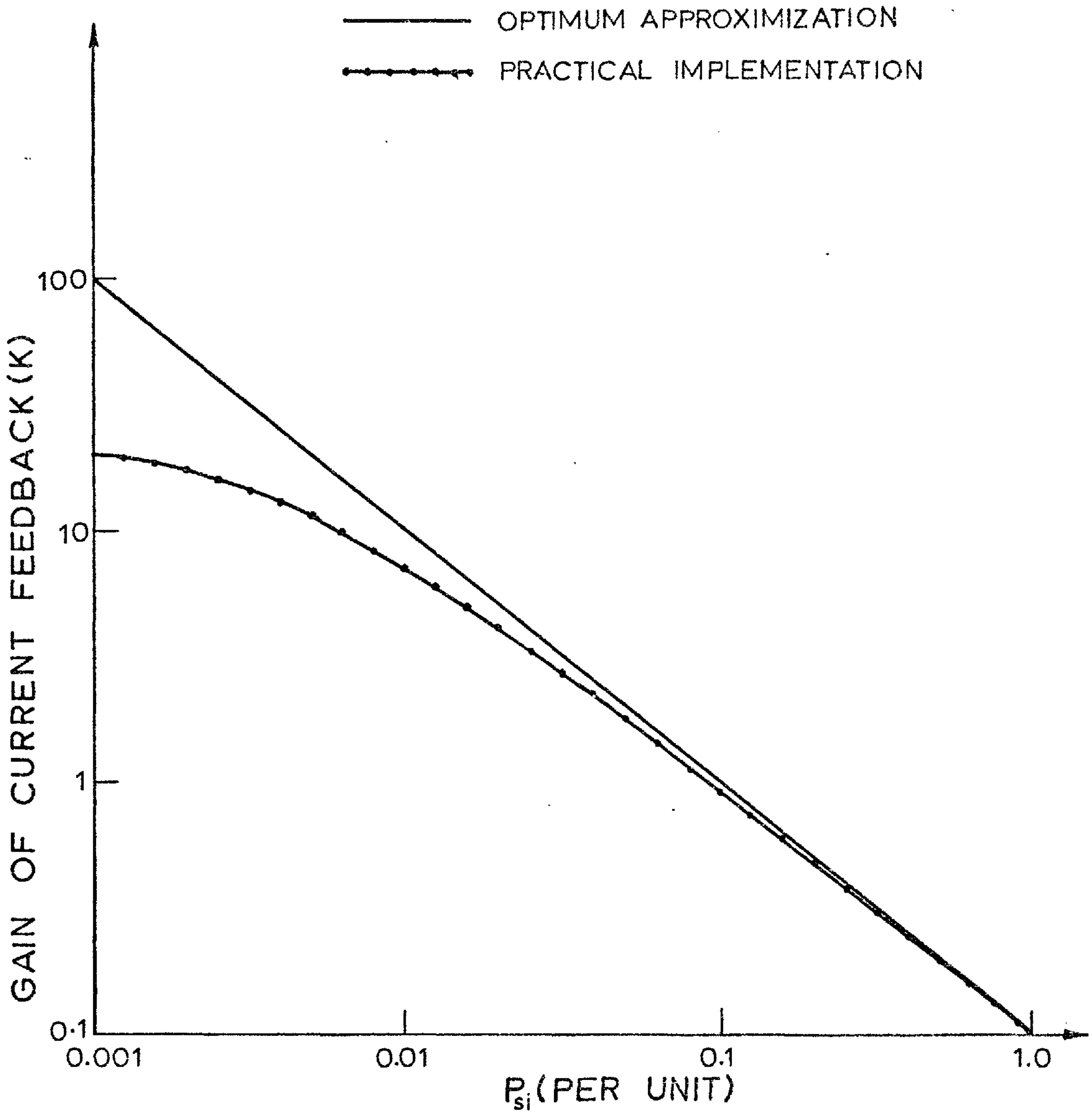

Fig. 3.11. Variation of the gain of the current feedback loop with the power level

time constant varied from 5 to 10 miliseconds. If it is assumed that the simulator behaves with a fixed time lag, this inherent delay could be compensated as shown in Fig. 3.12b. However, if very fast turbine transients are not being studied this last compensation may not be required as the time constants normally involved in turbine dynamic problems are of the order of seconds, the response of the simulator, being two orders of magnitude faster, can be neglected without serious error.

Furthermore, considerations of transient performance demand a small overlap angle for the rectifier (see chapter 4 for explanation of the phenomenon) and therefore a mains transformer of small leakage reactance, which results in high short circuit levels and expensive rectifier design.

3.7 Other control schemes

In this project a three-phase fully controllable rectifier was used to feed the armature of the d.c. machine. The simulator transient response if required can be improved if the sampling interval is reduced (chapter 4), this can be accomplished either by increasing the frequency of the rectifier a.c. supply or the number of phases. Alternatively, d.c. to dc. convertors, such as pulse width modulators could be used. However, all these improvements are expensive to implement.

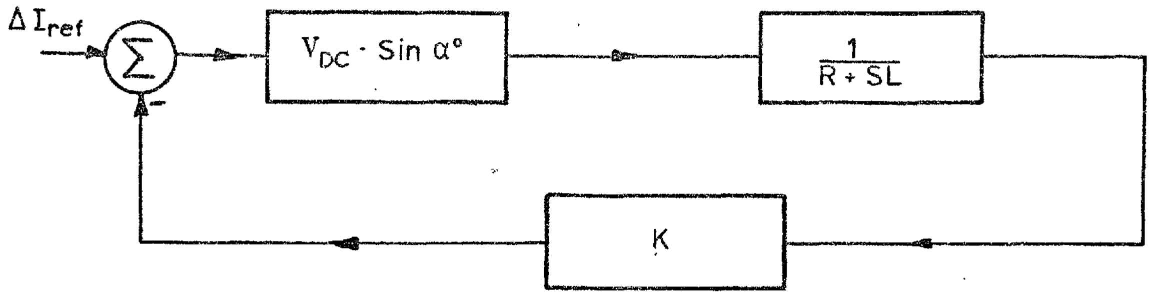

Fig. 3.12a. Dynamic model of the rectifier-d.c. machine-current feedback loop for estimating transient performance

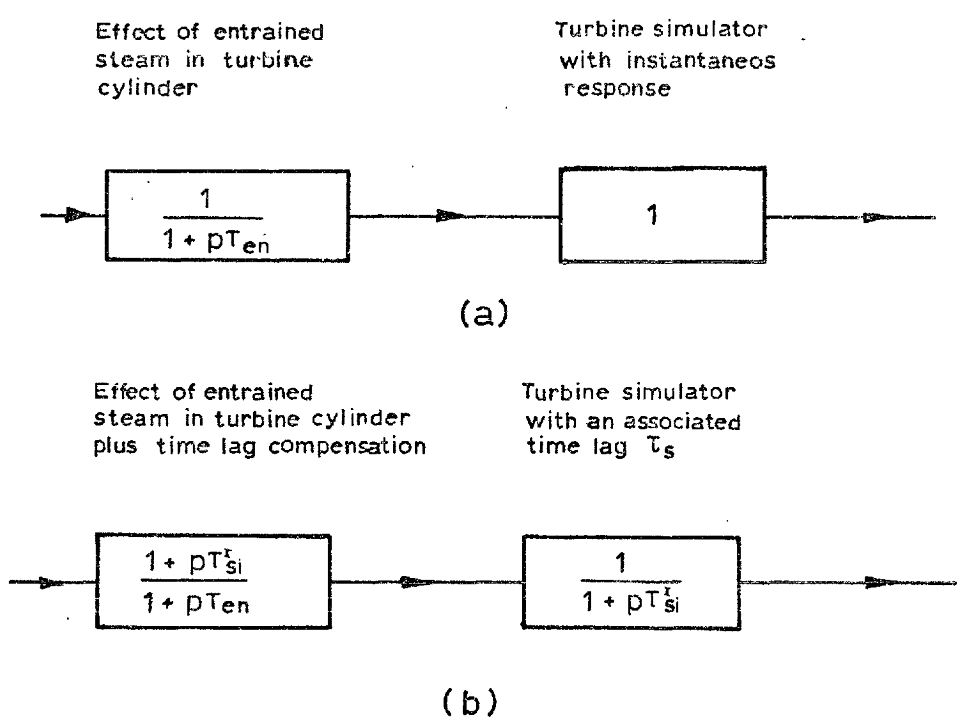

Fig. 3.12b. Time lag compensation of turbine simulator

Electromechanical convertors have been used in the past for quick speed control of d.c. machines but these convertors do not compete in speed of response with solid state devices. However, d.c. machines with a number of windings, such as metadynes, could result in satisfactory modelling, but at the expense of increased complexity and cost.

If the microalternator prime mover torque were directly sensed, the controllable rectifier employed in this project can be used, incorporating this sensor, to produce the torque speed characteristics of a real turbine . This approach would have the advantage of being independent of all prime mover losses. However, such a simulator would be more complex.

CHAPTER 4

SIMULATION OF RECTIFIER DYNAMICS

4.1 General

As mentioned in chapter 3 the author met considerable difficulties in the design of the rectifier speed control system for the micromachine set drive. It was found that existing dynamic models of controlled rectifiers that have appeared in various papers failed to describe the real system behaviour under transient conditions. It was therefore felt that the modelling of a controlled rectifier in a closed loop system should be looked at again. In this chapter first, a rigorous mathematical model is developed which describes the rectifier transient behaviour under small or large signal conditions. This model is complex, requires the use of a digital computer for the evaluation of characteristics, can be applied only to simple system configurations and does not give much insight into system design. On the other hand, such a model is the only tool known to the author capable of analysing accurately the system behaviour under large disturbances.

A rigorous small-signal model for the rectifier was then developed. This model represents accuratelly the sampling nature of the rectifier together with its pulsing units, and takes into account for the first time the commutating impedance. With this model the dynamics of a system can be assessed throughout a range of possible variables and thus an optimum solution to the design problem can be chosen.

Finally, the small-signal models suggested in the literature were examined critically and their step response, Nyquist plots and stability boundaries compared with the author's models.

4.2 Steady-state output of a controlled rectifier

The instantaneous output voltage of the generalized q-phase controlled rectifier of Fig. 4.1 is shown in Fig. 4.2 for finite α and u. This waveform, as well as $i_d(t)$ and $v_c(t)$, admit a Fourier series expansion resulting in a summation of an infinite number of terms. In contrast, Laplace methods result in a closed form expression for $i_d(t)$ and $v_c(t)$ and convergence is achieved at the discontinuities of the waveform. This is of great importance as the behaviour of $v_c(t)$ at the instants of discontinuity is vital in the analysis of rectifier systems.

As far as the author is aware, Bayoumi[108] was first to apply Laplace techniques to the mathematical formulation of the rectifier output. This approach is here generalized to include a finite commutation angle and a feedback loop.

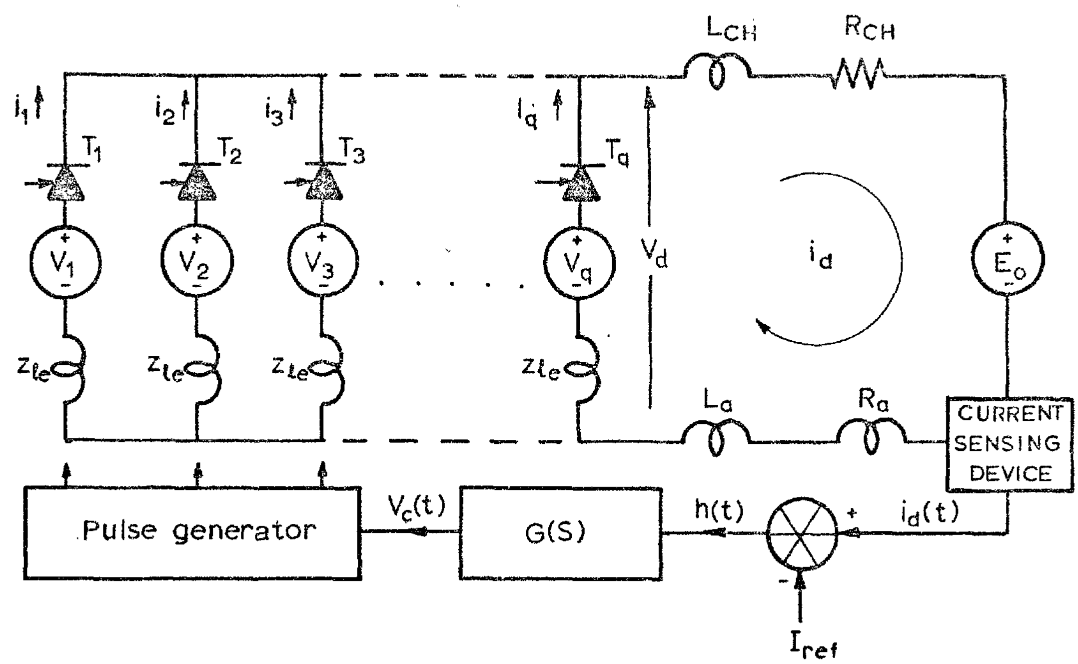

Fig. 4.1. Circuit diagram of a q-phase controlled rectifier

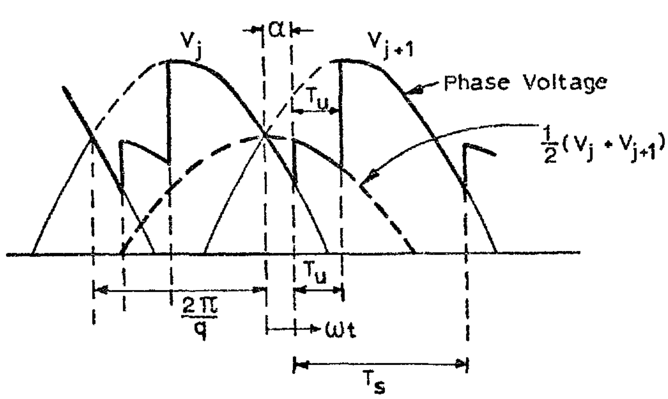

Fig. 4.2. Instaneous output voltage of the generalized
q-phase rectifier

The output voltage of the rectifier $v_d(t)$ is assumed to consist of the two components $v_1'(t)$ and $v_2'(t)$ representing the output voltage with u = 0 and the voltage drop due to commutation respectively. Therefore

$$v_d(t) = v_1'(t) - v_2'(t) \tag{4.1}$$

Over one conduction period T_s these components can be defined as follows (Fig. 4.2):

$$v_1'(t) = V \sin(\omega_o t + \alpha') \qquad 0 \le t \le T_s$$

$$v_2'(t) = \begin{cases} V \sin\frac{\pi}{q} \sin(\omega_o t + \alpha^o) & 0 \le t \le T_u \\ 0 & T_u \le t \le T_s \end{cases} \tag{4.2}$$

where $\alpha' = \alpha^o + \frac{\pi}{2} - \frac{\pi}{q}$

The Laplace transform of expression 4.2 is

$$v_1'(s) = V \frac{\omega_o(\cos\alpha' - e^{-sT_s}\cos\gamma') + s(\sin\alpha' - e^{-sT_s}\sin\gamma')}{(\omega_o^2 + s^2)(1 - e^{-sT_s})} \tag{4.3}$$

$$v_2'(s) = V\sin\frac{\pi}{q} \frac{\omega_o(\cos\alpha^o - e^{-sT_u}\cos\gamma'') + s(\sin\alpha^o - e^{-sT_u}\sin\gamma'')}{(\omega_o^2 + s^2)(1 - e^{-sT_s})} \tag{4.4}$$

where $\gamma' = \alpha' + \frac{2\pi}{q}$ and $\gamma'' = \alpha^o + u^o$

The Laplace transform of the output current i_d and the control voltage v_c are given respectively by

$$i_d(s) = \frac{v_1'(s) - v_2'(s) - E_o/s}{R_t(1 + s\,T_2)} \tag{4.5}$$

$$v_c(s) = K\left[\frac{v_1'(s) - v_2'(s) - E_o/s}{R_t(1 + sT_1)(1 + sT_2)} - \frac{I_{ref}}{s(1 + sT_1)}\right] \quad (4.6)$$

where it is assumed that

$$G(s) = \frac{K}{1 + sT_1} \quad \text{and} \quad T_2 = \frac{L_t}{R_t}$$

The constants R_t and L_t include both the load and the internal rectifier resistance and inductance. The internal effective resistance and inductance of the rectifier change from R_{1e} and L_{1e} when one element is only conducting, to $R_{1e}/2$ and $L_{1e}/2$ when two elements are conducting. These constants can be averaged as follows:

$$R_{av} = (\frac{2\pi}{q} - u^o)\ \frac{q}{2\pi}\ R_{1e} + u^o\ \frac{q}{2\pi}\ \frac{1}{2}\ R_{1e}$$

$$L_{av} = (\frac{2\pi}{q} - u^o)\ \frac{q}{2\pi}\ L_{1e} + u^o\ \frac{q}{2\pi}\ \frac{1}{2}\ L_{1e}$$

The steady-state control voltage $v_c^o(t)$ and the steady-state current output $i_d^o(t)$ can be found in a closed form from equations 4.3 to 6 using Laplace transform or modified z-transform. Both derivations are equivalent and equally lenghty, and only the Laplace formulation is presented in appendix 7.

The classical method of solution of differential equations provides a simpler approach to the determination of the steady-state characteristics of a controlled rectifier (appendix 8), as compared with either Laplace transform or modified z-transform. The classical method does not require the simplification of averaging rectifier internal impedances. This is of particular importance because an exact solution of the rectifier initial conditions problem is thus obtained. If transform methods are used to determine the steady-state characteristics of controlled rectifiers taking into account the effect of varying rectifier internal impedances, the solution is obtained in the form of an infinite Volterra series expansion, and this makes these methods extremelly difficult to treat numerically.

4.3 Rigorous mathematical dynamic model

The operation of a rectifier consists of a succession of similar processes. If a mathematical description of one process is developed, the repeated use of the same process will describe the dynamic behaviour of the rectifier[78].

The rectifier of Fig. 4.1 can operate with none, one, two or more elements conducting simultaneously at an instant in time. In the analysis that follows, a sequence of periods with none, one or two elements conducting is only considered i.e. the current can become discontinuous but double commutation on overcurrent is not antecipated. These restrictions can, of course, be lifted if the operating conditions so demand.

With one element conducting the rectifier circuit of Fig. 4.1 becomes equivalent to circuit A in Fig. 4.3. The output current of the rectifier during the one element conduction period Δt_1 can now be found through network analysis. It is given by:

$$i'_{d,1}(t) = \frac{V}{Z_1} \cos(\omega_o t + \beta'' - \theta_1) + \left[\frac{E_o}{R_1} + I_{o1} - \frac{V}{Z_1}\cos(\beta'' - \theta_1)\right] e^{-\frac{t}{T'_1}} - \frac{E_o}{R_1} \tag{4.7}$$

for $i_1(t) \geq 0$ and $0 \leq t \leq \Delta t_1$. Otherwise $i'_{d,1}(t) = 0$

where $Z_1 = \sqrt{\left[R_1^2 + (\omega_o L_1)^2\right]}$, R_1 and L_1 being the effective resistance and inductance under these conditions

$$\theta_1 = \tan^{-1}(\omega_o L_1/R_1), \quad T'_1 = L_1/R_1, \quad \beta'' = \alpha - \frac{\pi}{q} + u$$

$I_{o1} =$ final current of the anterior process. Let us also define $I_{o2} = i_1(\Delta t_1)$.

With two elements conducting, the q-phase rectifier comes to be equivalent to circuit c in Fig. 4.3. Further, by means of a Thevenin equivalent circuit across points A and B, circuit B assumes the form of circuit C. Thus, the output current during the interval of commutation Δt_2 is finally obtained as

$$i'_{d,2}(t) = \frac{V}{Z_2} \cos\frac{\pi}{q} \cos(\omega_o t + \alpha - \theta_2) + \left[\frac{E_o}{R_2} + I_{o2} - \frac{V}{Z_2}\cos\frac{\pi}{q}\sin(\alpha - \theta_2)\right] e^{-\frac{t}{T'_2}} - \frac{E_o}{R_2} \tag{4.8}$$

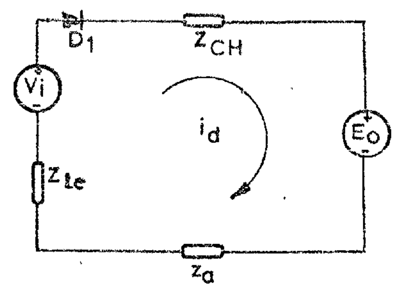

CIRCUIT A

(a) Rectifier equivalent circuit with one valve conducting

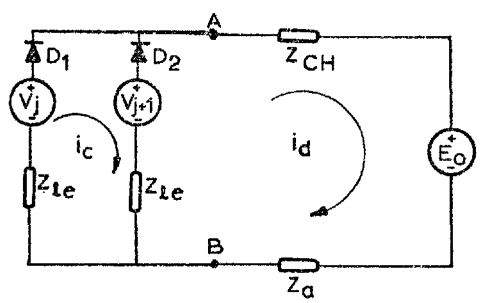

CIRCUIT B

(b) Rectifier equivalent circuit with two valves conducting.

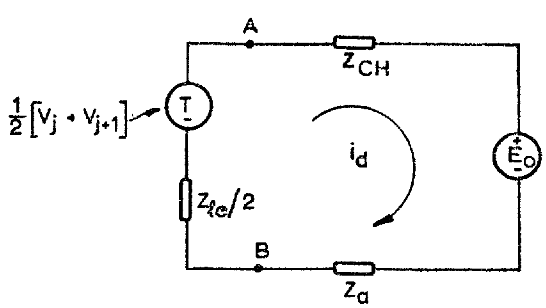

CIRCUIT C

(c) Thevenin equivalent circuit of (b)

Fig. 4.3. Rectifier equivalent circuit under different modes of operation

for $0 \leq t \leq \Delta t_2$. Otherwise $i_{d,2}(t) = 0$. Also for the case $I_{o2} = 0$, $i_2(t) = 0$.

where $Z_2 = \sqrt{\left[R_2^2 + (\omega_o L_2)^2\right]}$, R_2 and L_2 being the effective resistance and inductance under these conditions.

$$\theta_2 = \tan^{-1}(\omega_o L_2/R_2), \quad T_2' = L_2/R_2$$

Let us now define $I_{o1} = i_{d,2}(\Delta t_2)$

The interval Δt_1 is dependent on the transfer function G(s) and on the nature of the pulse generator.

From Fig. 4.1

$$v_c(t) = h(t) * \mathcal{L}^{-1}(G(s)) \tag{4.9}$$

The function h(t) is a piece-wise continuous function with discontinuities in the first derivative at the transition instants when the one element or two element process finishes.

If G(s) can be expressed as a rational function of s the function $v_c(t)$ can be determined explicitly. For the present investigation it is assumed that

$$G(s) = \frac{K}{1 + sT_1} \tag{4.10}$$

In the rectifier circuit depicted in Fig. 4.1, both the current sensor and the amplifier have their outputs constrained within an upper and lower limit. The system under discussion can operate in certain cases with very large gains, as a consequence, the ripple content of the rectifier output current is greatly amplified and under these conditions the limiters have a marked influence in the system transient behaviour. Hence, in the rigorous mathematical model, constraints are imposed upon the variations of the current sensor and the amplifier outputs. Incidentally, in certain cases, before the stability boundary of the real system is reached, a limit in the maximum gain is imposed owing to scaling difficulties in the amplifier circuitry and to system noise.

The pulses firing the rectifier elements can be retarded or advanced with respect to the a.c. voltages through the action of the control voltage v_c. There are several ways of generating pulses synchronized to the supply frequency. In the method considered here, $v_c(t)$ is compared to a ramp reference $v_r(t)$, a pulse being generated when the two signals are equal. If the response of the system to a perturbation is to be analysed, the firing instants are determined through the successive solution of the following equation

$$v_r^j(t_j) = v_c(t_j) \tag{4.11}$$

where t_j is the instant at which element j is fired and Δt_1 is linearly related to t_j.

The ramp reference signals are initiated at the instants at which the a.c. phase voltages e_j and e_{j-1} are equal. Equation 4.11 may be solved by means of a Newton-

-Raphson iterative procedure. Provided the initial conditions are judiciously chosen, five to six iterations are sufficient for convergence.

At the firing of an element, the two element process takes over from the one element process. The time duration of the two elements conduction is determined by the time required for the current of the outgoing element to reach zero. This current consists of $i_2(t)$ of eqn. 4.8 plus the commutating current given by

$$i_c(t) = -\frac{2V}{Z_3}\sin\frac{\pi}{2q}\sin(\omega_o t+\alpha-\theta_3)+\left[\frac{I_o 2}{2}+\frac{2V}{Z_3}\sin\frac{\pi}{2q}\sin(\alpha-\theta)\right]e^{-t/T_3} \tag{4.12}$$

where $Z_3 = \sqrt{\left[R_{1e}^2 + (\omega_o L_{1e})^2\right]}$, R_{1e} and L_{1e} being the commutating resistance and inductance

$$\theta_3 = \tan^{-1}(\omega_o L_{1e}/R_{1e}),\quad T_3 = L_{1e}/R_{1e}$$

The interval Δt_2 is obtained from the solution of

$$i_{d,2}(\Delta t_2) + i_c(\Delta t_2) = 0 \tag{4.13}$$

Again a Newton-Raphson iterative procedure can be used, five to six iterations normally resulting in convergence.

4.4 Linear incremental Model of the pulsing unit

The open loop gain of the pulsing system ($\Delta\alpha/\Delta v_c$) is a necessary and sufficient constant for the prediction of behaviour under open loop conditions, due to the harmonic content of v_c, dv_c/dt is different to zero at the instants of firing. Bjäresten[83] was first to introduce the concept of a gain correction factor that considers these harmonics. In this section, the gain correction factor is generalized to include the effect of system resistance and commutation angle at any operating point.

The d.c. gain of the pulsing circuitry is defined in Fig. 4.4a as the ratio $\Delta\alpha/\Delta v_c$ with the rectifier on open loop i.e. with no harmonics present in v_c. In the analysis that follows, this gain is assumed to be unity.

The effective gain of the pulsing circuitry is defined as $\Delta\alpha/\Delta v_c$ with the rectifier operating on closed loop i.e. with harmonics present in v_c. The expression for the gain correction factor can be determined if the behaviour of the pulsing circuitry is studied under perturbed conditions. This is ilustrated in Fig.4.4b where a perturbation in v_c is followed by a change in α. In Fig.4.4c the relevant portion of Fig.4.4b is shown magnified.

For small perturbations, the effective gain can be expressed as the d.c. gain multiplied by a correction factor F^*.

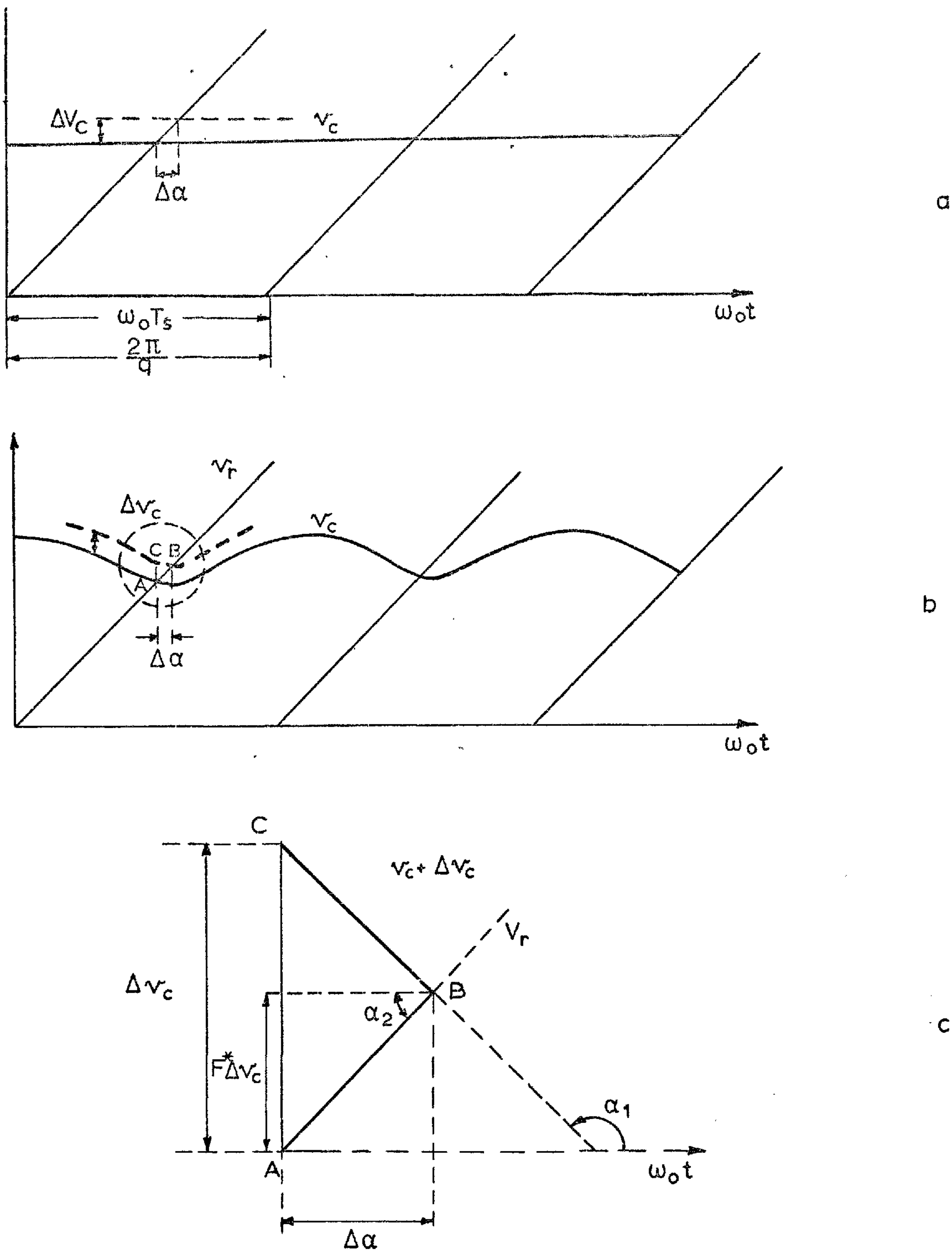

Fig. 4.4. Effect of the ripple on the control voltage

(a) D.C. gain of the pulsing circuitry

(b) Effective gain of the pulsing circuitry

(c) Definition of the correction factor

From Figure 4.4c

$$\tan \alpha_1 = \frac{dv_c}{dt} = -\frac{\Delta v_c - F\Delta v_c}{\Delta\alpha}\,\omega_o$$

$$\tan \alpha_2 = \frac{dv_r}{dt} = \frac{F^*\Delta v_c}{\Delta\alpha}\,\omega_o$$

Solving for F*we get

$$F^* = \lim_{\Delta v_c \to 0} \frac{\Delta\alpha}{\Delta v_c} = \frac{1}{1 - \dfrac{\frac{dv_c}{dt}}{\frac{dv_r}{dt}}} \qquad (4.14)$$

As

$$\frac{d\alpha}{dt} = \omega_o, \qquad (4.15)$$

$$\frac{dv_r}{dt} = \frac{dv_r}{d\alpha}\,\frac{d\alpha}{dt} \qquad \frac{\Delta v_c}{\Delta\alpha}\,\frac{d\alpha}{dt}$$

therefore using equation 4.15

$$\frac{dv_r}{dt} = \omega_o \qquad (4.16)$$

Expressions for the control voltage as a function of time and in a closed form are derived in appendices 7and 8. Introducing dv_c/dt as obtained in appendix 7 and $dv_r/dt = \omega_o$ into equation 4.14 the correction factor is obtained as

$$F^* = \left\{1 - \frac{VK}{R_t}\left[\frac{\sin(\gamma' - \theta - \beta)}{\sqrt{\{1 + (\omega_o T_1)^2\}}\sqrt{\{1 + (\omega_o T_2)^2\}}} - \frac{K_3\,(1 - K_1)}{\omega_o(e^{T_s/T_1} - 1)} - \frac{K_3'(1 - K_1')}{\omega_o(e^{T_s/T_2} - 1)} + \sin\frac{\pi}{q}\left(\frac{K_4(1 - K_2 e^{T_u/T_1})}{\omega_o(e^{T_s/T_1} - 1)} + \frac{K_4'(1 - K_2' e^{T_u/T_2})}{\omega_o(e^{T_s/T_2} - 1)}\right)\right]\right\}^{-1} \qquad (4.17)$$

The various constants in this expression are defined in appendix 7. The overall loop effective gain is now obtained from

$$K_e = K\ F^* \tag{4.18}$$

4.5 Continuous dynamic models

4.5.1 Simple continuous model

If the commutation angle is negligible, the response of the rectifier output in the time domain under open loop conditions and for a step disturbance can be found from equation 4.5 (appendix 7)

$$i_d(t) = \frac{V}{R_L}\ \frac{\sin(m\beta - \theta + \alpha')}{\sqrt{\{1 + (\omega_o T)^2\}}} + \frac{\omega_o T_2 \cos\alpha' - \sin\alpha'}{1 + (\omega_o T_2)^2} \times$$

$$\times\ (1 - K_4\ d(-T_s))\ \frac{e^{-T_s(m-1)/T_2}}{e^{-T_s/T_2} - 1}\ (1 - e^{-T_s n/T_2}) -$$

$$- \frac{E_o}{R_2}\ (1 - e^{-t/T_2}) + I_o\ e^{-t/T_2} \tag{4.19}$$

where $T_2 = R_L/L_L$, and R_L and L_L are the load resistance and inductance respectively. Remaining constants are defined in appendix 7.

Equation 4.19 admits the following structure

$$i_d(t) = I_d - I_d' \, e^{-t/T_2} + r(t) \qquad (4.20)$$

where $r(t)$ is a periodic function and describes the ripple content of the rectifier output current, I_d and I_d' are constants.

Equation 4.20 proves that for a step disturbance and under open loop conditions, even in the presence of ripple, the perturbed behaviour of the rectifier output current is exponential. The process is depicted in Fig.4.5 where the rectifier output current $i_d(t)$ is decomposed in its three components I_d, $I_d' e^{-t/T_2}$ and $r(t)$. This suggests a modelling of the rectifier as a voltage source

$$V_d = (q/\pi)\ V \sin\ (\pi/q)\ \cos\ \alpha = V_{dc}\ \cos\ \alpha$$

feeding the d.c. circuit. The pulsing circuit gain has been lumped with the amplifier transfer function in G (s), therefore the system model under closed loop conditions is as shown in Fig.4.6. With due regard to the simplifying assumptions, this model will predict the transient behaviour of the d.c. component of the output current of the rectifier if the system were stable and slow disturbances were only considered.

4.5.2 Transportation time delay model

In an attempt to account for the sampling nature

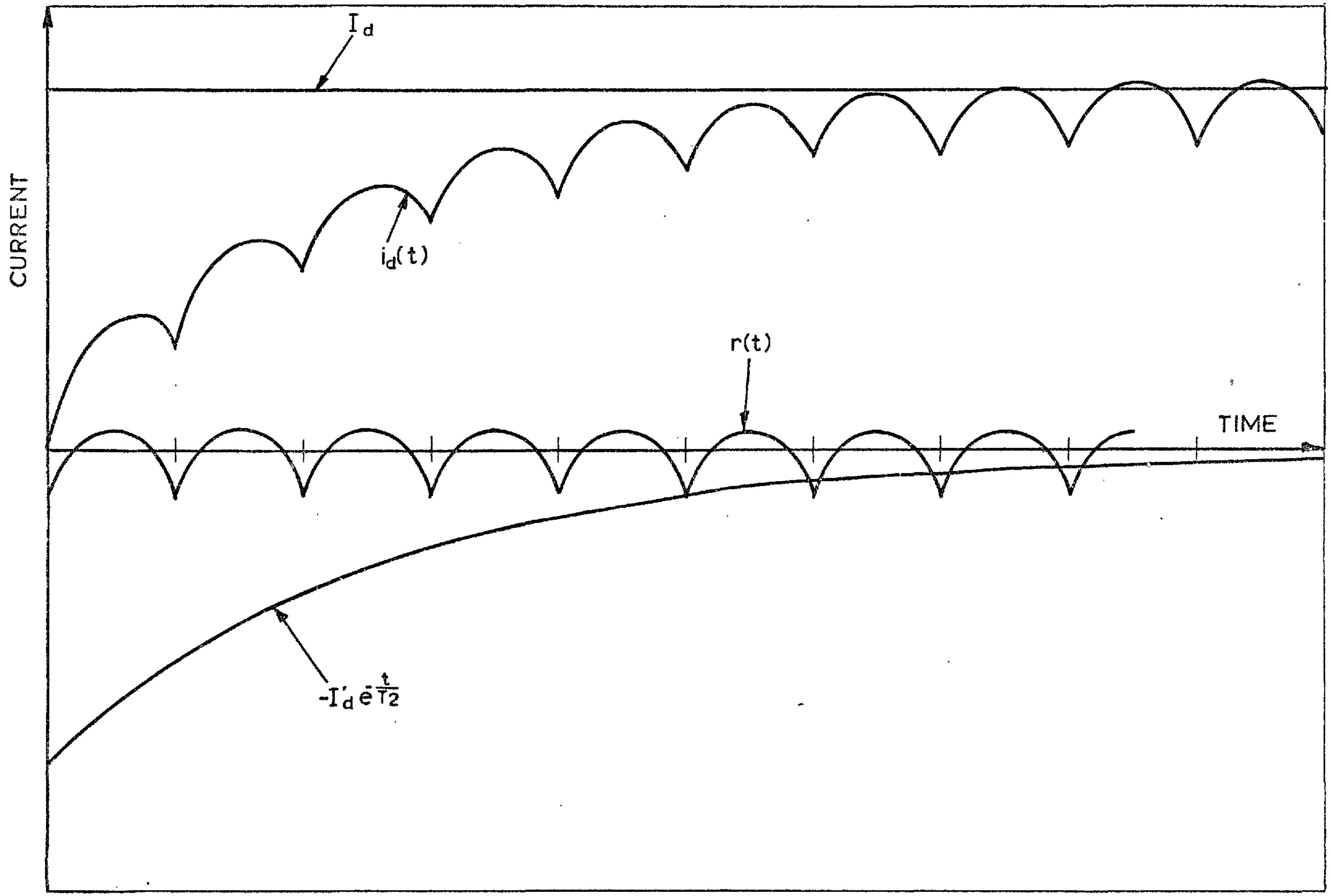

<u>Fig. 4.5. Evolution of the rectifier output current after a step disturbance and under open loop conditions (u=0)</u>

of the rectifier, the inclusion in the loop of a probabilistic transportation time delay has been suggested[88,90]. This is justified by the fact that the rectifier can not be controlled during the interval between two successive firings therefore a statistical transportation time delay equal to $T_s/2$ can be postulated. A linearised model based on this assumption is shown in Fig.4.7.

4.6 Discrete dynamic models

4.6.1 Sample and hold model

The rigorous mathematical model developed earlier results in a system of non-linear difference equations. To determine a linear incremental model which accounts for the sampling nature of the system, the rectifier should be studied under perturbed conditions. In Fig.4.8 a perturbation $\Delta\alpha$ results in an output variation Δv_d. Assuming that $\Delta\alpha \to 0$ and therefore the height of the pulse train is constant the system operates on a pulse width modulation principle.

First Reider[80] and then others[88,89] modelled this behaviour by spreading the area of the train of pulses over the sampling period as shown in Fig.4.8c. The resulting model is shown in Fig.4.9 where the rectifier has been replaced by a sampler followed by a zero order hold with gain $V_{dc} \sin \alpha^o$.

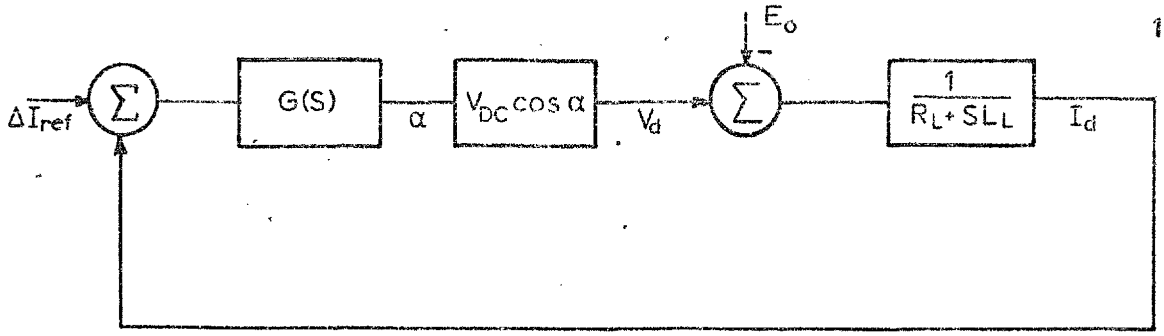

(a) Nonlinear dynamic model

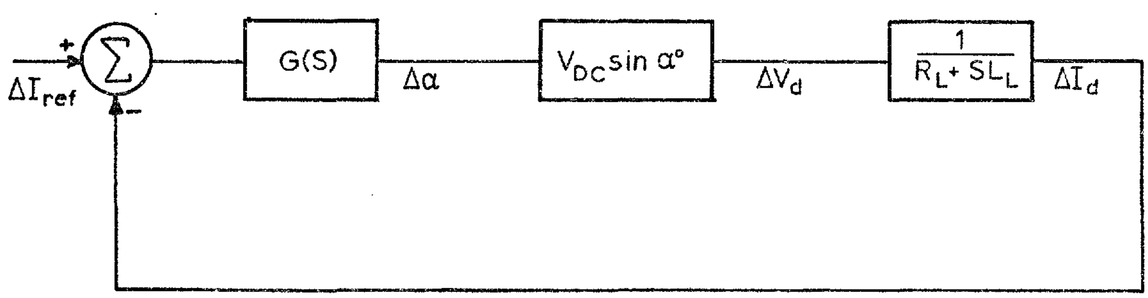

(b) Linearised dynamic model

Fig. 4.6. Continuous dynamic model of a rectifier under current control (u=0)

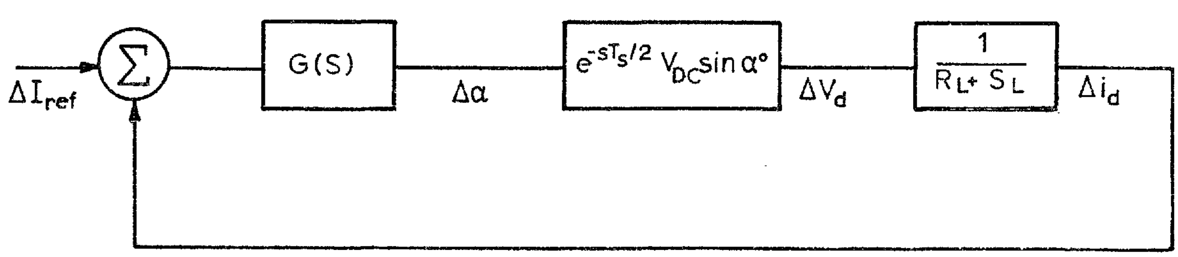

Fig. 4.7 Probalistic transportation time delay model of a rectifier under current control (u=0)

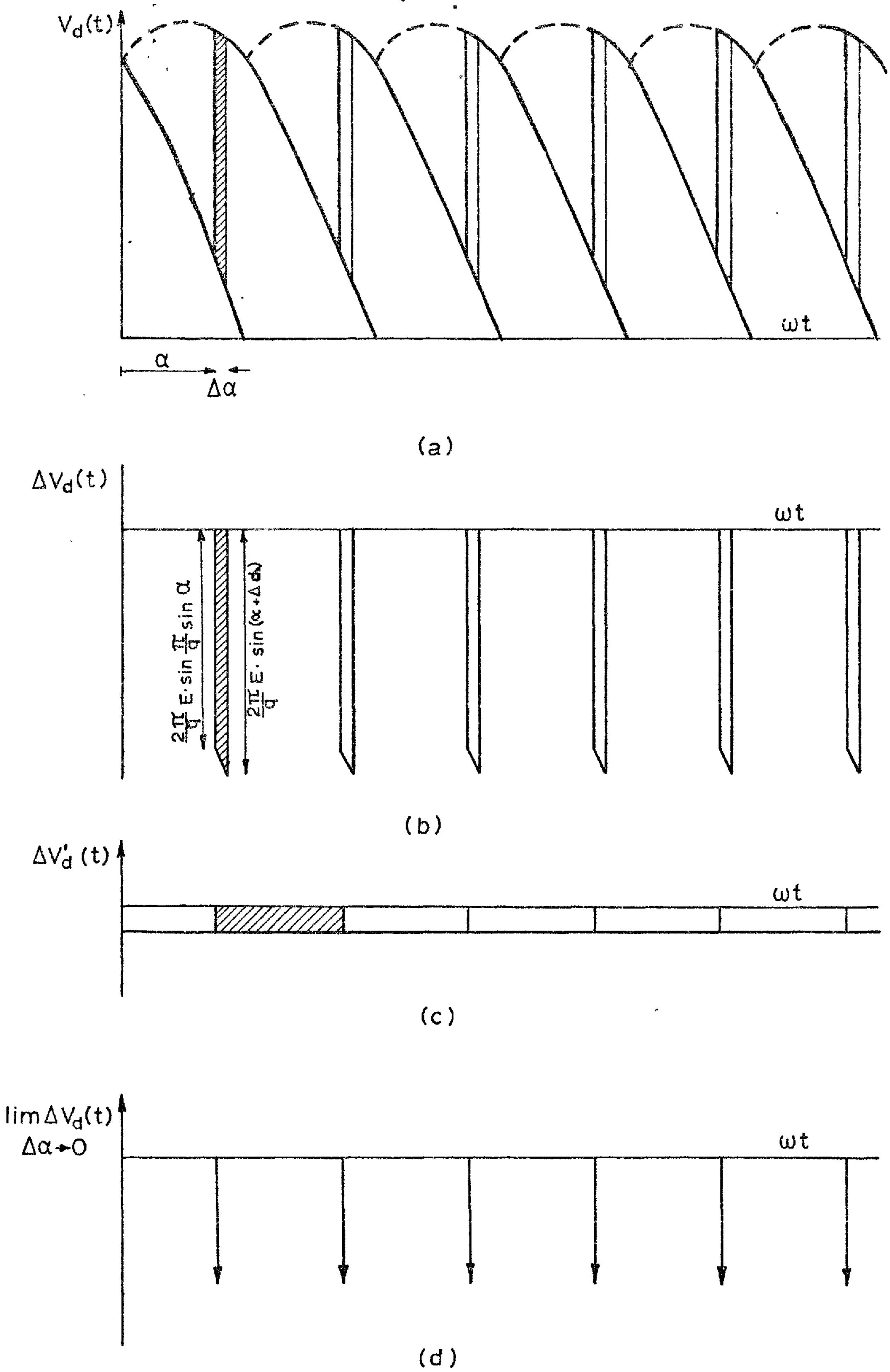

Fig. 4.8. Rectifier output voltage under small perturbations in the firing angle (u=0)

Reider[80] justifies the sample and hold model on the grounds that the evolution of a sampled system would be fully characterized from the knowledge of the state of the system at the sampling instants only, provided that there are no hidden oscillations. On this principle the incremental voltage output can be replaced by another voltage waveform of the same "equivalent area", if the rectifier load is highly inductive.[81,82] The "equivalent areas" principle is derived mathematically as follows.

If the load circuit is purely inductive the rectifier output current satisfies the following law

$$L_L \frac{di_d}{dt} = v_d(t) \tag{4.21}$$

The incremental rectifier output current at the end of the j^{th} sampling period is thus given by

$$\Delta i_d\ (jT_s) = \Delta i_d\ ((j-1)T_s) + \int_{(j-1)T_s}^{jT_s} \frac{\Delta v_d(t)}{L_L}\, dt \tag{4.22}$$

and, therefore

$$\Delta i_d\ (jT_s) = \Delta i_d\ ((j-1)T_s) + (\Delta V_{d,average}) \frac{T_s}{L_L} \tag{4.23}$$

Equation 4.23 proves that, under the simplifying assumptions stated earlier, the incremental output voltage of the rectifier can be replaced by any voltage waveform with the same "equivalent area".

The "equivalent areas" assumption is valid if resistances are neglected and if in a closed loop system, $G_1(s)$ is not frequency dependent. It is of great importance that $v_c(t)$ is of the correct value at the sampling instants and if, therefore, $G_1(s)$ is frequency dependent $v_c(t)$ at these instants is a function not only of the "area" but also of the waveshape of the current. Under these conditions the "equivalent areas" concept breaks down.

Parish et al[88] and Hazel et al[89] advocate the sample and hold modelling of a rectifier on "shape similarity" premises. They argue that the rectifier output voltage depicted in Fig.4.10a is "similar in shape" to the sample and hold output in Fig.4.10b. The modelling of nonlinear discrete systems, by means of steady-state "shape similarity" with a small perturbation model, is valid if, and only if, the system operates on an amplitude modulation principle. As the system operates on a width pulse modulation fashion, the "shape similarity" argument is not valid.

It is interesting to note that the transportation time delay model can be derived from the sample and hold model if the pulse transfer function of the latter is expanded in series and only the first term is considered[88]. This is valid for low-pass systems, both methods therefore yielding the same characteristics for high values of time constant T_1.

4.6.2 The impulse model (u=0)

As mentioned above, as $\Delta\alpha \longrightarrow 0$ the height of the train of pulses $\Delta v_d(t)$ becomes constant and equal to $2\ V \sin\frac{\pi}{q} \sin\alpha^o$. The Laplace transform of one of these pulses is given by

$$\mathcal{L}\,(\Delta v_{d,j}(t)) = -2V\sin\frac{\pi}{q}\sin\alpha^o \frac{1-e^{-\frac{\Delta\alpha}{\omega_o}s}}{s} \qquad (4.24)$$

Expanding $e^{-\frac{\Delta\alpha}{\omega_o}s}$ in Taylor series and finding the limit when $\Delta\alpha \longrightarrow 0$ we get

$$\lim_{\Delta\alpha \longrightarrow 0} \mathcal{L}(\Delta v_{d,j}(t)) = -2V\sin\frac{\pi}{q}\ \sin\alpha^o\ \frac{\Delta\alpha}{\omega_o} \qquad (4.25)$$

Obtaining now the inverse Laplace transform of equation 4.25

$$\lim_{\Delta\alpha \longrightarrow 0} \Delta v_{d,j}(t) = -T_s\ V_{dc}\ \sin\alpha^o\ \delta(t)\ \ \Delta\alpha \qquad (4.26)$$

where $\delta(t)$ = impulse function.

It now follows, that when $\Delta\alpha$ becomes infinitesimal the train of pulses forming the incremental perturbed output of the rectifier assumes the form of the train of impulses shown in Fig. 4.8d of strength $- T_s\ V_{dc}\ \sin\alpha^o\ \Delta\alpha$. As a quasi-steady-state condition is being considered the sampling time is constant. The resulting model is now depicted in Fig. 4.11. This model is a linear sampled data system trully representing the sampling structure of the rectifier

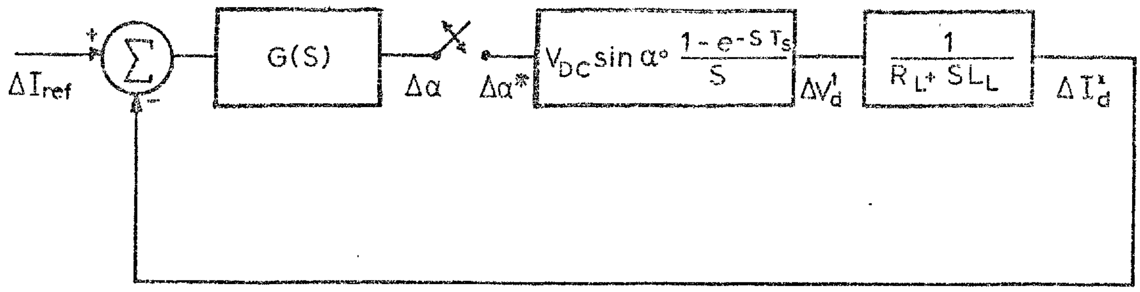

Fig. 4.9. Sampler and hold model of a rectifier under current control (u=0)

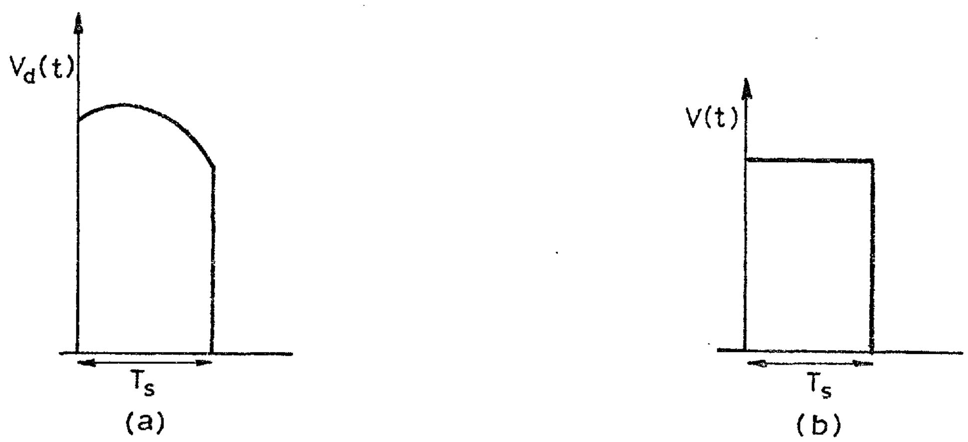

Fig. 4.10. Pulse shapes for (a) the q-phase rectifier (u=0) and (b) the sampler and hold voltage output

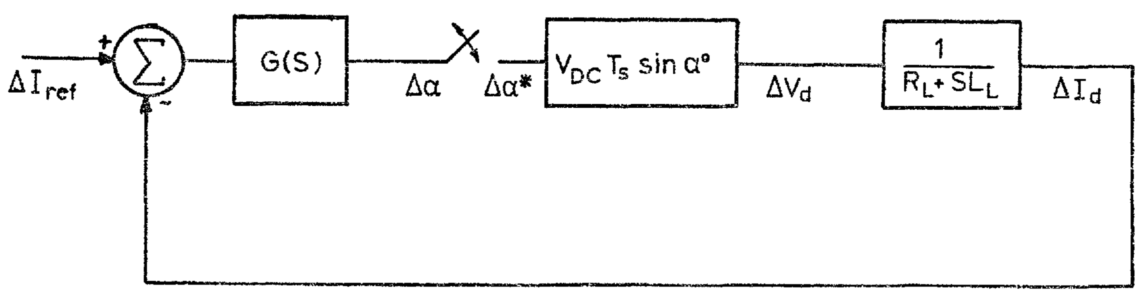

Fig. 4.11. Impulse model of a rectifier under current control (u=0)

when infinitesimal variations in the firing angle are considered and overlap angles are neglected.

4.6.3 The impulse model ($u \neq 0$)

As overlap angles are now considered, the difference between the perturbed output and the unperturbed output voltage of the rectifier is obtained with a finite commutation time as shown in Fig. 4.12. By analogy with the case where no overlap was considered as the width of the train of pulses becomes infinitesimal they can be replaced by impulses of the same area of the original pulses. In this case, however, there are two impulses for each sampling period

$$\Delta v_{d,1}(t) = -\ 1/2\ T_s\ V_{dc}\ \sin\alpha^o\ \delta(t)\ \Delta\alpha$$

$$\Delta v_{d,2}(t) = -\ 1/2\ T_s\ V_{dc}\ \sin\alpha^o\ \delta(t-T_u)\Delta u \qquad (4.27)$$

The strength of the second train of impulses $\Delta v_2(t)$ must be explicitly obtained as a function of both, the increment in the firing angle $\Delta\alpha$ and the increment in the rectifier output current ΔI_d. With the resistances of the commutation circuit neglected, a simplification introducing negligible error if the ratio $\omega_o L_c/R_c$ is high, α and u are related by the well known expression[109]

$$\cos\alpha - \cos(\alpha + u) = \frac{\omega_o L_c}{V\ \sin\pi/q} \qquad (4.28)$$

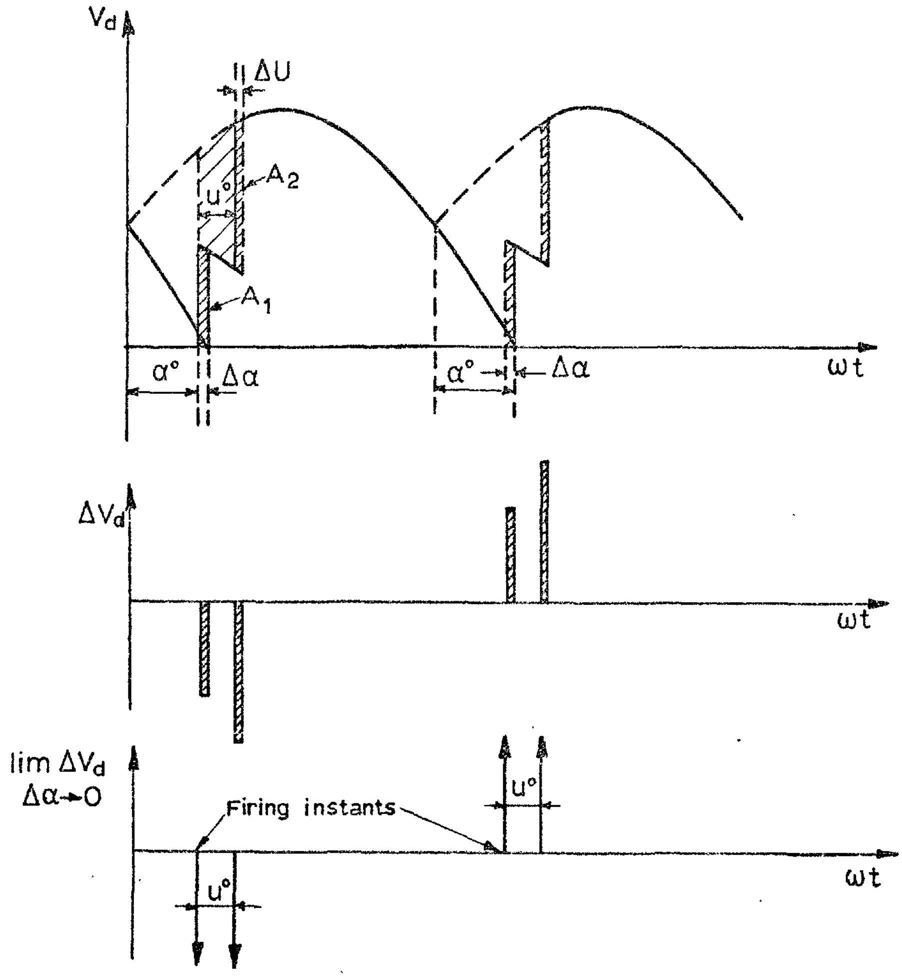

Fig. 4.12. Rectifier output voltage under small perturbations in the firing angle ($U \neq 0$)

Equation 4.28 under perturbed conditions becomes

$$\cos(\alpha^o+\Delta\alpha) - \cos(\alpha^o+u^o+\Delta\alpha+\Delta u) = \frac{\omega_o L_c}{V \sin\pi/q} (I_d^o+\Delta I_d) \quad (4.29)$$

Expanding in Taylor series the nonlinear terms, neglecting high order infinitesimals and subtracting the steady-state components, we get

$$\Delta u = \frac{\sin \alpha^o}{\sin(\alpha^o+u^o)} \Delta\alpha - \frac{\omega_o L_c}{V \sin\pi/q \, \sin(\alpha^o+u^o)} \Delta I_d \quad (4.30)$$

Finally, substituting equation 4.30 into 4.27

$$\Delta v_{d,2}(t) = -1/2 \; T_s \; V_{dc} \; \sin\alpha^o \; \delta(t) \; \Delta\alpha + L_c \; \Delta I_d \; \delta(t-T_u) \quad (4.31)$$

A block diagram of the resulting linearised discrete model of the rectifier is shown in the broken-line box of Fig. 4.13, where

$$G_1(s) = 1/2 \; T_s \; V_{dc} \; \sin\alpha^o \; (1 + e^{-sT_u})$$

$$G_2(s) = \frac{1}{R(1 + sT_2)} \quad (4.32)$$

$$G_3(s) = - L_{1e} \; e^{-sT_u}$$

The model depicted in Fig. 4.13 is based upon eqn. 4.28. As mentioned earlier, this equation neglects the effect of resistances in the commutation circuit. If on the other hand, the effect of these resistances were taken into account, equation 4.12 instead of 4.28 ought to be studied under per-

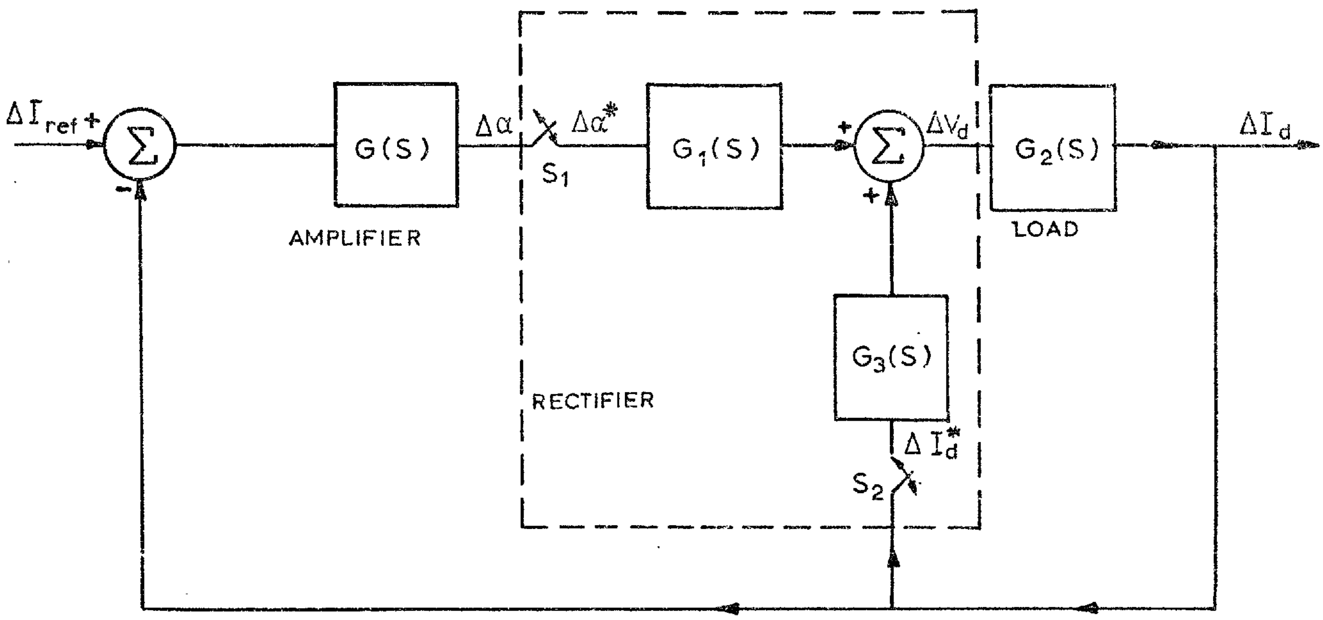

Fig. 4.13. Comprehensive impulse model of rectifier system under current control ($u \neq 0$)

turbed conditions. This would result in a slightly better approximation of the transfer function $G_3(s)$.

4.6.4 Approximate impulse model ($u \neq 0$)

Sucena-Paiva[110] has shown that, as is generally the case, $T_2 \gg T_s$ and $L_c \ll L_L$ and it is possible to a very good approximation to disregard the impulsive nature of the voltage drop due to the commutating reactance and simply to consider this drop as caused by an equivalent resistance

$$R_{eq} = L_c \ / \ T_s = q \ \omega_o \ L_c \ / \ 2\pi \qquad (4.33)$$

The block diagram of this simplified impulse model is shown in Fig. 4.14 where

$$G_3'(s) = \frac{1}{R' + sL} \quad \text{and} \quad R' = R + L_c/T_s \qquad (4.34)$$

It can be shown that the poles and zeros of the models in Figs. 4.13 and 4.14 are very close to each other. Numerical calculation carried out with $L/L_c = 100$ and $T_2/T_s = 50$ have shown that the error in the critical gain (at the onset of instability) predicted by the approximate model amounts to less than 0.5%. In many practical cases in which the assumptions stated at the begining of this sub-section are valid, this proposed model is a very acceptable representation.

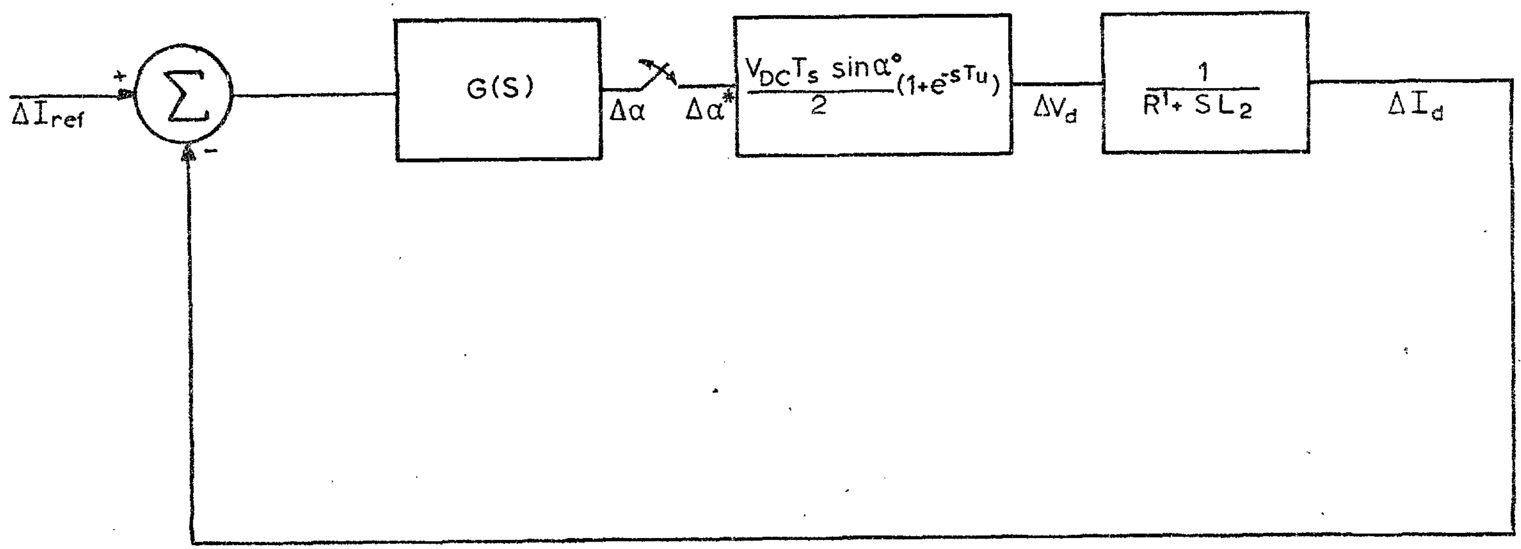

Fig. 4.14. Approximate impulse model of rectifier under current control ($U \neq 0$)

4.7 Step response of models

The performance of the various models to a step change in the feedback amplifier gain is illustrated in Fig. 4.15 for $T_1 = 0$ and negligible commutation angle. The agreement between the rigorous mathematical model and test results is seen to be good. The disturbance occurs at some instant between $t = 0$ and $t = t_a$ and unlike the discrete models, the continuous model responds immediately. The current as represented by the discrete models changes at fixed intervals although as is obvious from the test results the intervals with a noninfinitesimal disturbance are not equal.

The principle of "equivalent areas" is illustrated by the fact that the current predicted by the two discrete models at the end of each interval is approximately equal. However, the stair-case representation of incremental current predicted by the impulse model is closer to the truth than the ramp waveform of the sample and hold model. This is confirmed by Fig. 4.16 where the difference between the perturbed and unperturbed output current of the rectifier is illustrated as derived from the rigorous mathematical model. The case shown is an extreme one where the system has reached a limit cycle of instability at half the sampling frequency.

Figure 4.17 shows the evolution of the rectifier output current as predicted by the rigorous dynamic model after disturbance in the gain of the current feedback loop has occured. The system goes instable at 1/3 of the sampling

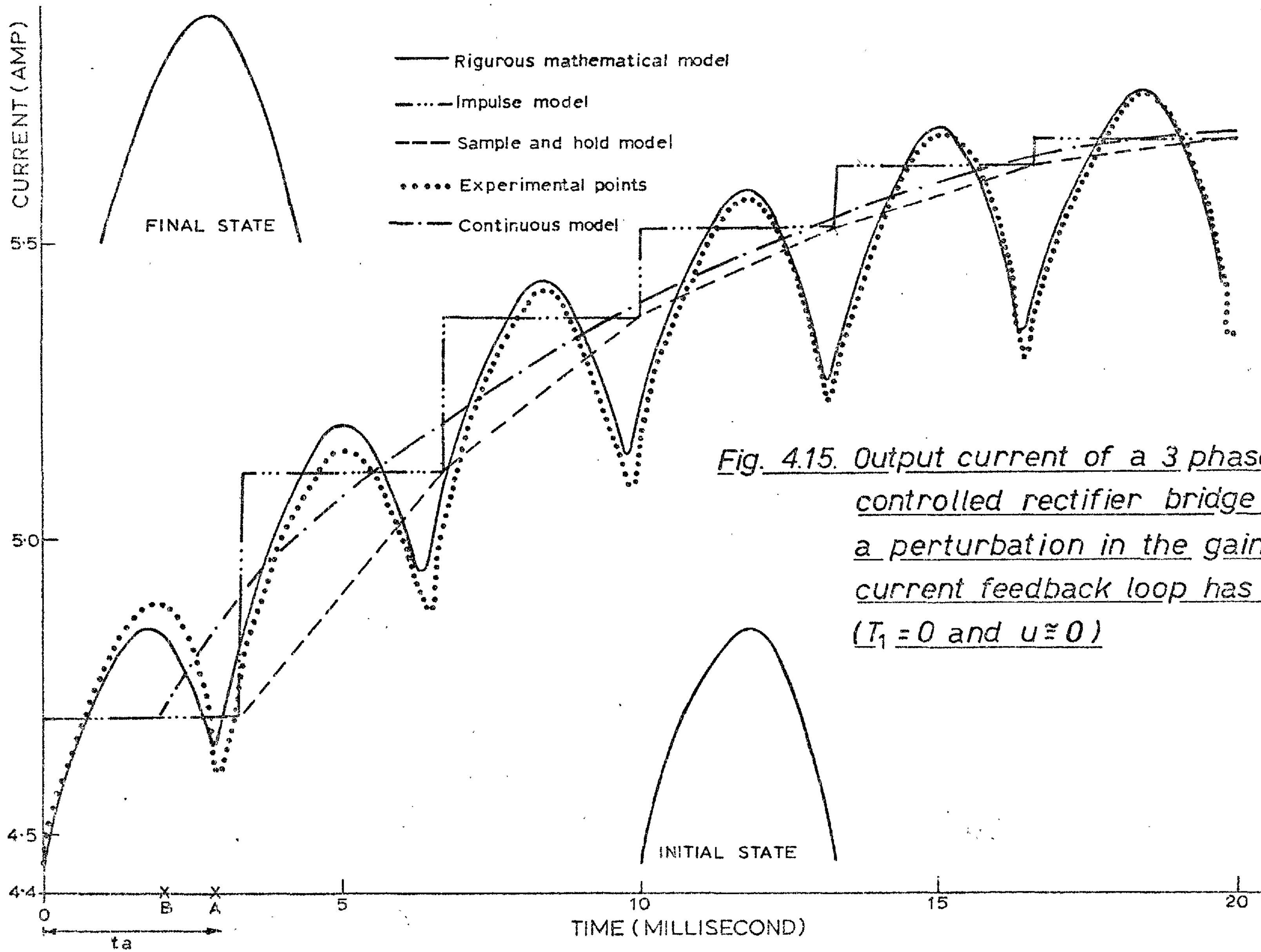

Fig. 4.15. Output current of a 3 phase fully controlled rectifier bridge after a perturbation in the gain K of the current feedback loop has occured. ($T_1 = 0$ and $u \cong 0$)

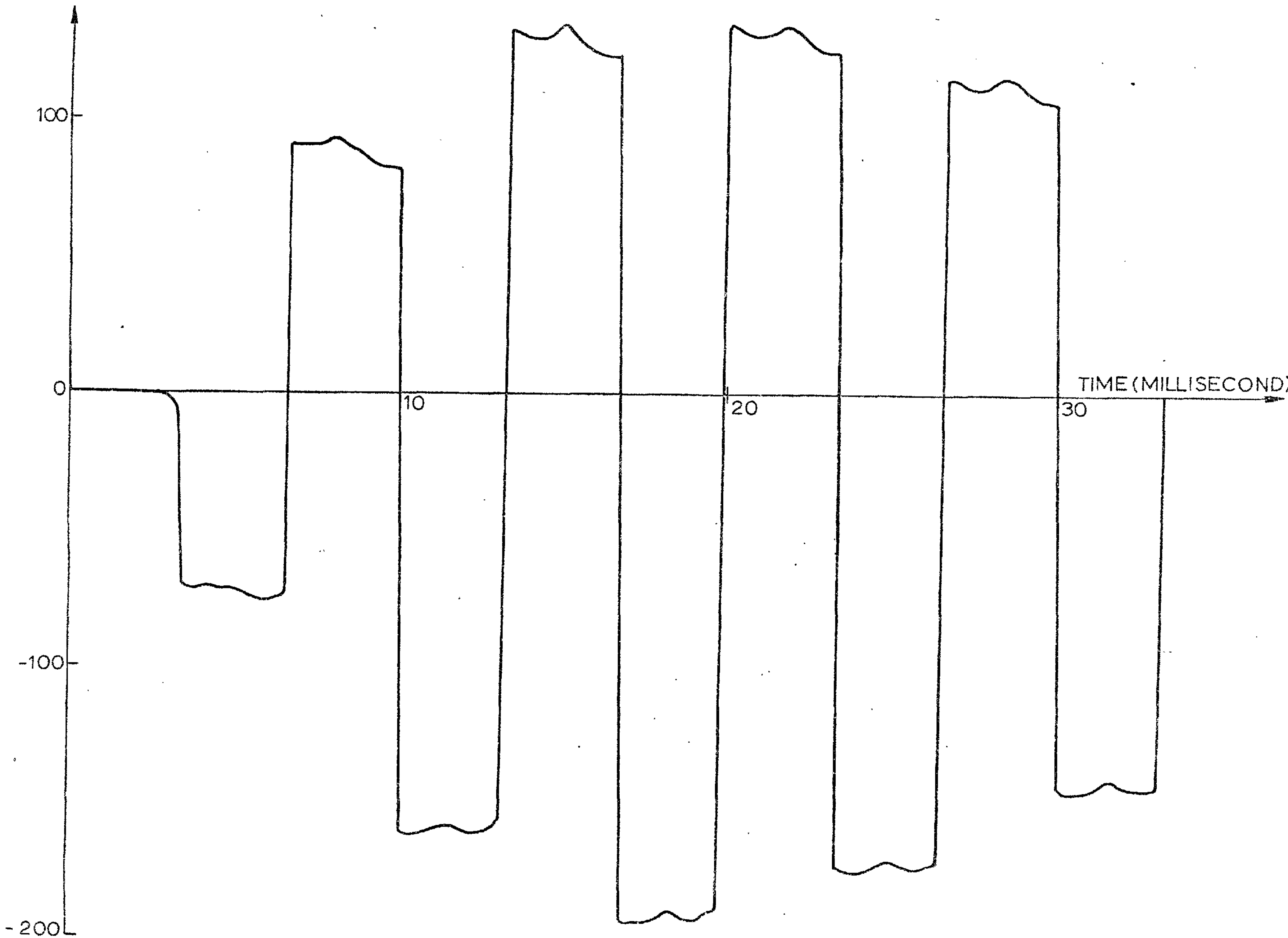

Fig. 4.16. Difference between the perturbed and the unperturbed output current of a rectifier (u ≅ 0)

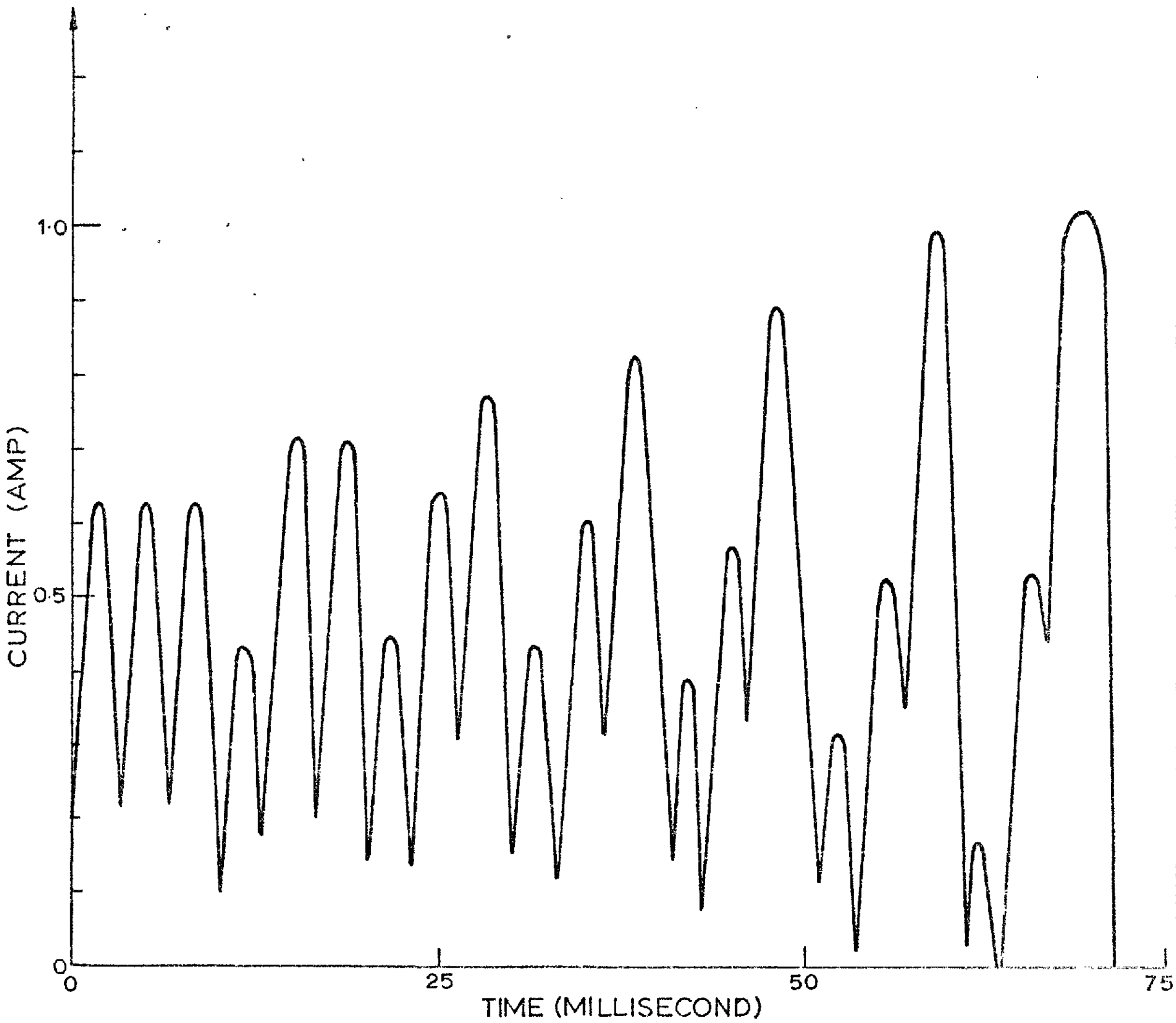

Fig. 4.17 Evolution of the rectifier output current as predicted by the rigorous mathematical model after a step disturbance in the gain K has occured (u ≡ 0)

frequency and instead of forming a limit cycle, the oscillations grow until the thyristor constraint $i_d \geq 0$ is violated. However, as the perturbations are made smaller the system goes unstable at 1/2 of the sampling frequency. Similar results were reported by Bjäresten[83] who modelled the rectifier using analogue techniques. This is in agreement with the impulse model of the rectifier which predicts that the critical frequency of oscillations in this case is 1/2 of the sampling frequency, if small perturbations are involved.

4.8 Stability analysis on small of rectifier systems in the frequency domain

4.8.1 Continuous model

The qualitative Nyquist plot of the simple continuous model of Fig. 4.6b is shown in Fig. 4.18a. This model predicts no instability.

4.8.2 Transportation time delay model

The probabilistic time delay model possesses a Nyquist plot shown in Fig. 4.17b. Analysis of the model using continuous control system theory gives the following critical gain at the first crossover:

$$K_{crit} = \frac{R}{V_{dc}\ \sin\alpha^{o}} \sqrt{\left[(1+\omega_c^2\ T_1^2)(1+\omega_c^2\ T_2^2)\right]} \quad (4.35)$$

where the critical angular frequency is given by

$$\tan^{-1}(\omega_c T_1) + \tan^{-1}(\omega_c T_2) + \frac{1}{2}\omega_c T_s = \pi \qquad (4.36)$$

These results mean that self-oscillations can occur at any frequency less than $\omega_s/2$, a fact that contradicts practical tests and predictions from the impulse model with $u \cong 0$.

4.8.3 Sample and hold model

The sample and hold model of Fig. 4.8 possesses two Nyquist plots depending on whether instability occurs at $\omega_s/2$, Fig. 4.18c, or at less than $\omega_s/2$, Fig. 4.18d. Analysis of the model using sampled-data theory gives the following two critical gains (appendix 9):

$$K_{crit} = \frac{R_L}{V_{dc}\sin\alpha^o} \quad \frac{\exp(T_s/T_1)\exp(T_s/T_2) - 1}{T_1(\exp(T_s/T_1)-1) - T_2(\exp(T_s/T_2)-1)} \qquad (4.37)$$

for instability at less than $\omega_s/2$ and

$$K_{crit} = \frac{R_L}{V_{dc}\sin\alpha^o} \quad \frac{T_2 - T_1}{T_2 \tanh\frac{T_s}{2T_2} - T_1 \tanh\frac{T_s}{2T_1}} \qquad (4.38)$$

for instability at $\omega_s/2$.

4.8.4 Impulse model (u=0)

The impulse model (u=0) shown in Fig. 4.11 possesses a Nyquist plot whose qualitative shape is depicted in Fig. 4.18c. The shape of this Nyquist plot shows that self--oscillations commence at half the sampling frequency. In appendix 10, the critical gain of the system under study with u = 0 is determined by means of z-transform and it is given by

$$K_{crit} = \frac{2R_1(T_2 - T_1)}{V_{dc}T_s \sin\alpha^o(\tanh T_s/2T_2 - \tanh T_s/2T_1)} \qquad (4.39)$$

The critical gain expressions derived by Busemann [79] and Bjäresten [83] are special cases of equation 4.39 for purely inductive load ($T_2 \longrightarrow \infty$)

$$K_{crit} = \frac{2L_1}{V_{dc}T_s \sin\alpha^o \tanh T_s/2T_1} \qquad (4.40)$$

Fallside[84] developed an alternative approach using Fourier transform. Fallside's method, however, has two main disadventages namely, a) it requires the hypothesis of the self-oscillations to be at half the sampling frequency, and b) the critical gain is obtained through a series expansion.

Fallside's series expansion can be added using Laplace transform techniques and it can be shown that it yields equation 4.39.

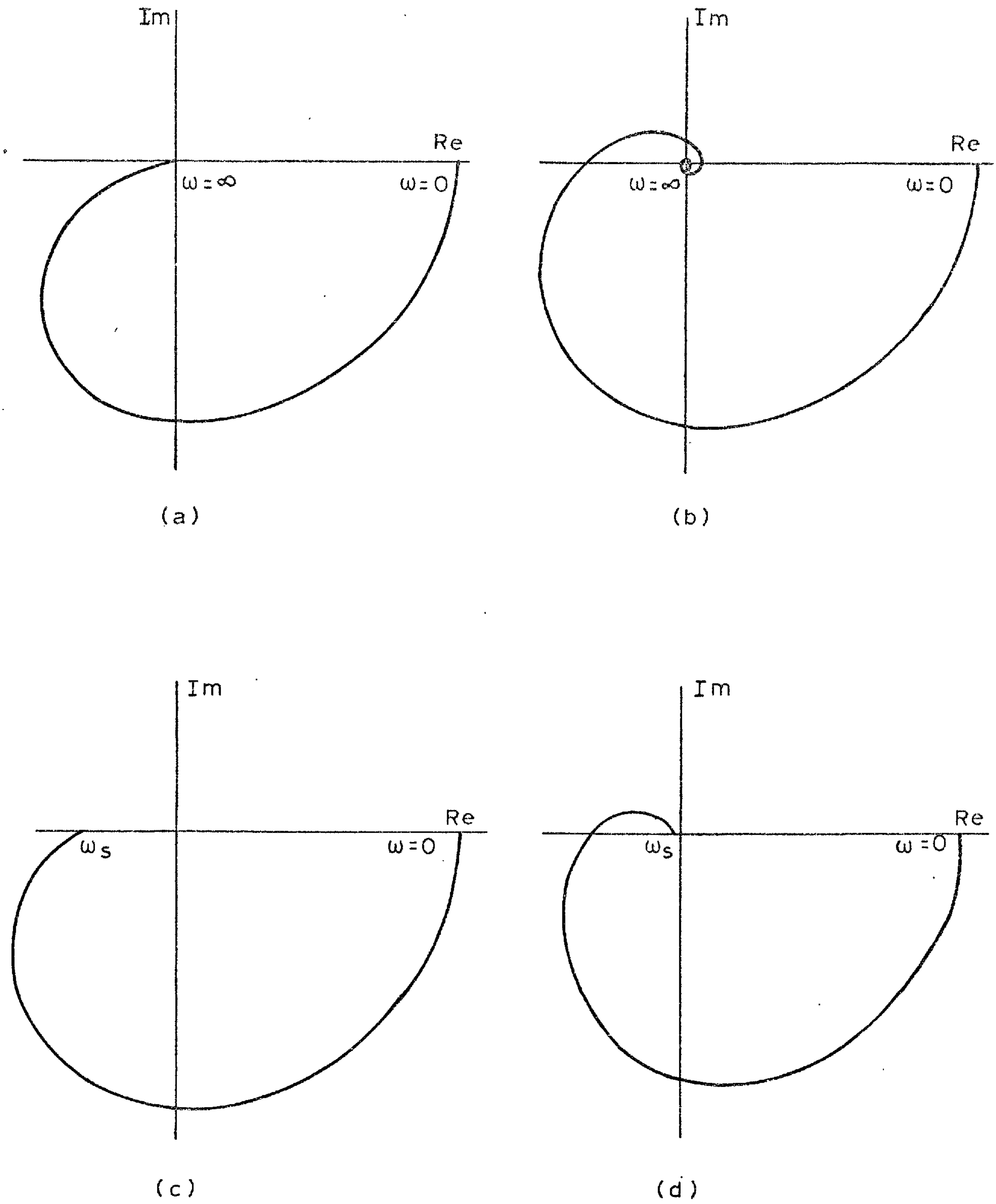

Fig. 4.18. Nyquist diagrams

A so-called "describing function" method was introduced by Fallside[84] by taking only the first harmonic of the series expansion. This gives the following critical gain for oscillations at half the sampling frequency:

$$K_{crit} = \frac{R_1}{V_{dc}\ \sin\alpha^o} \cdot \frac{T_s + \pi^2(T_1+T_2) + (\pi^2 T_1 T_2/T_s)^2}{2(\pi^2 T_1 T_2 - T_s^2)} \qquad (4.41)$$

Sucena-Paiva[110] has generalized this approach by expressing F(z) in an infinite series of s and considering only the first two terms. The Nyquist stability criterion can now be used replacing s by jω. The resulting equation for the critical gain using this method is identical to equation 4.41. This procedure offers a very important advantage, the hypothesis of the frequency of self-oscillations is not necessary.

The so-called "describing function" method rests on the following important a priori assumption: "the self--oscillations, when they take place, are quasi-sinusoidal, i.e. they can be approximated by their first harmonic". It may of course happen that this assumption is not valid.

4.8.5 Impulse model ($u \neq 0$)

The stability analysis of the comprehensive impulse model depicted in Fig. 4.13 is presented in appendix 11. The system admits either of the two different Nyquist diagrams qualitatively shown in Figs. 4.18c and d. Therefore, depending upon the system parameters, instability may occur at, or less than, half the sampling frequency.

Instability at half the sampling frequency occurs at a critical gain given by

$$K_{crit} = \frac{2R(T_2 - T_1)}{V_{dc}T_s\sin\alpha^o \left\{ \left[\dfrac{1 - e^{-\frac{T_s - T_u}{T_1}}}{1 + e^{-\frac{T_s}{T_1}}} - \dfrac{1 - e^{-\frac{T_s - T_u}{T_2}}}{1 + e^{-\frac{T_s}{T_2}}} \right] - \left[\dfrac{e^{-\frac{T_s - T_u}{T_1}}}{1+e^{-\frac{T_s}{T_1}}} - \dfrac{e^{-\frac{T_s - T_u}{T_2}}}{1+e^{-\frac{T_s}{T_2}}} \right] \left[1 - \dfrac{1 - \frac{L_c}{L_1}\left(1 + e^{\frac{T_s}{T_1}}\right)^{-1}}{1 - \frac{L_c}{L_1} e^{-\frac{T_s - T_u}{T_1}} \left(1 + e^{-\frac{T_s}{T_1}}\right)^{-1}} \right] \right\}} \qquad (4.42)$$

In most practical cases $L_c \ll L_1$, $T_s \ll T_2$ and, to a good approximation

$$K_{crit} = \frac{2R\ (T_2 - T_1)}{V_{dc}T_s\sin\alpha^o \left\{ \dfrac{1 - e^{-\frac{T_s - T_u}{T_1}}}{1 + e^{-\frac{T_s}{T_1}}} - \dfrac{1 - e^{-\frac{T_s - T_u}{T_2}}}{1 + e^{-\frac{T_u}{T_2}}} \right\}} \qquad (4.43)$$

Furthermore, if $T_2 \ll T_s$, the resistance in the load circuit may be neglected without incuring any significant error, therefore,

$$K_{crit} = \frac{2L_1}{V_{dc}T_s \sin\alpha^o \dfrac{1 - e^{-\frac{T_s - T_u}{T_1}}}{1 - e^{-\frac{T_s}{T_1}}}} \qquad (4.44)$$

Instability at frequencies less than the sampling frequency occurs at a critical gain given by

$$K_{crit} = \frac{2(T_1 - T_2)\ R}{V_{dc}T_s \sin\alpha^o} \; \frac{1 - e^{-\frac{T_s}{T_2}} \left(e^{-\frac{T_s}{T_1}} - (L_c/L_1)\ e^{-\frac{T_s - T_u}{T_1}} \right)}{e^{-\frac{T_s - T_u}{T_2}}\ e^{-\frac{T_s}{T_1}} - e^{-\frac{T_s - T_u}{T_2}}\ e^{-\frac{T_s}{T_2}}}$$

(4.45)

For given values of the parameters two critical gain values will be obtained from equations 4.42 and 4.45. The smallest of the two will define a point on the stability boundary.

4.8.6 Approximate impulse model ($u \neq 0$)

The Nyquist diagram of the approximate impulse model is very similar to the Nyquist plot of the comprehensive impulse model. Sucena-Paiva[110] has shown, using z-transform theory, that the critical gain for instability, at half the sampling frequency and less than half the sampling frequency is given respectively by

$$K_{crit} = \frac{2R'\,(T_2'-T_1)}{V_{dc}T_s\,\sin\alpha^o}\;\frac{1}{\dfrac{1-e^{-\frac{T_s-T_u}{T_1}}}{1+e^{-\frac{T_s}{T_1}}}-\dfrac{1-e^{-\frac{T_s-T_u}{T_2'}}}{1+e^{-\frac{T_s}{T_2'}}}}$$

$$K_{crit} = \frac{2R'\,(T_2'-T_1)}{V_{dc}T_s\,\sin\alpha^o}\;\frac{e^{-\frac{T_s}{T_1}}\,e^{-\frac{T_s}{T_2'}}-1}{e^{-\frac{T_u}{T_1}}-e^{-\frac{T_u}{T_2'}}} \qquad (4.46)$$

4.9 The convertor transfer function

In section 4.6 it was shown that under quasi-steady-state conditions a rectifier admits a linear sampled data system equivalent.

Hence it is possible to define a pulse transfer function for a convertor, this being the ratio of the sampled output to the sampled input into the system. Clearly it is not possible to measure the pulse transfer function using a conventional transfer function analyser. The analyser will correlate the output to the fundamental harmonic of the input without an indication of the output harmonics.

The transfer function of a linear sampled data system measured with a transfer function analyser requires special interpretation owing to the harmonics generated in the sampler. This measurement will become increasingly difficult in the region $\omega_s/3 < \omega < \omega_s/2$ due to the presence of the

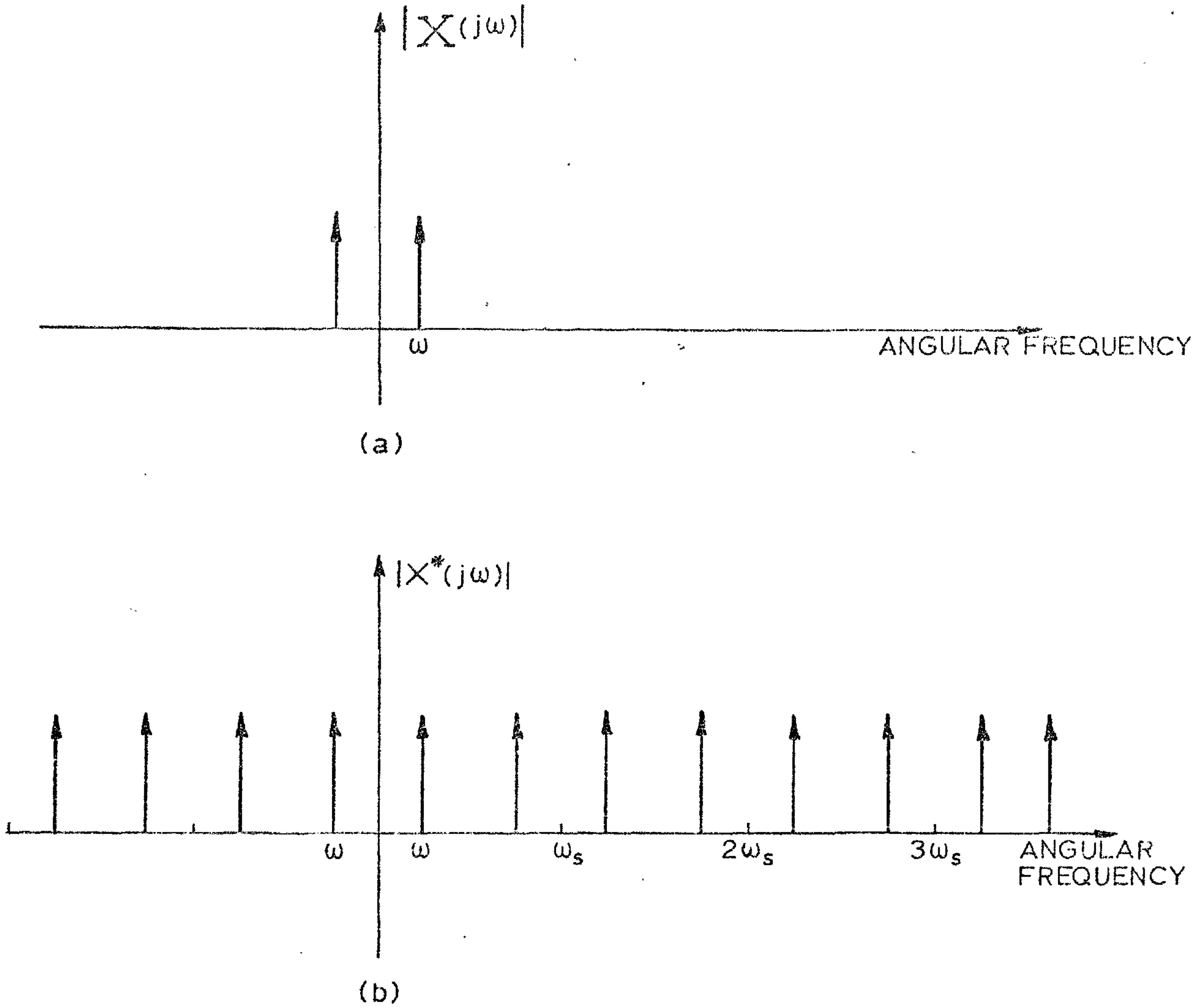

Fig. 4.19. Frequency spectrum of a sinusoidal waveform ($X(t) = \sin wt$)

(a) no sampled signal, $x(t)$

(b) sampled case, $x^*(t)$

lower side-band $\omega_s - \omega$ in fig. 4.19.[111] At $\omega = \omega_s/2$ the side band coincides with the signal frequency and the measured transfer function depends on the phase of the input signal, the transfer function locus at this frequency describing a closed path.

Fig. 4.20 shows a comparison between the calculated transfer function and experimental points determined by a transfer function analyser for small conditions.

The rectifier can be simulated by a pure linear sampled data system only for infinitesimal perturbations. If the disturbance signal is non-infinitesimal, oscillations will occur at other subharmonic frequencies given by qf/2n and not predicted by the small signal models of this chapter.

In general, all oscillations at $\omega_s/2n$ where n is any integer greater than one, produce a fixed "phase" between the harmonic $\omega_s/2n$ of v_c and the ramp waveform v_r of frequency ω_s. As a consequence, a 2π phase shift of the $\omega_s/2n$ disturbance will result in a closed locus for the rectifier transfer function at this frequency.

Assymmetries in the supply voltages and the firing circuitry will accentuate the subharmonic oscillation phenomena. As the system is highly non-linear subharmonic loci will depend on the amplitude of the disturbance signals.

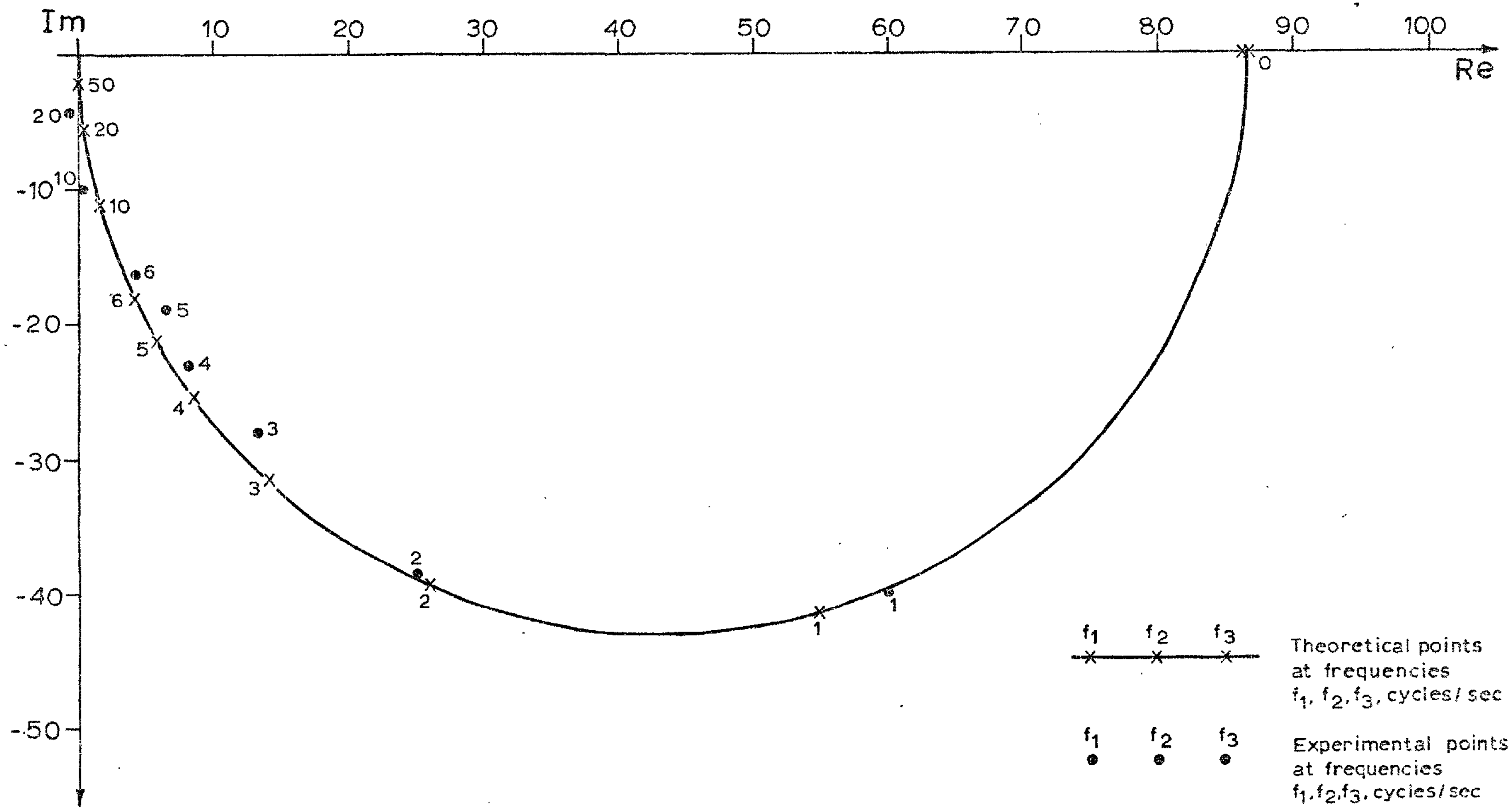

Fig. 4.20. Rectifier transfer function as measured with a conventional transfer function analyser, $u \cong 0$ (low frequency region)

Figure 4.21 shows measurements of the two most important subharmonic loci of the system under discussion carried out with a transfer function analyser for small signal conditions. The relatively large sizes of these subharmonic locies emphasize the importance of subharmonic dynamic characteristics.

System assymetries are manifested particularly at 150 Hz (half the sampling frequency) and at 50 Hz and hence the twisted shape of the transfer function measurements when the locus passes near these two frequencies.

Large signal subharmonic oscillations were studied in reference 84 using an approximate approach based on describing function techniques.

4.10 Comparison of performance of various models with experimental results

A comparison between the models developed in this chapter and other models suggested in the literature was made with the three-phase bridge rectifier supplying the d.c. machine driving the microgenerator connected to a three-phase a.c. infinite busbar. The d.c. motor was working with constant excitation and a feedback loop was enforcing constant armature current.

In fig. 4.22 the stability boundaries for $u = 0$ as

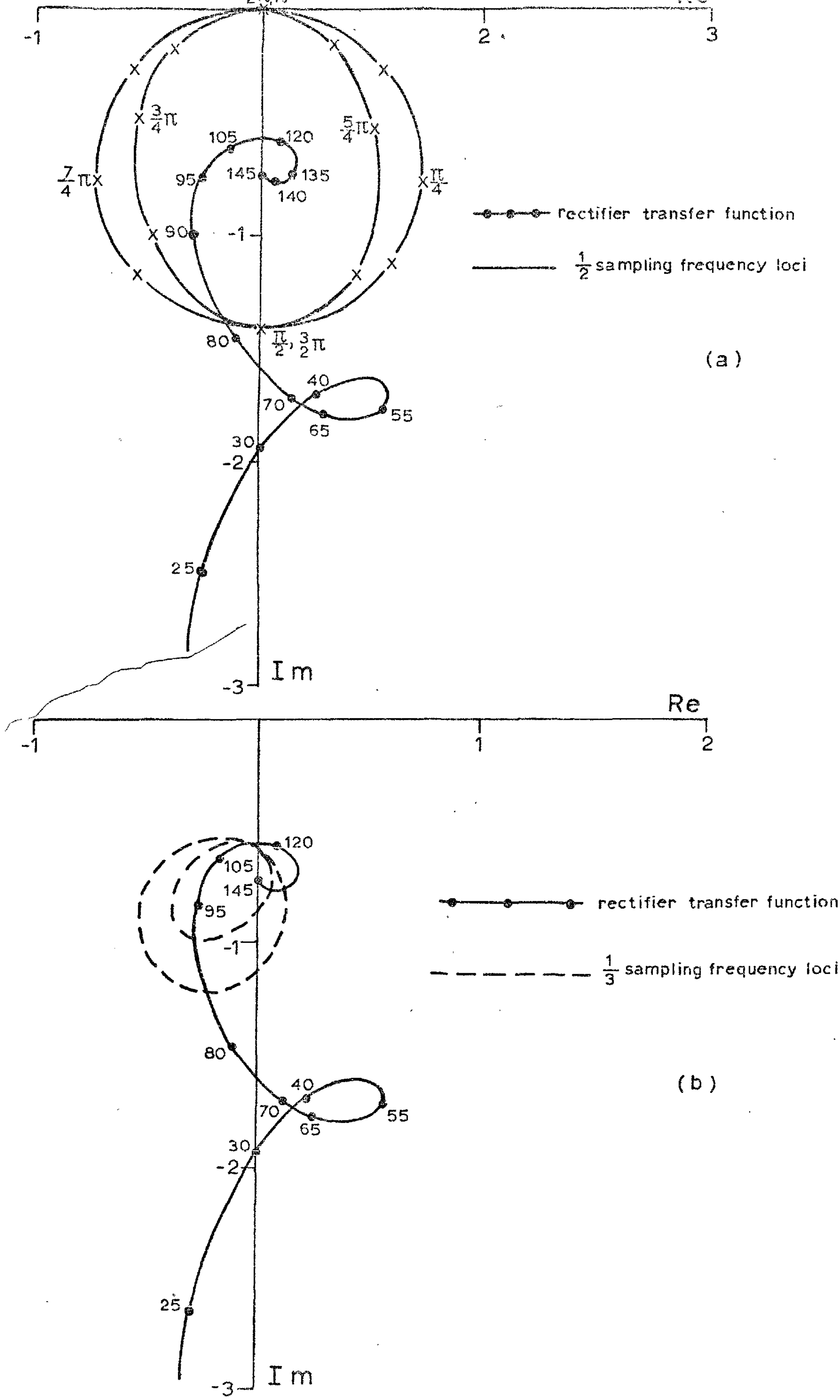

Fig. 4.21. Rectifier transfer function as measured with a transfer function analyser, $u \simeq 0$ (high frequency region)

(a) $\frac{1}{2}$ sampling frequency loci (b) $\frac{1}{3}$ sampling frequency loci predicted by different models are compared to experimental results under negligible commutation angle conditions. The boundary is a plot of time constant T_1 against the critical gain. Points on the left of the boundary are stable.

Curve 1 presents the results with the rectifier modelled as a pure transportation lag of half the sampling time in a continuous control loop. Curve 2 results from the sample-and-hold model of reference 7. Curve 3 uses equation 4.42. To view the models of curve 1 and 2 in the most favourable light in comparison with the models developed in this chapter, in all three cases the gain correction factor F^* of equation 4.17 was implemented.

Curve 4 was obtained from Fallside's describing function approximation.[84] As the attraction of this method is its simplicity, the gain correction factor was not used.

Curve 5 was obtained from the rigorous mathematical model described in section 4.3, by means of a digital computer which solved exactly the difference equations of the system. With this programme it was possible to determine whether a particular operating point was stable by applying a small perturbation to the current reference value. This method, which was incidentally very time consuming, showed that for small perturbations, instability occured at half the sampling frequency. It also showed that if the perturbations were large, the system could become instable at other subharmonics of the sampling frequency.

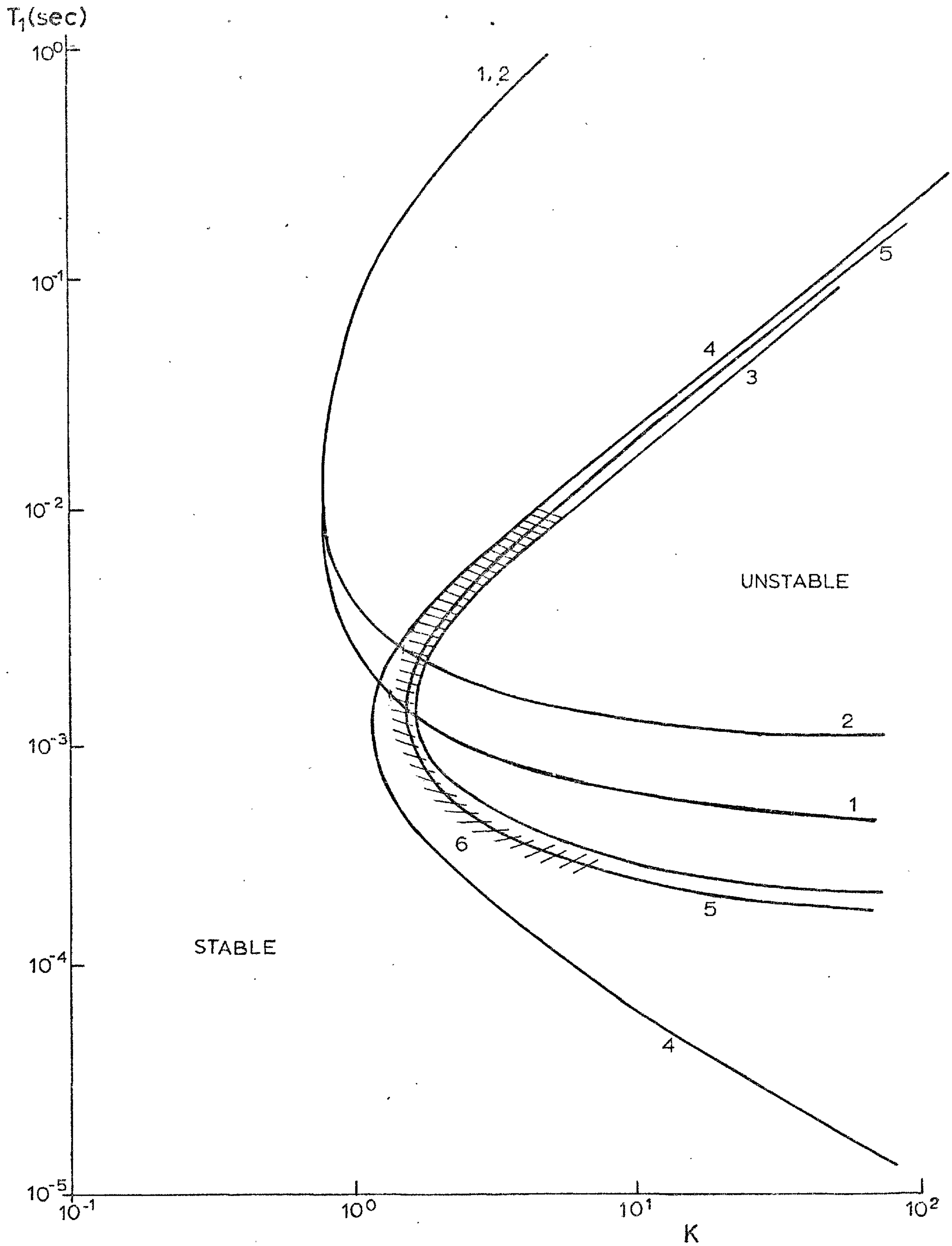

Fig. 4.22. Stability boundaries of a 3-phase bridge rectifier (u=0°)

1. Pure delay model.
2. Sample and hold model.
3. New discrete model.
4. Describing function model.
5. Rigorous mathematical model.
6. Experimental results.

Because of the small uncertainty involved in determining the value of gain at which self-oscillations are sustained, the experimental results are shown in Figure 4.22 as band 6 rather than as a curve.

From figure 4.22 we can conclude that the pure delay model and the sample and hold model, even when improved by the gain correction factor, give unacceptable stability boundaries.

The discrete model developed in this chapter gives results consistent with the rigorous mathematical model and the experimental data, over the whole range of the region explored.

The describing function method gives perfectly acceptable results for large time constants but diverges for low time constants.

With u = 0 and neglecting the gain correction factor, the exact solution gives curve 1 of Figure 4.23. In the describing function method, the effect of neglecting all terms but the first is a fortunate shift of the boundary towards closer proximity with the exact solution corrected for gain, viz. curves 4 and 3 of Figure 4.22.

The influence of the gain correction factor on the stability boundary is shown in Figure 4.23. At low values of T_1, the ripple in the control voltage reduces the effective

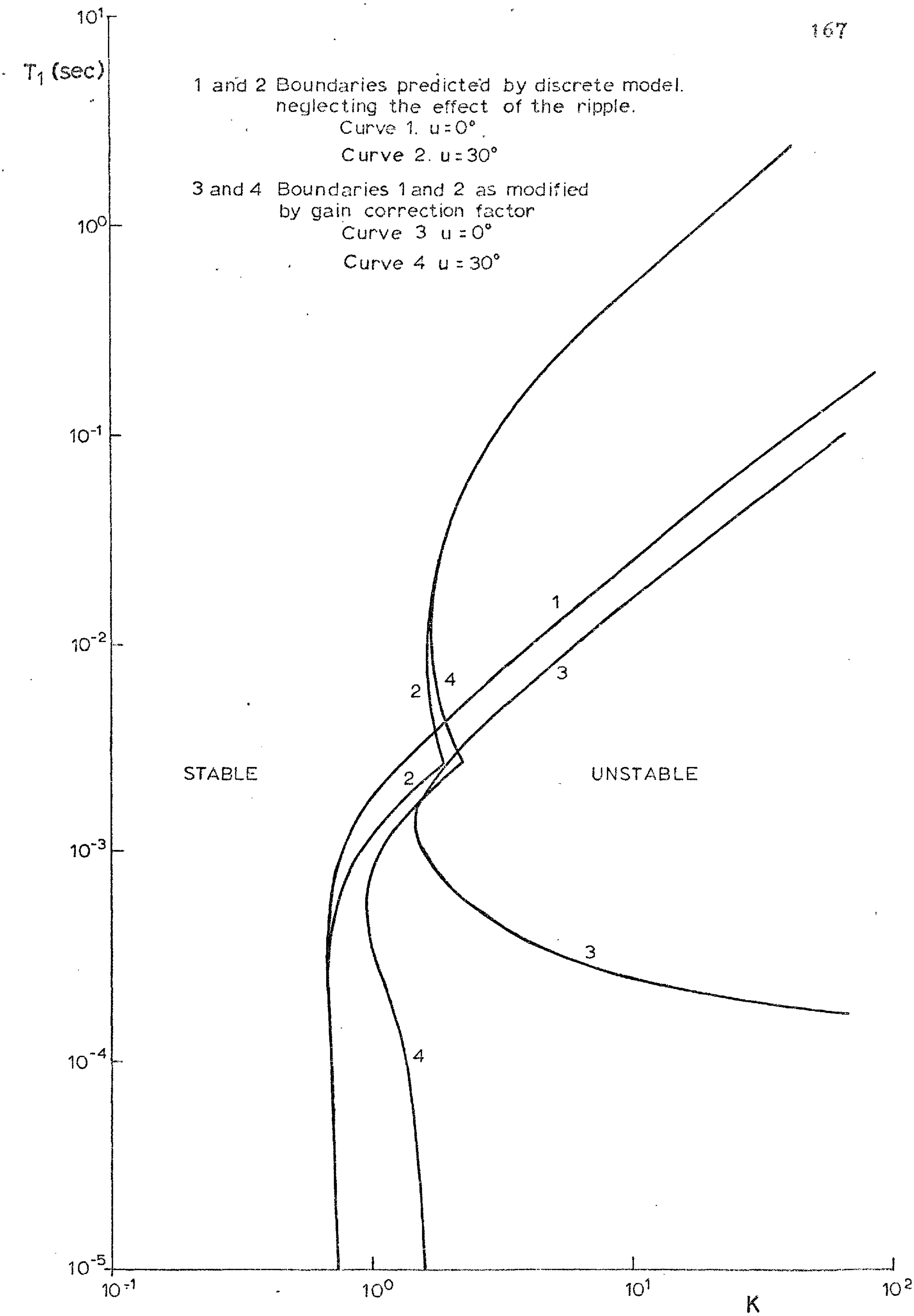

Fig. 4.23. Influence of the ripple on the stability boundary

gain as shown earlier in Fig. 4.3c. This loss of gain increases the region of stable operation under the T_1 - K boundary and the expansion of the stable region becomes more pronounced the nearer u approaches zero.

From Figure 4.23 we can conclude that the gain correction factor has a very marked effect on the boundary especially at small commutation angles and should be taken into account if accuracy is required at low time constants.

The influence of the commutation angle on the stability boundary is illustrated by Figure 4.24. With increase of commutation angle, the stable region contracts. The point of slope discontinuity on the stability boundary is caused by the intersection of the boundaries described by equations 4.42 and 4.45. For points on the stability boundaries of Figure 4.24 located below the discontinuity instability occurs at half the sampling frequency; for points above the discontinuity instability takes place at lower frequencies. The experimental points determined for the case $u = 20^{o}$ show a good agreement with the corresponding theoretical boundary.

Figure 4.24 shows that the effect of commutation is to decrease the region of stability. At high time constants T_1 this decrease is caused by oscillations at frequencies lower than half the sampling frequency. At low time constants the decrease is caused by a different mechanism. The presence of commutation decreases the slope of the control voltage which, in turn, increases the gain-correction factor.

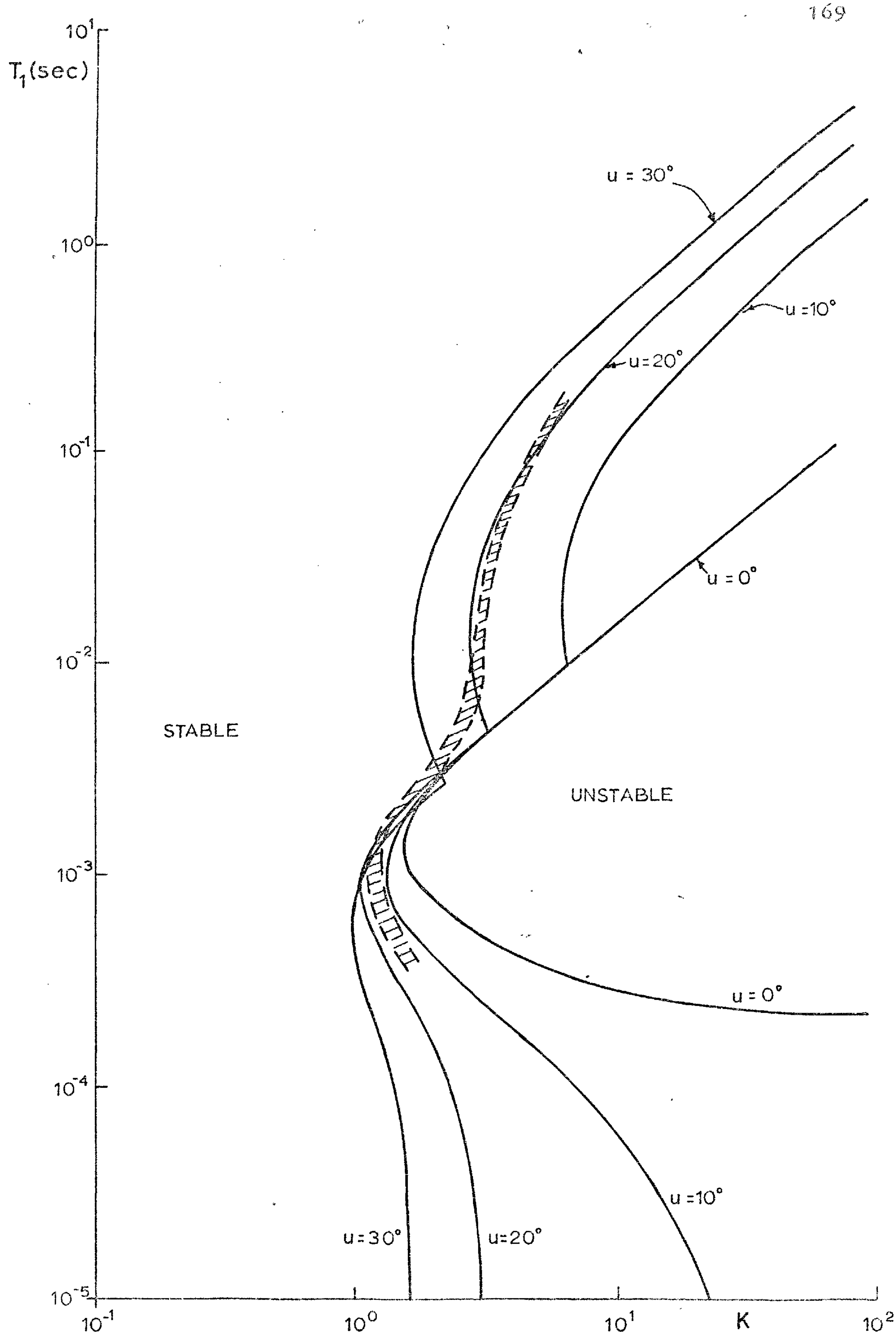

Fig 4.24. Influence of the commutation angle on the stability boundary

For non-infinitesimal disturbances, oscillations at other subharmonics will be experienced even for $u = 0$. These modes of instability have been analysed using approximate methods e.g. describing-function techniques. Alternatively, the rigorous mathematical dynamic model developed in this chapter can be used. In this model a perturbation of varying severity can be imposed. For non-infinitesimal amplitude disturbances the model corroborates the test results of Fig. 4.15. For large amplitude perturbations, limit cycles at other subharmonics were predicted by the model and encountered in practice during tests on a controlled rectifier. These oscillations occur at frequencies given by $qf/2n$ for $u \cong 0$ and at these frequencies as well as at frequencies unrelated to the sampling frequency for $u \neq 0$.

To summarise, the discrete model developed in this chapter enables us to take into account the process of commutation and to apply successfully sample data theory to determine the frequency of self-oscillations and stability boundaries. It is shown that even moderate commutation angles have a marked influence on the stability and frequency of self-oscillation of the system. A generalized gain correction factor is also used to allow for the variation of the loop gain caused by the presence of ripple in the control voltage.

The test results show that the small perturbation model developed in this chapter gives better prediction of stability compared to other techniques for $u \cong 0$ and is the only model known to the author capable of predicting stability boundaries for $u \neq 0$.

CHAPTER 5

RESULT OF SIMULATION STUDIES OF STEAM POWER PLANTS

5.1 General

In this chapter the simulation of a simple non-reheat turbogenerator system is discussed. The evolution of this system after a severe disturbance on the turbogenerator is compared to results from the mathematical modelling of synchronous generators and excitation systems described in chapter 2 and to tests on a real system. A full load rejection of this turbogenerator is used next to corroborate the mathematical modelling of this simple type of turbine and governor system. The analysis of this disturbance validates the assumptions of prime-mover simulation on micromachines.

The simulation is extended to a modern large type of prime-mover and a reheat turbogenerator is then introduced. Full load rejections of this more general form of prime-mover are analysed. More severe disturbances are studied when pole-slipping conditions are considered. As the boiler plays an important part in long term dynamic studies, the restriction of infinite boiler capacity is lifted and the boiler model developed in chapter 2 is incorporated in the simulation.

Finally, the role of governors in power systems is discussed and some methods for improving their dynamic behaviour are suggested in chapter 6.

5.2 Goldington simulation

The Goldington tests[28] were used to corroborate the synchronous generator and excitation system model developed in chapter 2. A 3-phase short circuit of short duration, electrically close to the turbogenerator terminals was employed to test the quality of these mathematical models. A comparison of the load angle oscillations that follow this type of fault in the actual system and a digital computer solution of the mathematical model of the Goldington synchronous machine and exciter is shown in Fig. 5.1. The correlation shown in this figure, within the limitations of the model, gives a good enough indication that a 1st order Cauer expansion of the excitation system transfer function and the simplified synchronous machine modelling of chapter 2 are representative of an actual system. The results compare favourably with other approximate models e.g. reference 25.

The full load rejection test of Goldington power station[28] was next considered for the purpose of validating the quality of the prime-mover simulation.

An analogue simulation was first used to obtain a rough approximation of the real system and then a digital

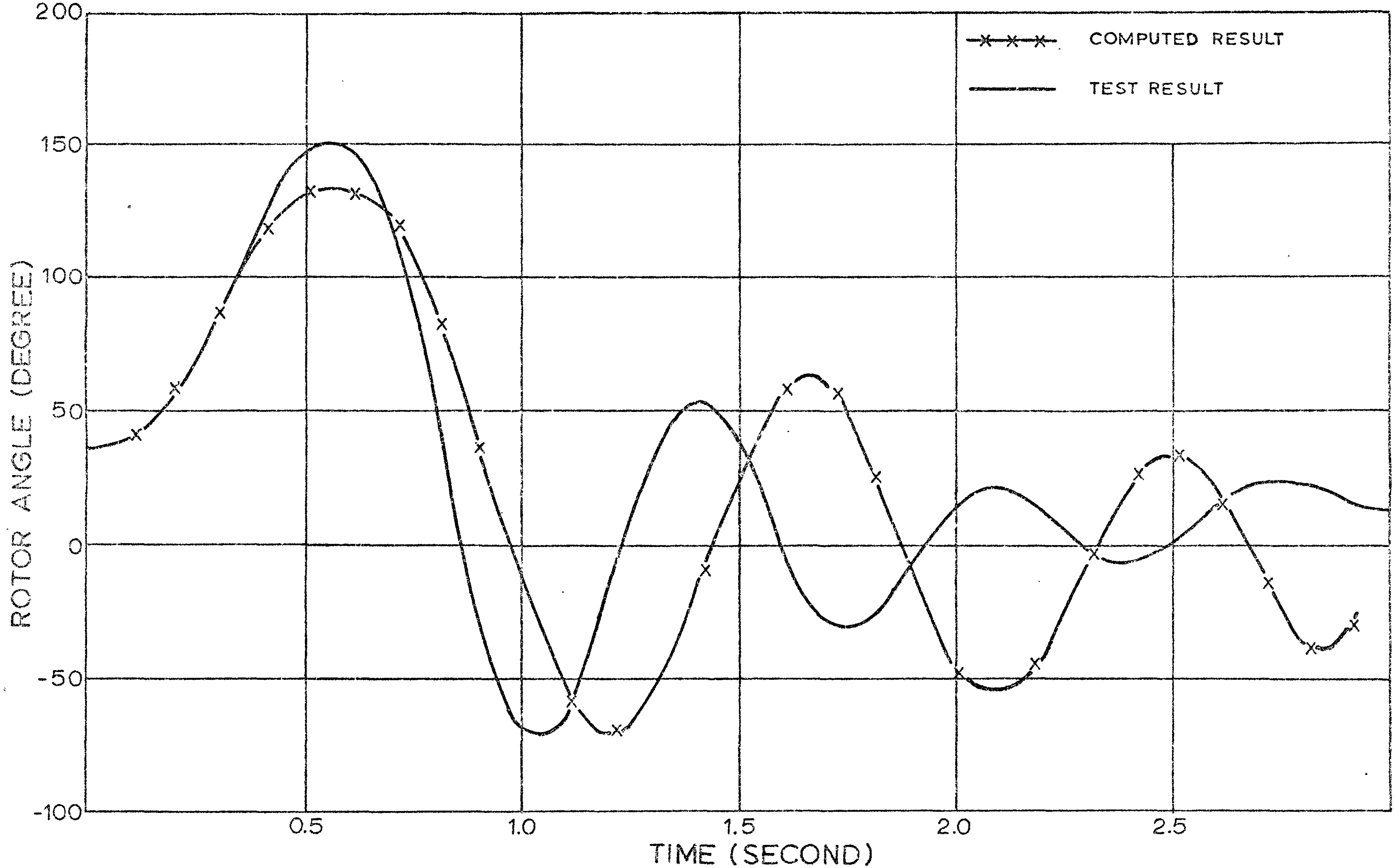

Fig. 5.1. Rotor angle variations after three phase fault has occured (Alternator and AVR constants as given in reference 28.)

representation was employed to improve the accuracy of the parameters in the mathematical model and to carry out a sensitivity study.

The original set of constants of reference 28 were modified so that the same transient response was obtained from the mathematical model as from the original system. In fact, this new set differed little from the original, only the droop and the time lag due to the turbine entrained steam were reduced by 20%.

A sensitivity analysis has shown that small changes in the governor droop, the time constant caused by the entrained steam or the inertia constant of the system are the only constants influencing considerably the transient response of the system. Changes of 25% in all other parameters do not cause significant variations in the evolution of the shaft speed after a full load rejection has taken place.

The evolution of the shaft speed with time, as obtained by the different methods of analysis, is presented in Fig. 5.2 after a full load rejection has taken place.

The Goldington load rejection results show that the turbogenerator shaft overspeeds rapidly just after load has been rejected. The throttle valve is fully closed by governor action at t = .45s. Owing to the entrained steam the shaft reaches its maximum overspeed of 5.85% at

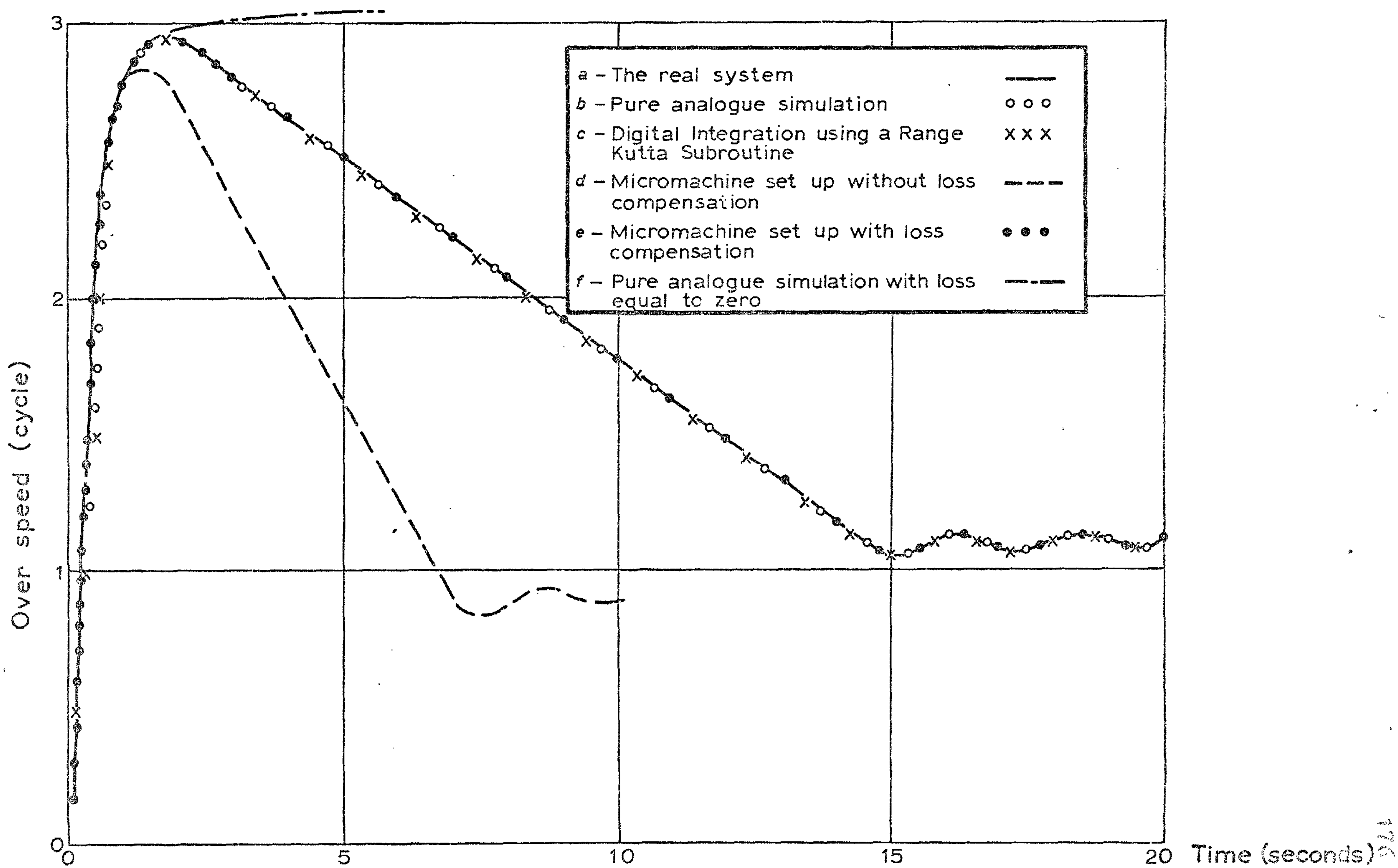

Fig.5.2. Goldington Load Rejection Test

t = 1.8s i.e. some time after the throttle valve has been fully closed. The shaft speed then, under the action of the set losses, slows down with a slope given by

$$\frac{dn}{dt} = \frac{P_{loss}}{H} \qquad (5.1)$$

The machine eventually reaches its final speed given by its governor droop multiplied by the amount of load being rejected. Some oscillations occur before reaching this final overspeed. With the original data of reference 28 these oscillations do not die away but form limit cycles. The analogue simulations shows that if, as depicted in Fig. 5.3, the synchronous machine is represented as an integration, i.e. the model is valid if open circuit operation is considered, the system becomes steady-state unstable. The micromachine and digital simulations confirm this steady-state instability of the system. The eigenvalues of the plant in fact show that the governor and turbine representation form an unstable system. However, if the micromachine is connected to the microreseaux infinite bus bar the generator synchronizing torque stabilizes the system. With the revised set of Goldington parameters the shaft speed reaches a final stable state as $t \longrightarrow \infty$.

Fig. 5.2 also illustrates the effect of the loss term on the shape of this transient. If the loss term is not simulated (curve f), the shaft speed does not slow down and tends to show a larger numerical value for the maximum over-

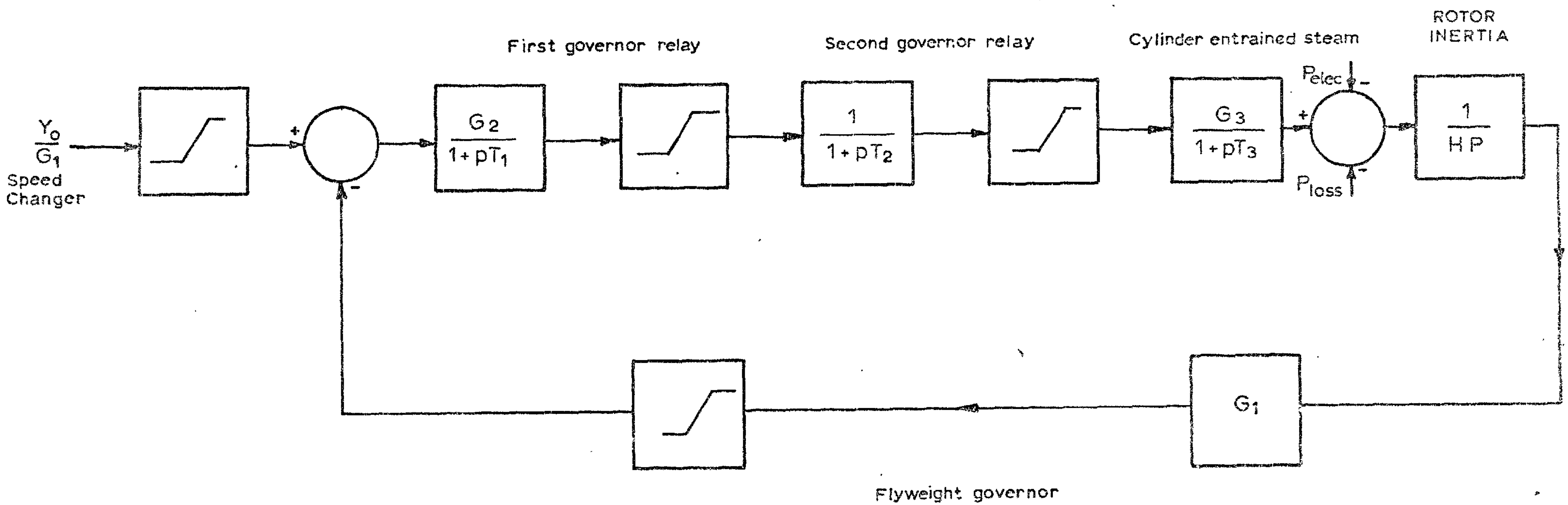

Fig. 5.3. Goldington governor system

speed as compared with the real system. If the loss term is too large (curve d), the system simulation gives a smaller numerical value for the maximum overspeed, the rate of decay of speed is larger and the final speed smaller as compared with the real system.

5.3 Northfleet simulation-general

As mentioned in section 5.1 after simulating a simple form of turbogenerator prime-mover, the simulation methods were extended to analyse a more representative large modern type of turbogenerator including a reheat section.

Northfleet power station was chosen as a test system because its data and test results were readily available in reference 16. Furthermore, the main parameters of Northfleet turbogenerator resemble those of a 660 MW unit and therefore the simulation of this generator offered additional attractions.

5.4 Northfleet simulation-load rejection

The simulation of a full load rejection of this power station was carried out using a digital computer, a micromachine set and an analogue computer. The evolution in time of the most important states, as predicted by all simulations, are presented in Figs. 5.4, 5.5 and 5.6.

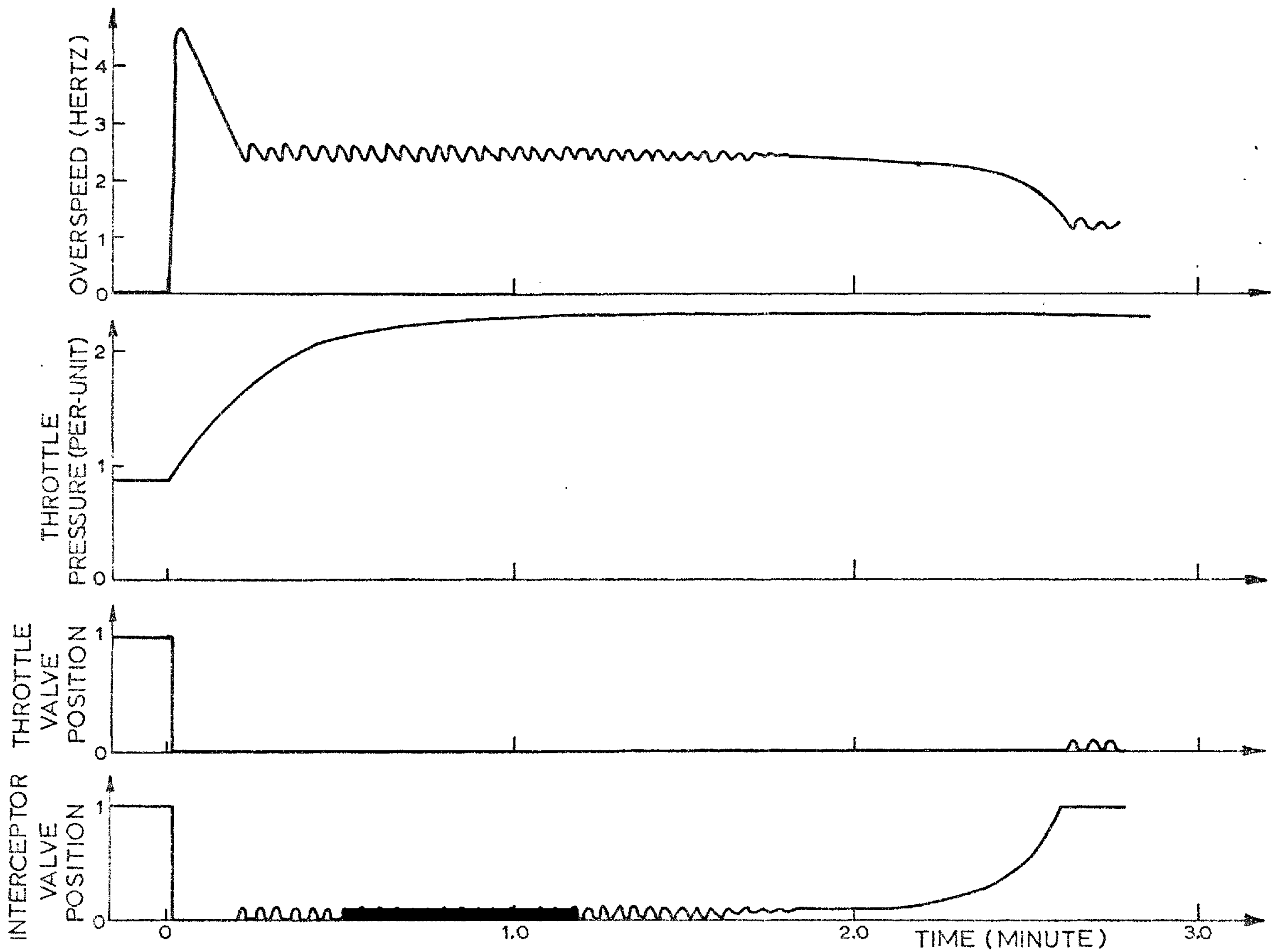

Fig. 5.4. Digital simulation of Northfleet load rejection

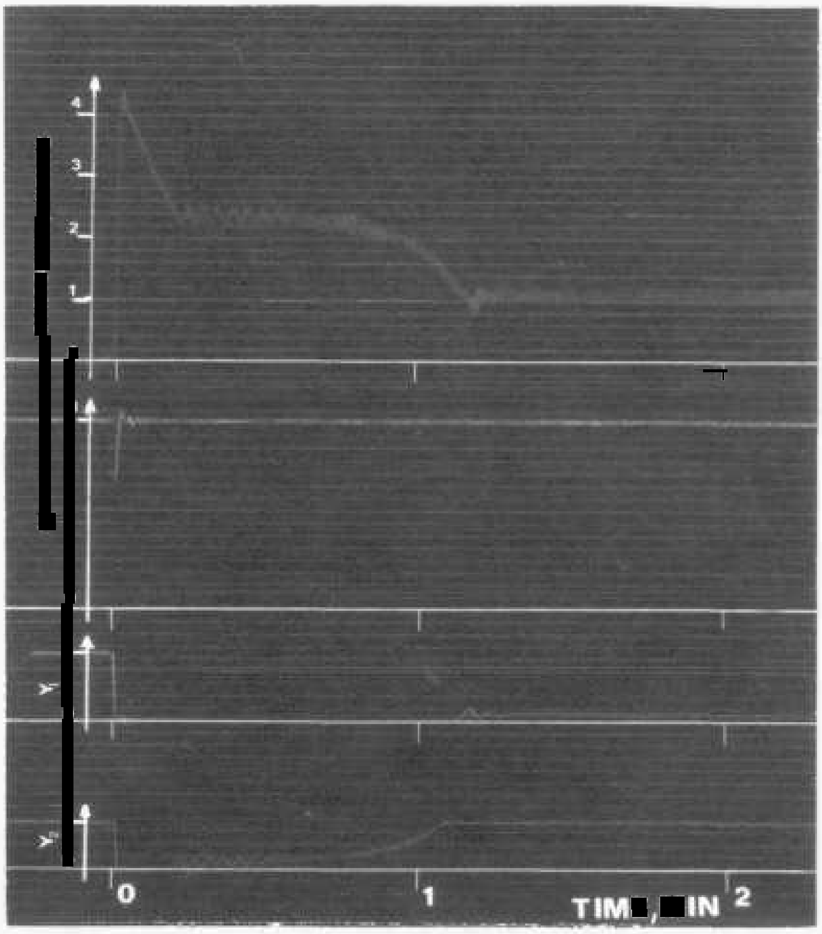

Fig. 5.5 Micromachine simulation of Northfleet load rejection

V_T machine terminal voltage

Y_1 throttle valve position

Y_2 interceptor valve position

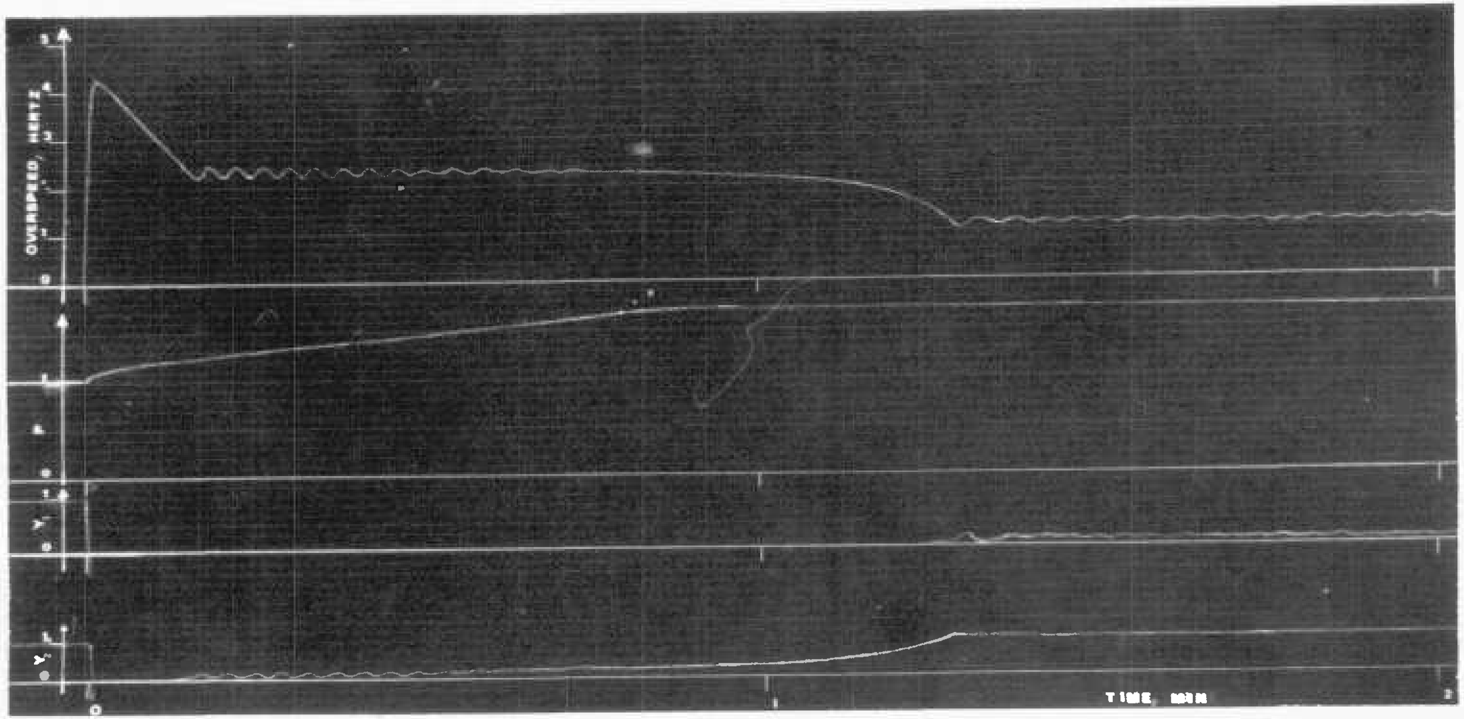

FIG. 5.6 PURE ANALOGUE SIMULATION OF NORTHFLEET LOAD REJECTION

P BOILER PRESSURE

Y_1 THROTTLE VALVE POSITION

Y_2 INTERCEPTOR VALVE POSITION

As with the Goldington turbine, the shaft overspeeds rapidly after load has been rejected. By governor action, the throttle valve is closed fully at t = .25 s. and the interceptor valve at t = 1 s. There is a delay between the closing of both interceptor valves and the time the shaft reaches its maximum overspeed of 9.3% at t = 2.0 s., this is due to the entrained steam between both governor valve chests and the respective turbine cylinder inlets and between the IP cylinder outlet and the LP cylinder inlet. The entrained steam continues accelerating the rotor for some time after all governor valves have been fully closed. All simulations estimated this effect very well.

Having arrived at a maximum, the shaft speed slows down under the action of the losses as given by equation 5.1. The shaft speed, however, does not return to its final state given by the governor droop and the amount of load being rejected as in the Goldington load rejection test, but hunts around the overspeed setting of the interceptor valve. The turbogenerator losses are now supplied from the energy stored in the reheater. All simulations show hunting at this particular operating condition. The oscillations form a limit cycle of instability. The shape of this limit cycle exhibited by the micromachine is similar to that of the pure analogue simulation. The digital simulation however, shows a somewhat different limit cycle. These differences are mainly due to two reasons:

a) inaccuracies in both analogue and micromachine simulations of the constraints imposed upon the motion of governor relays, and

b) the system is highly nonlinear at this operating condition and in the digital solution the relevant nonlinearities were taken into account more thoroughly.

The energy stored in the reheater runs out just over two minutes after the full load rejection has taken place according to the digital computer solution. The micromachine simulation, however, gives 1.2 minutes for this time interval. This difference is due to the fact that a small error in the setting of the loss term is integrated over this relatively long time period. Only a small change in the loss term of the analogue model was required to reduce this time interval to the magnitude obtained from the micromachine test.

When the energy stored in the reheater is exhausted the interceptor valve opens fully and the throttle valve commences to regulate the shaft speed. After some oscillations the rotor speed finally reaches its final state as given by the governor droop multiplied by the load being rejected.

As soon as the load is rejected the pressure before the throttle valve begins to rise quickly until it reaches the same level as the boiler pressure. These two pressures then rise slowly owing to the energy stored in the boiler piping circuitry. The final boiler pressure is about 2 per-unit and is reached about 1 minute after the load rejection occurs. Of course, long before the boiler pressure attains this level, the safety valves open.

In a load rejection, relatively long time intervals are involved before the system reaches the final stable state. This is due to the uncoordinated action of the control system and is not due to the numerical values of the plant time constants. For instance, a reheater time constant of 6 seconds is capable of holding the turbogenerator speed 5% above rated for more than 2 minutes.

5.5 Northfleet simulation-pole-slipping

The next disturbance considered is Northfleet test No. 6. Here, the turbogenerator is operating at a leading power factor and a short circuit near the generator terminals is applied for a short time interval. As a result, the generator loses synchronism. The machine is allowed to slip poles until by governor action it automatically recovers synchronism. Relevant results of this test are reproduced from reference 16 in Fig. 5.7.

The object of the simulation studies is to analyse governor behaviour after a severe disturbance to the power station has occured. A digital computer solution of the ma-

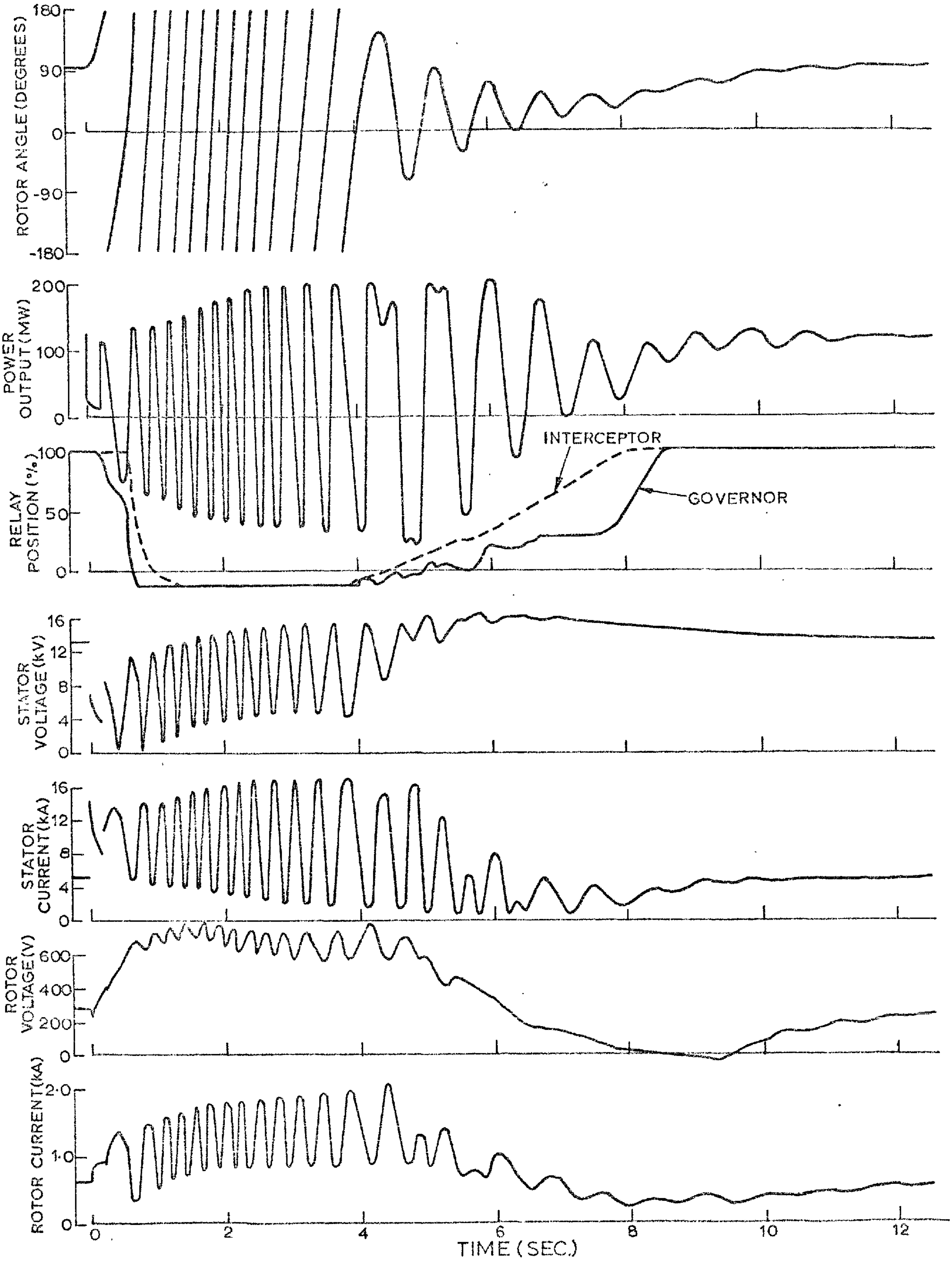

Fig. 5.7. Results of Northfleet test N° 6

thematical model representing Northfleet power station and a micromachine simulation of the same station were employed to analyse this transient.

Figures 5.8, 5.9, 5.10 and 5.11 show the results from the micromachine simulation with various ratios of governor relays opening-to-closing time constants. For comparison, Figs. 5.12 and 5.13 show digital computations of the evolution of the same transient for a range of system parameters. The data for all simulations is given in Table 5.1.

The processes of turbogenerator loss of synchronism and subsequent recovery can be divided into five parts:

1) rotor backswing,

2) loss of synchronism,

3) rotor deceleration,

4) resynchronization and

5) post-synchronization.

These will each be considered in more detail in the following sections.

5.5.1 Rotor backswing

The rotor movement 0 - 100 ms after the disturbance

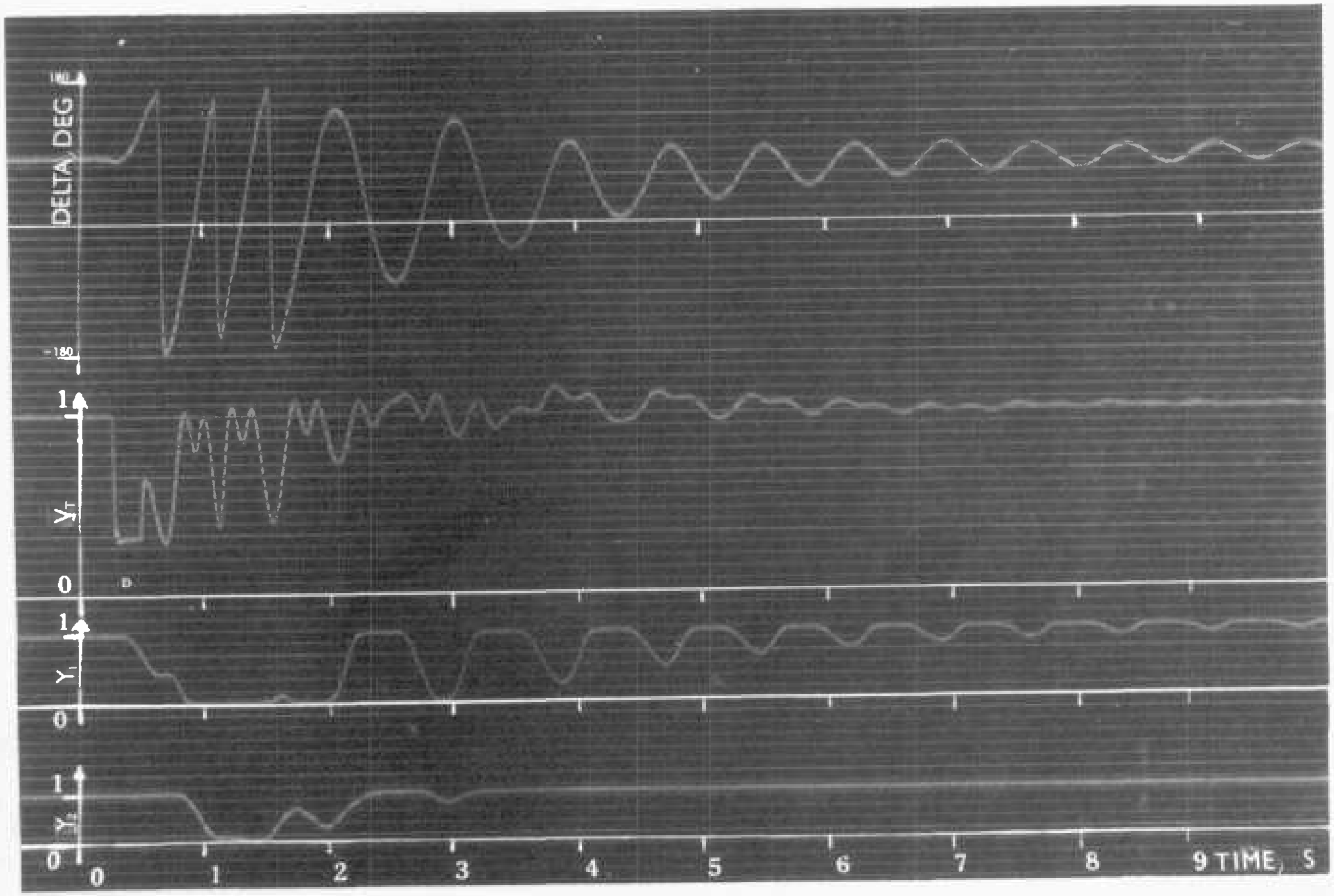

FIG. 5.8 MICROMACHINE SIMULATION OF NORTHFLEET TEST No. 6

V_T MICROMACHINE TERMINAL VOLTAGE

Y_1 THROTTLE VALVE POSITION

Y_2 INTERCEPTOR VALVE POSITION

RELAY OPENING TIME CONSTANTS = RELAY CLOSING TIME CONSTANTS

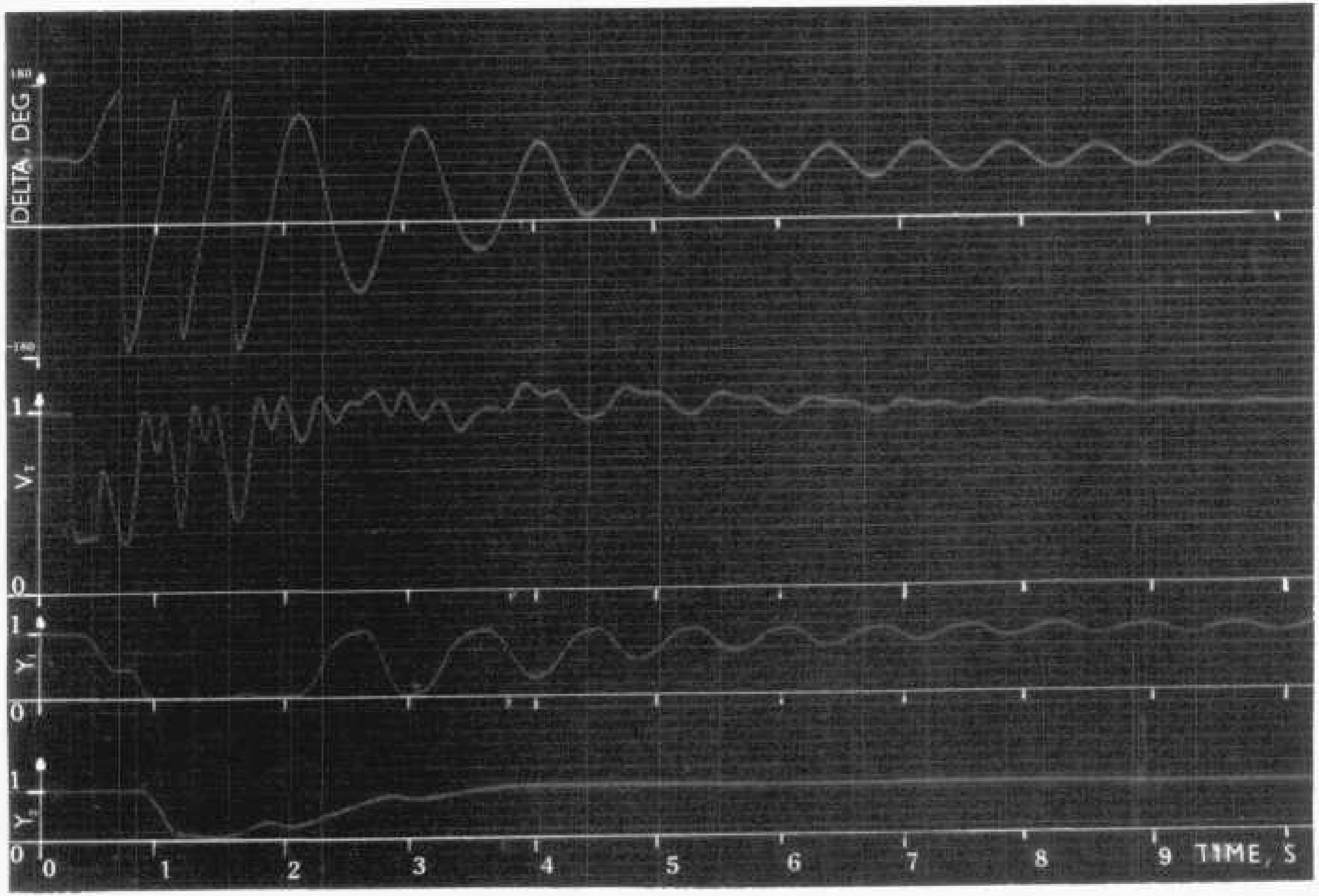

FIG. 5.9 MICROMACHINE SIMULATION OF NORTHFLEET TEST No. 6

V_T MICROMACHINE TERMINAL VOLTAGE

Y_1 THROTTLE VALVE POSITION

Y_2 INTERCEPTOR VALVE POSITION

RELAY OPENING TIME CONSTANTS = 3 (RELAY CLOSING TIME CONSTANTS)

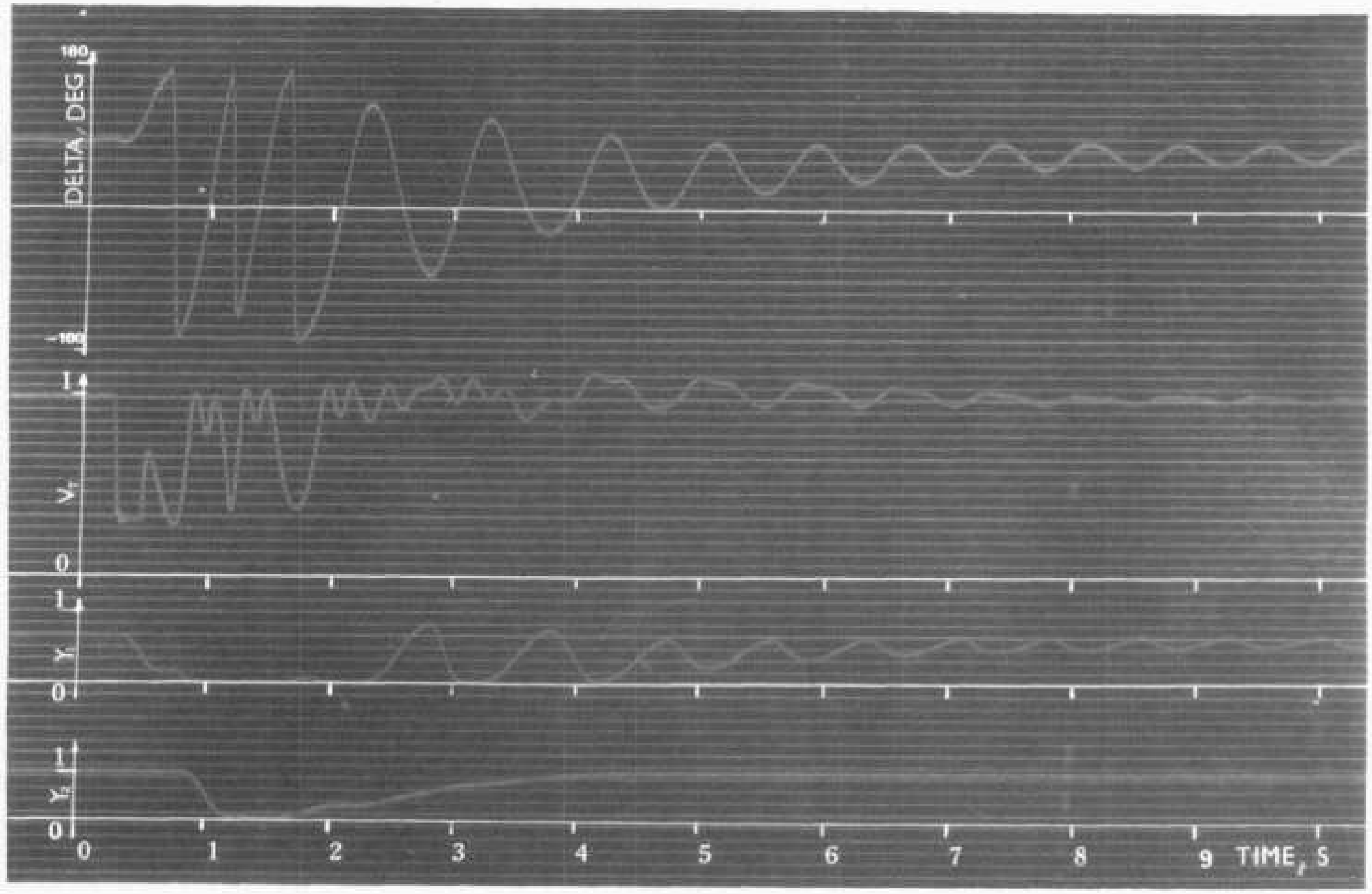

Fig. 5.10 MICROMACHINE SIMULATION OF NORTHFLEET TEST No.6

V_T MICROMACHINE TERMINAL VOLTAGE

Y_1 THROTTLE VALVE POSITION

Y_2 INTERCEPTOR VALVE POSITION

RELAY OPENING TIME CONSTANTS = 5 (RELAY CLOSING TIME CONSTANTS)

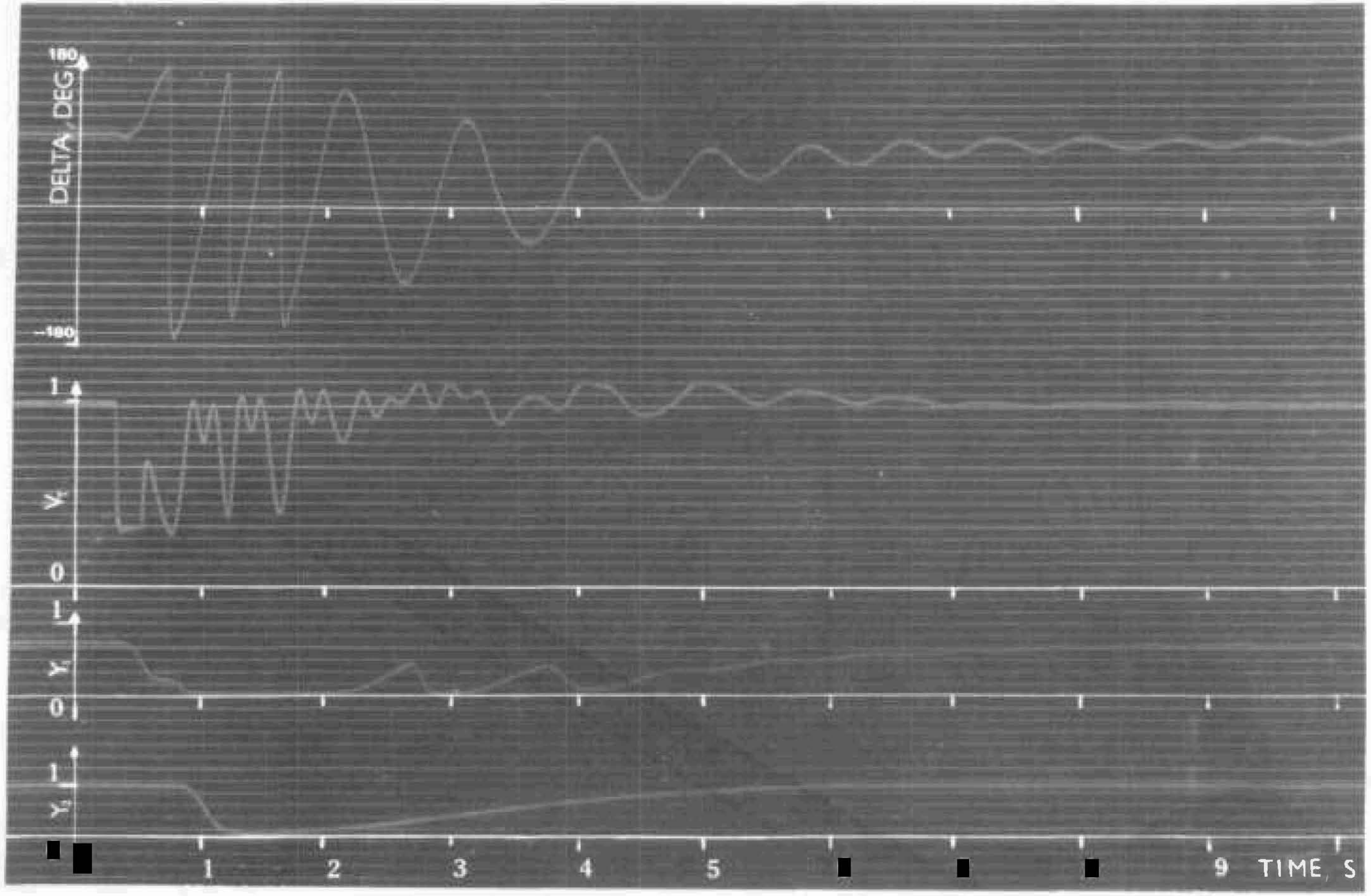

Fig. 5.11 MICROMACHINE SIMULATION OF NORTHFLEET TEST No. 6

V_T MICROMACHINE TERMINAL VOLTAGE

Y_1 THROTTLE VALVE POSITION

Y_2 INTERCEPTOR VALVE POSITION

RELAY OPENING TIME CONSTANTS = 10 (RELAY CLOSING TIME CONSTANTS)

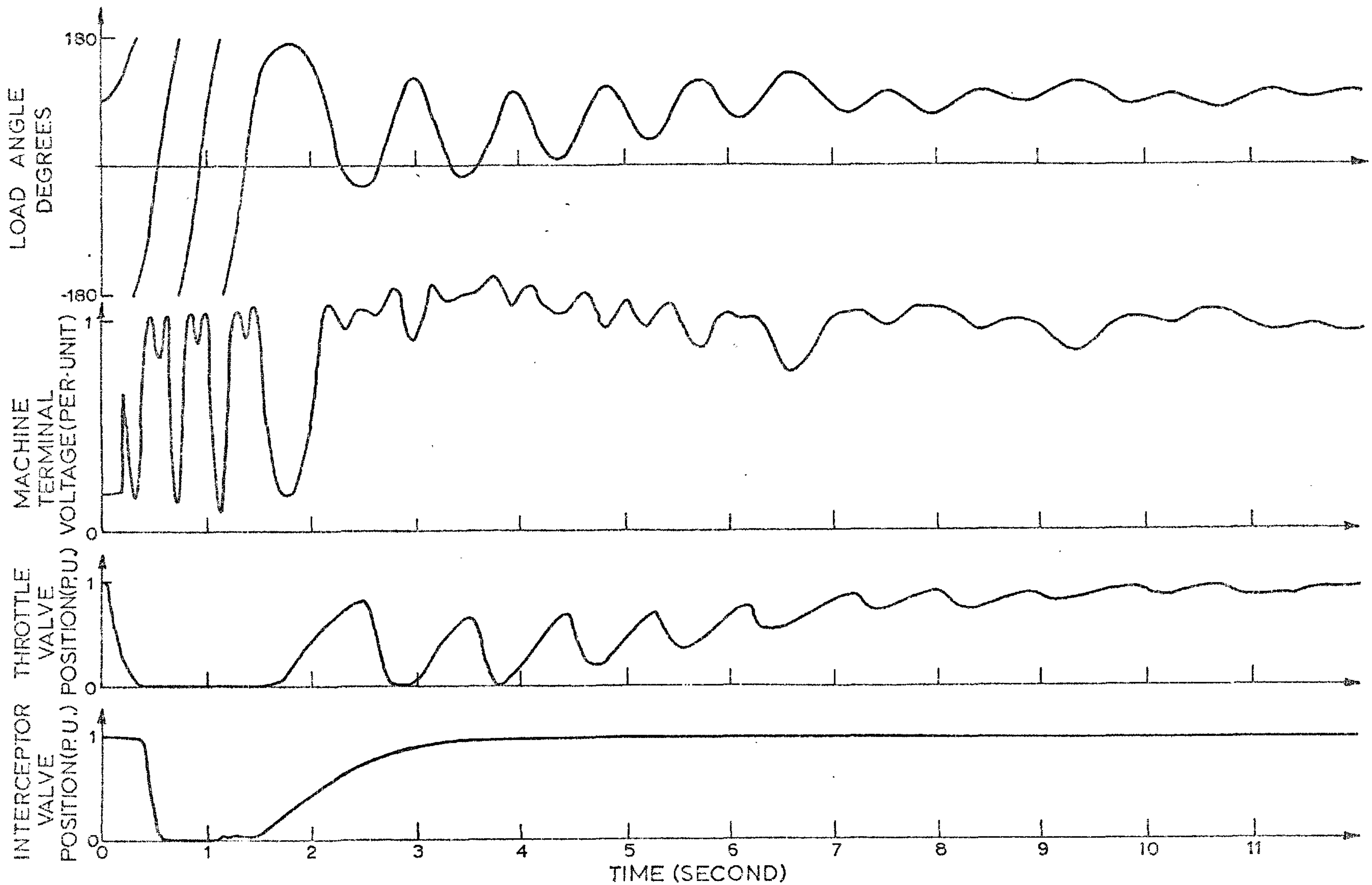

Fig. 5.12. Digital simulation of Northfleet test N° 6 (data in table 5.1)

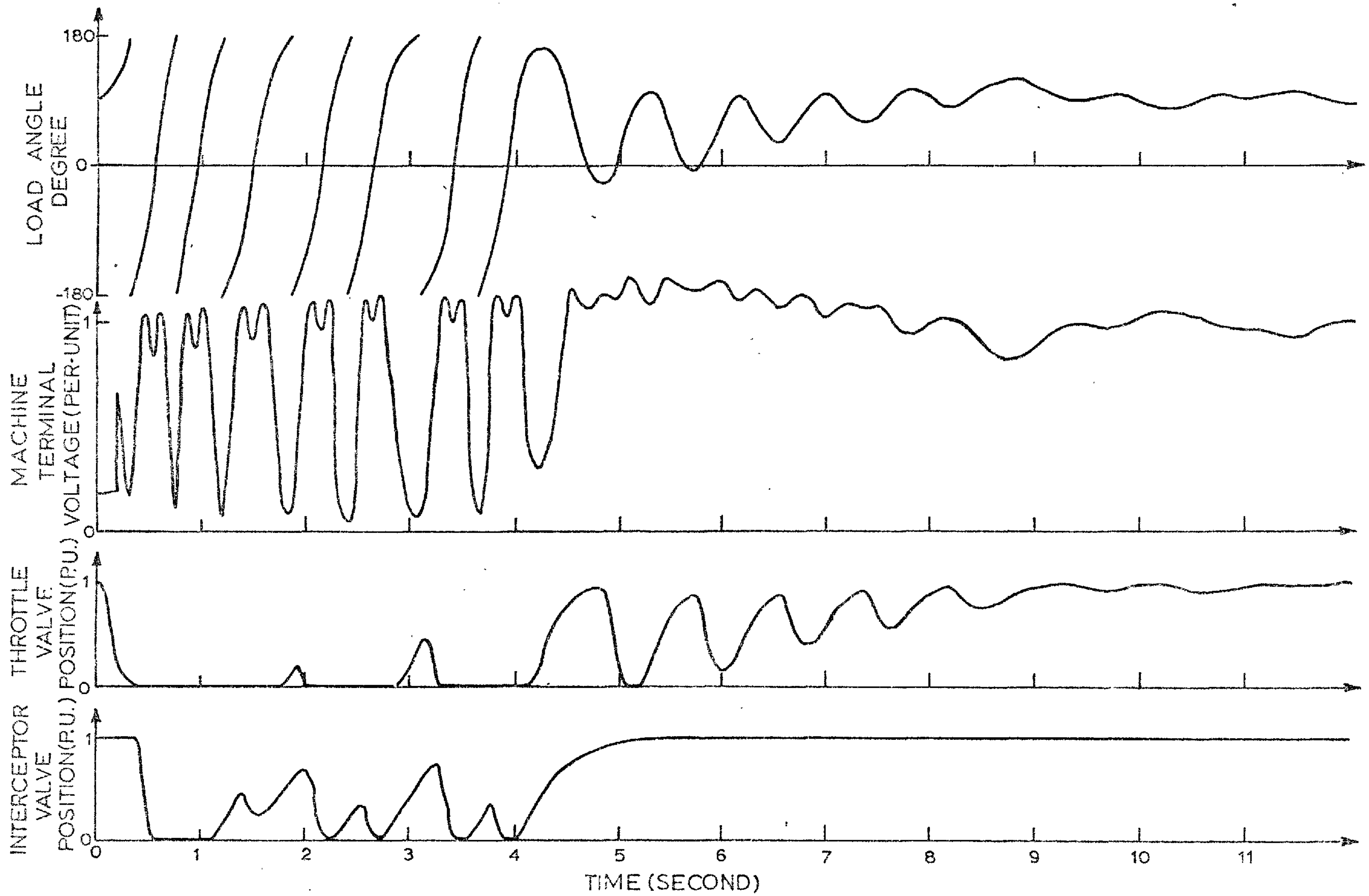

Fig. 5.13. Digital simulation of Northfleet test N° 6 (Data in table 5.1.)

has received considerable attention recently in the literature.[8,31,95]

The microgenerator shows that approximately during the first 80 milliseconds after the fault is applied there is no increase in the load angle. In fact, the rotor is recorded swinging marginally backwards, a fact which is in agreement with the findings of reference 15. The digital solution neglects both $p\psi_d$ and $p\psi_q$ terms and therefore does not show the backward swing. The Northfleet machine was reported as swinging backwards for about 35 milliseconds.[16] Mehta and Adkins,[8] Shackshaft,[95] and Harley and Adkins[31] have explained the backswing phenomenon and discussed the effects of neglecting $p\psi_d$ and $p\psi_q$. They also stress the importance of using the correct numerical values of synchronous machine resistances so that turbogenerator rI^2 losses can be modelled adequately. The microgenerator has larger per-unit resistances than the Northfleet machine and therefore a more severe backswing would be expected.

In Norhtfleet test No. 6, 200 milliseconds elapse before any significant movement of the throttle valve is observed. This long delay in the throttle valve motion, which has been interpreted as a transportation time delay, is of a more complex nature. Initially, the throttle valve is operating at its limits. To simulate this test, it is therefore necessary to determine the speed changer setting so that the additional dead band introduced by operating the system in this manner can be assessed. Furthermore, the rotor back-swing and governor multiple time lags described in section 2.8 accentuate this delay effect. Northfleet test No. 3 was carried out with the governor operating within its constraints and hence no additional dead band was introduced. As a result only 100 milliseconds elapsed before throttle action commenced. In the case of the microturbine, the governor operated within its constraints, and the throttle valve recording shows that only 120 milliseconds after the fault has been applied a significant movement in the closing direction can be observed. Of these 120 milliseconds, approximatelly 80 are due to the machine swinging backwards and 40 due to the governor multiple time lags. This delay effect is more marked in the microturbine owing to its more severe back-swing. It is interesting to point out that no closing movement of the Northfleet throttle valve should be expected for at least 75 milliseconds. Of these, 35 milliseconds are due to the machine swinging backwards and 40 to governor multiple time lags. The digital simulation of the throttle valve motion shows a delay of 40 milliseconds.

5.5.2 Loss of synchronism

After the generator rotor has swung backwards the second part of the transient begins. The rotor accelarates owing to a power surplus that exists until the short circuit is cleared. With conventional controllers the synchronous generator may come back to its original operating conditions with or without pole-slipping depending mainly upon the numerical value of the load angle when the fault is cleared.

If the machine does not slip poles after the fault has been cleared, the rotor decelerates. In the case under discussion the machine slips poles, the shaft being accelerated for a short interval. The load angle, however, continues to grow, initially at a slow rate. With the throttle valve closing, the turbine torque diminishes only marginally owing to the relatively long time delays involved in the reheater. As the load angle increases, the generator electrical power decreases, hence, the rotor starts accelerating again. This results in a kink in the rotor velocity and an inflection in the motion of the load angle. As in Northfleet, the micromachine governor senses this variation in the rotor velocity and stops closing the throttle valve for 200 ms. In the digital solution the rotor backswing was not present, hence, the throttle valve is almost fully closed when the kink in the rotor velocity occurs.

As the load angle approaches 180 degrees, the electrical torque is reduced and the rotor acceleration increases.

Beyond 180 degrees, the synchronous generator operates as a motor and the rotor acceleration is a maximum. It is only then that the microturbine interceptor valve starts closing (t = 600 ms), reaching its fully closed position at t = 900 ms. The real system gives 600 and 950 ms, the digital solution 400 and 600 ms respectively. This completes the first part of the transient.

5.5.3 Rotor deceleration

This third part of the transient is characterized by the synchronous machine pole-slipping and a period of average deceleration. Each time the generator slips one pole, the difference between the power supplied to the infinite bus bar and the motoring power taken from the infinite bus bar is negative and therefore the rotor velocity slowly diminishes.

The real system slips 13 poles before resynchronization is achieved; in contrast the micromachine slips only 3 poles. The cause of this difference is the high per unit resistances of the microalternator, which produces high losses and quick deceleration. This was proved with the digital simulation where low values of the damping coefficient produces a large number of pole-slips before resynchronization (Figs. 5.12 and 5.13).

All simulations show violent swings in the electrical states of the system while the synchronous generator is pole-slipping. In particular the machine terminal voltage swings from a maximum of about 1.0 per-unit to a minimum of around 0.1 per-unit. The maximum occurs approximately when the back EMF produced by the field exciting current and the infinite bus bar voltage are in phase and the minimum when these two phasors are about 180 degrees out of phase. Both, the micromachine and the digital simulations show a notch in the oscillograms of the generator terminal voltage when the trace passes through a maximum. This notch does not appear in the recordings of the real system. No explanation has been found for this discrepancy.

This part of the transient ends when the rotor speed is small enough for resynchronization to commence.

5.5.4 Resynchronization

Part 3 of the transient begins when conditions are such that resynchronization can take place. According to Poliack[112] when the rotor speed is about 2% higher than synchronous, resynchronization is initiated. All simulations and measurements in the system under discussion confirm Poliack's observation.

The condition arising when the rotor speed first becomes equal to synchronous is of particular importance. At this instant the load angle is at a maximum in the range of 150 to 170 degrees. The load angle can stay at this maximum for a relatively long time interval depending upon system conditions. If the system recovers synchronism slowly, the plateau part of the load angle oscillagram is relatively long.

A large depression in the machine terminal voltage occurs because at this operating condition the voltage behind the subtransient reactance is nearly 180 degrees out of phase with the infinite bus voltage, therefore, large currents circulate through the generator armature. This phenomena actually occured in the digital simulations shown in Figs. 5.12 and 5.13. The micromachine simulation presented in Fig. 5.14 is another example of slow resynchronization. In contrast, the Northfleet test and the micromachine simulation depicted in Figs. 5.8 to 5.11 are examples of quick resynchronization and do not show this long plateau region in the load angle oscillogram, nor the depression in the machine voltage.

If after the plateau region in the load angle oscillogram has been reached the load angle commences to decrease, synchronism has been regained and part 4 of this transient ends.

5.5.5 Post-synchronization

After synchronization, fluctuations in all system states occur till the final state is reached. The early portion of this last part of the transient is characterized by relatively large oscillations and the latter by small oscillations.

In order to simulate the post-synchronization phenomena it is of prime importance to model accurately the dy-

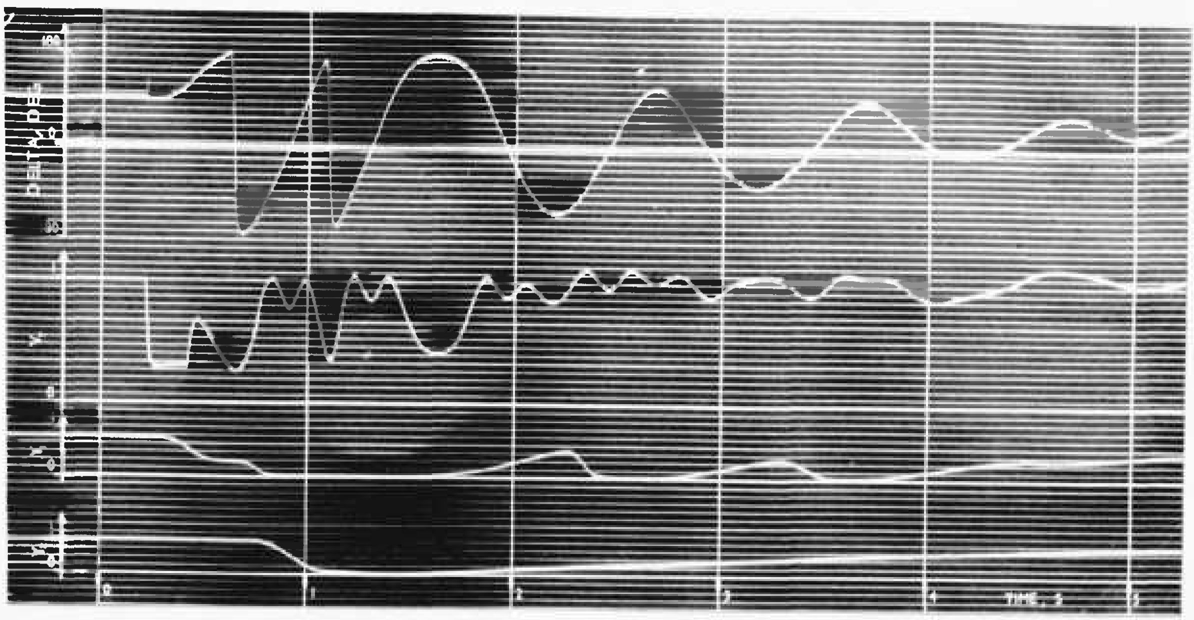

Fig. 5.14 MICROMACHINE SIMULATION OF NORTHFLEET TEST No. 6

V_T MICROMACHINE TERMINAL VOLTAGE

Y_1 THROTTLE VALVE POSITION

Y_2 INTERCEPTOR VALVE POSITION

RELAY OPENING TIME CONSTANTS = 10 (RELAY CLOSING TIME CONSTANTS)

namic behaviour of the opening action of governor relays.

By successively reducing opening time constants with respect to the closing time constants, in Figs 5.8 to 5.11 it is shown that the part of the transient under discussion cannot be successfully simulated.

When the opening time constants of the governor relays are made equal to the closing time constants, the system shows a marked tendency to hunt and stability margins under small oscillations are reduced considerably. In general, both Northfleet valves show very sluggish reopening. The simulation of the load angle motion becomes similar to the real system when both governor valves are opened in such a manner that they are decoupled from the load angle oscillations.

The simulation studies carried out by the author confirm observations of two early investigators[112,113] who have found evidence that limiting the opening rate of both governor valves facilitates resynchronization. In particular the opening rate of the interceptor valve must be limited because this valve has the ability to control quickly a relatively large amount of power.

Minor alterations in power plant design can be made with useful improvements in turbogenerator dynamic behaviour under pole-slipping conditions. This is illustrated in Fig. 5.15 where the opening rate of all governor relays in the digital simulation of Northfleet power station was made 25 times slower than the closing rate. This is about the maximum that can be used safely so that if both governor valves are fully closed prefault loading is restored about 10 seconds after the closing motion of governor valves takes place. Relatively large changes in the most important system parameters failed to change the number of poles-slipped for the example depicted in Fig. 5.15. This emphasizes, as mentioned previously, that a decrease in the opening rate of governor relays is beneficial for quick recovery of synchronism. Further, the interaction between the governor system and the AVR is minimized and therefore both controllers can be designed as if they were decoupled. This is favorable from a dynamic point of view, and the time evolution of the load angle is better damped now than in all previous simulations, see for instance Figs. 5.12 and 5.13.

In general, the system being simulated is very sensitive to small changes in main system parameters in either the synchronous machine or the governor system. Mathematically, the simulation of this transient can be regarded as a numerically ill conditioned problem. However, this system is not very sensitive to relatively large changes in the AVR parameters, due to the relatively low exciter ceiling voltages and slow transient response of this particular excitation system. This effect is illustrated in Fig. 5.16 where it is shown that a variation of 2.5 times in the exciter time constant fails to modify significantly the system transient response.

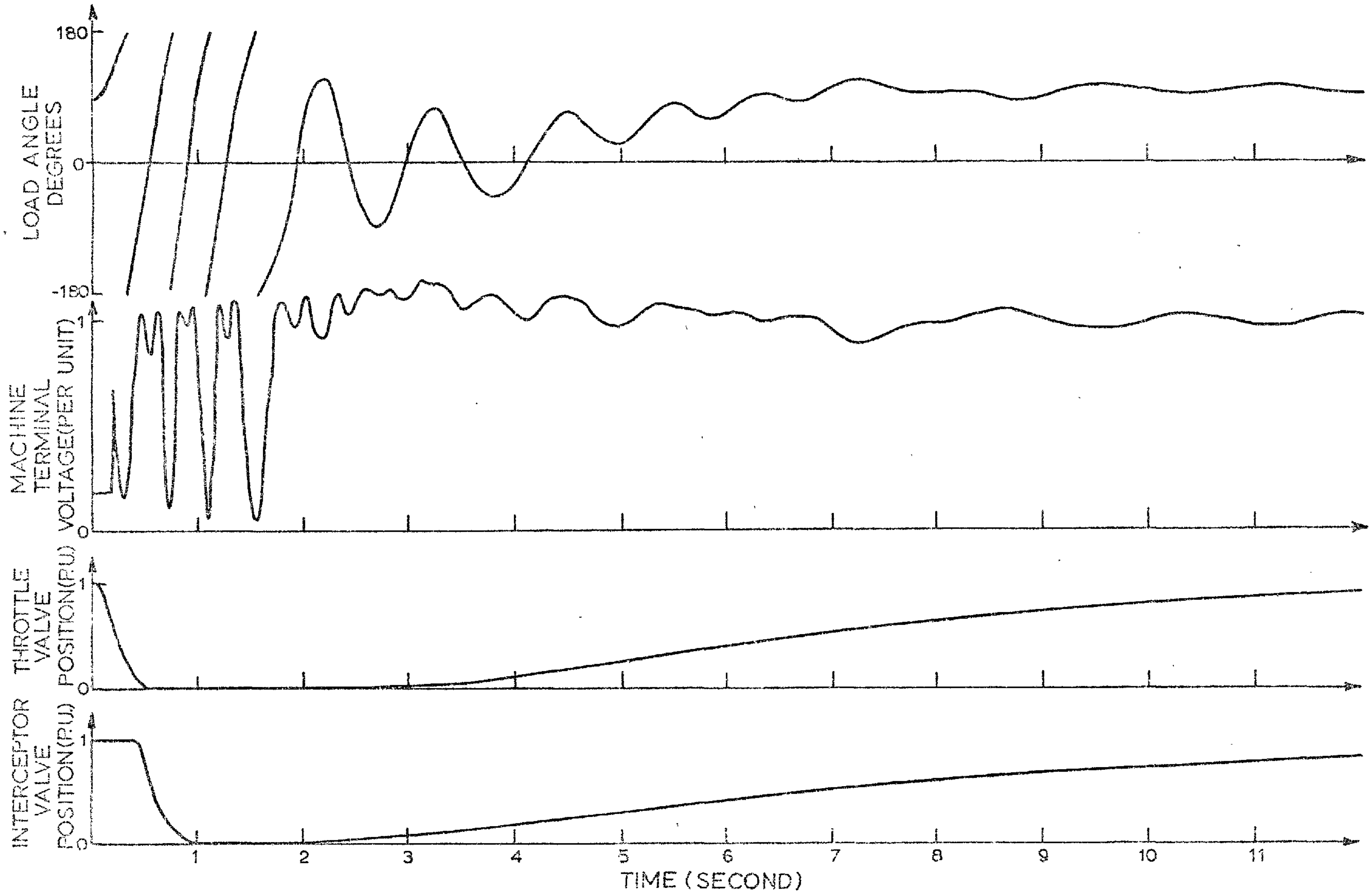

Fig. 5.15. Digital simulation of Northfleet test N°6 (Data in table 5.1)

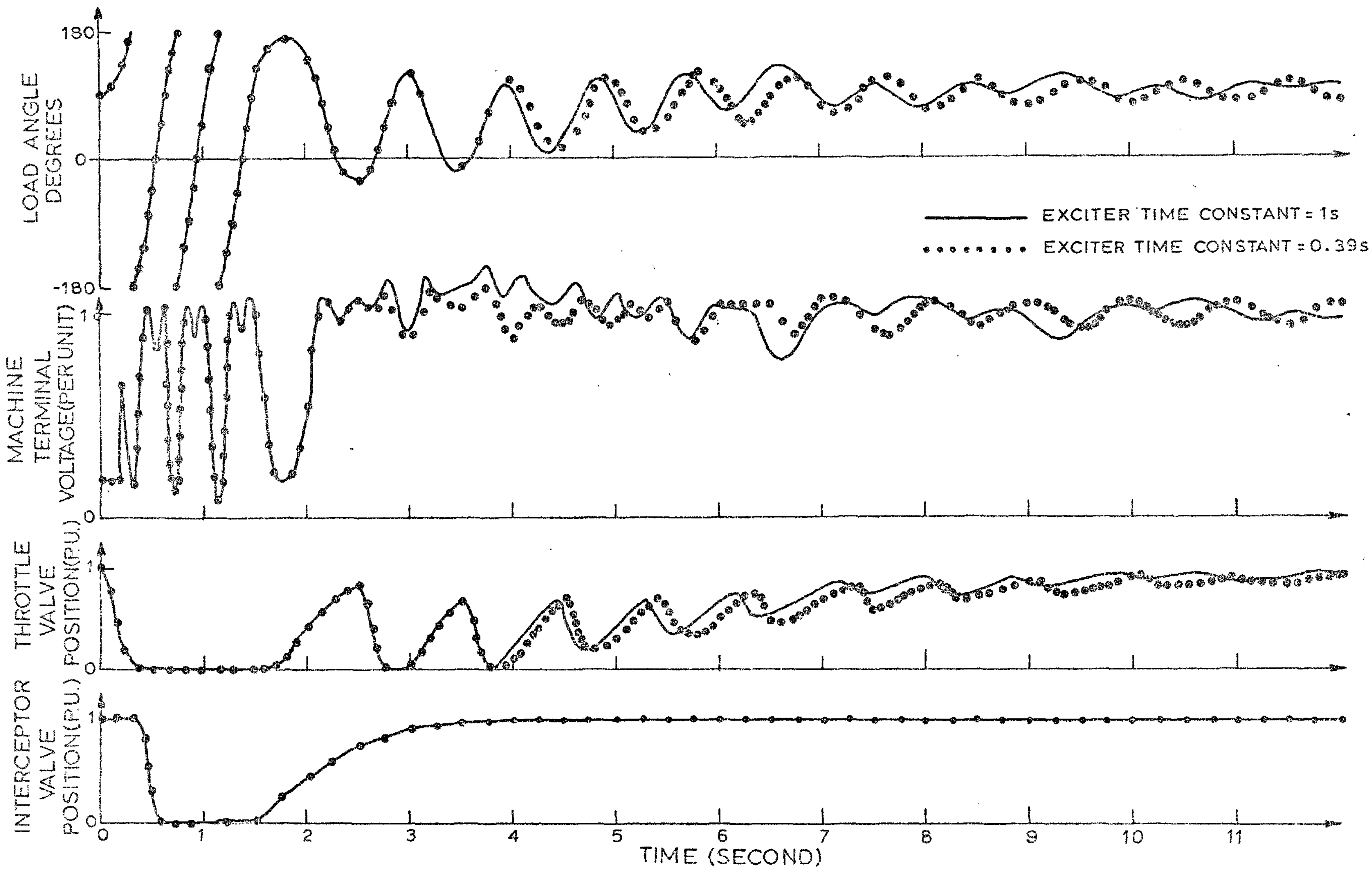

Fig. 5.16. Comparison of digital simulations of Northfleet test N° 6 for two different exciter time constants

5.6 Limit cycles involving pole-slipping

Pole-slipping transients are complex and three different types of instability have been observed as a result of this severe operating condition:

a) The generator may never regain synchronism automatically, because as soon as the rotor speed slows down the interceptor valve opens and the rotor is again accelerated. This type of instability has been reported in an actual power station.[114] According to the simulation studies carried out by the author this type of instability is prominent in systems which exhibit poor damping characteristics.

b) The machine can recover synchronism and lose it a short time after. The digital simulation of Northfleet depicted in Fig. 5.17 is an example of this type of instability.

c) The machine recovers synchronism and loses it a short time after from excessive deceleration. This type of instability has been reported by Busemann.[115]

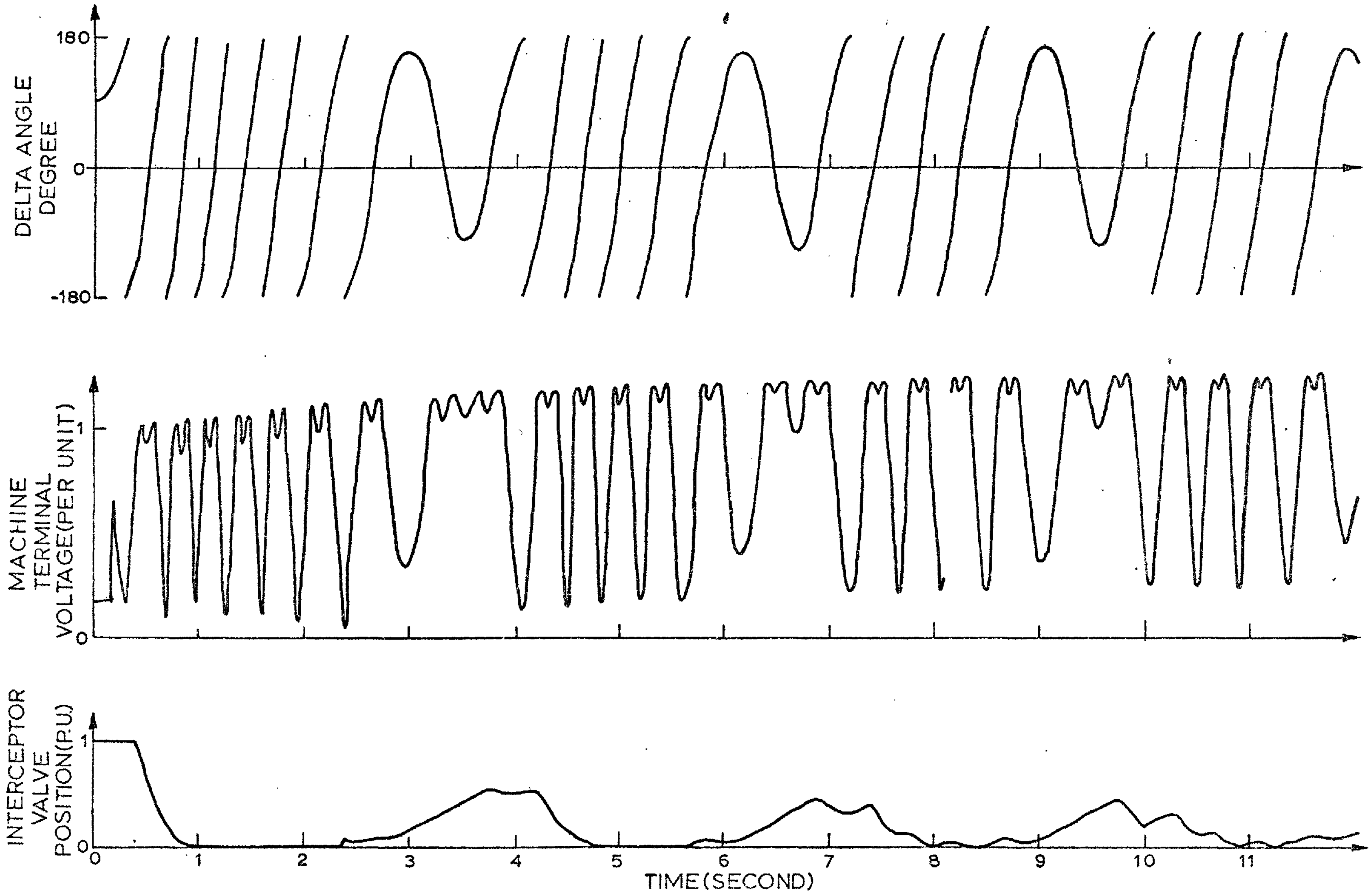

Fig. 5.17. Digital simulation of Northfleet test N° 6 (Data in table 5.1)

TABLE 5.1

DATA FOR NORTHFLEET SIMULATION STUDIES

Simulation results depicted in figures	Turbogenerator power output (per-unit)	Exciter time constant (second)	Subtransient time constant $T''_d = T''_q$	M*
5.5,5.6,5.7	.80	1	-	3
5.8	.84	1	See table 2.1	1
5.9	.84	1	See table 2.1	3
5.10	.84	1	See table 2.1	5
5.11	.84	1	See table 2.1	10
5.12	.84	1	.322	10
5.13	.84	1	.42	5
5.14	.80	1	See table 2.1	10
5.15	.84	1	.45	25
5.16**	.84	1./.39	.322	10
5.17	.84	1	.184	5

Note: Other data as given in reference 16 for test No 6

*all governor relays opening time constant = M relays closing time constant

**Fig. 5.16 shows a comparison of the simulation depicted in Fig. 5.12 with a case of reduced exciter time constant

CHAPTER 6

DISCUSSION ON THE IMPROVEMENT OF PLANT DYNAMIC BEHAVIOUR

6.1 General considerations on governor dynamic behaviour

The governor of a turbogenerator in a large power system is required to:

1) control system frequency by means of:
   a) a fast automatic action if a disturbance in the demand-supply power balance occurs, and
   b) a response to load dispatching signals in order that the steady-state errors owing to governor droops can be slowly compensated,

2) damp power system oscillations,
3) damp turbogenerator oscillations, and
4) protect turbogenerators against overspeeds.

The first of these tasks requires alteration of turbogenerator loadings with system frequency variations. Changes in loading by governor action stabilize power system oscillations and should be carried out with an optimum management of the power plant stored energy capabilities. Disturbances under these circunstances are normally slow with periods of several seconds and governor control is effected only by the throttle valve.

As power systems grow in size, the ratio of a particular generator power output to the total system generation diminishes, thus variations in the turbogenerator load is no longer a governor feedback problem but an open loop process because changes in a generator loading do not affect significantly system frequency. The governor structure, however, should be preserved because the fast automatic action is of prime importance for power system frequency stability.

In general, faster governing systems combined with reduced dead-bands improve frequency control, contribute beneficially towards damping of turbogenerator oscillations and offer better protection in the event of overspeeds.

A comprehensive analysis of governor performance involves a complete examination of power system design philosophy. An analysis of this nature is outside the scope of this study. This investigation is confined to the discussion of transient conditions arising from faults, in particular the dynamic behaviour of the most affected power station.

For the purpose of the following discussion, faults are classified into two broad groups:

a) long duration faults which result in a complete interruption of power transfer from the power station, and

b) short duration faults, i.e. faults in the transmission system which are cleared within a few cycles.

6.2 Long duration faults

Long duration faults present a very difficult operating condition. If during the fault the station loses its auxiliaries, the problem becomes even worse and valuable time is spent in restarting units and restoring them to full load. Hence, it has been suggested[116,117,118] that after a fault of this type the power station should be designed to withstand a full load rejection and to continue supplying its own auxiliaries for as long as required. This procedure improves power system reliability and reduces power system operational costs. In the debit side, power station design becomes more expensive.

Akers et al[119] have estimated that every single occurence of such a fault can result in approximatelly 1/4 to one per-cent of the total fatigue capacity of the turbine rotor owing to thermal stresses. Fast disturbances in the turbine operating conditions are critical for the turbine rotor as can be assessed from this fatigue figure. However, these severe stresses are not developed if load is restored in less than 10 minutes.

6.3 Short duration faults

In order to cope with short duration faults, in a planning stage, the following alternatives may be considered:

a) design options,

b) power control, and

c) operational strategies.

6.3.1 Design options

The most important design options are:

1) fast clearing times,

2) modifications in the turbogenerator or grid conventional design,

3) fast AVRs and high exciter ceiling voltages, and

4) optimum control strategies.

Fast clearing times have been specified in the past to achieve a given transient stability margin each time a new generation of turbogenerators with increased power rating and reduced inertia was brought into service. Fault clearing times have been reduced as far as modern technology permits. It has been reported[117,120,121] that in some cases, clearing times were insufficient to maintain the transient stability of a unit. With the next generation of turbogenerators, and bearing in mind that more remote sites are sought, the transient stability problem becomes more acute. It is therefore important to consider other alternatives if stability margins are to be maintained or even improved.

Advances in technology have made it possible to increase turbogenerator ratings one hundredfold in the last sixty years. This trend in growth might stop when the economical gains from increased unit ratings are more than compensated by the increase in system complexity and hence cost. The transient stability is one of the many problems which becomes more expensive to solve with increased ratings. The economical gains obtained from larger sets, however, more than compensates today these extra expenses.[122]

Modifications in the turbogenerator design in order to increase its inertia constant, reduce two of the main savings in increasing turbogenerators power output namely reduced relative physical dimensions and weight. The design of the rotor windings however, offers two interesting possibilities:

1) a divided winding rotor arrangement[101], and
2) closed turns linking the interpole axis thus providing support for the rotor flux in the quadrature axis.[123]

In both cases, investigators[101,123] have claimed substantial improvements in turbogenerator stability.

The grid provides alternatives which can be beneficial from a dynamic point of view :

1) reduction in the step-up transformer leakage reactance[124],

2) series capacitors[124],

3) phase shift insertion[125], etcetera.

Fast AVR action with high ceiling voltages combined with an optimum strategy marginally increase "critical clearing times". The basic problem however, remains, i.e. "a power surplus" exists at the end of the short circuit and therefore the load angle can go above its critical value with subsequent loss of synchronism.

Optimum control has been suggested during the last few years as a method of improving transient stability. Such methods do not solve the "power surplus problem" per se but optimize the control strategy of existing controllers.

6.3.2 Power control

The "power surplus" problem can only be solved by direct power control, e.g. through the use of

a) braking resistors or

b) fast turbine valving.

Braking resistors are applied to the machine terminals through circuit breakers by means of a somewhat complicated control system after a fault has occured. Part of the "power surplus" in the power station is thus prevented from accelerating turbogenerator rotors and hence there is a substantial gain in transient stability margins. Park reports that expenses of the order of £100000 are involved in braking resistor schemes for an 1000 MW station.[126]

Fast turbine valving aims to control the turbine power output and hence reduce the "power surplus" in the station. The main requirements for turbine valving to be effective are:

1) valve positioners should be fast acting and have a high degree of manoeuverability,

2) entrained steam between IP and LP cylinders, and between both governor valves and respective turbine cylinder inlets should be minimized, and

3) valves should be controlled in such a way as to minimize the power plant thermal stresses while making an optimum contribution to stability.

The first of these requirements has been met by the new electrohydraulic relay. Valve closing times of .05 second have been reported.[117,127]

Turbine cylinders and connecting pipes grow with turbogenerator sizes, hence larger time constants are associated with steam turbine piping circuitries the larger the set. However, if valves are mounted on the turbine casing the entrained steam between both governor valve chests and respective cylinder inlets can be reduced considerably. This last arrangement tends to increase marginally the turbine costs as piping forces acting on the cylinder casing become larger.

Fast turbine valving strategies can be divided into two groups,

a) controlling only the interceptor valve, and

b) controlling both throttle and interceptor valves.

The first of these strategies has been implemented by Westinghouse in several power stations. Aanstad and Lokay[128] claim that fast control of only the interceptor valve is the most practical way of varying turbine power output for transient stability purposes.

In order to obtain a significant improvement in transient stability margins by means of turbine valve control the feedback structure of classical governor systems has to be abandoned. A so-called "fast-valving-logic" has been introduced instead. This is a consequence of a trend towards optimality of the plant dynamic behaviour and therefore a form of supervisory control has to be used which looks after the plant when severe disturbances in the normal operating conditions occur. This is normally the case when non-linear systems of a large order are considered and optimisation of their dynamic behaviour is sought.

Fast valving control schemes take the form depicted in Fig. 6.1.[128,129] In the Westinghouse "fast valving logic" as soon as there is a significant unbalance between generated and prime mover power output closing of the interceptor valve is initiated and thus the turbine power output is considerably reduced. Lokay and Aanstad[128] have shown that an increase in critical clearing times of about one cycle can be obtained in this manner if fast valving is employed in only one set of the power station and two cycles if it is employed in all sets. The Westinghouse "fast valving logic" has a feedback structure, alternatively, open loop strategies, in a supervisory fashion can be implemented and as soon as a severe disturbance is detected full closing of the interceptor valve is initiated and governor action is inhibited.

Fast valving of both throttle and interceptor valves can increase even more transient stability margins. This is so because all turbogenerator power output can be controlled. As with strategies controlling only the interceptor valve large thermal stresses should not be expected in the turbine rotor if the prefault load is restored in less than 10

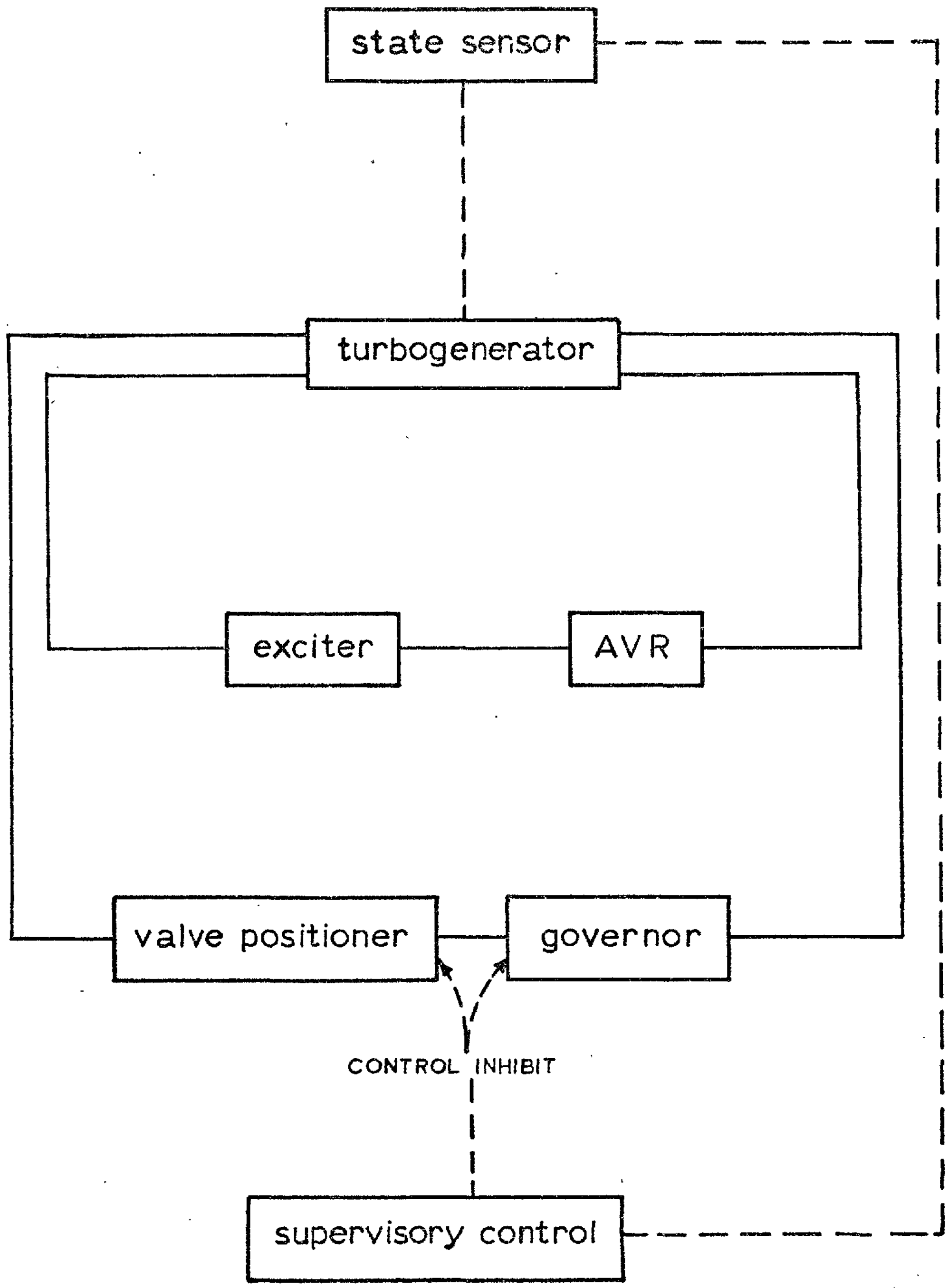

Fig. 6.1. Westinghouse fast-valving-logic as a form of Supervisory Control

seconds. In the debit side, boiler protection and design become more expensive as allowances for fast excursions in the normal boiler operating conditions have to be made. If such a control were implemented fault clearing times may not be critical for the transient stability of a unit.

6.3.3 Operational strategies

If the transient instability of a unit is economically inevitable, the turbogenerator is either shut down or allowed to pole-slip.

Shutting down the turbogenerator after a short duration fault decreases the system reliability and therefore increases the running spare capacity required with a detrimental effect on the economic operation.

Finally a possible strategy is to allow the generator to pole-slip after fault clearence and to implement automatic resynchronization. The biggest single difficulty of this scheme is to prevent power station auxiliaries from malfunctioning owing to the excessive fluctuations and depressions in the machine terminal voltage while pole-slipping takes place. The station can, however, be designed to allow for pole-slipping. If the behaviour of the control system approaches an optimum, the severity of the fault can be reduced to a large extent. If the number of pole-slips is limited to only one and an improved voltage supply to the power station auxiliaries is utilized, pole-slipping may be a very convenient way of dealing with the transient stability problem. Both the governor and the AVR are potentially capable of offering assistance during this transient.

If the time duration of the period of the transient when the machine is pole-slipping must be reduced, the governor and the AVR must act to prevent the rotor from being accelerated. As described in section 5.3 the acceleration of the turbogenerator rotor is due to two reasons:

a) the motoring action that takes place in the machine when the load angle is roughly between 180 and 360 degrees, and

b) the turbine power output.

If after the first cycle of motoring action the rotor has not overspeeded much above 2% (section 5.5.4) the turbogenerator can resynchronize slipping only one pole.

In order to reduce the motoring power while the synchronous generator is acting as a motor, the field excitation current must be reduced. From the recordings of the Northfleet pole-slip test it can be observed that the exciter voltage is being driven towards a maximum whilst motoring takes place. This action of the AVR is undesirable.

If the rotor is not allowed to overspeed much above 2% (section 5.5.4), then the governor does not sense an abnormal situation. As a result, the throttle valve is only partially closed and the interceptor valve is not closed at all. As the throttle valve controls turbine power output slowly owing to the long delays associated in the reheater, and as the interceptor valve is fully opened, the turbine power output is reduced only slightly.

As a consequence of poor performance by the excitation and governor systems during pole-slipping a supervisory control similar in structure to the fast-valving-logic can be very advantageous. If such a control scheme senses an abnormal situation with iminent pole-slipping, the excitation and governor systems should be inhibited, both turbine control valves closed and exciter voltage output reduced. A very significant reduction in the acceleration can be achieved in this way. If the prefault turbogenerator loading is restored in less than 10 seconds the plant may not suffer abnormal thermal stresses.

In order to improve power station auxiliary supply voltage, the auxiliaries can be fed from the local grid rather than from the generator terminals. Hence, from both improvements, power station auxiliaries can be saved from malfunction during pole-slipping.

6.4 Exceptional forms of power control

There are several other methods of dealing with the transient stability problem. For instance, h.v.d.c. links between power stations and consumer centers may be economically advantageous in certain cases. Furthermore, in conventional steam power stations there are many possibilities of power control which in the author's opinion has not received in the literature the attention they deserve. In one of these possibilities, a full load rejection is implemented after a short duration fault has developed outside the power station. This rejection is followed by very fast resynchronization in say less than 20 seconds, the prefault load restored in another 10 seconds. This strategy will now be discussed.

In the simulation results of Goldington full load rejection test presented in section 5.2 it can be observed that resynchronization can not be performed at the end of the transient when the shaft speed has reached its final value because the governor droop has introduced a relatively large speed error. Operator action is required to modify the speed changer setting in order to reduce the speed error and thus make resynchronization possible.

In the Northfleet case the situation is more complicated. Here the rotor speed is held near the overspeed setting of the interceptor valve for a long period. Again, operator intervention is needed to reduce rotor speed errors before resynchronization can be attained.

If a device were provided which inhibits the opening of governor valves after a full load rejection has taken place, the turbogenerator could be resyncronized as soon as the rotor speed equals synchronous; automatic governor control can then be restored. The station could thus generate prefault load in say 5 to 10 seconds after resynchronization has taken place.

In Fig. 5.19, curve "a" shows the estimated behaviour of the rotor speed of Northfleet power station when the unit does not run its own auxiliaries and it is resynchronized by inhibiting the opening of governor valves as described above.

Curve "b" describes a similar case but the unit supplies now the station auxiliaries. The situation is now more favourable because the station auxiliaries introduce a braking action.

Curve "c" present a hypothetical case in which braking resistors are used. This case is similar to the condition where the generator is left supplying a local load. Again an improved dynamic behaviour is obtained as more braking power is available. Braking resistors are applied to the turbogenerator terminals for the short time interval between the instant of time at which the turbogenerator rotor

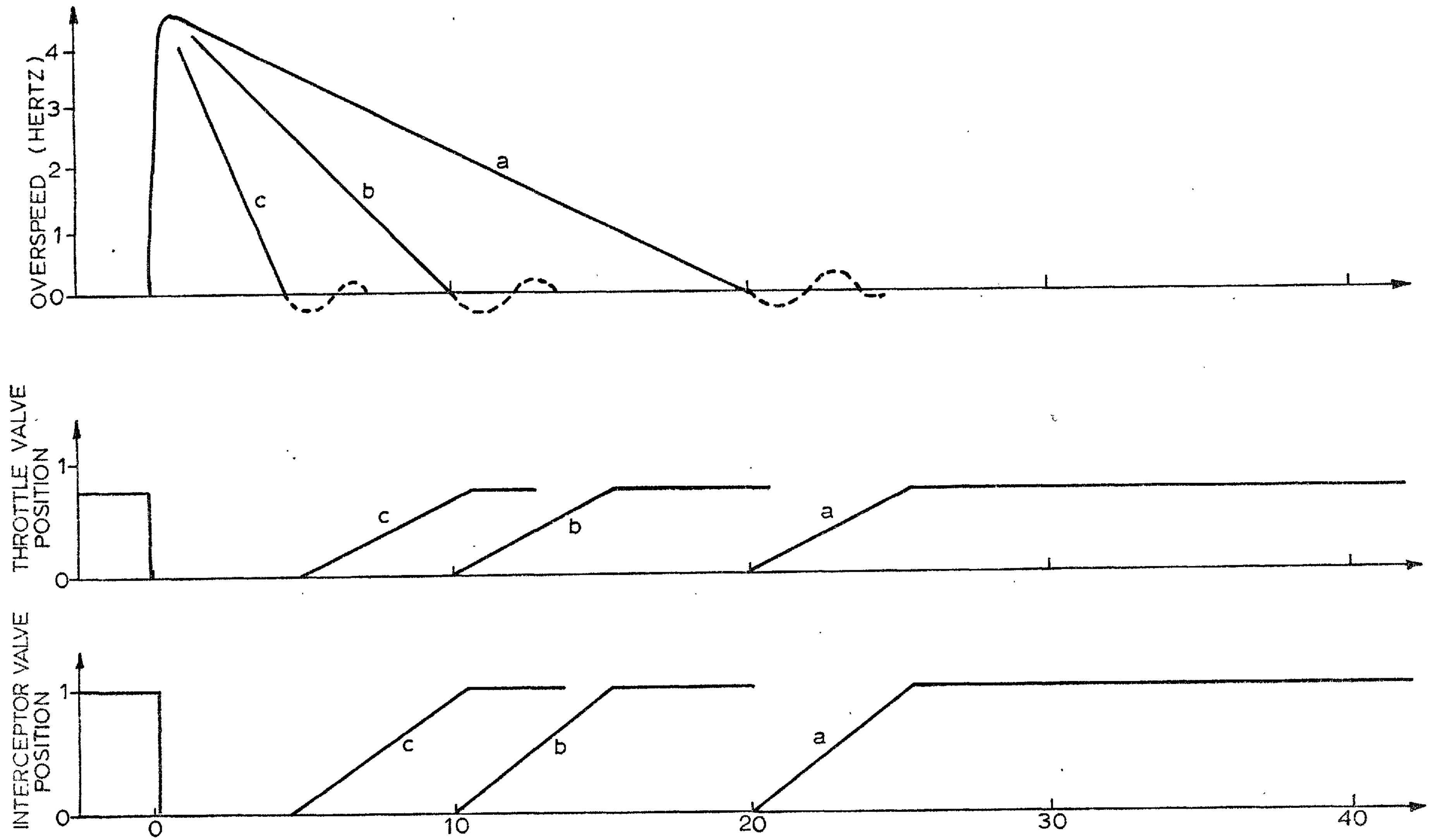

Fig. 6.2. Illustration of three possible types of full load rejections followed by very fast resynchronitation.

is at a maximum and when resynchronization is attained.

Undue stresses in turbine rotors are not likely to occur because load is restored before the rotor has cooled down. As with the case of fast valving of both governor valves the boiler is subjected to exceptional disturbances. It is doubtfull, however, in the author's opinion whether a full rejection cycle followed by very fast resynchronization would produce more severe stresses in the boiler superheaters than say during a hot start of the unit. Where an extra expense may be incured is in the boiler protection system which should discriminate between this full load rejection strategy from full trip of the unit. This is, however, a minor problem as compared with the potential benefits.

As the load is restored in less than 30 seconds problems involving system operation at low frequencies,owing to momentary power shortage, are not antecipated.

CHAPTER 7

CONCLUSIONS

7.1 General conclusions

The main purpose of this thesis has been the development of a large perturbation simulator of steam turbine characteristics for micromachine studies. This goal was accomplished and as a result much broader simulation studies using micromachines are now possible. The following general conclusions can be drawn from the studies described in this thesis:

1) Boiler characteristics are of increasing importance in power system dynamics. With the advent of large turboalternators, boiler characteristics have changed in such a way as to influence considerably the overall system dynamic behaviour.

2) The classical linear formulation of turbine characteristics shows deficiencies in both small and large perturbation simulations. In the nonlinear model of a turbine presented in this thesis an attempt has been made to correct these deficiencies.

3) The two turbine governor valves offer great potential for improving power system dynamics. With the advent of the new electro-hydraulic relay this potential can be easily exploited.

4) It was shown that slow opening as compared with closing rates of governor relays has beneficial effects in power system dynamic behaviour on small or large perturbations.

5) A study of pole-slipping conditions using a micromachine set and a digital computer resulted in a comprehensive explanation of the control aspects of the phenomena. It is concluded that if in the event of a short duration short circuit in the transmission system, pole-slipping follows, automatic resynchronization can be an effective way of dealing with this type of fault. Alternatively, this strategy could provide back-up protection in the event of circuit breaker malfunction.

6) Analysis of the simulation results of the load rejection tests of Goldington and Northfleet power stations has provided a detailed interpretation of this important transient and also resulted in devising another interesting alternative for dealing with short duration faults.

In this alternative the turbogenerator could be made to go through a full load rejection cycle and subsequent very fast resynchronization.

7) Micromachine losses have not received in the past much attention. It should be emphasized that in those cases where turbine characteristics are studied in detail, turbogenerator losses become very important, thus a high per--unit loss in a micromachine affects adversely simulation results.

8) Micromachines are eminently suitable for investigating the performance of new controllers. It is hoped that this thesis will encourage research in the analysis of turbine and boiler characteristics and the synthesis of optimum controllers.

9) Existing rectifier dynamic models were found to be incapable of describing the dynamic behaviour of the rectifier employed in the micromachine drive. The author therefore developed rigorously a large perturbation dynamic model for the rectifier in the micromachine drive. Owing to the complexity of this model, and poor performance of other existing models, the

author jointly with Sucena-Paiva developed a small perturbation model for a controlled rectifier. This small perturbation model permits the use of z-transform techniques for the dynamic analysis of rectifier systems. The rectifier speed control system of the microalternator drive is in many respects dynamically equivalent to rectifier systems employed in h.v.d.c. schemes connected to strong a.c. systems.

7.2 Original contributions

In the author's opinion the following contributions are considered to be original:

1) A nonlinear mathematical formulation of turbine characteristics for power system studies.

2) The development of a general purpose simulator of turbine characteristics for micromachine systems capable of simulating small or large perturbation conditions of steam turbines employed in power stations. The model was fully tested and good correlation was obtained with the results from real systems.

3) Two general purpose models of a steam power

plant were developed to investigate the interactions between the plant and its most important controllers i.e. boiler pressure controller, governor system and automatic voltage regulator. One of the models was specially designed for digital calculations and the other for analogue simulations.

4) A rigorous large perturbation model of the rectifier was developed. In this model allowances are made for overlap angles, the ripple content in the rectifier output quantities and the dynamic characteristics of the control system. Good correlation was obtained between this model and experimental measurements in a real system.

5) A small perturbation model for the rectifier was also developed jointly with Sucena-Paiva. This model is capable of taking into account overlap angles and the characteristics of the pulsing circuitry.

7.3 Suggestions for further work

The following are some of the limitations of the present study that need further investigation:

1) Further development of the boiler model. The parameters of this model should be determined from actual boiler characteristics. This model should also be capable of predicting accurately steam conditions before the throttle valve under any operating conditions.

2) The nonlinear formulation of turbine characteristics presented in this thesis need experimental corroboration.

3) A more detailed assessment of turbogenerator losses in connection with turbine dynamic studies is desired.

4) Power system simulation employing several micromachine sets furnished with turbine and boiler models can lead to deeper understanding of power system dynamics. Owing to the large amount of work that a project of this type would require, the formation of a small team of research students seems necessary.

5) In chapter 2 the dynamic model of a steam power plant was formulated mathematically and used to simulate only two power system transient faults. There is scope for the use of the model in investigating other transient conditions.

6) It is possible to devise strategies that will deal with exceptional operating conditions in a power system. Further research is required in this field. The micromachine system can validate the feasibility of the theories.

7) The dynamics of rectifier systems operating under constant current control could be understood better if the large perturbation behaviour of these systems were assessed more thoroughly. The application of the Liapunov Second Method to these rectifier systems offers an interesting area of research.

8) Using the discrete models presented in this thesis modern optimum control theory could be applied to rectifiers operating under constant current control.

BIBLIOGRAPHY

(1) Schurig, O. R.: "A miniature AC transmission system for the practical solution of network and transmission system problems", Trans.AIEE v42 1923, pp1033-40.

(2) Kostenko, M. P.: "Electrodynamic of the automatic control of power systems using electodynamic models", Institute of Electrodynamics, 1959.

(3) Robert, R.: "Micromachines and microreseaux: study of the problems of transient stability by the use of models similar electrodynamically to existing machines and systems", CIGRE v3 1950, paper No. 328.

(4) Robert, R.: "Le microreseau: modele dynamique des reseaux", Bulletin Societe Française des Electriciens v4 1954, pp67-87.

(5) Kostenko, M.P. : "Investigation of the automatic control of power systems using electrodynamic models" , Izdat. Akad. Nauk. U.S.S.R. 1957, pp60-91.

(6) Adkins, B.: "Micromachine studies at Imperial College", Elec. Times v138 1960, pp3-8.

(7) Mackley, K.W.: "Development of model power system", Elec. Engineer (Australia) v32 1955, pp17-22.

(8) Metha, D.B., and Adkins, B.: "Transient torque and load angle of a synchronous generator following several types of system disturbance", Proc. IEE v107-A 1960, pp61-73.

(9) Alford, R. G.,: "The stability of a synchronous gene-

rator associated with an induction motor load", Ph. D. Thesis, London University 1964.

(10) Harley, R. G. : "A general study of the transient stability of synchronous machines", Ph. D. Thesis, London University 1969.

(11) Kalsi, S. S. : "Transient phenomena in large induction motors in a power system", Ph. D. Thesis, London University 1970.

(12) Rao, K. V. N.: "Fault studies in synchronous generators with rectifier excitation", Ph. D. Thesis, London University 1970.

(13) Chorlton, A. : "Information about the work on a comparison of methods of studying stability", CIGRE 1964, paper No. 330.

(14) Scott, E.C., Casson, W., Chorlton, A., and Banks, J.H.: "Multigenerator transient stability performance under fault conditions", Proc. IEE v110 1963, pp1051-64.

(15) Chorlton, A., and Shackshaft, G.: "Report on comparison of accuracy of methods for studying stability. Northfleet exercise", CIGRE Study Committee No. 32, Working group C3.

(16) Shackshaft, G., and Neilson, R. : "Results of stability tests on an underexcited 120 MW generator", Proc. IEE v 119 1972, pp175-88.

(17) Jefferies, M. J., and Wright, A. : "New approach to micromachine construction ", Proc. IEE v 117 1970, pp1309-16.

(18) Hammons, T. J., and Parson, A. J. : "Design of microalternator for power system stability", Proc. IEE v118

1971, pp1421-41.

(19) Kabriel, B. J., and Evans, F. J. : "Electronic load angle measurement with unusually fast response", Trans. IEEE vIM-19 1970, pp51-6.

(20) Sheard, G. :"Elimination of time delay from shaft position or speed transducer outputs", Electronic Letters v6 1970, pp136-7.

(21) Stephenson, J. M. :"New low-noise tachogenerator", Proc. IEE v116 1969, pp1981-4.

(22) Winning, D. J. : "A fast response digital rotor angle transducer", Proc. EUPEC-1973, pp106-11.

(23) Sheard, G. and Evans, F. J. : "High speed pulse width modulated thyristor amplifier for motor control", Int. J. Control v12 1970, pp49-63.

(24) Hernandez, R., and Freris, L. L.: "Turbine and governor simulation on micromachines", Proc. SUPEC-1972, pp111-6.

(25) Hammons, T. J., Hogg, B. W., and Lewis, D. G. : "A microalternator system for power systems studies", Proc. SUPEC-1972.

(26) Farag,A. S. A., Malik, O. P., and Hope, G. S. : "Turbine model of generating unit", IEEE paper, No. C 72 578-3.

(27) Mesple, D. E., Tam, T. K. K., and Smith, O. J. M. : "Excitation control of synchronous generators", Electronic research laboratory, University of California, Berkeley, Memorandum No. ERL-M337.

(28) Shackshaft, G. : "General purpose turbo-alternator model", Proc. IEE v110 1963, pp703-13.

(29) Hammons, T. J., and Winning, D. J. : "Comparisons of

synchronous machine models in the study of the transient behaviour of electric power systems", Proc.IEE v118 1971, pp1442-58.

(30) Humpage, W. D., and Saha, T. N. :"Digital-computer methods in dynamic response analysis of turbogenerator units", Proc. IEE v114 1967, pp1115-30.

(31) Harley, R. G. and Adkins, B.: "Calculation of the angular back swing following a short circuit of a loaded alternator", Proc. IEE v117 1970, pp377-86.

(32) Cory, B. J. : "Personal communication"

(33) IBM : "Power system simulator description of models", Report No. GE20-0387-0.

(34) Young, C.C.: "Equipment and system modelling for large scale stability studies", Trans. IEEE vPAS-91 1972, pp163-72.

(35) Baldwin, C. J., and Byerly, R. T. : "Recent advances in the digital simulation of power system disturbances", Power System Computation Conference v1 1969, paper No. D. & C.4.

(36) Battlebury, D. R. : "Total power system model", Proc. SUPEC-1972, pp17-22.

(37) Berg, G. J. : "System and load behaviour following loss of generation. Experimental results and evaluation", Proc. IEE v119 1972, pp1483-6.

(38) Computer analysis of power systems working group : "System load dynamic simulation effects and determination of load constants", IEEE paper, No. T 72 427-3.

(39) Mauricio, W., Semley, A. : "Effect of load characteristics on the dynamic stability of power systems",

Trans. IEEE vPAS-91 1972, pp2295-304.

(40) Tesla, N.: "A new system of alternate current motors and transformers", Trans. AIEE v5 1888, pp308-27.

(41) Blondel, A. E. : "Synchronous motors and convertors", McGraw Hill 1913.

(42) Park, R. H. "Two reaction theory of synchronous machines", part 1, Trans. AIEE v48 1929, pp716-29; and part 2, Trans. AIEE v52 1933, pp352-5.

(43) Adkins, B.: "The general theory of electrical machines", Chapman and Hall 1959.

(44) Iyer, S. N. : "Dynamic optimization of synchronous turbogenerator performance under transient conditions", Ph. D. Thesis, London University 1969.

(45) White, D. C., and Woodson, H. H. :"Electromechanical energy conversion", John Willey and Sons 1959.

(46) Chen, C. F.:"A matrix Cauer model in multivariable systems analysis and design", IEE Conference publication No. 78, pp66-70.

(47) Devotta, J. B. X. : "The optimal control of a synchronous generator with a divided winding rotor", Ph. D. Thesis, London University 1972.

(48) Church, E. F. : "Steam turbines", McGraw Hill 1950.

(49) Waren, G. B., and Keenan, J. H. : "An experimental investigation of nozzle efficiency", Trans. ASME v48 1926, pp33-64.

(50) Dollin, F. : "Investigation of steam turbine nozzle and blading efficiency", Proc. Inst. Mech. Eng. v144 1941, pp144-64.

(51) Report of steam nozzle research commite : Proc. Inst. Mech. eng. 1923, pp1-22, and pp311-95; 1924, pp455-525 and pp715-35; 1925, pp747-843; 1928, pp31-60; 1930, pp215-58.

(52) Oakden, J. C. : "The significance of the term "efficiency" as applied to steam nozzles", Proc. Inst.Mech. Eng. v120 1931, pp603-9.

(53) Kearton, W. J. : "Effects of inertia on flow of steam through nozzles and blading of axial flow turbines", Proc. Inst. Mech. Eng., v166 1952, pp429.

(54) Bauer, G., and Lasche, O. : "Marine steam turbines", Crosbie Lockwood & Sons 1911.

(55) Bond, R. C. : "Ten years experience with LMS 4-6-2 non--condensing turbine locomotive", Journal of the Institute of Locomotive Engineers v36 1946, paper No. 458.

(56) Stodola, A.: "Steam turbines", volumes 1 and 2, McGraw Hill 1950.

(57) Kearton, W. J.: "Steam turbine theory and practice", Pitman 1972.

(58) Higgs-Walker, G. W.: "Some problems connected with steam turbine governing", Proc. Inst. Mech. Eng. v146, pp117-25.

(59) Waren, G. B. and Knowlton, P. H.: "Relative engine efficiencies realizable from large modern steam turbines", Trans. ASME v63 1941, pp125-35.

(60) Elston, C. W., and Knowlton, P. H.: "Comparative efficiencies of central-stations reheat and nonreheat steam-turbine-generator units", Trans. ASME v74 1952,

pp1389-99.

(61) Hegetschweiler, H., and Barlett, R. L.: "Predicting performance of large steam turbine-generator units for central stations", Trans. ASME v79 1957, pp1085-114.

(62) Spencer, R. C., Cotton, K. C.: "A method for predicting the performance of steam turbine generators 16500KW and larger", Trans. ASME v85 1963, pp249-301.

(63) Hardy, M.: "Personal communication".

(64) Jolley, W. P.: "General purpose turbine model", Conference on application of simulation to power units and systems, Huddersfield Polytechnic 1972.

(65) Aanstad, D. J.: "Dynamic response and data constants for large steam turbines", IEEE tutorial course, paper No 70 M 29-PWR.

(66) Bower, J. B. C., and Bradbury, K. J.: "DC link isolated generator real power control", IEE conference publication No. 22, pp161-68.

(67) Hughes, F. M.: "Improvement of turbogenerator transient performance by control means", Proc. IEE v120 1973, pp103-13.

(68) Hiorns, D. S.: "Control of control", Proc. IEE v120 1973, pp103-13.

(69) Profos, P.: "Dynamics of pressure and combustion control in steam generators", Sulzer Tech. Review v39 1955, pp13-28.

(70) Laubli, F., and Fenton, F. H.: "The flexibility of the supercritical boiler as a partner in power system design and operation", part 1 and 2, Trans. IEEE vPAS-90 1971, pp1719-33.

(71) Astrom, K. J., and Eklund, K.: "A simplified nonlinear model of a drum boiler turbine unit", Int. J. Control v16 1972, pp145-69.

(72) Chien, K. L., Ergin, E. I., Ling, C., and Lee, A.: "Dynamic analysis of a boiler", Trans. ASME v80 1958, pp1809-19.

(73) Daniels, J. H., Enns, M., and Hottenstine, R. D.: "Dynamic representation of a large boiler-turbine unit", ASME paper No. 61-SA-69.

(74) Nicholson, N.: "Dynamic optimisation of a boiler-turbo-alternator unit", Proc. IEE v113 1966, pp385-99.

(75) Thompson, F. T.: "A dynamic model of a drum-type boiler system", Trans. IEEE vPAS-86 1967, pp625-35.

(76) Kwan, H. W., and Anderson, J. H.: "A mathematical model of a 200 MW boiler", Int. J. Control v12 1970, pp977-98.

(77) Hammons, T. J.: "Simulation of once through boilers employed for steam supply to large thermo-electric power units", Proc. SUPEC-1972, pp222-30.

(78) Hingorani, N. G., Hay, J. L., and Crosbie, R. E.: "Dynamic simulation of h.v.d.c. transmission systems on digital computers", Proc. IEE v110 1963, pp793-802.

(79) Busemann, F.: "HVDC transmission: hunting of rectifiers with marked compounding", ERA Report B/T 104, 1951.

(80) Reider, A. M.: "Analysis of the stability of the control systems of the Kashira-Moscow direct current transmission line", Direct Current v3 1957, pp227-40.

(81) Andeen, R. E.: "The principle of equivalent areas", Trans. IEEE vAI-79 1960, pp332-6.

(82) Andeen, R. E.: "Analysis of pulse duration sampled-data systems with linear elements", Trans. IRE vAC-5 1960, pp306-13.

(83) Bjäresten, N. A.: "Tha static convertor as a high speed power amplifier", Direct Current v8 1963, pp154-65.

(84) Fallside, F., and Farmer, A. R.: "Ripple instability on closed-loop control systems with thyristor amplifiers", Proc. IEE v114 1967, pp139-52.

(85) Fallside, F., Goodman, C. J., and Jackson, R. D.: "Stability of first-order sampling and thyristor systems", Electronic Letters v5 1969, pp567-8.

(86) Whittaker, E. T., and Watson, G. N.: "Modern Analysis", Cambridge 1927.

(87) Persson, E. V.: "Calculation of transfer functions in grid-controlled convertor systems", Proc. IEE v117 1970, pp989-97.

(88) Parish, P. A., and McVey, E. S.: "A theoretical model for single-phase silicon controlled rectifier systems", Trans. IEEE vAC-12 1967, pp577-9.

(89) Hazell, P. A., and Flower, J. O.: "Stability properties of certain thyristor bridge control", part 1, Proc. IEE v117 1970, pp1405-12.

(90) Ibidem, part 2, Proc. IEE v117 1970, pp1413-20.

(91) Sucena-Paiva, J. P., Hernandez, R., and Freris, L. L.: "Stability study of controlled rectifiers using a new discrete model", Proc. IEE v119 1972, pp1285-93.

(92) Flower, J. O., and Hazell, P. A.: "Nonlinear analysis of a first-order thyristor bridge", Proc. IEE v118 1971, pp1511-16.

(93) Park, R. H.: "Definition of an ideal synchronous machine and formula for the armature flux linkages", G. E. Review v31 1928, pp332-4.

(94) Crary, S. B.: "Power systems stability", vol. 1 and 2, John Willey Sons 1955.

(95) Shackshaft, G.: "Effect of oscillatory torques on the movements of generator rotors", Proc. IEE v117 1970, pp1969-74.

(96) Kimbark E. W.: "Power systems stability", vol. 1, 2 and 3, John Willey Sons 1950.

(97) Kalderon, D.: "Large steam turbines for nuclear and conventional power stations", Journal of Science and Technology v38 1971, pp21-30.

(98) Pochobracksky, B.: "Effect of centrifugal forces in axial flow turbines", Engineering v163 1947, pp205-7.

(99) Kearton, W. J.: "The distribution of pressures in impulse steam turbines at varying loads", Engineering v122 1926, pp365-8.

(100) Cotton, K. C., and Schofield, P.: "Analysis of changes of the performance characteristics of steam turbines", Trans. ASME Journal of Eng. for power v93 1971, pp225-37.

(101) Soper, J. A., and Fagg, A. R.: "Divided winding rotor synchronous generator", Proc. IEE v116 1969, pp113-26.

(102) CEGB: "Modern power station practice", vol. 3, Pergamon Press 1971.

(103) Necleba, M.: "Theory of indirect speed control", John Willey & Sons 1964.

(104) IBM: "Application programs", Programmer's manual No. H20-0205-3.

(105) British Standard Institution: "Test code for acceptance test for steam turbines", BS752, 1958.

(106) Evans, F. J., Robinson, R. B., and Wilson, T.: "Model power systems", Elec. Eng. Trans. Aust. v6 1970, pp53-9.

(107) Kumar, D.: "Analogue and digital control of high voltage d.c. transmission systems under fault conditions", Ph. D. Thesis, London University 1969.

(108) Bayoumi, M.: "Transient and steady-state current of a q-phase controlled rectifier", Neue Technik v4 1962, pp141-5.

(109) Adamson, C., and Hingorani, N.: "High voltage direct transmission", Garraway 1964.

(110) Sucena-Paiva, J. P.: "A steady-state stability study of convertors and high voltage d.c. transmission systems", Ph. D. Thesis, London University 1972.

(111) Flower, J. O., Windett, G. P., and Forge, S. C.: "Aspects of the frequency response testing of sampled systems", Int. J. Control v14 1971, pp881-96.

(112) Poliack, M. A.: "Short circuit asynchronous drive and turbogenerator resynchronization", Electric Technology U.S.S.R. v4 1959, pp519-31.

(113) Cooper, C. B., Easton, V., John, M. N., Parton, R. C., Shackshaft, G., and Whitelegg, T. M.: "Problems associated with limited pole-slipping of turbogenerators", CIGRE 1966, paper No. 306.

(114) Mason, T. H., Fairney, W., Arnold, J. J., and Thelwell, M. J.: "Asynchronous operation of turbogenerators", CIGRE 1972, paper No. 11-02.

(115) Busemann, F., and Casson, W.: "Results of full-scale stability tests on the British 132 KV grid", Proc. IEE v105A 1958, pp347-62.

(116) Hillery, R. H., and Holdup, E.: "Load rejection testing of large thermal-electric generating units", Trans. IEEE vPAS-87 1968, pp1440-53.

(117) Cushing, E. W., Dreschler, G. E., Killgoar, W. P., Marshall. H. G., and Stewar, H. R.: "Fast valving as an aid to power systems transient stability and re-synchronization and rapid reload after a full load rejection", Trans. IEEE vPAS-91 1972, pp2517-27.

(118) Olken, M. I., and Wolfle, W. T.: "Load rejection of subcritical steam turbines generator units", IEEE paper No. T 72 580-9.

(119) Akers, H. T., Dickinson, J. D., and Skooglund, J. W.: "Operation and protection of large steam turbine generators under abnormal conditions", Trans. IEEE vPAS--87 1968, pp1180-8.

(120) Lokay, H. E., and Thoits, P. O.: "Effects of future turbine generator characteristics on transient stability", Trans. IEEE vPAS-90 1971, pp2427-31.

(121) Concordia, C., and Brown, P. G.: "Effects of trends in large steam turbine driven generator parameters on power system stability", Trans. IEEE vPAS-92, pp2211-8.

(122) James, L. W.: "Progress in the development of large turbine type generators", IEE Hunter Memorial Lecture 1973.

(123) Shackshaft, G.: "Generator stability improved by an interconnected winding rotor", Electrical Times v159 1971, pp2-6.

(124) Concordia, C.: "Future development of large electric generators", Disscussion meeting on recent advances in heavy electrical plant, The Royal Society 1973.

(125) O'Kelly, D., and Musgrave, G.: "Improvement of power--system transient stability on phase-shift insertion", Proc. IEE v120 1973, pp247-52.

(126) Park, R. H.: "Improved reliability of bulk power supply by fast load control", American Power Conference v30 1968, pp1128-41.

(127) Jervis, W. B.: "Electronic governor" applied to prime movers of synchronous generators, IEE Lecture 1973.

(128) Aanstad, O. J., and Lokay, H. E.: "Fast valve control can improve turbine generator response to transient disturbances", Westinghouse Engineer v30 1970, pp114-9.

(129) Martin, M. E., Triezenberg, D. M., and Krause, P. C.: "A study of fast turbine valving", IEEE paper No. C 73 080-9.

(130) Blackburn, J. F., Reethof, G., and Shearer, J. L. : "Fluid power control", The M.I.T. Press 1969.

(131) Shapiro, A. H.: "The dynamics and thermodynamics of compressible fluid flow", vol. 1, Ronald Press 1973.

(132) Jury, E.: "Sampled-data control systems", John Willey & Sons 1958.

APPENDIX 1

State space simplified formulation of synchronous machine dynamics

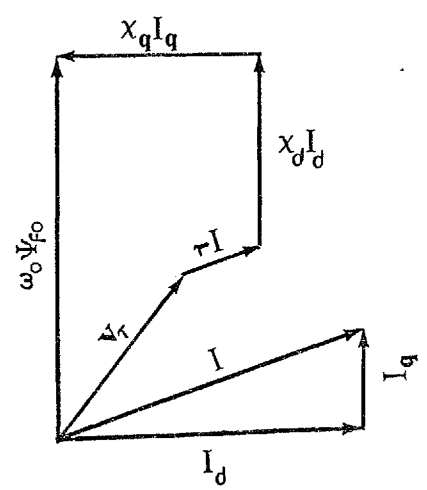

Fig. A1 Synchronous machine phasorial diagram

Equations 2.3 show that a synchronous machine is represented by the phasorial diagram drawn in Fig. A1. From this diagram the following vectorial equation may be written

$$\omega_o \vec{\Psi}_{fo} = r\,(\vec{I}_d + \vec{I}_q) + jx_d \vec{I}_d + jx_q \vec{I}_q + \vec{V}_t \qquad (A1.1)$$

where

r	$= r_a + r_{ext}$
x_d	$= x_{md} + x_{al} + x_{ext}$
x_q	$= x_{mq} + x_{al} + x_{ext}$
$\vec{I}_{d,q}$	vectors representing direct and quadrature currents in quasi steady-state.

$\overrightarrow{V_t}$ bus voltage

$$\overrightarrow{V_t} = \sqrt{2}\ V_b\ [\sin\delta + j\cos\delta]$$

$$\omega_o\ \overrightarrow{\Psi_{fo}} = (i_f\ x_{md})\ j$$

Equation A1.1 can be decomposed into two scalar equations

$$\begin{aligned} \omega_o\ \Psi_{fo} &= r\ I_q + x_d\ I_d + \sqrt{2}\ V_b\ \cos\delta \\ 0 &= r\ I_d - x_q\ I_q + \sqrt{2}\ V_b\ \sin\delta \end{aligned} \qquad (A1.2)$$

I_d and I_q can now be obtained as functions of Ψ_{fo} and δ

$$\begin{aligned} I_d &= \frac{x_q}{Z^2}\left[\omega_o\ \Psi_{fo}\frac{x_{md}}{x_{fd}} - \frac{r}{x_q}\sqrt{2}\ V_b\ \sin\delta - \sqrt{2}\ V_b\ \cos\delta\right] \\ I_q &= \frac{1}{Z^2}\left[\frac{x_{md}\ r}{x_{fd}}\ \omega_o\ \Psi_{fo} - x_d'\sqrt{2}\ V_b\ \sin\delta - r\sqrt{2}\ V_b\ \cos\delta\right] \end{aligned} \qquad (A1.3)$$

where

$$x_{fd} = x_{md} + x_{f1}$$

$$x_d' = x_d - \frac{x_{md}^2}{x_{fd}}$$

$$Z^2 = r^2 + x_d'\ x_q$$

From equation 2.3 the differential equation of the field winding can be written as follows

$$p\ [\omega_o\ \Psi_f] = \omega_o\ V_f - \omega_o\ r_f\ i_f \qquad (A1.4)$$

From equation 2.3 the flux linkage equation can also be written

$$\omega_o \Psi_f = (x_{md} + x_{f1}) i_f - x_{md} I_d \qquad (A1.5)$$

Eliminating i_f and I_d in equations A1.3, A1.4 and A1.5 the first state equation is obtained

$$p [\omega_o \Psi_f] = \omega_o V_f - B \omega_o \Psi_f + C \sin\delta + D \cos\gamma \qquad (A1.6)$$

where

$$B = \omega_o r_f \left[\frac{1}{x_{fd}} + \frac{x_q x_{md}^2}{Z^2 x_{fd}^2} \right]$$

$$C = \omega_o r_f \frac{r x_{md}}{Z^2 x_{fd}} \sqrt{2} V_b$$

$$D = \frac{x_q}{r} B$$

Finally, the electrical torque as a function of the state variables has to be determined. From equation 2.1 the electrical torque is given by

$$T_e = \frac{1}{2} \left[\omega_o \Psi_d i_q - \omega_o \Psi_q i_d \right] \qquad (A1.7)$$

After substituting equation A1.3, A1.5 and the flux linkage equation 2.3 into equation A1.7 the electrical torque can be obtained as a function of the state variables only

$$T_e = S_1 \sin^2\delta + S_2 \cos^2\delta + S_3 (\omega_o \Psi_f)^2 + \qquad (A1.8)$$

$$+ S_4 \sin\delta \cos\delta + S_5 \sin\delta \omega_o \Psi_f + S_6 \omega_o \Psi_f \cos\delta$$

where

$$S_1 = - \frac{x_{md}^2 \; x_d' \; r}{x_{fd} \; Z^4} V_b^2$$

$$S_2 = \frac{x_{md}^2 \; x_q \; r}{x_{fd} \; Z^4} V_b^2$$

$$S_3 = \frac{x_{md}^2 \quad r}{2 \; x_{fd}^2 \; Z^4} (r^2 + x_d' \; x_q + x_{md} \; x_q)$$

$$S_4 = \frac{x_{md}^2}{x_{fd} \; Z^4} (r^2 - x_q \; x_d') \; V_b^2$$

$$S_5 = \frac{x_{md}}{\sqrt{2} \; x_{fd} \; Z^2} \left[x_d' + \frac{x_{md}^2}{Z^2 x_{fd}} (x_q \; x_d' - r^2) \right] V_b^2$$

$$S_6 = - \frac{x_{md}}{\sqrt{2} \; x_{fd} \; Z^2} \left[r + \frac{x_{md} \; r}{Z^2 x_{fd}} (x_q \; x_{md} - r^2) \right] V_b^2$$

APPENDIX 2

EFFICIENCY OF A SYMMETRICAL REACTION STAGE

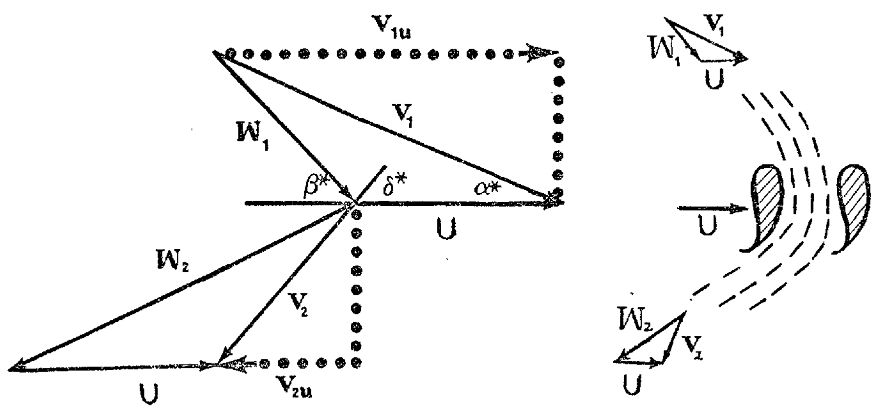

Fig. A2 velocity diagram of a symmetrical reaction stage

According to Newton's second law of motion, force is measured by the rate of change of momentum; hence, the force acting on a rotor blade per unit of steam mass is given by

$$\text{Force} = \frac{1}{g}\left(v_{1u} - v_{2u}\right) \qquad \text{(A2.1)}$$

The power supplied by the stage to the rotor is equal to the force multiplied by the distance moved per--second.

$$\text{Power} = \frac{1}{g}\,(v_{1u} - v_{2u})U \qquad \text{(A2.2)}$$

Equation A2.2 can be written as a function of the entering and leaving steam velocities

$$\text{Power} = \frac{U}{g}\,(v_1 \cos\alpha^* - v_2 \cos\delta^*) \qquad \text{(A2.3)}$$

From Fig. A2 it can be readily seen that

$$\text{Power} = \frac{U}{g}\,(2v_1 \cos\alpha^* - U) \qquad \text{(A2.4)}$$

Substituting the speed ratio ($r = \frac{U}{v_1}$) into equation A2.4

$$\text{Power} = \frac{v_1^2}{g}\,(2r \cos\alpha^* - r^2) \qquad \text{(A2.5)}$$

Assuming the same nozzle efficiency η_n for both stationary and moving rows and letting η_{co} be the carry over efficiency, the kinetic energy leaving one stage and available for work in the next is $\eta_{co} \frac{V_2^2}{2}$; therefore

$$J \eta_n \frac{\Delta hs}{2} = \frac{V_1^2}{2g} - \eta_{co} \frac{V_2^2}{2g} \qquad \text{(A2.6)}$$

For a stage consisting of two symmetrical rows the energy available is

$$J\, \eta_n \Delta h_s = \frac{2}{\eta_n}\left[\frac{V_1^2}{2g} - \eta_{co} \frac{V_2^2}{2g}\right] \qquad \text{(A2.7)}$$

The combined nozzle and blade efficiency (η_{nb}) can now be obtained dividing equation A2.5 into equation A2.7

$$\eta_{nb} = \frac{2\ r\ \cos\alpha^* - r^2}{1 - \eta_c \left(\frac{V_2}{V_1}\right)^2} \qquad (A2.8)$$

From Fig. A2, it can be shown that

$$\left(\frac{V_2}{V_1}\right)^2 = 1 + r^2 - 2r\ \cos\alpha \qquad (A2.9)$$

And substituting equation A2.9 into equation A2.8 the stage efficiency as a function of the velocity ratio is finally obtained[48]

$$\eta_{nb} = \eta_n \frac{2\ r\ \cos\alpha^* - r^2}{1 - \eta_{co}\ (1 + r^2 - 2r\ \cos\alpha^*)} \qquad (2.10)$$

The stage efficiency as a function of the velocity ratio is plotted in Fig. 2.17.

APPENDIX 3

GAS FLOW IN NOZZLES

The expansion of a gas in a nozzle can be analysed applying the first law of thermodynamic in both sides of the nozzle, thus

$$\frac{V_1^2}{2g} + u_1 + p_1\, v_1 = \frac{V_o^2}{2g} + u_o + p_o\, v_o \qquad (A3.1)$$

Where

$V_{o,1}$ steam velocity entering and leaving the nozzle

$u_{o,1}$ steam internal energy entering and leaving the nozzle

$p_{o,1}$ steam pressure entering and leaving the nozzle

$v_{o,1}$ steam specific volume entering and leaving the nozzle.

The difference of internal energies in equation A3.1 represents the isentropic work

$$u_o - u_1 = \int_{v_o}^{v_1} p\, dv \qquad (A3.2)$$

Substituting into equation A3.2 the equation describing the isentropic expansion of a gas ($pv^{\gamma} = c$. Where γ is the ratio of specific heats C_p/C_v and c is a constant) and integrating

$$u_o - u_1 = \frac{p_o v_o - p_1 v_1}{\gamma - 1} = \frac{RT}{\gamma - 1} \left(1 - \left(\frac{P_1}{P_o}\right)^{\frac{\gamma-1}{\gamma}}\right) \tag{A3.3}$$

The exit velocity of the gas can now be obtained by substituting equation A3.3 into equation A3.1

$$V_1 = \left[\frac{\gamma}{\gamma-1} 2g\, p_o\, v_o \left(1 - \left(\frac{P_1}{P_o}\right)^{\frac{\gamma-1}{\gamma}}\right) + V_o^2\right]^{\frac{1}{2}} \tag{A3.4}$$

The steam flow (W) can be obtained using the equation of continuity

$$W = \frac{A\, V_1}{v_1} \tag{A3.5}$$

If the gas behaviour is perfect, at the nozzle inlet

$$W = A\, p_o \sqrt{\left(\frac{2\gamma}{\gamma-1}\ \frac{1}{RT_o} \left[\left(\frac{P_1}{Po}\right)^{\frac{\gamma}{2}} - \left(\frac{P_1}{Po}\right)^{\frac{\gamma+1}{2}}\right] + V_o^2\right)} \tag{A3.6}$$

Where

T_o up stream stagnation temperature

R universal gas constant

In many cases the gas entering velocity can be neglected, thus

$$W = A\ p_o \sqrt{\left\{g\ \frac{2\gamma}{\gamma-1}\ \frac{1}{RT_o}\ \left[\left(\frac{P_1}{P_o}\right)^{\frac{\gamma}{2}} - \left(\frac{P_1}{P_o}\right)^{\frac{\gamma+1}{2}}\right]\right\}}$$

(A3.7)

A velocity discharge coefficient (c_d) is introduced by many investigators in order that equation A3.7[130] matches experimental measurements

$$W = A\ p_o\ c_d \sqrt{\left\{g\ \frac{2\gamma}{\gamma-1}\ \frac{1}{RT_o}\ \left[\left(\frac{P_1}{P_o}\right)^{\frac{\gamma}{2}} - \left(\frac{P_1}{P_o}\right)^{\frac{\gamma+1}{2}}\right]\right\}}$$

(A3.8)

If the gas flow is supersonic, equation A3.8 does not depend upon the down stream pressure[131]

$$W = A\ p_o\ c_d \sqrt{\left[\left(\frac{2}{\gamma+1}\right)^{\frac{\gamma+1}{\gamma-1}}\ g\ \ \frac{\gamma}{RT_o}\right]} \qquad (A3.9)$$

Summarizing, the flow of a gas through a nozzle is of the following form

$$W = A\ c_d\ \ f\ (P_o,\ T_o,\ \frac{P_1}{P_o}\ ) \qquad \text{(A3.10)}$$

where

$$f(P_o, T_o, \frac{P_1}{P_o}) = \begin{cases} P_o \sqrt{\left\{\frac{2\gamma}{\gamma-1}\ g\ \frac{1}{RT_o}\left[\ (\frac{P_1}{P_o})^{\frac{\gamma}{2}} - (\frac{P_1}{P_o})^{\frac{\gamma+1}{\gamma}}\ \right]\right\}} & \frac{P_1}{P_o} > (\frac{P_1}{P_o})_{critical} \\ P_o \sqrt{\left[(\frac{2}{\gamma+1})^{\frac{\gamma+1}{\gamma-1}}\ g\ \frac{\gamma}{RT_o}\right]} & \frac{P_1}{P_o} < (\frac{P_1}{P_o})_{critical} \end{cases}$$

APPENDIX 4

TIME LAG CAUSED BY ENTRAINED STEAM

CONTROL VOLUME

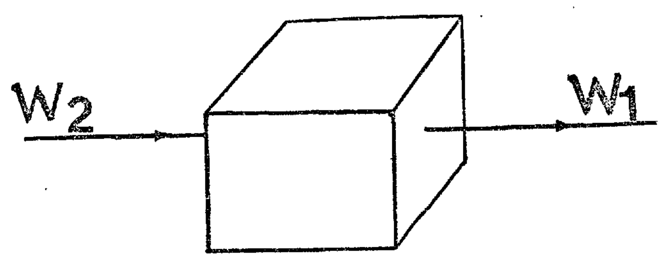

Fig. A4

The time delay caused by entrained steam will be evaluated here assuming a fill in process takes place in the control volume. The mass balance in the working medium of the system shown in Fig. A4 can be modelled mathematically by means of the following differential equation

$$W_{BASE} \left[W_2 - W_1\right] = p\left[\rho V\right] \qquad (A4.1)$$

Where

W_1 per-unit steam flow leaving the control volume

W_2 per-unit steam flow entering the control volume

W_{BASE} base in which steam mass flows are refered

V Volume under consideration

ρ steam density

Assuming steam behaves as a perfect gas, and an isothermal process takes place in the control volume equation, A4.1 becomes

$$W_2 - W_1 = T_\mu \; p(p_c) \tag{A4.2}$$

Where

$$T_\mu = \frac{V \; P_{BASE}}{W_{BASE} \; p \; v}$$

p_c control volume pressure

P_{BASE} base to which control volume pressure is refered

APPENDIX 5

ANALYSIS OF A HYDRAULIC RELAY

The basic assumptions associated with the modelling of a hydraulic relay, of the type shown in Fig. 2.20, are:

(1) the hydraulic fluid is incompressible,

(2) friction forces are negligible,

(3) inertia forces are small compared with hydraulic forces, and

(4) supply and drain fluid pressures are invariant.

Under these conditions, the flow of oil through an orifice of the type shown in Fig. 2.20 is given by[102]

$$q = c_d A_1 \sqrt{\left[2(P_p - P_B)/\rho\right]} \qquad \text{(A5.1)}$$

Where

q	hydraulic fluid flow
c_d	discharge factor
A_1	orifice area
P_p	supply pressure
P_B	drain pressure
ρ	hydraulic fluid density

As inertia and friction forces are assumed to be negligible and the fluid is treated as incompressible, the motion of the main piston is given by

$$A_1 \ p y = q = c_d \ A_1 \sqrt{\left[2 \ (P_p - P_B)/\rho\right]} \qquad (A5.2)$$

The area A_1 is proportional to the main piston displacement

$$A_1 = K_1^* \ v \qquad (A5.3)$$

Reagrouping equations A5.2 and A5.3 and taking the supply and drain pressures as invariants

$$py = K^* v \qquad (A5.4)$$

Where

$$K^* = \frac{c_d \ K_1^*}{A_1} \sqrt{\left[2 \ (P_p - P_B)/\rho\right]}$$

The linkage shown in Fig. 2.20 among points A, B and C constraints the motion of these three points; mathematically[103]

$$X = \frac{b}{a} y + \frac{a+b}{a} v \qquad (A5.5)$$

Substituting equation A5.5 into equation A5.4

$$py = K^* \frac{a}{a+b} \left(x - \frac{b}{a} y\right) \qquad (A5.6)$$

Therefore

$$y = \frac{G}{1+pT} x \qquad (A5.7)$$

Where

$$G = \frac{a}{b}$$

$$T = \frac{a+b}{K^* b}$$

APPENDIX 6

THE TURBINE SIMULATOR DESIGN

Some details of the turbine simulator design are given in this appendix.

The power circuitry of the rectifier is shown in Fig. A6.1. In order to satisfy accuracy, transient response performance and to isolate the power from the electronic circuitry, a Hall effect device was used to sense the d.c. machine armature current. The small voltage level of the output signal of this device was amplified by means of integrated circuits as shown in Fig. A6.2.

The firing circuitry for the thyristors of the rectifier is presented in Fig. A6.3. The pulsing units were developed by Kumar and are described[107] elsewhere. Ramp rising reference voltage signals are initiated for each thyristor at the cross over points of the corresponding commutating voltage. At the instant at which the ramp signal and the control voltage are equal a pulse is applied to the corresponding thyristor gate.

The protection system of Fig. A6.4 has been designed to provide proper action under any of the following faults:

1 field circuit of the d.c. machine opens suddently,

2 armature current of the d.c. machine increased above nominal levels, and

3 armature voltage of the d.c. machine increased above nominal levels.

Micromachine set details and list of components are shown in Tables A6.1 and A6.2

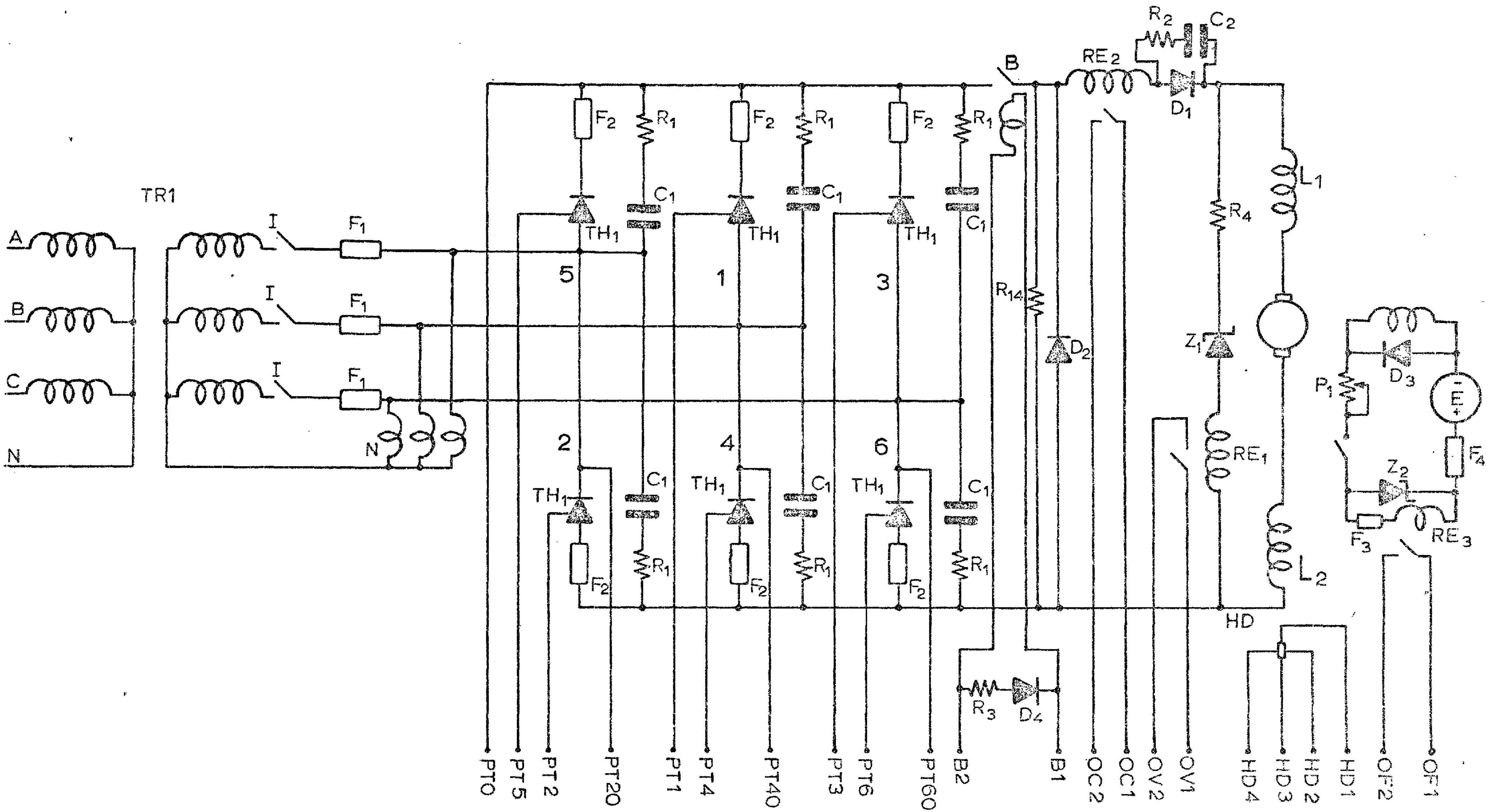

Fig. A6.1. Circuit diagram of the rectifier (Power side)

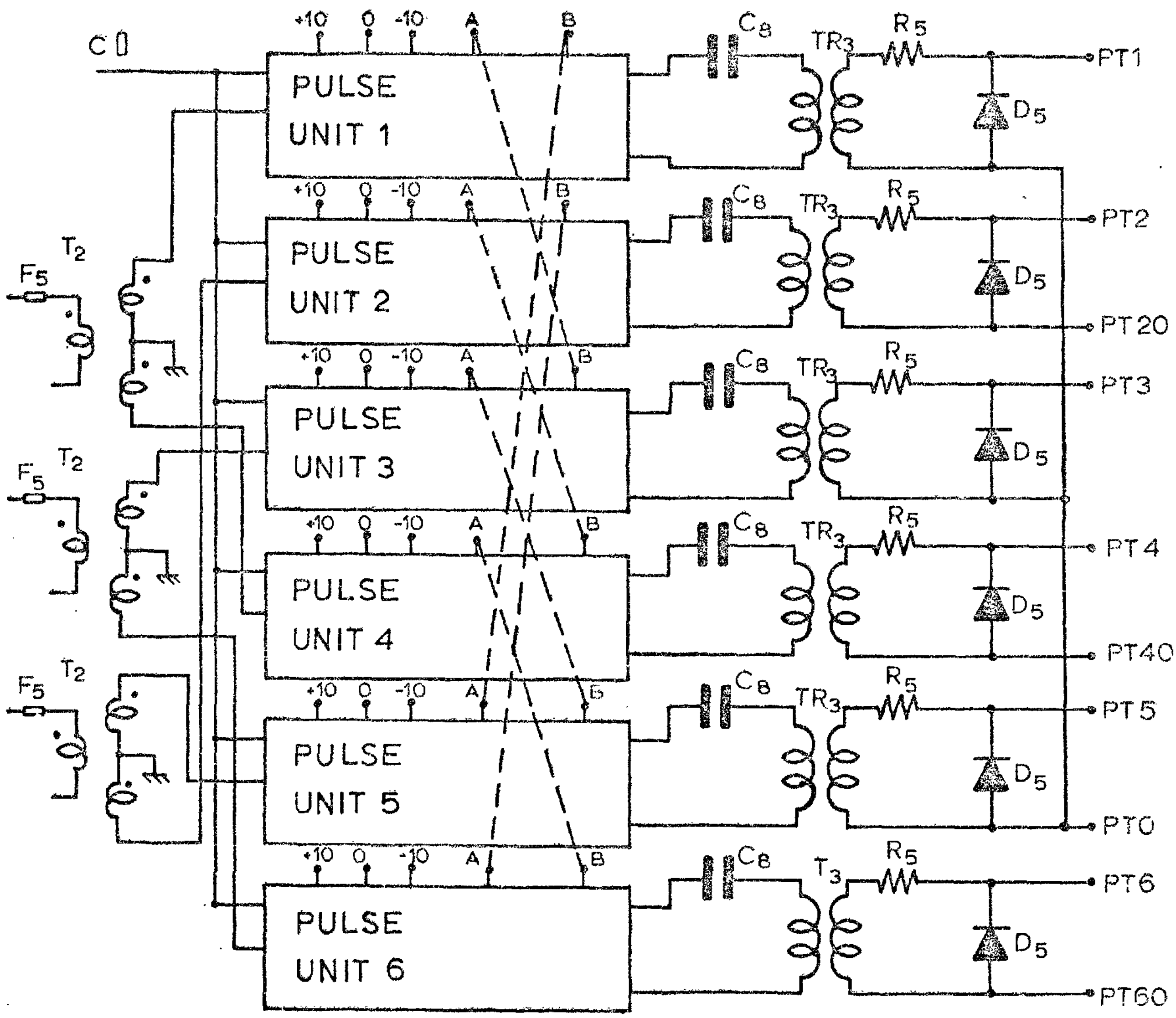

Fig. A6.2. Circuit diagram of the rectifier pulsing circuitry

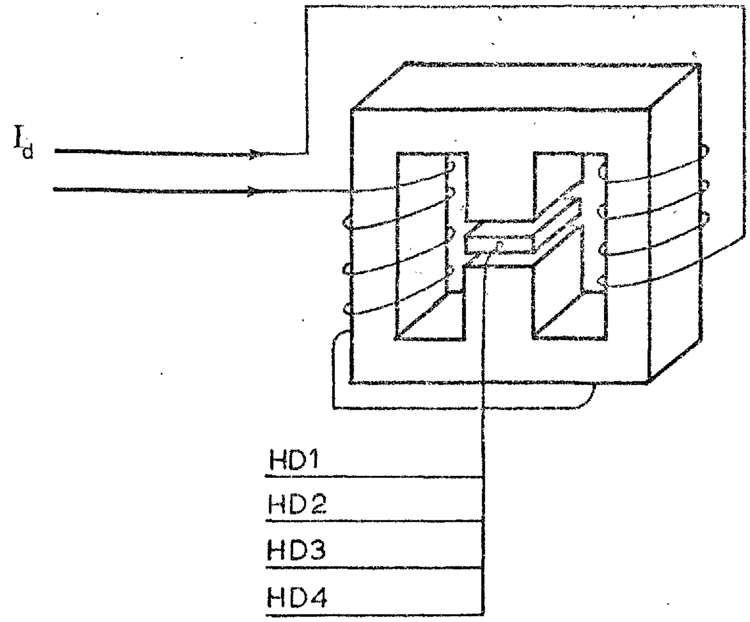

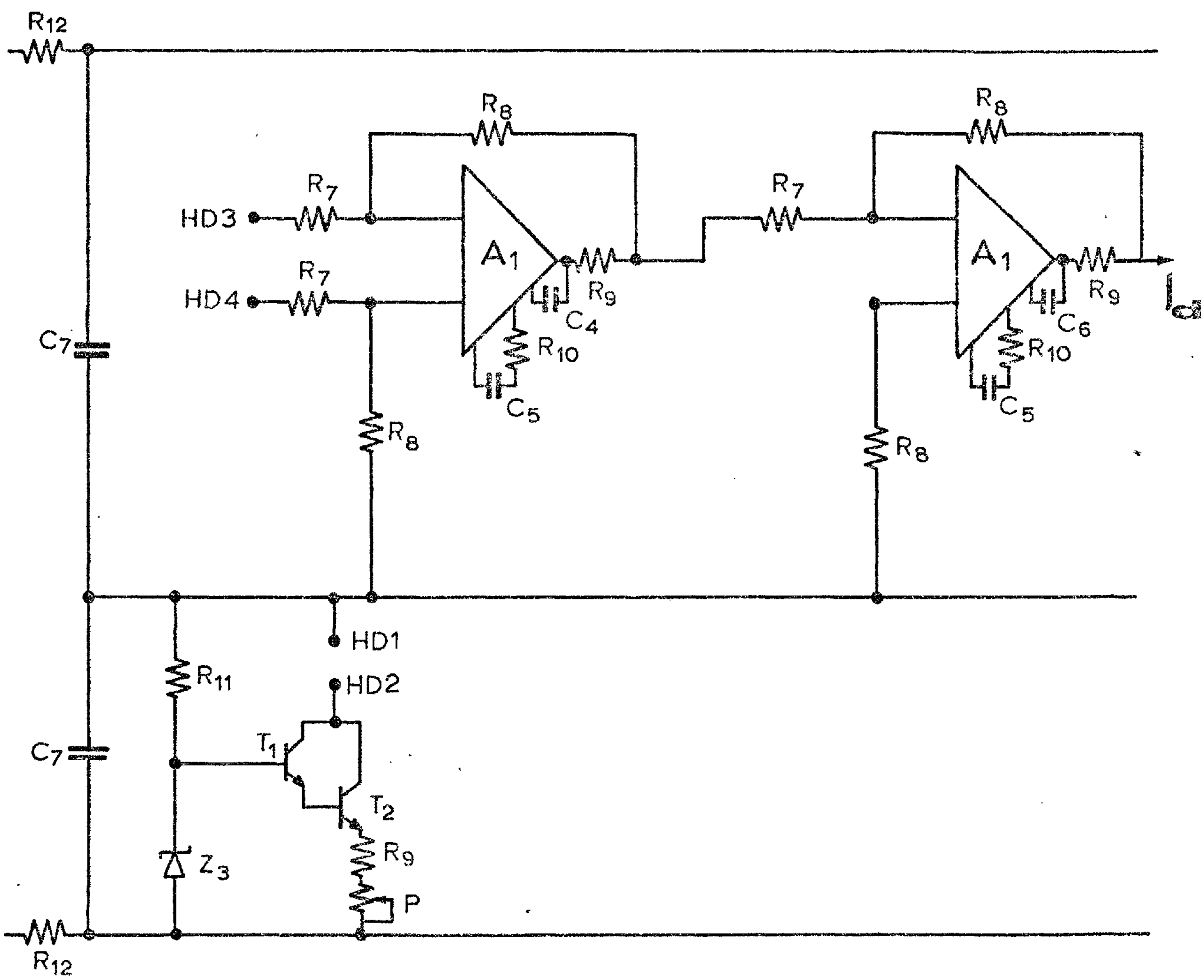

Fig. A6. 3. Current sensing device (Hall Effect Device)

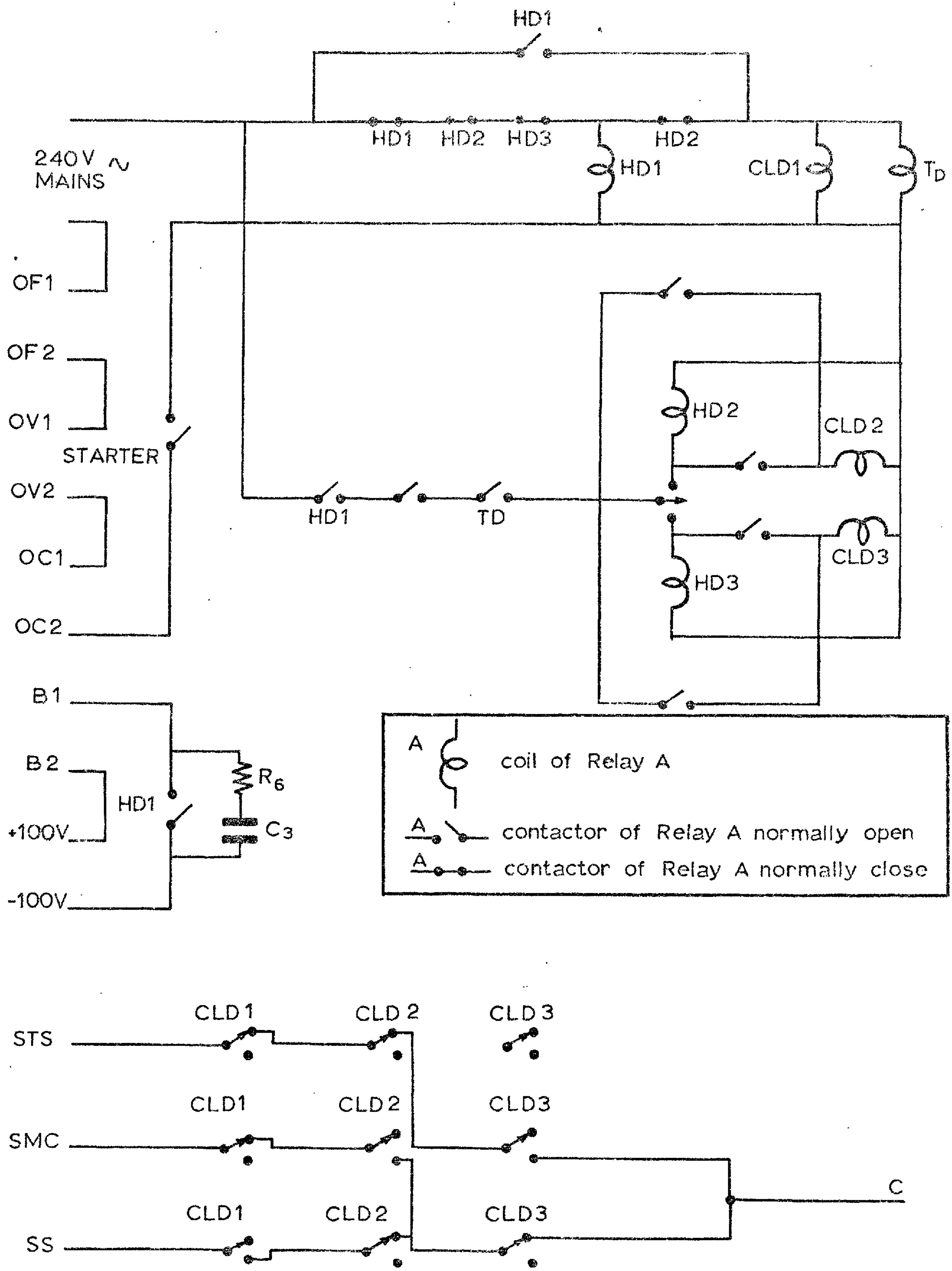

Fig. A6.4. Relays diagram and protection system

TABLE A6.1

PLATE of d.c. micromachine drive motor

	ALSTHOM				
NAP	TARBES	1954			
MOTEUR C^{t}	CONTINU TYPE	B5.42			
No 336305	t:mn	1500			
KW 2.2	Ch	3			
VOLTS 220	Amp	12			
SERV CONTINU	Echauf	UTE	Isol. Cl.	A.B	
EXCIT COMPOSEE	VOLTS	220	AMP	0.7	
PROTECT SEMI-PROTEGE		Poids 70 Kg			

PLATE of a.c. Microalternator

	ALSTHOM				
NAP	Belfort	1954			
ALTERNATEUR Y	TYPE	A 56,6 / 10,8			
No 334818	t: mn	1500			
Volts 190/250	Amp		KVA	0.6	4.5
Serv CONTINU	Echauf UTE		Isol. Cl.	A	
cos	Hz	50	Protct	SEMI-PROTEGE	
EXCITATION	V	A	Poids		Kg

TABLE A6.2

LIST OF COMPONENTS

R_1	300 Ω	.3A	C_1	1 μF	1200 V	F_1	5A - 600V	
R_2	300 Ω		C_2	1 μF	350 V	F_2	GSG 1000/25	
R_3	2000 Ω		C_3	2 μF	500 V	F_3	1A/250 V (DC)	
R_4	10 KΩ		C_4	200 pF		F_4	1A/250 V (DC)	
R_5	10 Ω		C_5	500 pF		F_5	.5A/415 V	
R_6	820 Ω		C_6	20 pF				
R_7	13 KΩ		C_7	50 μF		Z_1	260 V	5 W
R_8	130 KΩ		C_8	100 μF	25 V	Z_2	6.3 V	5 W
R_9	49 Ω					Z_3	5.1 V	.4 W
R_{10}	1.5 KΩ		T_1	2N2926		Z_4	6.2 V	1 W
R_{11}	1.2 KΩ		T_2	BFY50		THI	40A 400V THYRISTOR	
R_{12}	10 Ω							
R_{13}	1.3 KΩ							
R_{14}	200 Ω							

L_1 0.25 H (10A DC without saturation) (KESTON)

L_2 small inductance (10 turns) to be used in connection with the Hall device. Small core. See Fig. 11D for dimensions.

A_1 709-OPA (RADIOSPARE)

TR_1 415 Δ / 440 Y - 25 KVA - used as 415 - 254

TR_2 12 V TYPE S-M Mains transformer (RADIOSPARE)

TR_3 pulse transformer

RE_1 Magnetic devices Relay 305 EP8/1000/G2/12/CON/DIAC/ /9288113

RE_2 Electromagnetic overload Relay TYPE "SC" (ALLEN WEST)

RE_3 12 Ω coil - .3A d.c. RELAY

B Circuit breaker (2 air-break pattern d.c. Contactor TYPE "D") (ALLEN WEST)

HD-1- Heavy duty RELAY (11 pin, 230 V Coil, Three pole change over) (RADIOSPARE)

D_1	25 A	600 V
D_2	10 A	600 V
D_3	RS51A	
D_4	RS51A	
D_5	OA800	

APPENDIX 7

STEADY-STATE CHARACTERISTICS OF A CONTROLLED RECTIFIER-LAPLACE METHOD

The determination of the steady-state characteristics of a controlled rectifier was formulated in section 4.2, this appendix deals with the inversion of the resulting Laplace transform equations 4.5 and 4.6.

Equation 4.6 can be written as

$$v_c(s) = K\frac{v_1'(s)}{R_t(1+sT_1)(1+sT_2)} - K\frac{v_2'(s)}{R_t(1+sT_1)(1+sT_2)} -$$

$$- K\frac{E_o}{R_t(1+sT_1)(1+sT_2)} - K\frac{I_{ref}}{s(1+sT_1)} \qquad \text{(A7.1)}$$

The control voltage signal $v_c(s)$ can be decomposed into the following four parts:

$$v_c(s) = v_{c1}(s) + v_{c2}(s) + v_{c3}(s) + v_{c4}(s) \qquad \text{(A7.2)}$$

Where

$$v_{c1}(s) = K\frac{v_1'(s)}{R_t(1+sT_1)(1+sT_2)}$$

$$v_{c2}(s) = -K\frac{v_2'(s)}{R_t(1+sT_1)(1+sT_2)}$$

$$v_{c3}(s) = -K\frac{E_o}{R_t\ s(1+sT_1)(1+sT_2)}$$

$$v_{c4}(s) = -K\frac{I_{ref}}{s\ (1+sT_1)}$$

The Laplace inverse of $v_{c1}(s)$ is obtained next. Substituting equation 4.3 into the expression for $v_{c1}(s)$ we get

$$v_{c1}(s) = KV\frac{\omega_o(\cos\alpha'-\cos\gamma'\ e^{-sT_s}) + s(\sin\alpha'-\sin\gamma'\ e^{-sT_s})}{R_t(\omega_o^2+s^2)(1-e^{-sT_s})(1+sT_1)(1+sT_2)} \tag{A7.3}$$

Decomposing equation A7.3 into two parts

$$v_{c1}(t) = K\frac{V}{R_t}\mathcal{L}^{-1}\frac{\omega_o}{(\omega_o^2+s^2)(1+sT_1)(1+sT_2)} * \mathcal{L}^{-1}\frac{\cos\alpha'-\cos\gamma' e^{-sT_s}}{1-e^{-sT_s}} +$$

$$+ K\frac{V}{R_t}\mathcal{L}^{-1}\frac{s}{(\omega_o^2+s^2)(1+sT_1)(1+sT_2)} * \mathcal{L}^{-1}\frac{\sin\alpha'-\sin\gamma' e^{-sT_s}}{1-e^{-sT_s}} \tag{A7.4}$$

The first component of these two parts can be expressed as time functions, from tables

$$\mathcal{L}^{-1}\frac{\omega_o}{(\omega_o^2+s^2)\ (1+sT_1)\ (1+sT_2)} = \frac{\sin\ (\omega_o t-\theta-\beta)}{\sqrt{\left[1+(\omega_o T_1)^2\right]}\sqrt{\left[1+(\omega_o T_2)^2\right]}} + $$

$$+\frac{\omega_o\ T_1^2\ e^{-\frac{t}{T_1}}}{(T_1-T_2)\ (1+(\omega_o T_1)^2)} + \frac{\omega_o\ T_2^2\ e^{-\frac{t}{T_2}}}{(T_2-T_1)\ (1+(\omega_o T_2)^2)}$$

$$\mathcal{L}^{-1}\frac{\omega_o}{(\omega_o^2+s^2)\ (1+sT_1)\ (1+sT_2)} = \frac{\cos(\omega_o t-\theta-\beta)}{\sqrt{\left[1+(\omega_o T_1)^2\right]}\sqrt{\left[1+(\omega_o T_2)^2\right]}} + $$

$$+\frac{\omega_o\ T_1\ e^{-\frac{t}{T_1}}}{(T_1-T_2)\ (1+\omega_o T_1)^2)} + \frac{\omega_o\ T_1\ e^{-\frac{t}{T_2}}}{(T_2-T_1)\ (1+(\omega_o T_2)^2)}$$

where

$$\beta = \mathrm{ATAN}\ (\omega_o T_1)$$

$$\theta = \mathrm{ATAN}\ (\omega_o T_2)$$

Using these two time functions, equation A7.4 can be rewritten as

$$v_{c1}(t) = K\frac{V}{R_t}\Bigg\{\cos\alpha'\left[\frac{\sin(\omega_o t-\theta-\beta)}{\sqrt{\left[1+(\omega_o T_1)^2\right]}\sqrt{\left[1+(\omega_o T_2)^2\right]}} + \frac{\omega_o\ T_1^2\ e^{-\frac{t}{T_1}}}{(T_1-T_2)\ (1+(\omega_o T_1)^2)} + \right.$$

$$\left. + \frac{\omega_o\ T_2^2\ e^{-\frac{t}{T_2}}}{(T_2-T_1)\ (1+(\omega_o T_2)^2)}\right] * \mathcal{L}^{-1}\left[\frac{1}{1-e^{-sT_s}}\right] -$$

$$-\cos\gamma'\left[\frac{\sin(\omega_o t-\theta-\beta)}{\sqrt{\left[1+(\omega_o T_1)\right]}\ \sqrt{\left[1+(\omega_o T_2)^2\right]}} + \frac{\omega_o\ T_1^2\ e^{-\frac{t}{T_1}}}{(T_1-T_2)\ (1+(\omega_o T_2)^2)} + \right.$$

$$+\frac{\omega_o\ T_2^2\ e^{-\frac{t}{T_2}}}{(T_2-T_1)\ (1+(\omega_o T_2)^2)}\Bigg] * \mathcal{L}^{-1}\left[\frac{e^{-sT_s}}{1-e^{-sT_s}}\right]+$$

$$+\ \sin\alpha'\left[\frac{\cos(\omega_o t-\theta-\beta)}{\sqrt{[1+(\omega_o T_1)^2]}\sqrt{[1+(\omega_o T_2)^2]}}-\frac{T_1\ e^{-\frac{t}{T_1}}}{(T_1-T_2)\ (1+(\omega_o T_2)^2)}-\right.$$

$$-\frac{T_2\ e^{-\frac{t}{T_2}}}{(T_2-T_1)\ (1+(\omega_o T_2)^2)}\Bigg] * \mathcal{L}^{-1}\left[\frac{1}{1-e^{-sT_s}}\right]-$$

$$-\ \sin\gamma'\left[\frac{\cos(\omega_o t-\theta-\beta)}{\sqrt{[1+(\omega_o T_1)^2]}\sqrt{[1+(\omega_o T_2)^2]}}-\frac{T_1\ e^{-\frac{t}{T_2}}}{(T_1-T_2)\ (1+(\omega_o T_2)^2)}-\right.$$

$$-\frac{T\ \ e^{-\frac{t}{T_2}}}{(T_2-T_1)\ (1+(\omega_o T_2)^2)}\Bigg] * \mathcal{L}^{-1}\left[\frac{e^{-sT_s}}{1-e^{-sT_s}}\right]\Bigg\}$$

(A7.5)

Rearranging equation A7.5

$$v_{c1}(t) = \frac{K\ V}{R_t\sqrt{[1+(\omega_o T_1)^2]}\sqrt{[1+(\omega_o T_2)^2]}}\ \ (\sin(\omega_o t-\theta-\beta+\alpha') -$$

$$-\ \sin(\omega_o t-\theta-\beta+\gamma')\ \ d(-T_s)) * \mathcal{L}^{-1}\ \frac{1}{1-e^{-sT_s}}\ +$$

$$+\ \frac{KV}{R_t}\left\{\ \frac{T_1(\omega_o T_1\cos\alpha' - \sin\alpha')}{(T_1-T_2)\ (1+(\omega_o T_1)^2)}\ \ \mathcal{L}^{-1}\left[\frac{1-K_1 e^{-sT_s}}{1-e^{-sT_s}}\ \frac{1}{s+1/T_1}\right]+\right.$$

$$+\ \frac{T_2(\omega_o T_2\cos\alpha' - \sin\alpha')}{(T_2-T_1)\ (1+(\omega_o T_2)^2)}\ \ \mathcal{L}^{-1}\left[\frac{1-K_1' e^{-sT_s}}{1-e^{-sT_s}}\ \frac{1}{s+1/T_2}\right]\Bigg\}$$

(A7.6)

where

$$K_1 = \frac{\omega_o T_1 \cos\gamma' - \sin\gamma'}{\omega_o T_1 \cos\alpha' - \sin\alpha'}$$

$$K_1' = \frac{\omega_o T_2 \cos\gamma' - \sin\gamma'}{\omega_o T_2 \cos\alpha' - \sin\alpha'}$$

$d(-x)$ functional expressing a pure delay of x seconds on the function it multiplies.

Equation A7.6 consists of three parts. The first part is a portion of a periodically repeating sine wave. The second and third parts can be inverted by making use of Jury Laplace transform table of rational functions of s with pure delays.[132] Thus $v_{c1}(t)$ is obtained in a closed manner.

$$v_{c1}(t) = K \frac{V}{R_t} \left\{ \frac{\sin(m \frac{2\pi}{q} - \theta - \beta + \alpha')}{\sqrt{\left[1+(\omega_o T_1)^2\right]} \sqrt{\left[1+(\omega_o T_2)^2\right]}} + \right.$$

$$+ \frac{T_1(\omega_o T_1 \cos\alpha' - \sin\alpha')}{(T_1 - T_2)\ (1+(\omega_o T_1)^2)} (1 - K_1 d(-T_s)) \frac{e^{-T_s(m-1)/T_1}}{e^{T_s/T_1} - 1} (1 - e^{-n\frac{T_s}{T_1}}) +$$

$$\left. + \frac{T_2(\omega_o T_2 \cos\alpha' - \sin\alpha')}{(T_2 - T_1)\ (1+(\omega_o T_2)^2)} (1 - K_1' d(-T_s)) \frac{e^{-T_s(m-1)/T_2}}{e^{T_s/T_2} - 1} (1 - e^{-n\frac{T_s}{T_1}}) \right\}$$

(A7.7)

where

$t = (n-1+m)\ T_s$

n = number of sampling periods

m = a numeric such that at all times $0 \leq m \leq 1$.

The Laplace transform inverse of $V_{c2}(s)$ is obtained following the same method as for $V_{c1}(s)$. We get

$$v_{c2}(t) = K\frac{V}{R_t}\sin\pi/q\left\{\left[\frac{\sin(m2\pi/q-\theta-\beta+\alpha)}{\sqrt{[1+(\omega_oT_1)^2]}\sqrt{[1+(\omega_oT_2)^2]}}\right]_{m=0}^{m=\frac{u}{2\pi}q}\right.$$

$$+\frac{T_1(\omega_oT_1\cos\alpha-\sin\alpha)}{(T_1-T_2)\ (1+(\omega_oT_1)^2)}\ (1-K_2d(-T_u))\ \frac{e^{-T_s(m-1)/T_1}}{e^{T_s/T_1}-1}(1-e^{-n\frac{T_s}{T_1}})+$$

$$\left.+\frac{T_2(\omega_oT_2\cos\alpha-\sin\alpha)}{(T_2-T_1)\ (1+(\omega_oT_2)^2)}\ (1-K_2'd(-T_u))\ \frac{e^{-T_s(m-1)/T_2}}{e^{T_s/T_2}-1}(1-e^{-n\frac{T_s}{T_2}})\right\}$$

(A7.8)

where

$$K_1 = \frac{\omega_o\ T_1\ \cos\gamma'' - \sin\gamma''}{\omega_o\ T\ \ \cos\alpha\ \ - \sin\alpha}$$

$$K_2' = \frac{\omega_o\ T_2\ \cos\gamma'' - \sin\gamma''}{\omega_o\ T_2\ \cos\alpha\ \ - \sin\alpha}$$

The other two components of the control voltage $v_{c3}(t)$ and $v_{c4}(t)$ are readily obtained by mean of Laplace transform tables. The control voltage is finally obtained as

$$v_c(t) = v_{c1}(t) + v_{c2}(t) -$$

$$- K\frac{E_o}{R_t}\ (1+\frac{T_1e^{-t/T_1} - T_2e^{-t/T_2}}{T_2-T_1}) - I_{ref}\ (1-e^{-t/T_1})$$

(A7.9)

The steady state condition is obtained when n approaches infinity

$$v_c^o(t) = \lim_{n \to \infty} v_c(t) \tag{A7.10}$$

This limit is readily obtained using equations A7.7, A7.8, A7.9 and A7.10

$$\begin{aligned}
v_c^o(t) = K \frac{V}{R_t} \Bigg\{ & \frac{\left[\sin(m\frac{2\pi}{q} - \theta - \beta + \alpha') - \sin\frac{\pi}{q} \sin(m\frac{2\pi}{q} - \theta - \beta + \alpha)\right]_{m=0}^{m=\frac{u}{2\pi}q}}{\sqrt{\left[1+(\omega_o T_1)^2\right]}\sqrt{\left[1+(\omega_o T_2)^2\right]}} + \\
& + (1-K_1) \frac{T_1(\omega_o T_1 \cos\alpha' - \sin\alpha')}{(T_1-T_2)\ (1+(\omega_o T_1)^2)} \frac{e^{-T_s(m-1)/T_1}}{e^{T_s/T_1} - 1} + \\
& + (1-K_1') \frac{T_2(\omega_o T_2 \cos\alpha' - \sin\alpha')}{(T_2-T_1)\ (1+(\omega_o T_2)^2)} \frac{e^{-T_s(m-1)/T_2}}{e^{T_s/T_1} - 1} - \\
& - (1-K_2 d(-T))\sin\frac{\pi}{q} \frac{T_1(\omega_o T_1 \cos\alpha - \sin\alpha)}{(T_1-T_2)\ (1+(\omega_o T_1)^2)} \frac{e^{-T_s(m-1)/T_1}}{e^{T_s/T_1} - 1} - \\
& - (1-K_2' d(-T))\sin\frac{\pi}{q} \frac{T_2(\omega_o T_2 \cos\alpha - \sin\alpha)}{(T_2-T_1)\ (1+(\omega_o T_2)^2)} \frac{e^{-T_s(m-1)/T_2}}{e^{T_s/T_2} - 1} \Bigg\} \\
& - K \frac{E_o}{R_t} - I_{ref}
\end{aligned} \tag{A7.11}$$

The steady state output current is obtained if in equation A7.11, $K = 1$ and $T_1 = 0$. If $T_u = 0$ as well, equation A7.11 becomes Bayoumi expression for the rectifier output current.[108]

Bjäresten equation for the control voltage[83] is also a particular case of equation A7.11 when $T_u = R_t = 0$ and short circuit conditions are considered i.e. $\alpha = \pi/2$.

APPENDIX 8

STEADY-STATE CHARACTERISTIC OF A CONTROLLED RECTIFIER - TIME DOMAIN METHOD

The steady-state characteristics of a rectifier were determined in section 4.2 using Laplace transform techniques. The time domain technique presented here requires a somewhat different formulation to the steady-state problem if the simplifying assumption of averaging the rectifier internal impedance is not made. The time-domain technique is illustrated next.

The differential equation defining the current output of a q-phase rectifier can be written through network analysis

$$v_d(t) = R(t)\ i_d(t) + L(t)\ \frac{d\ i_d(t)}{d\ t} - E_o \qquad \text{(A8-1)}$$

where all time functions are periodically varying with a period T_s

$$v_d(t) = \begin{cases} V \cos\frac{\pi}{q} \cos(\omega_o t + \alpha) & 0 \le t \le T_u \\ V \cos(\omega_o t + \alpha - \frac{\pi}{q}) & T_u \le t \le T_s \end{cases}$$

$$R\ (t) = \begin{cases} \frac{1}{2} R_{1e} + R_{CH} + R_a & 0 \leq t \leq T_u \\ R_{1e} + R_{CH} + R_a & T_u \leq t \leq T_s \end{cases}$$

$$L\ (t) = \begin{cases} \frac{1}{2} L_{1e} + L_{CH} + L_a & 0 \leq t \leq T_u \\ L_{1e} + L_{CH} + L_a & T_u \leq t \leq T_s \end{cases}$$

In contrast with the Laplace transform formulation, steady-state conditions are assumed to exist throughout and hence the following border conditions apply

$$i_d\ (nT_s) \quad = I_1 \qquad n = \ldots -3,-2,-1,0,1,2,3,\ldots \text{(A8.2)}$$

$$n = \ldots -3,-2,-1,0,1,2,3,\ldots \text{(A8.2)}$$

$$i_d(nT_s + T_u) = I_2$$

Using these two border conditions, the solution of the differential equation A8.1 may be written

$$i_d(t) = \begin{cases} \dfrac{V\ \cos\frac{\pi}{q}\cos(\omega_o t + \alpha - \theta_2)}{Z_2} + \\ \quad + \left(I_1 + \dfrac{E_o}{R_2} - \dfrac{V\ \cos\frac{\pi}{q}\cos(\alpha - \theta_2)}{Z_2}\right) e^{-t/T'_2} - \dfrac{E_o}{R_2} & 0 \leq t \leq T_u \\ \dfrac{V\ \cos(\omega_o t + \alpha - \frac{\pi}{q} - \theta_1)}{Z_1} + \\ \quad + \left(I_2 + \dfrac{E_o}{R_1} - \dfrac{V\cos(\alpha + u + \frac{\pi}{q} - \theta_1)}{Z_1}\right) e^{-\frac{(t-T_u)}{T'_1}} - \dfrac{E_o}{R_1} & T_u \leq t \leq T_s \end{cases}$$

(A8.3)

where $R_{1,2}$ $Z_{1,2}$ $\theta_{1,2}$ and $T_{1,2}$ are defined in section 4.3.

As the current is continuous

$$i_d(T_u) = I_2 = \frac{V \cos\frac{\pi}{q} \cos(\omega_o T_u + \alpha - \theta_2)}{Z_2} +$$

$$+ \left(I_1 + \frac{E_o}{R_2} - \frac{V \cos\frac{\pi}{q} \cos(\alpha - \theta_2)}{Z_2} \right) e^{-T_u/T_2'} - \frac{E_o}{R_2}$$

$$i_d(T_s) = I_1 = \frac{V \cos(\omega_o T_s + \alpha - \frac{\pi}{q} - \theta_1)}{Z_1} +$$

$$+ \left(I_2 + \frac{E_o}{R_1} - \frac{V \cos(\alpha + u - \frac{\pi}{q} - \theta_1)}{Z_1} \right) e^{-(T_s - T_u)/T_1'} - \frac{E_o}{R_1}$$

$$(A8.4)$$

The two unknowns I_1 and I_2 can now be determined solving the system of two linear equations A8.4. With this solution, the steady-state rectifier output current is fully characterized in equation A8.3. Equation A8.3 can also be written as

$$i_d(t) = \begin{cases} I_{d1} \cos(\omega_o t + \alpha_{d1}) + I_{d1}' \, e^{-t/T_2'} - I_{d1}'' & 0 \le t \le T_u \\ I_{d2} \cos(\omega_o t + \alpha_{d2}) + I_{d2}' \, e^{-t/T_1'} - I_{d2}'' & T_u \le t \le T_s \end{cases}$$

$$(A8.5)$$

where

$$I_{d1} = V \cos(\pi/q) \, / \, Z_2$$

$$I_{d2} = V \, / \, Z_1$$

$$\alpha_{d1} = \alpha - \theta_2$$

$$\alpha_{d2} = \alpha - \pi/q - \theta_1$$

$$I'_{d1} = I_1 + E_o/R_2 - V\cos\pi/q \cos(\alpha-\theta_2) / Z_2$$

$$I'_{d2} = I_2 + E_o/R_1 - V\cos\pi/q \cos(\alpha+u-\frac{\pi}{q}\theta_1) / Z_1$$

$$I''_{d1} = E_o / R_2$$

$$I''_{d2} = E_o / R_1$$

The control voltage $v_c(t)$ is related with the output current through the following differential equation

$$K(i_d(t) - I_{ref}) = v_c(t) - T_1 \frac{d\ v_c(t)}{d\ t} \qquad (A8.6)$$

This equation is readily solved using superposition

$$v_c(t) = \begin{cases} = \dfrac{KI_{d1}\cos(\omega_o t+\alpha'_{d1})}{1+(\omega_o T_1)^2} + \dfrac{KI'_{d1}T'_2}{T'_2 - T_1} e^{-t/T'_2} + KI''_{d1} + \\ + \left[V_{c1} - \dfrac{KI_{d1}\cos\alpha'_{d1}}{1+(\omega_o T_1)^2} - K\left(\dfrac{I'_{d1}T'_2}{T'_2-T_1} + I''_{d1}\right)\right] e^{-t/T_1} & 0 \leq t \leq T_u \\ = \dfrac{KI_{d2}\cos(\omega_o t+\alpha'_{d2})}{1+(\omega_o T_1)^2} + \dfrac{KI'_{d2}T'_1}{T'_1-T_1} e^{-(t-T_u)/T'_1} + KI''_{d2} + \\ + \left[V_{c2} - \dfrac{KI_{d2}\cos(\alpha'_{d2}+u)}{1+(\omega_o T_1)^2} - K\left(\dfrac{I'_{d2}T'_1}{T'_1-T_1} + I''_{d2}\right)\right] e^{-\frac{(t-T_u)}{T_1}} & T_u \leq t \leq T_s \end{cases}$$

$$(A8.7)$$

where, $\alpha'_{d1} = \alpha_{d1} - \text{ATAN}(\omega_o T_1)$, and $\alpha'_{d2} = \alpha_{d2} - \text{ATAN}(\omega_o T_2)$.

As steady-state conditions are assumed, the following border conditions result

$$\begin{aligned} v_c(nT_s) &= V_{c1} \\ v_c(nT_s+T_u) &= V_{c2} \end{aligned} \qquad n=\ldots-3,-2,-1,0,1,2,\ldots \qquad (A8.8)$$

As the control voltage is continuous at the firing instants and at the end of commutation, the following two equations are satisfied

$$v_c(nT_s+T_u) = V_{c2} = \frac{KI_{d1}\cos(\omega_o T_u+\alpha'_{d1})}{\sqrt{\left[1+(\omega_o T_1)^2\right]}} + K\left(\frac{I'_{d1}T_2}{T'_2-T_1}\, e^{-T_u/T'_2} + I''_{d1}\right) +$$

$$+ \left[V_{c1} + K\left(\frac{I_{d1}\cos\alpha'_{d1}}{1+(\omega_o T_1)^2} + \frac{I'_{d1}T'_2}{T'_2-T_1} + I''_{d1}\right)\right] e^{-T_u/T_1}$$

$$v_c(nT_s) = V_{c1} = \frac{KI_{d2}\cos(\omega_o T_s+\alpha'_{d2})}{\sqrt{\left[1+(\omega_o T_2)^2\right]}} + K\left(\frac{I'_{d2}T'_1}{T'_1-T_1}\, e^{-(T_s-T_u)/T'_1} + I''_{d2}\right) +$$

$$+ \left[V_{c2} - K\left(\frac{I_{d2}\cos(\alpha'_{d2}+u)}{1+(\omega_o T_1)^2} + \frac{I'_{d2}T'_1}{T'_1-T_1} + I''_{d2}\right)\right] e^{-(T_s-T_u)/T_1}$$

(A8.9)

Solving the set of linear equations A8.9 both unknowns V_{c1} and V_{c2} are determined, thus the steady-state equation (A8.7) for the control voltage is fully defined.

APPENDIX 9

STABILITY BOUNDARY

OF CONTROLLED RECTIFIER - SAMPLE AND HOLD MODEL

The sample and hold model of the rectifier system operating under constant current control depicted in Fig. 4.9 is described by the following transformed equation

$$G(s)\,\Delta I_{ref} - H_1(s)\;G(s)\;\Delta\alpha^* = \Delta\alpha \qquad (A9.1)$$

where

$$H_1(s) = \frac{V_{dc}\;\sin\alpha^o}{R_L}\;\frac{1 - e^{-sT_s}}{(1+sT_2)s}$$

Converting equation A9.1 into an expression of transformed sampled functions, we have

$$G\;\Delta I^*_{ref} - H_1\;G(z)\;\Delta\alpha^* = \Delta\alpha^* \qquad (A9.2)$$

from which

$$\Delta\alpha^* = \frac{G\Delta I^*_{ref}}{1 + H_1G(z)} \qquad (A9.3)$$

The z-transform $H_1G(z)$ is obtained from tables[132]

$$H_1G(z) = \frac{V_{dc}\ K\ \sin\alpha^o}{R_L}\left(1 + \frac{T_1}{T_2-T_1}\ \frac{z-1}{z-e^{-T_s/T_1}} + \frac{T_2}{T_2-T_1}\ \frac{z-1}{z-e^{-T_s/T_2}}\right)$$

(A9.4)

Equation A9.4 possesses two qualitatively different Nyquist plots, depending upon the numerical values of the time constants T_1 and T_2, which are shown diagramatically in Figs. 4.18c and d. In Fig. c the plot intercepts the real axis twice, thus the critical frequency ω_c is half the sampling rate. In Fig. d the plot crosses the real axis three times, the critical frequency is now obtained making the imaginary part of equation A9.4 equal to zero. After some manipulations the frequency of the third crossing is obtained

$$\omega_c = \frac{1}{T_s}\ \cos^{-1}\left(\frac{T\ e^{T_s/2T_1}\ \sinh\frac{T_s}{2T1}\cosh\frac{T_s}{T2} - T\ e^{T_s/2T_2}\ \sinh\frac{T_s}{2T2}\sinh\frac{T_s}{T1}}{T_1 e^{T_s/2T_1}\ \sinh\frac{T_s}{2T_1} - T_2 e^{T_s/2T_2}\ \sinh\frac{T_s}{2T_2}}\right)$$

(A9.5)

The critical gain is fully determined making the real part of $HG^*(z)$ equal to one at the critical frequency

$$K_{crit} = \frac{R_1}{V_{dc}\sin\alpha^o\left(1 + \frac{T_1}{T_2-T_1}\ \frac{Z_c-1}{Z_c-e^{-T_s/T_1}} + \frac{T_2}{T_2-T_1}\ \frac{Z_c-1}{Z_c-e^{-T_s/T_2}}\right)}$$

(A9.6)

where $\quad Z_c = e^{jT_s\omega_c}$

Rearranging equation A9.6 the following two critical gains are obtained

$$K_{crit} = \frac{R_L}{V_{dc}\sin\alpha^{o}} \; \frac{e^{T_s/T_1} \; e^{T_s/T_2} - 1}{T_1(e^{T_s/T_1} - 1) - T_2(e^{T_s/T_2} - 1)}. \qquad (A9.7)$$

for instability at less than $\omega_s/2$, and

$$K_{crit} = \frac{R_L}{V_{dc}\sin\alpha^{o}} \; \frac{T_2 - T_1}{T_2 \; \tanh T_s/2T_2 - T_1 \; \tanh T_s/2T_1} \qquad (A9.8)$$

for instability at $\omega_s/2$.

APPENDIX 10

STABILITY BOUNDARY

OF CONTROLLED RECTIFIER - IMPULSE MODEL (u=0)

The impulse model of the rectifier system operating under constant current control (Fig. 4.11) is characterized by the equation

$$G(s)\ \Delta I_{ref} - H_2(s)\ G(s)\ \Delta\alpha^* = \Delta\alpha \qquad \text{(A10.1)}$$

where

$$H_2(s) = \frac{V_{dc}T_s\ \sin\alpha^o}{R_L}\ \frac{1}{1+sT_2}$$

Equation A10.1 can be converted into an expression of sampled functions

$$G\ \Delta I^*_{ref} - H_2G\ (z)\ \Delta\alpha^* = \Delta\alpha^* \qquad \text{(A10.2)}$$

Whereform

$$\Delta\alpha^* = \frac{G\Delta I^*_{ref}}{1+H_2G(z)} \qquad \text{(A10.3)}$$

The z-transform of $H_2G(s)$ is obtained from tables[132]

$$H_2G(z) = \frac{V_{dc}\ K\ T_s\ \sin\alpha^o}{R_L\ (T_1-T_2)} \left(\frac{z}{z-e^{-Ts/T_1}} - \frac{z}{z-e^{-Ts/T_2}} \right) \qquad (A10.4)$$

It can be shown that the Nyquist plot of $H_2G^*(z)$ intercepts the real axis only twice, hence the critical frequency can only be half the sampling frequency. The critical gain is therefore obtained from the equation

$$H_2G^*(-1) = -1 \qquad (A10.5)$$

Substituting equation A10.4 into equation A10.5, we get

$$K_{crit} = \frac{2R_L\ (T_1 - T_2)}{V_{dc}\ T_s\ \sin\alpha^o \left(\frac{1-e^{-T_s/T_2}}{1+e^{-T_s/T_2}} - \frac{1-e^{-T_s/T_1}}{1+e^{-T_s/T_1}} \right)}$$

$$= \frac{2R_L\ (T_1 - T_2)}{V_{dc}\ T_s\ \sin\alpha^o\ (\tanh\frac{T_s}{T_2} - \tanh\frac{T_s}{T_1})} \qquad (A10.6)$$

APPENDIX 11

STABILITY BOUNDARY
OF CONTROLLED RECTIFIER - IMPULSE MODEL ($u \neq 0$)

The comprehensive impulse model of the rectifier system operating under current control (Fig.4.13) is fully characterized by the following set of two equations

$$\left\{\begin{aligned} -G(s)G_1(s)G_2(s).\Delta\alpha^* - G(s)G_2(s)G_3(s)\Delta I_d^* + G(s)\Delta I_{ref} &= \Delta\alpha \\ G_1(s)G_2(s)\Delta\alpha^* + G_2(s)G_3(s)\Delta I_d^* &= \Delta I_d \end{aligned}\right. \qquad (A11.1)$$

Where $G_1(s)$, $G_2(s)$ and $G_3(s)$ are defined in section 4.6.3.

The set of equations A11.1 can be converted into a set of transformed sampled functions

$$\begin{bmatrix} (1+GG_1G_2(z)) & GG_2G_3(z) \\ G_1G_2(z) & (1+G_2G_3(z)) \end{bmatrix} \times \begin{bmatrix} \Delta\alpha^* \\ \Delta I_d^* \end{bmatrix} = \begin{bmatrix} G\Delta I_{ref}^* \\ 0 \end{bmatrix} \qquad (A11.2)$$

The determinant of equation A11.2 determines the characteristic equation

$$D(z) = 1+GG_1G_2(z)+G_2G_3(z)+GG_1G_2(z)G_2G_3(z)-G_1G_2(z)GG_2G_3(z)$$

(A11.3)

The z-transforms in equation A11.3 are obtained from tables[132]

$$GG_1G_2(z) = \frac{K\ V_{dc}\ T_s\ \sin\alpha^o}{2R(T_1-T_2)}\left(\frac{z+e^{-(T_s-T_u)/T_1}}{z-e^{-T_s/T_1}} - \frac{z+e^{-(T_s-T_u)/T_2}}{z-e^{-T_s/T_2}}\right)$$

$$G_2G_3(z) = -\frac{Lc}{L}\ \frac{e^{-(T_s-T_u)/T_2}}{z-e^{-T_s/T_2}}$$

(A11.4)

$$G_1G_2(z) = \frac{V_{dc}\ T_s\ \sin\alpha^o}{2L}\ \frac{z+e^{-(T_s-T_u)/T_2}}{z-e^{-T_s/T_2}}$$

$$GG_2G_3(z) = \frac{KLc}{R(T_1-T_2)}\left(\frac{e^{-(T_s-T_u)/T_1}}{z-e^{-T_s/T_1}} - \frac{e^{-(T_s-T_u)/T_2}}{z-e^{-T_s/T_2}}\right)$$

Using equations A11.3, A11.4 and A11.5 an explicit expression for D(z) is now obtained

$$D(z) = 1 + \frac{K\ VdcT_s\ \sin\alpha^o}{2(T_1-T_2)} \left[\frac{z+e^{-(T_s-T_u)/T_1}}{z-e^{-T_s/T_1}} - \frac{z+e^{-(T_s-T_u)/T_2}}{z-e^{-T_s/T_2}}\right] \times$$

$$\times \left[1 - \frac{Lc}{L}\ \frac{e^{-(T_s-T_u)/T_2}}{z-e^{-T_s/T_2}}\right] - \frac{Lc}{L}\ \frac{e^{-(T_s-T_u)/T_2}}{z-e^{-T_s/T_2}} - \frac{K\ VdcT_s\ \sin\alpha^o}{2(T_1-T_2)} \times$$

$$\times \left[\frac{e^{-(T_s-T_u)/T_1}}{z-e^{-T_s/T_1}} - \frac{e^{-(T_s-T_u)/T_2}}{z-e^{-T_s/T_2}}\right] \left[\frac{Lc}{L}\ \frac{z+e^{-(T_s-T_u)/T_2}}{z-e^{-T_s/T_2}}\right]$$

(A11.5)

Reaaranging equation A11.5, an equation with the following structure is obtained

$$D(z) = 1 + \frac{(K\ a+b) + Kc + d}{(z-e)\ (z-f)} \qquad (A11.6)$$

The critical condition for stability is given by

$$1 + \frac{z\ (K\ a+b) + Kc + d}{(z-e)\ (z-f)} = 0 \qquad (A11.7)$$

Equation A11.7 can also be written as

$$1 + K\ \frac{az + c}{(z-e)\ (z-f) + bz + d} = 0 \qquad (A11.8)$$

Factorising the denominator and substituting the constants, we obtain

$$1 + \frac{K\ V_{dc}\ T_s\ \sin\alpha^o}{2R(T_1-T_2)}\ \frac{z\left\{(1-\frac{L_c}{L})(e^{-(T_s-T_u)/T_1}-e^{-(T_s-T_u)/T_2})+e^{-\frac{T_s}{T_1}}-e^{-\frac{T_s}{T_2}}\right\}-(e^{-(T_s-T_u)/T_1}e^{-\frac{T_s}{T_2}}-e^{-(T_s-T_u)/T_2}e^{-\frac{T_s}{T_1}})}{(z-e^{-T_s/T_1})\ (z-(e^{-T_s/T_2}-L_c e^{-(T_s-T_u)/T_1}/L))} = 0$$

(A11.9)

The system possesses two qualitatively different Nyquist plots depending upon the system parameters as shown in Figs. 4.18 c and d. Therefore, the system can become instable at half the sampling frequency or less. The gain is critical when equation A11.9 is satisfied, mathematically

$$K_{crit} = \frac{2(T_1-T_2)R}{V_{dc}\ T_s\ \sin\alpha^o}\ \frac{1-e^{-T_s/T_1}(e^{-T_s/T_2}+L_c\ e^{-(T_s-T_u)/T_2}/L)}{e^{-T_s/T_1}e^{-(T_s-T_u)/T_2}-e^{-T_s/T_2}e^{-(T_s-T_u)/T_1}}$$

(A11.10)

for instability at less than half the sampling frequency ,

and

$$K_{crit} = \frac{2R(T_1-T_2)\ (1+e^{-Ts/T1})\ (1+e^{-Ts/T2}-Lec\ e^{-(Ts-Tu)/T1}/L)}{V_{dc}\ T_{\mu}\ \sin\alpha^{o}\ \left[(1-\frac{Le}{L}c)(e^{-(Ts-Tu)/T1}-e^{-(Ts-Tu)/T2}) + e^{-(Ts-Tu)/T1}\ e^{-Ts/T2} - e^{-(Ts-Tu)/T2}\ e^{-Ts/T1}\right]} \tag{A11.11}$$

for instability at half the sampling frequency.

APPENDIX 12

SUPPORTING PUBLICATION

PROCEEDINGS

THE INSTITUTION OF ELECTRICAL ENGINEERS

Volume 119 Power

Stability study of controlled rectifiers using a new discrete model

J.P. Sucena-Paiva, Dipl. Eng., R. Hernandez, Ing. Elec., and L.L. Freris, M.Sc.(Eng.), Ph.D., D.I.C., C.Eng., M.I.E.E.

Indexing terms: Rectifiers, Stability, Modelling, Commutation)

ABSTRACT

The paper is concerned with the stability of closed-loop control systems incorporating controlled rectifiers. A suitable small-signal model for a convertor is developed which takes into account the discrete behaviour of the controlled rectifier. This model permits the use of standard sampled-data control-system theory in the stability analysis of the system. Contrary to usual practice, the a.c. system reactance is not neglected in the modelling. It is shown that the commutation angle is an important factor in the determination of stability boundaries. Finally, a gain-correction factor is employed to allow for the effect of the ripple under finite-commutation-angle conditions. Discrete Laplace transformation (z transformation) is used throughout the analysis together with root-locus techniques. Stability boundaries derived from the new model and other existing models are compared, and it is shown that experimental results are in good agreement with the theory developed in this paper.

LIST OF SYMBOLS

α = firing angle
u = commutation angle
v_d = output voltage of rectifier
V_d = d.c. component of v_d
q = number of controlled phases
v_c = control voltage
v_r = ramp reference voltage
V_d' = d.c. back voltage of load
V_{do} = V_d under no load and $\alpha = 0°$
V_p = r.m.s. phase voltage
i_d = rectifier output current
I_d = d.c. component of i_d
I_r = direct-current reference value
R = load resistance plus effective resistance of rectifier
L = load inductance plus effective inductance of rectifier
R_c = commutating resistance per phase
L_c = commutating inductance per phase
T_s = firing or sampling period
T_1 = time constant of control amplifier
T_2 = L/R
T_u = commutation time
ω_0 = mains angular frequency
ω_s = firing or sampling frequency
K = control-amplifier gain
K' = overall loop gain
K_e = overall effective loop gain
F = gain correction factor
s = Laplace operator
z = $\exp(T_s s)$
Superscript ^{0} denotes steady-state values.
Superscript * denotes sampled variable

1 INTRODUCTION

Since the advent of the thyristor, a.c./d.c. convertors have been extensively used in light and heavy industrial applications, such convertors being, in many instances, part of a closed-loop system.

Paper 6766 P, first received 29th March and in revised form 13th June 1971

The authors are with the Department of Electrical Engineering, Imperial College of Science & Technology, Exhibition Road, London SW7 2BT, England

In power systems, mercury-arc valves (and, in convertors under construction, thyristors) form an integral part of h.v.d.c. transmission links. In such schemes, closed-loop control is also utilised.

Owing to this large growth of convertor applications, the stability problem of control systems incorporating rectifiers has recently attracted the attention of several authors. As early as 1951, Busemann,[1] who was primarily interested in h.v.d.c. transmission, studied the hunting of rectifiers operating under constant current control. He found that hunting occurred at half the firing frequency.

Bjäresten[2] and Fallside[4] modelled the rectifier as a pure sampler and, using small-perturbation analysis, were able to derive, respectively, a closed form and an infinite series for the critical gain of the closed-loop system at half the firing frequency. With the introduction of a correction factor, Bjäresten[2] and later Fallside[5] were able to take into account the effect that the ripple present in the control voltage has on the closed-loop gain.

Other authors[3,7] modelled the rectifier as a sampler followed by a zero-order hold element, or, even more approximately, by a transportation lag of half the firing period.[6]

The model proposed in this paper represents accurately the sampling nature of the rectifier and takes into account for the first time the effect of the commutating reactance. The commutation angle is by no means negligible in a large number of convertor applications. In heavy industrial applications and d.c. motor drives, as well as in h.v. d.c. transmission, considerable commutating reactance is designed into the system so that short-circuit currents are limited. As a result, commutation angles in excess of 30° are not unusual in 3-phase bridge convertors.

Discrete Laplace transform (z transform) and root-locus techniques are used to determine the system stability boundaries and closed-form expressions are derived for the critical gain. With negligible commutation angles, the model developed in this paper is reduced to the pure sampler model suggested by Bjäresten and Fallside.

2 DISCRETE MODEL OF q-PHASE CONTROLLED RECTIFIER

2.1 General

A general q-phase rectifier and its output waveform are shown in Fig. 1. It is assumed that the capacity of the a.c.

system is much larger than the convertor rating, so that no voltage-loop instability can occur.[8,10] The voltage drop across the rectifying elements during conduction is neglected, but the reactance of the convertor transformer is taken into account. The load is assumed to be inductive and the output current continuous.

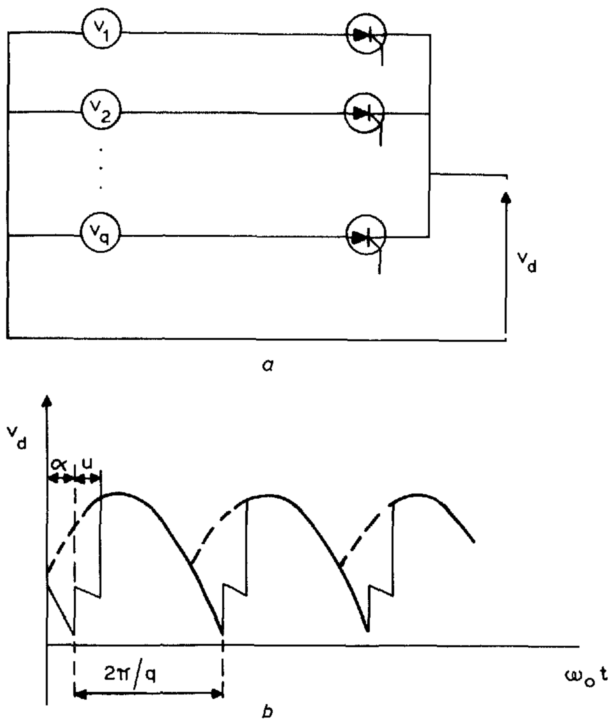

Fig. 1

q-phase rectifier

a Circuit diagram
b Output voltage

The firing system considered in this analysis is the so-called constant-α system. A ramp voltage v_r is initiated for each element when the associated commutating voltage passes through zero and becomes positive. A firing pulse is generated at the intersection of v_r and a control voltage v_c. The control voltage can be either an independent reference voltage if the system is operating on an open loop, or the difference between the reference and a fedback quantity if the system is operating on a closed loop. In this type of firing arrangement, α is proportional to the control voltage and has the advantage over the inverse-cosine system that better definition of α is achieved at small firing angles.

The inverse-cosine system, however, possesses the advantage of a firing system-convertor gain which is independent of α.

The analysis in this paper, although based on the constant-α system, can be applied to any alternative type of firing arrangement.

2.2 Derivation of mathematical model

The general block diagram of a closed-loop system incorporating a controlled rectifier is shown in Fig. 2. Control of the output voltage is not continuous, but only effective at discrete instants of time that correspond to the instants of firing. Under steady-state conditions, the interval between successive firings is $2\pi/q$ rad. The output voltage is primarily influenced by the control voltage, which introduces changes in the firing angle; it is also influenced by the output current due to the regulation introduced by the commutating reactance.

If a small variation $\Delta\alpha$ of the firing angle is considered with the output current kept constant, the increment in output voltage will consist of two pulses in each firing period. This is illustrated in Fig. 3 for positive and negative $\Delta\alpha$. As shown in Appendix 8.1, for an infinitesimal change of $\Delta\alpha$, the two pulses can be replaced by impulses having the same strength as the pulses they replace. This permits us to consider the rectifier as an ideal sampler which samples the incremental firing angle and produces two impulses, one at the sampling instant and another delayed by the time $T_u = u^0/\omega_0$.

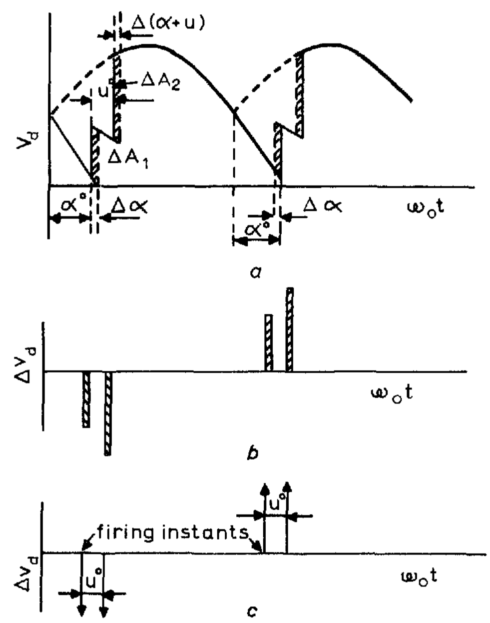

Fig. 3

Small variations of firing angle α (I_d = constant)

a Output voltage
b Incremental output voltage
c As b when $\alpha = 0$

The voltage-time area of the first pulse is given by

$$\Delta A_1 = \sqrt{2}V_p \sin(\pi/q) \sin\alpha^0 (\Delta\alpha/\omega_0) \tag{1}$$

Also

$$\omega_0 = 2\pi/qT_s \tag{2}$$

and

$$V_{do} = \frac{q}{\pi}\sqrt{2}V_p \sin(\pi/q) \tag{3}$$

Substituting eqns. 2 and 3 into eqn. 1 gives

$$\Delta A_1 = \frac{1}{2} V_{do}T_s \sin\alpha^0 \Delta\alpha \tag{4}$$

The area of the second pulse is given by

$$\Delta A_2 = \sqrt{2}V_p \sin\frac{\pi}{q} \sin(\alpha^0 + u^0)\frac{\Delta(\alpha+u)}{\omega_0}$$

$$= \frac{1}{2} V_{do}T_s \sin(\alpha^0 + u^0)\Delta(\alpha + u) \tag{5}$$

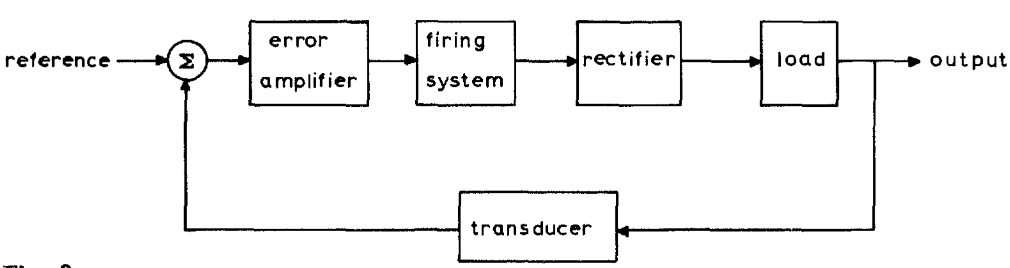

Fig. 2

Block diagram of closed-loop system incorporating controlled rectifiers

With the resistance of the commutating circuit neglected, a simplification introducing negligible error if the ratio $\omega_0 L_c R_c$ is high, α and u are related by the well known expression

$$\cos\alpha - \cos(\alpha + u) = \frac{\omega_0 L_c}{\sqrt{2}V_p \sin(\pi/q)} I_d \tag{6}$$

From eqn. 6, assuming constant current,

$$\Delta\{\cos\alpha - \cos(\alpha + u)\} = 0$$

and therefore

$$\sin\alpha^0 \Delta\alpha = \sin(\alpha^0 + u^0)\Delta(\alpha + u) \tag{7}$$

From eqns. 4, 5 and 7, it is clear that $A_1 = A_2$.

If a small variation ΔI_d of the output current is now considered, with the firing angle kept constant, the increment in output voltage will be one single pulse delayed by T_u with respect to the sampling instant as shown in Fig. 4.

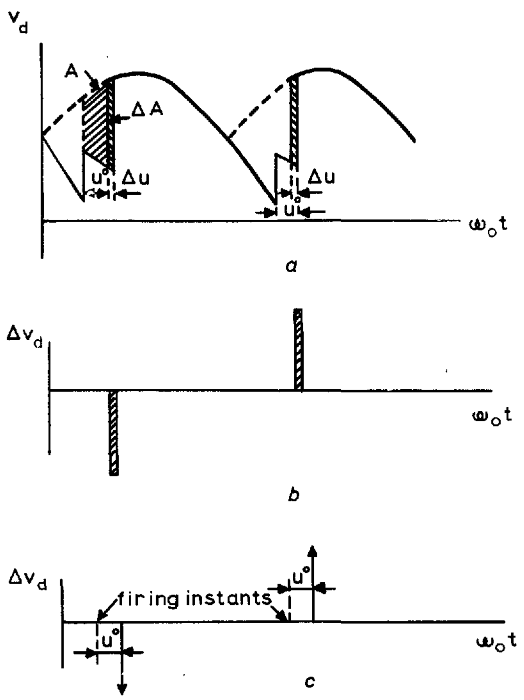

Fig. 4

Small variations of output current I_d (α = constant)

a Output voltage
b Incremental output voltage
c As b when $I_d = 0$

From basic rectifier considerations, it can be shown that the commutation area A in Fig. 4 is given by

$$A = \frac{\sqrt{2}V_p}{\omega_0} \sin\frac{\pi}{q}\{\cos\alpha - \cos(\alpha + u)\} \tag{8}$$

From eqns. 6 and 8, we obtain

$$A = L_c I_d \tag{9}$$

and therefore

$$\Delta A = L_c \Delta I_d \tag{10}$$

If the current variation during the commutation periods is assumed to be negligible, the action of the rectifier can now be represented by a sampler which samples the current at the firing instants and produces impulses delayed by T_u with respect to the firing instants. The area of an impulse is proportional to the deviation of current from the steady-state value.

A block diagram of the linearised discrete model of the rectifier is shown in the broken-line box of Fig. 5.

The voltage increment ΔV_d is given by

$$\Delta V_d = G_4(s)\Delta I_d^* + G_2(s)\Delta\alpha^* \tag{11}$$

From eqns. 4 and 10, we obtain

$$G_2(s) = -\frac{1}{2} V_{d0} T_s \sin\alpha^0\{1 + \exp(-sT_u)\} \tag{12}$$

and

$$G_4(s) = -L_c \exp(-sT_u) \tag{13}$$

3 STABILITY ANALYSIS

The complete block diagram incorporating a feedback loop for constant-current control is shown in Fig. 5. This system will be analysed using linear sampled-data control-system theory.

The firing or sampling period T_s will be considered constant, an assumption which is valid since only the onset of instability is to be predicted. An inductive load possessing a large time constant T_2 is assumed. Owing to the impulsive output of the convertor, the output current will be discontinuous at the sampling instants, and therefore the current sampled by S_2 is taken to be the value just after the discontinuity. Finally, the time constant of the current transducer (e.g. a Hall-effect device) is neglected.

The error amplifier is assumed to have a low-pass characteristic represented by a single time constant T_1.

In Appendix 8.2, it is shown that the z transform of the sampled output of the system is given by

$$\Delta I_d(z) = \frac{\Delta I_r G_1(z) G_2 G_3(z)}{1 + G_1 G_2 G_3 G_5(z) - G_3 G_4(z) - G_1 G_2 G_3 G_5(z) G_3 G_4(z) + G_1 G_3 G_4 G_5(z) G_2 G_3(z)} \tag{14}$$

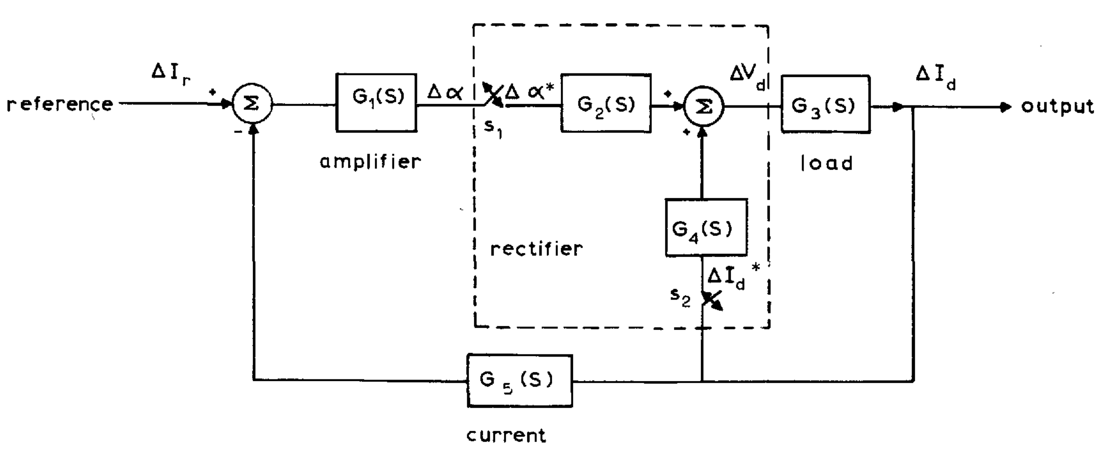

Fig. 5

Block diagram of linearised discrete model of rectifier under current control

Transfer functions $G_2(s)$ and $G_4(s)$ are given by eqns. 12 and 13. The remaining transfer functions are

$$G_1(s) = -\frac{K}{1 + sT_1} \tag{15}$$

$$G_3(s) = \frac{1}{R + sL} = \frac{1}{R(1 + sT_2)} \tag{16}$$

$$G_5(s) = 1 \tag{17}$$

The constants R and L include both the load and the internal rectifier resistance and inductance.* The internal effective resistance and inductance of the rectifier change from R_c and L_c when one element only is conducting, to $R_c/2$ and $L_c/2$ when two elements are conducting. These constants can be averaged as follows:

$$R_{av} = \left(\frac{2\pi}{q} - u^0\right)\frac{q}{2\pi}R_c + u^0\frac{q}{2\pi}\frac{1}{2}R_c$$

$$L_{av} = \left(\frac{2\pi}{q} - u^0\right)\frac{q}{2\pi}L_c + u^0\frac{q}{2\pi}\frac{1}{2}L_c$$

The gains of the amplifier, pulsing units and current transducer have been lumped into one factor K.

Let

$$TF(z) = G_1G_2G_3G_5(z) - G_3G_4(z) - G_1G_2G_3G_5(z)G_3G_4(z) + G_1G_3G_4G_5(z)G_2G_3(z) \tag{18}$$

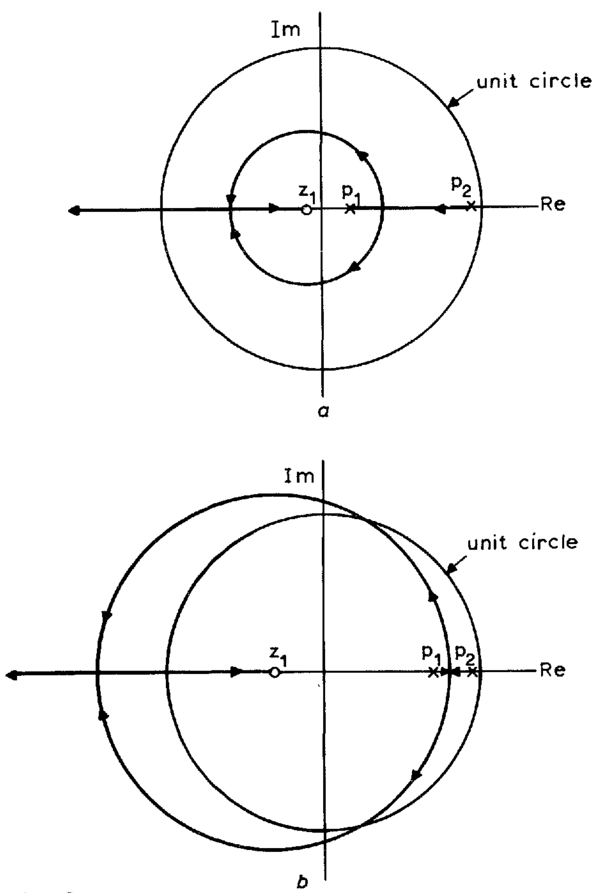

Fig. 6

Root loci for closed-loop systems

a Small time constant T_1

b Large time constant T_1

The dynamic behaviour of the closed-loop system is specified by the position of the roots of the characteristic equation

$$1 + TF(z) = 0 \tag{19}$$

The open-loop transfer function TF(z) is derived in Appendix 8.2. The poles and zeros are determined in Appendix 8.3. From eqns. 42 and 43, it is clear that the two poles are located on the positive real axis. Since the load time constant T_2 is assumed to be large compared with the sampling period, pole P_2 is close to point (+1, 0).

The zero is situated on the negative real axis between the origin and the point (−1, 0). Its location is determined by the commutation time T_u and time constants T_1 and T_2 (eqn. 44).

The root loci in Fig. 6 are for two values of T_1. With T_1 small (Fig. 6a), increase of loop gain beyond a critical value results in instability when the root locus crosses the unit circle at the point (−1, 0). Self-sustained oscillations therefore occur at half the sampling frequency.

With T_1 large, the root locus intersects the unit circle as shown in Fig. 6b, with the result that oscillations may occur at any frequency less than half the sampling frequency.

With a negligible commutation angle, the zero is located on the origin. Under these conditions, the root locus intersects the unit circle only at the point (−1, 0); i.e. oscillations may occur only at half the sampling frequency. The authors experimental results are in agreement with this prediction. In contrast, the root-locus analysis based on the sample-and-hold model for u = 0° predicts that oscillations are possible at any frequency.[7]

Oscillations at other subharmonics of the sampling frequency are, however, liable to occur for u = 0° if the disturbances are large. These modes of instability cannot be predicted by the small-signal model of this paper and can only be analysed using approximate methods, e.g. describing-function techniques.[4]

Closed-form expressions for the critical gain that leads to instability can be found by means of the modified Routh-Hurwitz criterion. If the change of variable $z = (r + 1)/(r - 1)$ is carried out in the characteristic equation, eqn. 19, we obtain

$$TF'(r) = 0 \tag{20}$$

The gain leading to instability can be determined from the coefficients of eqn. 20. Instability at half the sampling frequency occurs at a critical gain given by

$$K'_{crit} = \left(\frac{T_2 - T_1}{T_s}\right)\left(\left\{\frac{1 - \exp(-k_3)}{1 + \exp(-k_1)} - \frac{1 - \exp(-k_4)}{1 + \exp(-k_2)}\right\} - \left\{\frac{\exp(-k_4)}{1 + \exp(-k_2)} - \frac{\exp(-k_3)}{1 + \exp(-k_1)}\right\}\left[1 - \frac{1 - (L_c/L)\{1 + \exp(-k_2)\}^{-1}}{1 - (L_c/L)\exp(-k_4)\{1 + \exp(-k_2)\}^{-1}}\right]\right)^{-1} \tag{21}$$

where k_1, k_2, k_3 and k_4 are defined in Appendix 8.2.

In most practical cases, $L_c \ll L_s$, $T_2 \gg T_s$ and, to a good approximation,

$$K'_{crit} = \frac{T_2 - T_1}{T_s\left\{\frac{1 - \exp(-k_3)}{1 + \exp(-k_1)} - \frac{1 - \exp(-k_4)}{1 + \exp(-k_2)}\right\}} \tag{22}$$

If the commutation angle is negligible, eqn. 22 becomes

$$K'_{crit} = \frac{T_2 - T_1}{T_s\{\tan h(T_s/2T_1) - \tan h(T_s/2T_2)\}} \tag{23}$$

It can be shown that the critical gain expressions derived by Busemann[1] and Bjäresten[2] are special cases of eqn. 23 for a purely inductive load ($T_2 \to \infty$).

Instability at frequencies less than the sampling frequency occurs at a critical gain given by

$$K'_{crit} = \left(\frac{T_2 - T_1}{T_s}\right)\left[\frac{1 - \exp(-k_1)\{\exp(-k_2) + (L_c/L)\exp(-k_4)\}}{\exp(-k_3)\exp(-k_2) - \exp(-k_4)\exp(-k_1)}\right] \tag{24}$$

* *The internal rectifier resistance R_c is here included as it may, in some cases, represent a considerable proportion of the total resistance R*

For given values of T_1, T_2 and T_u, two critical-gain values will be obtained from eqns. 21 and 24. The smaller of the two will define a point on the stability boundary.

4 GAIN-CORRECTION FACTOR

The model developed above does not take into account the presence of ripple in the control voltage v_c. Bjäresten[2] was the first to introduce the concept of a gain correction factor that considers the effect of the ripple. In this Section, the gain-correction factor is generalised to include the effect of system resistance and commutation angle at any operating point.

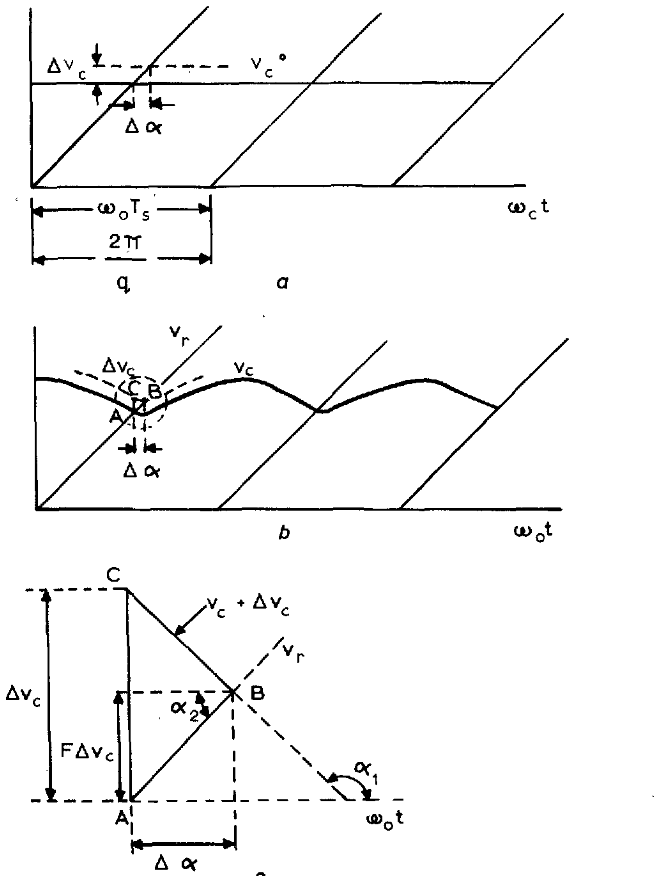

Fig. 7

Effect of ripple on control voltage

a D.C. gain of pulsing circuitry
b Effective gain of pulsing circuitry
c Definition of correction factor

The d.c. gain of the pulsing circuitry is defined in Fig. 7a as the ratio $\Delta\alpha/\Delta v_c$ with the rectifier on open loop, i.e. with no harmonics present in v_c. In the analysis that follows, this gain is assumed to be unity.

The effective gain of the pulsing circuitry is defined as $\Delta\alpha/\Delta v_c$ with the rectifier operating on closed loop, i.e. with harmonics present in v_c. Owing to these harmonics, dv_c/dt at the firing instant is not zero. This is illustrated in Fig. 7b, where a perturbation in v_c is followed by a change in $\Delta\alpha$. In Fig. 7c, the relevant portion of Fig. 7b is shown magnified.

For small perturbations, the effective gain can be expressed as the d.c. gain multiplied by a correction factor F.

From Fig. 7c,

$$\tan\alpha_1 = \frac{dv_c}{dt} = -\frac{\Delta v_c - F\Delta v_c}{\Delta\alpha}\,\omega_0$$

$$\tan\alpha_2 = \frac{dv_r}{dt} = \frac{F\Delta v_c}{\Delta\alpha}\,\omega_0$$

Solving for F, we get

$$F = \lim_{\Delta v_c \to 0}\frac{\Delta\alpha}{\Delta v_c} = 1/[1 - \{(dv_c/dt)/(dv_r/dt)\}] \tag{25}$$

As $$\frac{d\alpha}{dt} = \omega_0 \tag{26}$$

$$\frac{dv_r}{dt} = \frac{dv_r}{d\alpha}\,\frac{d\alpha}{dt} = \frac{\Delta v_c}{\Delta\alpha}\,\frac{d\alpha}{dt}$$

Therefore, using eqn. 26,

$$\frac{dv_r}{dt} = \omega_0 \tag{27}$$

An expression for the derivative of the control voltage with respect to time and in a closed form is presented in Appendix 8.5 and is given by eqn. 45.

Introducing dv_c/dt and $dv_r/dt = \omega_0$ into eqn. 23, the correction factor is obtained as

$$F = \Bigg\{1 - \frac{\sqrt{2}V_pK}{R}\Bigg(\frac{\sin(\gamma-\theta-\delta)}{\sqrt{\{1+(\omega_0T_1)^2\}}\sqrt{\{1+(\omega_0T_2)^2\}}} - \frac{K_3(1-K_1)}{\omega_0\{\exp(Ts/T_1)-1\}} - \frac{K_3'(1-K_1')}{\omega_0\{\exp(T_s/T_2)-1\}} + \sin\frac{\pi}{q}\left[\frac{K_4\{1-K_2\exp(T_u/T_1)\}}{\omega_0\{\exp(T_s/T_1)-1\}} + \frac{K_4'\{1-K_2'\exp(T_u/T_2)\}}{\omega_0\{\exp(T_s/T_2)-1\}}\right]\Bigg)\Bigg\}^{-1} \tag{28}$$

The various constants in this expression are defined in Appendix 8.5. The overall loop effective gain is now obtained from

$$K_e = K'F \tag{29}$$

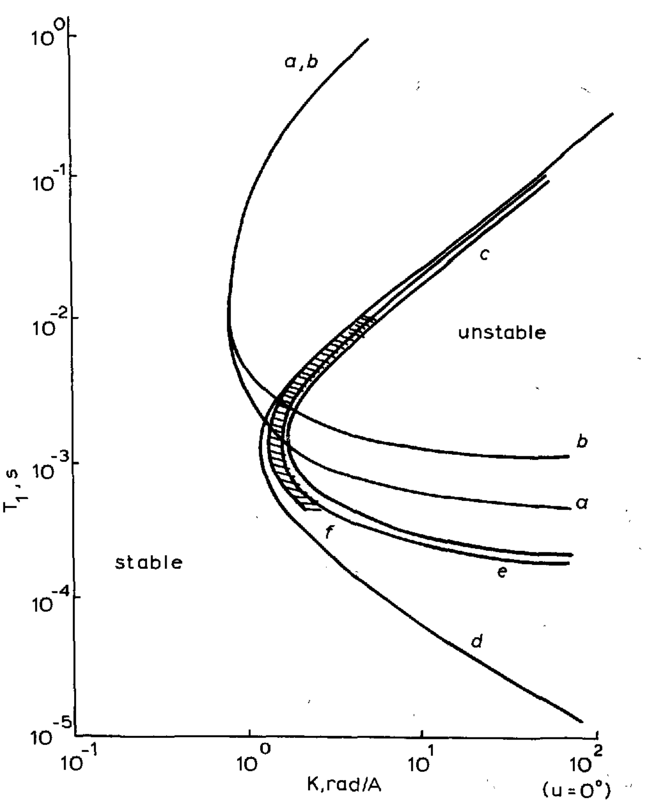

Fig. 8

Stability boundaries of 3-phase bridge rectifier

a Pure-delay model
b Sample-and-hold model
c New discrete model
d Describing-function model
e Digital-computer solution
f Experimental results

5 COMPARISON OF PERFORMANCE OF VARIOUS MODELS WITH EXPERIMENTAL RESULTS

A comparison between the model developed in this paper and other models suggested in the literature was made for a

3-phase bridge rectifier supplying a d.c. machine driving an a.c. generator connected to 3-phase a.c. mains. The d.c. motor was working with constant excitation and a feedback loop was enforcing constant armature current.

In Fig. 8, the stability boundaries for $u = 0°$ as predicted by different models are compared to experimental results under negligible-commutation-angle conditions. The boundary is a plot of time constant T_1 against the critical gain. Points on the left of the boundary are stable.

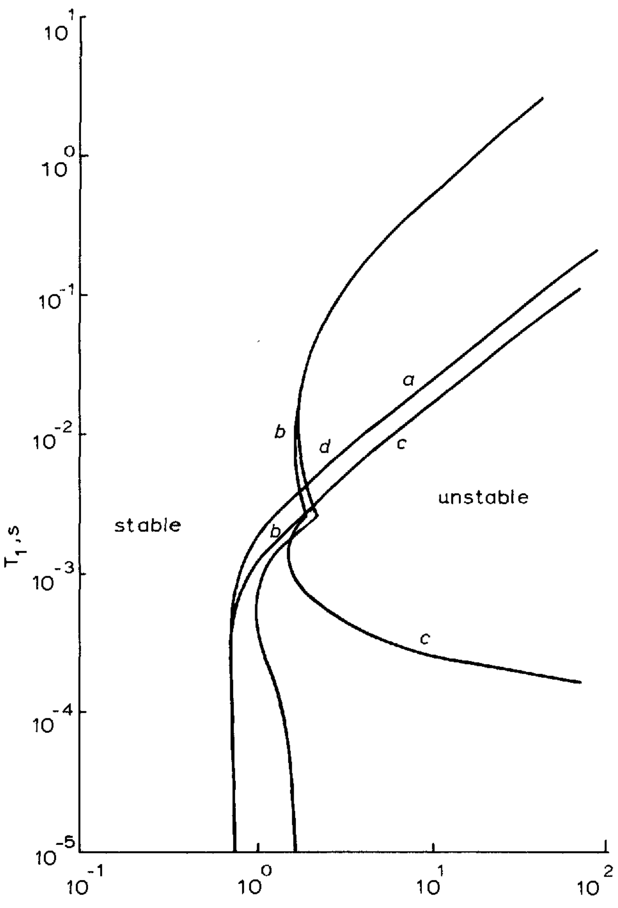

Fig. 9

Influence of ripple on stability boundary

a Boundary predicted by discrete model, neglecting effect of ripple, $u = 0°$
b As a, but $u = 30°$
c Boundary a as modified by gain-correction factor
d As c, but $u = 30°$

Curve a presents the results with the rectifier modelled as a pure transportation lag of half the sampling period in a continuous control loop.[6] Curve b results from the sample-and-hold model of Reference 7. Curve c uses eqn. 21 of this paper. To view the models of curves a and b in the most favourable light in comparison with the model of this paper, in all three cases the gain-correction factor F of eqn. 28 was implemented.

Curve d was obtained from Fallside's describing-function approximation.[4] As the attraction of this method is its simplicity, the gain-correction factor was not used.

Curve e was obtained from an elaborate digital program which solved exactly the differential equations of the system. With this program, it was possible to determine whether a particular operating point was stable by applying a small perturbation to the current reference value. This method, which, incidentally, was very time consuming, showed that, for small perturbations, instability occured at half the sampling frequency. It also showed that, if the perturbations were large, the system could become unstable at other subharmonics of the sampling frequency.

Because of the small uncertainty involved in determining the value of gain at which self oscillations are sustained, the experimental results are shown in Fig. 8 as band f rather than as a curve.

The influence of the gain-correction factor on the stability boundary is shown in Fig. 9. At low values of T_1, the ripple in the control voltage reduces the effective gain as shown earlier in Fig. 7c. This loss of gain increases the region of stable operation under the T_1K boundary, and the expansion of the stable region becomes more pronounced the nearer u approaches zero.

The influence of the commutation angle on the stability boundary is illustrated by Fig. 10. With increase of commutation angle, the stable region contracts. The point of slope discontinuity on the stability boundary is caused by the intersection of the boundaries described by eqns. 21 and 24. For points on the stability boundaries of Fig. 10 located below the discontinuity, instability occurs at half the sampling frequency; for points above the discontinuity, instability takes place at lower frequencies. The experimental points determined for the case $u = 20°$ show a good agreement with the corresponding theoretical boundary.

Spot checks of the experimental frequency of oscillations at high values of T_1 gave good agreement with theoretical predictions.

The oscillograms of Fig. 11 confirm visually some of the results arrived at in this paper. In Fig. 11a, the time constant is low (T_1 = 1ms) and self oscillations occur at 150 Hz. In Fig. 11b, the time constant is high (T_1 = 100 ms), oscillations now taking place at approximately 25 Hz, which compares favourably with the predicted frequency of 26 Hz.

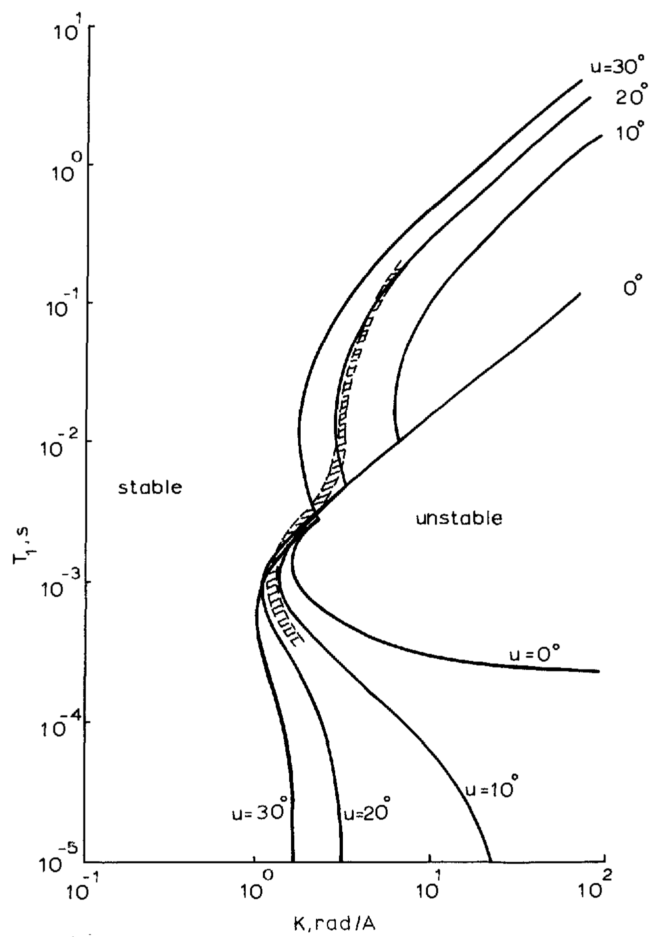

Fig. 10

Influence of commutation angle on stability boundary

6 CONCLUSIONS

From Fig. 8, we can conclude that the pure-delay model and the sample-and-hold model, even when improved by the gain-correction factor, give unacceptable stability boundaries.

The discrete model developed in this paper gives results consistent with the digital-computer solution and the experimental data over the whole range of the region explored.

The describing-function method gives perfectly acceptable results for large time constants but is pessimistic for low time constants. This technique, as developed in Reference 4, uses only the first term of a solution in series form derived by impulse analysis. The result obtained by taking into account a large number of terms is identical to the closed-form solution for $u = 0°$ of this paper. Further, if TF(z) of eqn. 18 is expressed as a function of s in infinite-series form and only the first two terms are considered, the approximate results obtained are identical to those from the describing-function method.

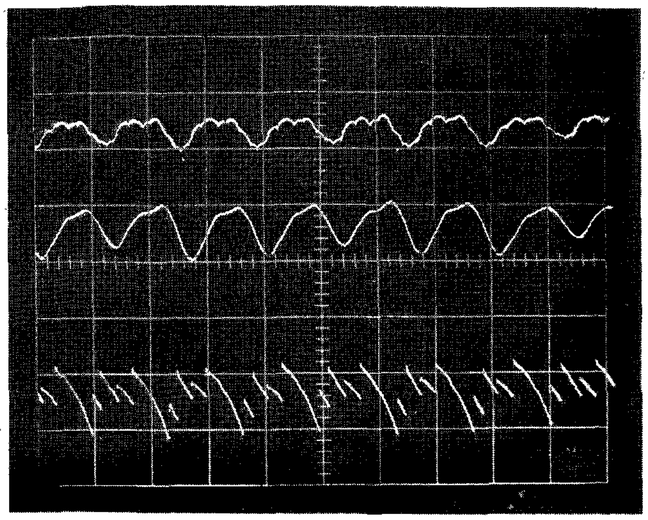

(i)
(ii)
(iii)

a

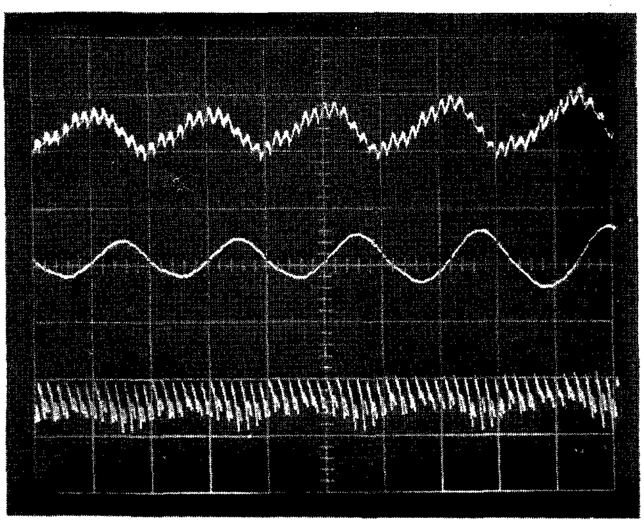

(i)
(ii)
(iii)

b

Fig. 11

Oscillatory behaviour of rectifier

$\alpha° = 15°$ $u° = 20°$
a $T_1 = 1$ ms, time scale = 5 ms/division
Frequency of oscillation = 150 Hz
(i) Direct current
(ii) Control voltage
(iii) Rectifier output voltage
b $T_1 = 100$ ms, time scale = 20 ms/division
Approximate frequency of oscillation = 25 Hz
Traces (i), (ii) and (iii) as in a

With $u = 0°$, and neglecting the gain correction factor, the exact solution gives curve a of Fig. 9. In the describing-function method, the effect of neglecting all terms but the first is a fortunate shift of the boundary towards closer proximity with the exact solution corrected for gain; i.e. curves d and c of Fig. 8.

From Fig. 9, we can conclude that the gain-correction factor has a very marked effect on the boundary, especially at small commutation angles, and should be taken into account if accuracy is required at low time constants.

Fig. 10 shows that the effect of commutation is to decrease the region of stability. At high time constants T_1, this decrease is caused by oscillations at frequencies lower than half the sampling frequency. At low time constants, the decrease is caused by a different mechanism. The presence of commutation decreases the slope of the control voltage which, in turn, increases the gain-correction factor. As the influence of the gain-correction factor is particularly pronounced at low time constants, the region of stability contracts as u increases.

Finally, from Fig. 8, it can be concluded that, with $u = 0$, the 1st-order system resulting if T_1 is reduced to zero is unconditionally stable. However, from Fig. 10, we can see that, for u larger than some specific value lying between 0° and 10°, the 1st-order system is only conditionally stable.

To summarise, the discrete model developed in this paper enables us to take into account the process of commutation and to apply successfully sampled-data theory and root-locus techniques to determine the frequency of oscillations and stability boundaries. It was shown for the first time that even moderate commutation angles have a marked influence on the stability and frequency of oscillation of the system.

A generalised gain-correction factor was also used to allow for the variation of the loop gain caused by the presence of ripple in the control voltage.

The test results show that the model developed in this paper gives a better prediction of stability compared to other techniques for $u = 0°$ and is the only model known to the authors capable of predicting stability boundaries for $u \neq 0°$.

7 REFERENCES

1 BUSEMANN, F.: 'H.V.D.C. transmission: hunting of rectifiers with marked compounding', ERA Report B/T 104, 1951

2 BJÄRESTEN, N.A.: 'The static converter as a high-speed power rectifier', Direct Current, 1963, 8, pp. 154-165

3 REIDER, A.M.: 'Analysis of the stability of the control systems of the Kashira-Moscow direct current transmission line', ibid., 1957, 3, pp. 227-240

4 FALLSIDE, F., and FARMER, A.R.: 'Ripple instability on closed-loop control systems with thyristor amplifiers', Proc. IEE, 1967, **114**, (1), pp. 139-152

5 FALLSIDE, F., GOODMAN, C.J., and JACKSON, R.D.: 'Stability of first-order sampling and thyristor systems', Electron. Lett., 1969, 5, pp. 567-568

6 PARRISH, E.A., and McVEY, E.S.: 'A theoretical model for single-phase silicon-controlled rectifier systems', IEEE Trans., 1967, AC-**12**, pp. 577-579

7 HAZELL, P.A., and FLOWER, J.O.: 'Stability properties of certain thyristor-bridge control systems. Pt. I—The thyristor bridge as a discrete control system', Proc. IEE, 1970, **117**, (7), pp. 1405-1412

8 AINSWORTH, J.D.: 'Harmonic instability between controlled static convertors and a.c. networks', ibid., 1967, **114**, (7), pp. 949-957

9 BAYOUMI, M.: 'Transient and steady-state current of a q-phase controlled rectifier', Neue Tech., 1962, 4, pp. 141-145

10 PERSSON, E.V.: 'Calculation of transfer functions in grid-controlled convertor systems', Proc. IEE, 1970, **117**, (5), pp. 989-997

8 APPENDIXES

8.1 Approximation of narrow pulse by impulse

The Laplace transform of a narrow pulse of height h and duration r is

$$\mathcal{L}\{v(t)\} = h\,\frac{1 - \exp(-\tau s)}{s} \qquad (30)$$

Expanding exp $(-\tau s)$, eqn. 30 becomes

$$\mathcal{L}\{v(t)\} = h\left[\frac{1 - \{1 - \tau s + (\tau s)^2/2! - \ldots\}}{s}\right]$$

Letting $\tau \to 0$ and neglecting high-order infinitesimals,

$$\lim_{\tau \to 0} \mathcal{L}\{v(t)\} = h\tau \qquad (31)$$

As

$$\mathcal{L}^{-1}\left[\lim_{\tau \to 0} \mathcal{L}\{v(t)\}\right] = \lim_{\tau \to 0} v(t)$$

therefore

$$\lim_{\tau \to 0} v(t) = h\tau\delta(t) \tag{32}$$

where $\delta(t)$ is the impulse function.

8.2 Input-output relationship of closed-loop system

Referring to Fig. 5, the following expressions can be written. [The notation $G_1 \ldots G_n(z)$ denotes the z transform of $G_1(s) \ldots G_n(s)$, where $z = e^{sT_s}$]

$$\Delta I_d(z) = \Delta\alpha(z)G_2G_3(z) + \Delta I_d(z)G_3G_4(z)$$

Therefore

$$\Delta I_d(z) = \frac{G_2G_3(z)}{1 - G_3G_4(z)}\Delta\alpha(z) \tag{33}$$

Also

$$\Delta\alpha(z) = -G_1G_2G_3G_5(z)\Delta\alpha(z) - G_1G_3G_4G_5(z) + \Delta I_rG_1(z) \tag{34}$$

Eliminating $\Delta\alpha(z)$ between eqns. 33 and 34, we obtain

$$\Delta I_d(z) = \frac{\Delta I_rG_1(z)G_2G_3(z)}{1 + G_1G_2G_3G_5(z) - G_3G_4(z) - G_1G_2G_3G_5(z)G_3G_4(z) + G_1G_3G_4G_5(z)G_2G_3(z)} \tag{35}$$

8.3 Derivation of transfer function TF(z)

Using eqns. 12, 13 and 15-17, and letting

$$K' = \frac{1}{2}(KV_{d0}\sin\alpha^0)/R$$

we get

$$G_1G_2G_3G_5(z) = K'T_s Z\left\{\frac{1 + \exp(-sT_u)}{(1 + sT_1)(1 + sT_2)}\right\} \tag{36}$$

$$G_3G_4(z) = \frac{L_c}{R}Z\left\{\frac{\exp(-sT_u)}{1 + sT_2}\right\} \tag{37}$$

$$G_1G_3G_4G_5(z) = \frac{KL_c}{R}Z\left\{\frac{\exp(-sT_u)}{(1 + sT_1)(1 + sT_2)}\right\} \tag{38}$$

$$G_2G_3(z) = -\frac{K'T_s}{K}Z\left\{\frac{1 + \exp(-sT_u)}{1 + sT_2}\right\} \tag{39}$$

Let

$$k_1 = \frac{T_s}{T_1} \qquad k_2 = \frac{T_s}{T_2} \qquad k_3 = \frac{T_s - T_u}{T_1}$$

$$k_4 = \frac{T_s - T_u}{T_2}$$

Now

$$Z\left\{\frac{1}{(1 + sT_1)(1 + sT_2)}\right\} = \frac{1}{T_2 - T_1}\left\{\frac{z}{z - \exp(-k_2)} - \frac{z}{z - \exp(-k_1)}\right\}$$

$$Z\left\{\frac{\exp(-sT_u)}{(1 + sT_1)(1 + sT_2)}\right\} = \frac{1}{T_2 - T_1}\left\{\frac{\exp(-k_4)}{z - \exp(-k_2)} - \frac{\exp(-k_3)}{z - \exp(-k_1)}\right\}$$

$$Z\left\{\frac{1}{1 + sT_2}\right\} = \frac{1}{T_2}\left\{\frac{z}{z - \exp(-k_2)}\right\}$$

$$Z\left\{\frac{\exp(-sT_u)}{1 + sT_2}\right\} = \frac{1}{T_2}\left\{\frac{\exp(-k_4)}{z - \exp(-k_2)}\right\}$$

Substituting the above expressions into eqns. 36-39 and using eqn. 18, we obtain the following expression for TF(z):

$$TF(z) = \Bigg\{z\Bigg(K'\left(\frac{T_s}{T_2 - T_1}\right)[(1 - L_c/L)\{\exp(-k_4) - \exp(-k_3)\} + \exp(-k_2) - \exp(-k_1)] + (L_c/L)\exp(-k_4)\Bigg) + K'\{T_s/(T_2 - T_1)\}\{\exp(-k_3)\exp(-k_2) - \exp(-k_4)\exp(-k_1)\} - (L_c/L)\exp(-k_4)\exp(-k_1)\Bigg\}[\{z - \exp(-k_2)\}\{z - \exp(-k_1)\}]^{-1} \tag{40}$$

8.4 Pole-zero pattern

Substituting eqn. 40 into the characteristic equation, eqn. 19, we obtain an expression that has the following structure:

$$1 + \frac{z(K'a + b) + K'c + d}{(z - e)(z - f)} = 0$$

or, after rearrangement,

$$1 + K'\frac{az + c}{(z - e)(z - f) + bz + d} = 0$$

Factorising the denominator and substituting the constants, we obtain

$$1 + K'\left(\frac{T_s}{T_2 - T_1}\right)(z[\{1 - (L_c/L)\}\{\exp(-k_4) - \exp(-k_3)\} + \exp(-k_2) - \exp(-k_1)] - \{\exp(-k_4)\exp(-k_1) - \exp(-k_3)\exp(-k_2)\})(\{z - \exp(-k_1)\}[z - \{\exp(-k_2) - (L_c/L)\exp(-k_3)\}])^{-1} = 0 \tag{41}$$

It is clear from eqn. 41 that there are two poles and one zero. The poles are situated on the real axis and are given by

$$P_1 = \exp(-T_s/T_1) \tag{42}$$

$$P_2 = \exp(-T_s/T_2) - (L_c/L)\exp\{-(T_s - T_u)/T_1\} \tag{43}$$

The only zero is also situated on the real axis, its abscissa being given by

$$Z_1 = \frac{\exp(-k_4)\exp(-k_1) - \exp(-k_3)\exp(-k_2)}{\{1 - (L_c/L)\}\{\exp(-k_4) - \exp(-k_3)\} + \exp(-k_2) - \exp(-k_1)} \tag{44}$$

8.5 Derivative of steady-state control voltage

The steady-state control voltage of a q-phase controlled rectifier with finite commutation angle can be obtained in a closed form by means of a Laplace transform.

The first derivative with respect to time of the steady-state control voltage at the firing instant is given by

$$\frac{dv_c}{dt} = \frac{K\sqrt{2}V_p}{R}\left(\frac{\omega_0\cos\{(2\pi/q) + \alpha' - \theta - \delta\}}{\sqrt{\{1 + (\omega_0T_1)^2\}}\sqrt{\{1 + (\omega_0T_2)^2\}}} - \frac{K_3(1 - K_1)}{\exp(T_s/T_1) - 1} - \frac{K_3'(1 - K_1')}{\exp(T_s/T_2) - 1} + \sin(\pi/q)\left[\frac{K_4\{1 - K_2\exp(T_u/T_1)\}}{\exp(T_s/T_1) - 1} + \frac{K_4'\{1 - K_2'\exp(T_u/T_2)\}}{\exp(T_s/T_1) - 1}\right]\right) \tag{45}$$

where

$$\alpha' = \alpha^0 + \frac{\pi}{2} - \frac{\pi}{q}$$

$$K_1 = \frac{\omega_0T_1\cos\gamma - \sin\gamma}{\omega_0T_1\cos\alpha' - \sin\alpha'} \qquad K_1' = \frac{\omega_0T_2\cos\gamma - \sin\gamma}{\omega_0T_2\cos\alpha' - \sin\alpha'}$$

$$K_2 = \frac{\omega_0T_1\cos\gamma' - \sin\gamma'}{\omega_0T_1\cos\alpha^0 - \sin\alpha^0} \qquad K_2' = \frac{\omega_0T_2\cos\gamma' - \sin\gamma'}{\omega_0T_2\cos\alpha^0 - \sin\alpha^0}$$

$$K_3 = \frac{\omega_0 T_1 \cos \alpha' - \sin \alpha'}{(T_1 - T_2)\{1 + (\omega_0 T_1)^2\}} \qquad K'_3 = \frac{\omega_0 T_2 \cos \alpha' - \sin \alpha'}{(T_2 - T_1)\{1 + (\omega_0 T_2)^2\}}$$

$$K_4 = \frac{\omega_0 T_1 \cos \alpha^0 - \sin \alpha^0}{(T_1 - T_2)\{1 + (\omega_0 T_1)^2\}} \qquad K'_4 = \frac{\omega_0 T_2 \cos \alpha^0 - \sin \alpha^0}{(T_2 - T_1)\{1 + (\omega_0 T_2)^2\}}$$

$$\theta = \tan^{-1}(\omega T_2) \qquad \delta = \tan^{-1}(\omega T_1)$$

If the commutation angle and all the resistances in the circuit are set to zero and operation under short-circuit conditions with $\alpha = 90°$ is assumed, eqn. 45 is reduced to the expression derived by Bjäresten.[2]

Discussion on
Thermal insulation for energy storage

L.C. Parker: I feel that much of what we have been hearing about today I would be unwilling to accept for the conventional free-standing controlled-input storage radiator. I think that this type of radiator has probably reached its optimum size, that is somewhere near 22·5 cm in depth. It is using materials to their maximum advantage, and is giving excellent results. There is another reason. Mr. Dickson mentions the fact that, to obtain improved performance, one must increase the core temperature. I think there are several reasons why one should not increase the core temperature. The first is that refractories become electrically conductive, and element temperatures should not be much above 950°C. I see the use of evacuated insulation in storage radiators as being applicable to heaters connected by a pipework, probably evacuated from a central site, and this is a quite different animal from the conventional storage radiator to which I have just referred.

Another important aspect which I feel must be taken cognisance of is that, in storage appliances incorporating air movement, most manufacturers use an insulation which is moderately flexible because this gives a sealed joint, and so a core box is not necessary to prevent leakage of air. Therefore, when specifying the desirable qualities of insulation, one thing should be added, that is to make certain that it maintains its rigidity. If one is thinking in terms of using a board, not only conductivity but also rigidity must be taken into account. The author does mention that he feels that there is a future for dense board. I have seen quoted costs, and I felt that they were far too high, but, if there are more recent figures I am interested to know if they are now more realistic.

In Table 1, the author has analysed one of the insulations and suggests a maximum temperature of 650°C because of the envelope. Is this envelope necessary after manufacture? I see nothing wrong with the envelope disappearing, being burnt off, once it is in situ, provided that one has stability, and in this material I know that, when the envelope is burnt off at high temperature, it in no way affects the conductivity. I wonder if the author isn't being a little harsh with the manufacturer.

Mr. Dickson has summarised the 'pros and cons' of powder insulation excellently, and I feel that, for storage radiators, they are negative, because the balance between particle size and density could not economically be maintained on a production line.

The crux of the paper is the economics. Mr. Dickson says that 'the cost multiplied by the conductivity should not be used as a yardstick for choosing insulations, as it seriously undervalues the best materials'. I feel that what has been done is a start, but that we have now to find the right material; and this is based neither on a K value nor on a material density, but on a material which strikes a correct balance between size, price and performance to give maximum acceptability. What we are talking about is heating people, and it must be quite clearly shown that the effects of the improved insulation are noticed by Mr. and Mrs. Smith as they are watching Coronation Street. That is what matters.

Miss M.V. Griffith: Has any work been done to establish the life of vacuum insulation at high temperature in terms of the maintenance of the high thermal resistivity? Vacuum insulation has been used for many years for low-temperature work, but, at high temperatures, outgassing of metal containers in use may cause difficulty, for example. It is not realistic to consider continuous evacuation with appliances such as storage radiators.

Mr. Parker's point about stability of thermal insulation is important. When storage radiators are dismantled for moving, the insulation may partially collapse. When the heater is put together again by people who perhaps do not realise the consequences of inadequate insulation, bad performance or even the danger of fire may result.

The variation of thermal resistivity with temperature has a great influence on the performance of storage heaters, and the use of opacified silica aerogel, the conductivity of which increases very little with temperature up to 700°C, has already led to better performance. It is a pity that we cannot find a material with a positive temperature coefficient of thermal resistivity for this purpose.

The maximum permissible temperature of storage-heater cores should not be too restricted. The better types of refractory do not increase rapidly in electrical conductivity until about 1200°C, and just below that temperature are still better electrical insulators than firebrick at 700°C. Kanthal heating elements can be used up to 1250°C, and some thermal insulation is usable up to 1150°C or more. Unless it has been decided that only electrically conducting storage materials such as feolite are to be used, so that sheathed elements become necessary, it is still feasible to reduce the size of storage heaters without paying the penalty of increased weight by the use of refractory cores at temperatures up to 1000°C.

J. Belson: I was particularly interested in your curves showing the change of conductivity with gas pressure for an aluminosilicate blanket. If you wanted to utilise this change in a device of variable conductivity, would you have to take account of the resilience (or rather, the possible lack of resilience) of the material? Presumably, you would be confining the blanket at different pressures, and would want to reproduce repeatedly a given thickness for a given pressure. Have you considered this at all?

D. J. Dickson (in reply): In general, I agree with Mr. Parker's comments, and, in particular, that storage radiators incorporating evacuated insulation must be considered as a complete central-heating system rather than as individual radiators.

Regarding the 650°C limit imposed by the glass-cloth envelope of the microporous insulation, if it will never be necessary to dismantle and reassemble that part of the heater using the original materials, this insulation can be used up to 1000°C.

The question of economics is a difficult one at this stage, and we must be careful not to discard a promising line of investigation prematurely because it looks too expensive.

While a 'factory-sealed' evacuated insulation as envisaged by Miss Griffith would be very attractive, I do not consider it to be economically feasible at the moment, but continuous evacuation is not out of the question using a central vacuum pump.

It is true, as Mr. Bilson suggests, that, on evacuating a fibrous blanket under load-bearing conditions, a large initial compression is experienced, and that the original thickness is not regained on returning to atmospheric pressure. The curves showing the change of conductivity with gas pressure refer to the blanket after this large initial compression has taken place. Subsequent evacuation produces much smaller changes in thickness, and, although the thickness for a given pressure may not be exactly reproducible, the resultant variation in thermal conductance is very small compared with the total change throughout the pressure range considered.

Paper 6495 P by DICKSON, D. J. [see 1971, **118**, *(10), pp. 1399-1407]*

Read before IEE Power Division Professional Group P5, 5th April 1972